



HAL
open science

Enhanced agent-based models for pedestrian crowds : insights from empirical data at the Festival of Lights and refinements of mechanical interactions, pedestrian shapes, and decisional aspects

Oscar Dufour

► To cite this version:

Oscar Dufour. Enhanced agent-based models for pedestrian crowds: insights from empirical data at the Festival of Lights and refinements of mechanical interactions, pedestrian shapes, and decisional aspects. Physique [physics]. Université Claude Bernard - Lyon I, 2024. Français. NNT : 2024LYO10338 . tel-04953804

HAL Id: tel-04953804

<https://theses.hal.science/tel-04953804v1>

Submitted on 18 Feb 2025

HAL is a multi-disciplinary open access archive for the deposit and dissemination of scientific research documents, whether they are published or not. The documents may come from teaching and research institutions in France or abroad, or from public or private research centers.

L'archive ouverte pluridisciplinaire **HAL**, est destinée au dépôt et à la diffusion de documents scientifiques de niveau recherche, publiés ou non, émanant des établissements d'enseignement et de recherche français ou étrangers, des laboratoires publics ou privés.

**THESE de DOCTORAT de
L'UNIVERSITE CLAUDE BERNARD LYON 1**

Ecole Doctorale N° 52

Physique et ASTrophysique [PHAST]

Discipline : Physique

Soutenue publiquement le 06/12/2024, par :

Oscar DUFOUR

**Enhanced agent-based models for pedestrian
crowds: insights from empirical data at the
Festival of Lights and refinements of
mechanical interactions, pedestrian shapes,
and decisional aspects**

Devant le jury composé de :

ZURIGUEL, Iker	PU, Univ. Navarra	Rapporteur, Président
SCHADSCHNEIDER, Andreas	PU, Univ. Köln	Rapporteur
VENEL, Juliette	MCF, Univ. Polytechnique Hauts-de-France	Examinatrice
RAMOS, Osvanny	MCF HDR, Univ. Claude Bernard Lyon 1	Examineur
TORDEUX, Antoine	JUN-PROF, Univ. Bergische Wuppertal	Membre invité
RODNEY, David	PU, Univ. Claude Bernard Lyon 1	Directeur de thèse
NICOLAS, Alexandre	CR HDR, UMR 5306	Encadrant de thèse

**PHD DISSERTATION from
The UNIVERSITY CLAUDE BERNARD LYON 1**

**Doctoral School N° 52
Physics et ASTrophysics [PHAST]**

Field: Physics

Public defence scheduled for 6 December 2024, by:

Oscar DUFOUR

**Enhanced agent-based models for pedestrian
crowds: insights from empirical data at the
Festival of Lights and refinements of
mechanical interactions, pedestrian shapes,
and decisional aspects**

In front of a jury composed of:

ZURIGUEL, Iker	PU, Univ. Navarra	Reviewer, President
SCHADSCHNEIDER, Andreas	PU, Univ. Köln	Reviewer
VENEL, Juliette	MCF, Univ. Polytechnique Hauts-de-France	Examiner
RAMOS, Osvanny	MCF HDR, Univ. Claude Bernard Lyon 1	Examiner
TORDEUX, Antoine	JUN-PROF, Univ. Bergische Wuppertal	Invited Member
RODNEY, David	PU, Univ. Claude Bernard Lyon 1	PhD Director
NICOLAS, Alexandre	CR HDR, UMR 5306	PhD Supervisor

RÉSUMÉ

TITRE: Modèles d'agents améliorés pour les foules de piétons : analyse des données empiriques de la Fête des Lumières et affinement des interactions mécaniques, des formes de piétons et des aspects décisionnels.

MOTS CLÉS: physique ; matière active ; dynamique de foules ; modélisation ; prise de décision ; instabilités dynamiques ; expériences de terrain

RÉSUMÉ: Avec la multiplication des événements de masse, la dynamique des foules est devenue un sujet d'étude de plus en plus important. Comprendre comment les groupes se déplacent et évoluent dans l'espace, en particulier à des densités moyennes et élevées, est crucial pour l'organisation de tels événements.

La première section de cette thèse de doctorat présente l'un des premiers ensembles de données de terrain sur les foules denses. Cet ensemble comprend aussi bien des trajectoires de piétons que des méta-informations collectées lors de la Fête des Lumières 2022 à Lyon, dans le cadre du projet franco-allemand **MADRAS**. Il comprend jusqu'à 7000 trajectoires, des données GPS, ainsi que des statistiques sur les collisions entre personnes. Par ailleurs, des événements rares ont été identifiés, offrant ainsi une description approfondie de la dynamique des piétons dans des scénarios réels complexes.

Je présente ensuite un cadre théorique de modélisation de la dynamique des foules qui intègre une composante décisionnelle, où les piétons ajustent régulièrement leur vitesse désirée, et une couche mécanique qui confronte ces décisions à la réalité physique environnante. La plupart des modèles existants échouent à reproduire fidèlement les interactions mécaniques, car ils reposent souvent sur des forces d'interaction idéalisées et des formes circulaires simplifiées. En m'inspirant de la littérature scientifique sur la dynamique granulaire, j'intègre aux équations newtoniennes, des interactions mécaniques plus réalistes, en utilisant des ressorts amortis à la fois tangentiels et normaux aux surfaces de contact. J'utilise de plus des données anthropométriques pour représenter le plus fidèlement possible le contour humain, en deux dimensions, plutôt que de recourir à de simples disques. Cela me permet de créer une foule synthétique qui intègre les hétérogénéités anatomiques.

En ce qui concerne la composante décisionnelle, les piétons s'efforcent de sélectionner une vitesse souhaitée tout en tenant compte de diverses contraintes métaboliques, physiques et psychologiques, la plupart étayées par des données empiriques. Ces contraintes incluent :

- ★ Une **contrainte de destination** qui prend en compte l'objectif d'atteindre un lieu spécifique.
- ★ Des **limites biomécaniques** liées aux capacités musculaires et articulaires des piétons.
- ★ Un coût lié à la **différence d'alignement entre le corps et la direction de mouvement souhaité**.
- ★ Une volonté de préserver sa **bulle sociale**, une zone que les individus souhaitent maintenir libre de toute intrusion, qu'il s'agisse d'obstacles ou de piétons voisins.

★ Une intention d'**éviter les collisions** ou interpénétration des espaces de confort lors d'un déplacement, basée sur des estimations de temps avant collision.

Cette zone de confort est modélisée par un champ scalaire d'inconfort dont les courbes de niveau ne sont pas simplement circulaires. Le modèle, dans sa globalité, est implémenté en C++ et testé dans divers scénarios. Après validation dans des situations simples impliquant des paires de piétons ou un piéton près d'un mur, les prédictions du modèle concordent avec les résultats d'expériences impliquant la propagation d'une poussée à travers une rangée de personnes, ou encore d'évacuations et de mouvements de faufilement entre murs et piétons.

J'étudie enfin les phénomènes collectifs qui se manifestent non seulement dans les foules, mais aussi dans le trafic véhiculaire, en particulier les ondes stop-and-go résultant de la croissance d'instabilités dynamiques. Pour mieux comprendre ces phénomènes, je simule un modèle de suivi automobile en file qui repose sur la tendance à maintenir un temps de retard constant par rapport au véhicule suivi. Bien que la version déterministe de ce modèle soit inconditionnellement stable, l'ajout de bruit entraîne de manière inattendue l'apparition d'ondes stop-and-go. J'explique cette observation en utilisant une analogie avec le pendule de Kapitza, qui développe un nouvel état stationnaire sous l'effet de fortes vibrations. Plus précisément, une discontinuité d'un paramètre d'ordre bien choisi apparaît lorsque le niveau de bruit ou la densité dépasse un certain seuil, faisant écho à une transition liquide-gaz. Ce bruit peut provenir d'inexactitudes dans les observations des conducteurs et des piétons, de difficultés dans le traitement cérébral de l'information ou d'interactions non prises en compte.

Mes recherches sur la dynamique des foules soulignent l'importance d'intégrer les processus décisionnels aux interactions mécaniques pour approfondir la compréhension des comportements collectifs complexes, en particulier dans les environnements bondés.

ABSTRACT

TITLE: Enhanced agent-based models for pedestrian crowds: insights from empirical data at the Festival of Lights and refinements of mechanical interactions, pedestrian shapes, and decisional aspects.

KEYWORDS: physics; active matter; crowd dynamics; modelling; decision-making; dynamic instabilities; field experiments

ABSTRACT: With the surge in mass events, crowd dynamics have become an increasingly important subject of study. Understanding how groups move and evolve in space, particularly at medium and high densities, is crucial for organising such events.

The first section of this PhD dissertation presents one of the first field datasets on dense crowds. This dataset includes pedestrian trajectories and meta-information collected during the 2022 Festival of Lights in Lyon as part of the Franco-German **MADRAS** project. It includes up to 7000 trajectories, GPS data, and contact information. In addition, some rare events have been identified, providing an in-depth description of pedestrian dynamics in complex, real-life scenarios.

Subsequently, I develop a theoretical framework for modelling crowd dynamics that integrates a decision-making component, where pedestrians regularly adjust their desired speed, and a mechanical layer that confronts these decisions with the surrounding physical reality. Most existing models fail to faithfully reproduce mechanical interactions, often relying on idealised interaction forces and simplified circular shapes. Drawing inspiration from the scientific literature on grain dynamics, I integrate more realistic mechanical interactions into the Newtonian equations, using damped springs that are tangential and normal to the contact surfaces. I also use anthropometric data to represent the human contour as faithfully as possible, in two dimensions, rather than using simple disks. This allows me to create a synthetic crowd that incorporates individual heterogeneity.

Regarding decision-making, pedestrians strive to choose a desired speed while adhering to various metabolic, physical, and psychological constraints, largely supported by empirical data. These constraints include:

- ★ A **destination constraint** which considers the goal of reaching a specific location.
- ★ **Biomechanical limits** related to the muscular and articular capacities of pedestrians.
- ★ A cost associated with the **misalignment between the body and the desired direction of movement**.
- ★ A desire to preserve one's **social bubble**, a zone that individuals wish to keep free of any intrusion, whether from obstacles or neighbouring pedestrians.
- ★ An intention to **avoid collisions** or interpenetration of comfort spaces during movement based on the estimation of time to collision.

This comfort space is modelled by a scalar field of discomfort whose contours are not simply circular. The full model is implemented in C++ and tested in various scenarios. After validation in simple situations involving pairs of pedestrians or a pedestrian near a wall, I successfully compare the model's

predictions with experiments involving the propagation of a push through a row of people, evacuations, and weaving movements between walls and pedestrians.

Finally, I investigate collective phenomena that occur not only in crowds but also in vehicular traffic, specifically stop-and-go waves resulting from the growth of dynamical instabilities. To better understand these phenomena, I simulate a car-following model that relies on maintaining a constant time gap with the lead vehicle. Although the deterministic version of the model is unconditionally stable, introducing noise intriguingly leads to the emergence of stop-and-go waves. I explain this observation using an analogy with the Kapitza pendulum, which develops a new stationary state under strong vibrations. Specifically, discontinuities in a suitably defined order parameter appear when noise or density exceeds a finite threshold, echoing a liquid-gas transition. This noise may stem from inaccuracies in drivers' and pedestrians' observations, difficulties in brain information processing, or unaccounted interactions.

My research on crowd dynamics highlights the importance of integrating decision-making processes with mechanical interactions to deepen our understanding of complex collective behaviours, notably in crowded environments.

ACKNOWLEDGEMENTS

First and foremost, I would like to express my deep gratitude to my supervisor, Alexandre Nicolas, who welcomed me with kindness in November 2021, when I was at the beginning of my journey. He witnessed my growth, guiding me step by step until I found my voice and spoke with confidence. Alexandre provided me with a nurturing, structured, challenging and protective environment - an ideal framework that allowed me to thrive with complete peace of mind. I can never thank him enough. I am deeply grateful for the valuable knowledge he has imparted to me, often through small phrases that, once analysed and reflected upon, illuminate and structure thought with remarkable clarity. Words cannot fully convey how thankful I am for his support.

I am equally indebted to Antoine Tordeux, with whom I had the privilege of working for three months. His encouragement to step out of my comfort zone introduced me to Germany and its vibrant cities like Cologne, Wuppertal, and Jülich, where I encountered exceptionally warm and friendly people. These experiences broadened my horizons and exposed me to innovative ways of working, such as incorporating physical activities like juggling into daily routines—a practice I adopted and shared with colleagues upon returning to France.

I wish to express my heartfelt gratitude to Rava Azeredo Da Silveira, my supervisor in Paris, who consistently encouraged me to delve deeper into theoretical neuroscience, particularly in exploring cognitive biases in decision-making tasks under risk—a line of work that, while not included in this PhD thesis for administrative reasons, could have undoubtedly found its place. His guidance not only expanded my intellectual horizons but also inspired me to embrace and celebrate the uniqueness that defines me.

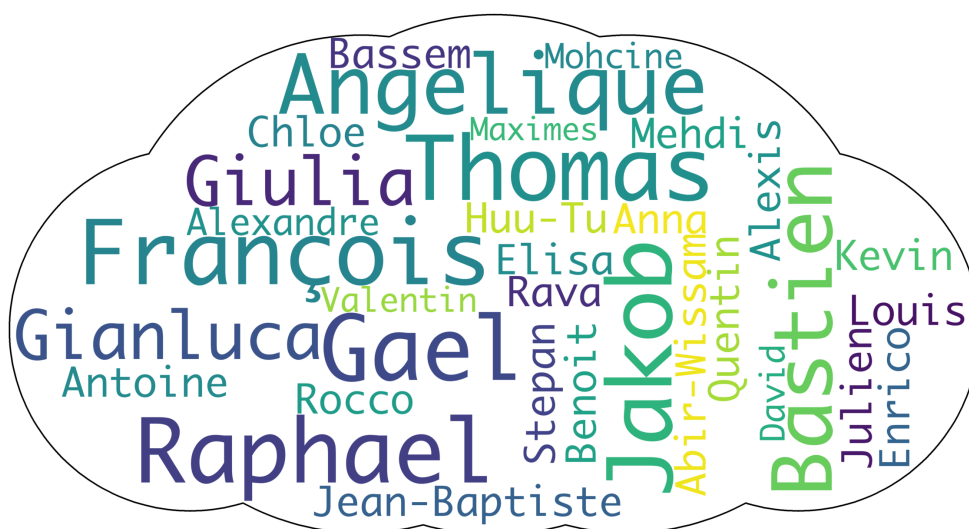


FIGURE 1: A word cloud shaped like a pedestrian slice featuring the first names of close young individuals who frequently interacted with me and contributed much to my PhD journey.

My heartfelt appreciation also goes to David Rodney, whose wisdom and experience were a beacon during moments of doubt when my handicap began to become unbearable. His guidance helped me navigate challenging times with clarity and resolve.

To my close and very close friends—whose names are illustrated in Fig. 1—I owe a special acknowledgment. Bastien and Elisa enriched my journey with stimulating psychological discussions, while Guillaume’s insights into political issues were endlessly fascinating. I hold dear the memory of Mehdi, whose passionate debates on constituent assemblies, inspired by those dedicated to climate disorder, left an indelible mark on me. Alexis brought boundless energy, and infectious joy to play Magic and Yu-Gi-Oh cards at a competitive level; Sensei Gaël generously shared his expertise through specialized informatics courses; Chloé brightened the often austere fourth floor with her dynamism and good humor; Kevin stood by me during the most trying times, especially in the hospital; and Julien, the Prince of Lebanon, exemplified openness, manners, enthusiasm for bodybuilding and meditation while floating in a salt-saturated water bath within a sensory isolation chamber. Each of you has profoundly impacted my life—thank you from the bottom of my heart.

I am also deeply grateful to the members of the Madras project—Benoît, Tu, Raphaël, and Mochine—whose camaraderie made this journey unforgettable. The wonderful moments we shared will always hold a special place in my memories.

A special mention goes to my family: to my mother, who fought to stay alive despite the many problems she had to overcome; and to my brothers for our late-night discussions on topics ranging from soil microbiology’s underground networks in Sweden to early childhood education—and even the order of food in a meal! These eclectic conversations have been both enriching and stimulating.

Lastly, I extend immense gratitude to the fifty-eight doctors who supported me over these three years. Their expertise and kindness taught me how to manage my chronic illness, embrace behavioural uniqueness, and continue advocating for a fairer and more inclusive society. While too numerous to name individually, each has played a vital role in this journey of personal growth.

CONTENTS

List of abbreviations	xi
Introduction	1
1 State of the art	5
1.1 Modelling crowds at different levels	6
1.1.1 Strategic level	6
1.1.2 Route choice (tactical level)	8
1.1.3 Operational level	14
1.1.4 Discussion	23
1.2 Physical modelling of crowds at the operational level: insights from microscopic models	24
1.2.1 The Social Force Model: a pioneering approach to simulating crowd dynamics	24
1.2.2 Mechanical aspects	28
1.2.3 Decision-making layer	33
1.2.4 Discussion	42
2 A multi-scale field study at the Festival of Lights in Lyon	43
2.1 Introduction	44
2.1.1 Controlled experiments in the real world	44
2.1.2 Controlled experiments in Virtual Reality	45
2.1.3 Field data	45
2.1.4 Scientific contribution	46
2.1.5 Lyon’s Festival of Lights	46
2.2 Methods	47
2.2.1 General organisation of the data collection campaign	47
2.2.2 GPS data of recruited participants and collision counts	47
2.2.3 Video processing and pedestrian tracking for the <i>TopView</i> cameras	48
2.2.4 Video processing and pedestrian tracking for the <i>LargeView</i> cameras	49
2.2.5 Conversion into global coordinates	50
2.2.6 Quantitative indicators	50
2.3 Data description	51
2.3.1 Size of the crowd and flow directions	51
2.3.2 Global view of the flow patterns on <i>Place des Terreaux</i>	54
2.3.3 Complex flow in a region of high density near the centre of the square	55
2.3.4 Unidirectional and bidirectional flow at diverse densities along the northern building	58
2.3.5 Identification of singular qualitative phenomena	62
2.4 Technical Validation	65

2.4.1	Trajectory datasets for the <i>TopView</i> recordings.	65
2.4.2	Trajectory datasets for the <i>LargeView</i> recordings	66
2.4.3	Mapping to real-world coordinates	67
2.4.4	Surveys	67
3	Modelling 2D pedestrian dynamics with non-circular comfort & physical spaces	69
3.1	Mechanical layer	72
3.1.1	Physical shape	72
3.1.2	Creating a synthetic crowd	72
3.1.3	Mechanical interactions	74
3.2	Decision-making layer	76
3.2.1	Proxemics	77
3.2.2	Time to collision cost	79
3.2.3	Privacy cost	81
3.3	Numerical results	82
3.3.1	Qualitative replication of simple situations	82
3.3.2	Forward propagation of a push through a row of people	83
3.3.3	Competitive egress of pedestrians	84
3.3.4	Two pedestrians passing each other in a corridor	87
4	A noise-induced Kapitza’s pendulum instability to account for stop-and-go dynamics in traffic	89
4.1	Car-following models and stochastic terms	94
4.2	Numerical evidence of a noise-induced instability and its empirical plausibility	95
4.3	Rationalisation with oscillatory driving	96
4.4	Stability switch: analogy with the Kapitza pendulum	97
4.5	Back to the first-order liquid-gas transition alluded to in previous works	99
	Conclusion	101
	Appendices	102
	Appendix A State of the art	103
A.1	Bio-mechanical cost (back on pages 36, 37 and 37)	103
A.2	Self-organisation phenomena in crowd dynamics (back on page 17)	106
A.3	Assessment of a pedestrian model (back on page 28)	107
	Appendix B A multi-scale field study at the Festival of Lights in Lyon	109
B.1	Extrinsic and intrinsic calibration (back on page 49)	109
B.2	Camera distortion in intrinsic calibration (back on page 48)	116
B.3	Uncertainty due to differences in height (back on page 49)	118
B.4	Spatio-temporal diagram to compute output flow (back on page 53)	118
B.5	Reference fundamental diagrams (back on page 58)	119
	Appendix C Modelling 2D pedestrian dynamics with non-circular comfort & physical spaces	121
C.1	Mechanical layer	121
C.1.1	Compact random packing of pedestrians (back on pages 69, 73)	121
C.1.2	Hertzian interaction law (back on page 74)	121
C.1.3	Mechanical interactions (back on pages 75, 76)	127
C.1.4	Moment of inertia calculation (back on page 81)	129

C.1.5	Mechanical equations summary (back on page 75)	129
C.1.6	Algorithm structure (back on page 76)	131
C.2	Decision-making cost	133
C.2.1	Static floor field term (back on page 42)	133
C.2.2	Bio-mechanical term (back on page 42)	135
C.2.3	Decision-making equations summary (back on page 42)	136
C.2.4	Derivation of the free walking speed (back on page 81)	136
C.2.5	Discomfort contour levels (back on page 78)	137
C.2.6	Computation of the minimal swelling coefficient such that the two discomfort fields overlap (back on page 79)	137
C.2.7	Numerical calculation of the integral for the Time to collision cost (back on page 80)	139
Appendix D Recovering stop-and-go dynamics in traffic flow with noise-induced Kapitza pendulum instability		141
D.1	Simulation setup (back on page 94)	141
D.2	Equilibrium solutions and linear stability analysis (back on page 95)	145
D.3	Extended stability analysis of the periodically driven system (back on page 98)	148
Bibliography		164

LIST OF ABBREVIATIONS

- 3LP** Three Linear Pendulum. 104
- ACC** Adaptive Cruise Control. 91
- ANSURII** ANthropometric SURvey 2. 69, 72–74
- ATG** Adaptive Time Gap. 95, 142
- CCD** Charge Coupled Device. 116
- CCTV** Closed-Circuit TeleVision. 46, 49
- CoM** Center of Mass. 36, 104, 127–130
- CSV** Comma-Separated Value. 50
- CT** Computed Tomography. 72
- DoF** Degree of Freedom. 112, 114
- EIF** Edinburgh Informatics Forum. 45, 46
- EMG** ElectroMyoGraphy. 37
- EORCA** Elliptical Optimized Reciprocal Collision Avoidance. 29
- EPSG** European Petroleum Survey Group. 50
- ETH** Eidgenössische Technische Hochschule. 45, 46
- FSE** Faster-is-Slower Effect. 33
- GC** Ground Clearance. 104
- GCS** Grand Central Station. 45, 46
- GPS** Global Positioning System. 3, 43, 47, 48, 53, 54, 101
- ICF** Inertial Car-Following. 94
- ILM** Institut Lumière Matière. 47
- KdV** Korteweg-de-Vries. 23

MADRAS Multi-Agent modelling of Dense cRowd dynAmicS. [i](#), [iii](#), [43](#)

MRI Magnetic Resonance Imaging. [72](#)

NHANES National Health and Nutrition Examination Surveys. [72](#)

NLM National Library of Medicine. [72](#)

ODE Ordinary Differential Equation. [147](#)

OV Optimal-Velocity. [94](#), [142](#)

OVM Optimal-Velocity Model. [18](#)

PAM Predictive-Avoidance Model. [26](#), [27](#)

PDE Partial Differential Equation. [23](#)

RGF Réseau Géodésique Français. [50](#)

RMSD Root Mean Square Differences. [65](#)

SATG Stochastic Adaptive Time Gap. [94–100](#), [142–145](#)

SD Stanford Drone. [45](#), [46](#)

SFF Static Floor Field. [42](#), [81](#), [133](#)

SFM Social Force Model. [24](#), [26–28](#), [42](#)

SICF Stochastic Inertial Car-Following. [96](#), [142](#)

SID Stochastic Intelligent Driver. [94](#), [96](#), [97](#), [142](#)

SOV Stochastic Optimal Velocity. [94](#), [96](#), [142](#)

TTC Time To Collision. [40](#), [41](#), [77–81](#)

UCY University of Cyprus. [45](#), [46](#)

US United States of America. [69](#), [72](#)

VR Virtual Reality. [19](#), [34](#), [45](#)

WS Weight Support. [104](#)

INTRODUCTION

A month into my doctoral contract in Lyon, my supervisor encouraged me to shift from reading scientific papers about crowd dynamics (Karamouzas et al., 2014; Helbing and Molnar, 1995; van Toll et al., 2020; Chen et al., 2018) to observing pedestrians in their natural environment. I left the institute and headed to the city centre, where I began my observations on a bench along *Rue de la République*, one of Lyon’s busiest pedestrian streets. I meticulously noted people’s actions, hoping these observations would spark new ideas. For instance, when people are waiting at the bus stop, they are not at all lined up according to a specific pattern; the distribution of these people at the stop is not trivial at first glance, especially during peak hours. Empty spaces appear around people discussing and disappearing; some of them continuously fidget and bump into others without realizing it. Although these insights were valuable, I wished to explore scenarios involving much larger crowds.



FIGURE 2: **Left** A crowded scene on *Rue du Président Édouard Herriot* during Lyon’s Festival of Lights in December 2022, captured through point-of-view photography. **Right** A mesmerizing light animation from the festival, seen through the same lens.

Conversations with locals revealed a significant city-wide event, gathering millions of people in total, ideal for observation: the [Festival of Lights](#). Held every December, this event began as a tribute to the Virgin Mary for protecting Lyon from the plague during the religious wars. It has since evolved into a massive international festival, celebrated for its remarkable light displays and artistic projections on historic buildings as illustrated in Fig. 2. We contacted city officials to understand how such an event is organised. Through our discussions, we realised our study on crowd dynamics could be practically relevant for them in organising the Festival of Lights. Indeed, they shared situations where they had been concerned about rapidly escalating issues: bottlenecks at *Place de la Bourse* and *Place des Célestins*, excessive density at *Place des Terreaux* in 2005, and *Rue Sainte-Catherine* being partially obstructed by opposing flows that could potentially lead to fatal consequences, in the worst conceivable case, without proper management.

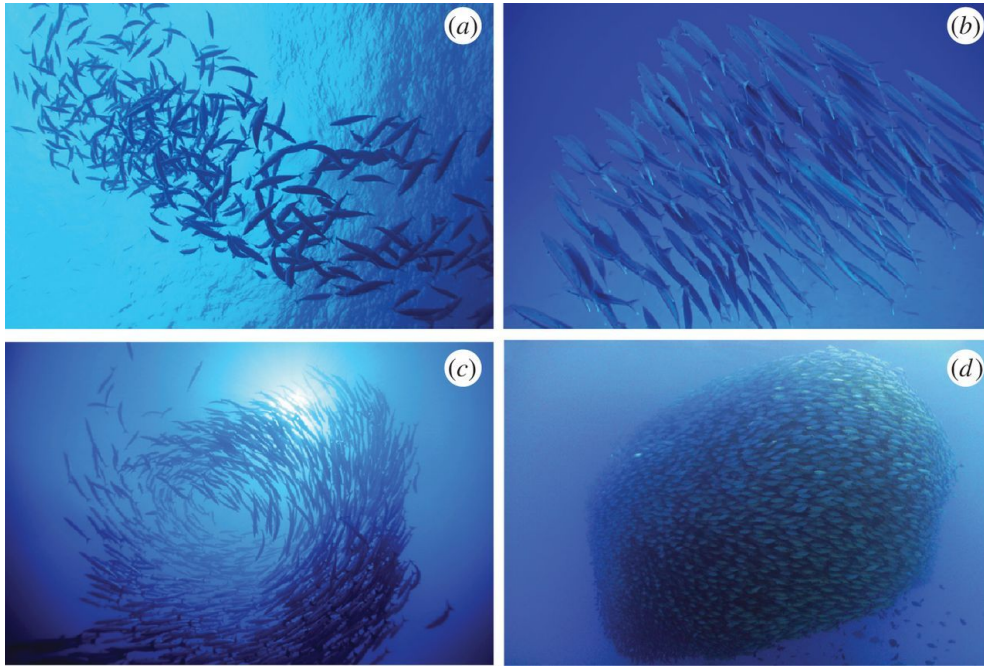


FIGURE 3: Collective motion patterns in fish schools. Individuals’ interactions give rise to a variety of dynamical structures that can be (a) poorly or (b) highly polarized. Other configurations of fish schooling include milling (c) and bait ball (d) structures. The figure is taken from Lopez et al. (2012).

Observing pedestrians on the street reveals that they typically walk at a constant speed, adjusting their pace to maintain this preferred speed, as though they were driven by a self-propelling force enforcing constant speed. Strikingly, the observed dynamics are not time-reversible, strictly speaking (if time were reversed, pedestrians would appear to move backwards while looking over their shoulders, which is not observed empirically). All this points to a non-equilibrium assembly distinct from more traditional physical systems like materials. In the latter, particles interact through spring-like forces and can often (but not always) be approximated as being in (or close to) equilibrium. In contrast, the non-equilibrium physics of active matter deals with multi-agent systems made of self-propelled agents that convert energy into work, similar to how pedestrians convert the chemical energy from food digestion into mechanical work as they walk. Assemblies of such self-propelled entities can exhibit intriguing large-scale collective behaviours like stop-and-go waves. Other examples of self-organized phenomena are illustrated for fish in Fig. 3.

Many models describing these movements are grounded in Newtonian physics, considering each pedestrian as a disk moving with a preferred speed according to Newton’s laws (Johansson et al., 2007; Czirók and Vicsek, 2000). Recently, some researchers have incorporated decision-making aspects from game theory through the preferred speed (Hoogendoorn and H.L. Bovy, 2003; Zanardi et al., 2021). The preferred speed is, therefore, no longer constant but the result of a decision process.

However, most models simplify pedestrians into basic shapes that fail to capture their true characteristics or effects. For example, representing pedestrians as disks with shoulder-width diameters cannot accurately replicate the observed densities at the Festival of Lights and simultaneously capture pedestrian weaving.

To address current limitations in pedestrian dynamics research and provide valuable insights for both the pedestrian community and potentially the organizers of the Festival of Lights, our study will proceed as follows:

Review of existing research We will begin by examining the current literature on crowd dynamics to establish the current state of crowd dynamics research, focusing on theoretical and empirical studies, identifying gaps in existing models, particularly regarding their ability to incorporate psychological and social factors alongside physical interactions.

Data collection We will provide a detailed overview of the data collection process during the Festival of Lights in Lyon, focusing on the various data types: pedestrian trajectories, [GPS](#) data, contacts and surveys.

Introduction of a novel model Building on our collected data, we will introduce a novel model that incorporates more realistic characteristics based on anthropometric data, moving beyond the simplistic representations used in current models. In particular, I will explain how this model uses damped springs for realistic mechanical interactions and integrates decision-making processes based on constraints such as destination goals and collision avoidance.

Exploration of decision-making and collective behaviours Finally, we will explore how decision-making can reproduce emergent collective behaviours, such as stop-and-go waves, offering new insights into how individual choices influence collective dynamics.

CHAPTER 1

STATE OF THE ART

Managing pedestrian flows is crucial during large-scale events like the Festival of Lights in Lyon. Systematic planning and monitoring of crowd motion help identify and prevent potential risks, such as high-density areas or erratic behaviours. However, flow management is not limited to pedestrians.

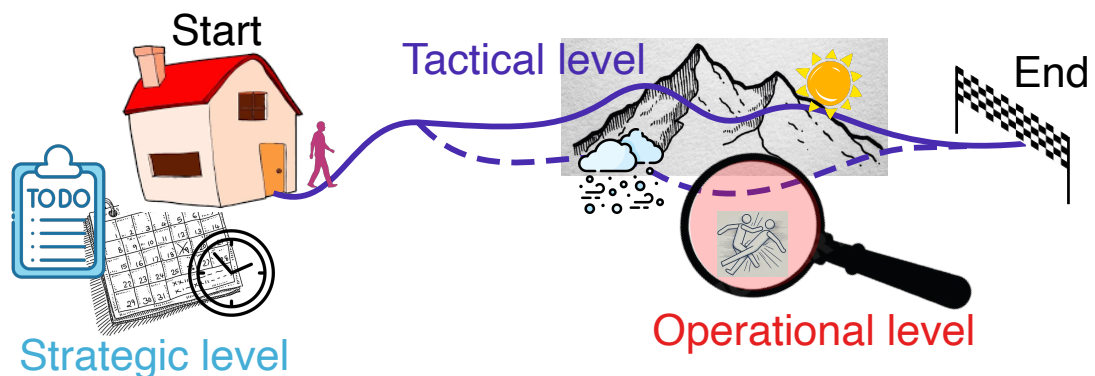


FIGURE 1.1: Schematic illustration of pedestrian dynamics modelling description levels. The **strategic level** entails planning and scheduling activities. This includes determining which activities to undertake, selecting their origin and destination, deciding the sequence in which they will occur, specifying the time and day for each activity, and choosing the mode of transport—whether public, private or on foot. The **tactical level** defines a set of routes to reach the chosen activity and, ultimately, selects the most suitable route. The **operational level** handles local motion along the chosen route, focusing on collision avoidance to ensure safe and efficient travel.

Large gatherings also generate significant vehicle traffic, including bicycles, cars, and public transport, for the arrival and departure of visitors or circulation in surrounding cities. Therefore, a comprehensive approach to flow management, encompassing pedestrians and vehicles, is essential to ensure the smooth running of major events like the Festival of Lights. This approach can be conceptualised at three distinct levels: strategic, tactical, and operational, using the terminology of Hoogendoorn and Bovy (2004), which are illustrated in Fig. 1.1. Each level plays a crucial role in ensuring the safety and enjoyment of attendees while maintaining order and efficiency. The **strategic level** forms the foundation of event planning, encompassing broad decisions about schedules, potential routes, and transportation

methods. At the **tactical level**, authorities focus on specific route selection and crowd guidance. Finally, the **operational level** delves into the minutiae of individual movements and interactions within the crowd. Understanding these three levels allows for a comprehensive approach to crowd management, addressing the big picture and the finer details of event organisation.

1.1 MODELLING CROWDS AT DIFFERENT LEVELS

1.1.1 STRATEGIC LEVEL

At the strategic level, on which we will focus here, the organisers plan the broad outlines of the event. They determine the activities to be carried out and their chronological order, identify the different possible routes and the nature of the terrain (asphalt, grass, mixed or clay paths, and so on), and choose the means of transporting the public and participants to these activities. While meticulous planning is vital, organisers must also account for their audience's typical behaviours and preferences, ensuring that the measures implemented align with the habits and expectations of festival attendees.

1.1.1.1 URBAN DATA AND TRAVEL BEHAVIOUR

Extensive research has been conducted on various daily activities and their planning. For instance, a study from [O'Fallon and Sullivan \(2003\)](#) was undertaken to analyse the differences in travel behaviour between weekdays and weekends in the three main urban areas of New Zealand, namely Auckland, Wellington, and Christchurch. The data collected from the household travel survey includes information on travelled distances, modes of transport, travel purposes, and vehicle occupancy. The analysis focuses on trips, defined as any displacement between two distinct activity locations with or without pausing for up to 90 minutes. Several key findings emerge from these data. Fewer trips are made on weekends, particularly on Sundays. However, the distances travelled per trip are longer on weekends. On weekdays, nearly 45 % of trips are related to work or study, as seen in [Fig. 1.2](#).

<i>Unweighted Count</i>		Total <i>N=41479</i>	Weekday <i>N=31007</i>	Saturday <i>N=5664</i>	Sunday <i>N=4808</i>
Purpose of trip leg	Home	29.5%	28.4%	32.4%	33.8%
	Work	14.4%	17.4%	5.3%	3.3%
	Education	3.7%	4.7%	.2%	.1%
	Shopping	10.7%	9.2%	17.2%	14.2%
	Personal business/services	5.3%	5.7%	3.9%	4.3%
	Social/recreational	17.0%	13.4%	26.7%	30.9%
	Change to another mode	9.1%	10.1%	6.1%	5.1%
	Accompanying someone else	10.3%	11.0%	8.1%	8.3%
	Left country	.0%	.0%	.1%	.0%
Total		100.0%	100.0%	100.0%	100.0%

FIGURE 1.2: Table showing the purpose of the trip by day of travel, taken from [O'Fallon and Sullivan \(2003\)](#).

Weekend travel patterns exhibit distinct characteristics compared to weekdays, with trips predominantly focused on leisure, shopping, and social or recreational activities. While car-sharing usage remains relatively constant throughout the week, a notable shift occurs from active modes (walking and cycling) and public transport towards car passenger trips during weekends. This transition results in higher vehicle occupancy on weekends, reflecting the nature of leisure activities and family or group travel. Although socio-demographic variables such as age, income, and household composition appear to

have limited influence on travel behaviour and mode choices in New Zealand's main urban areas, it's crucial to note that these findings are specific to regions grappling with significant congestion issues. Therefore, care should be taken when applying these findings to other contexts. The scope of travel behaviour studies varies widely, ranging from national analyses to hyper-local investigations. Fisher and Robinson (2010), in an article from the UK's Centre for Time Use, provides a comprehensive snapshot of daily behaviour across 22 countries for working individuals aged 18 to 64. Other studies focus on different scales: Ravalet (2007) examines travel patterns at the agglomeration level, Seneviratne and Morrall (1985) explores city centre dynamics, and Sparnaaij et al. (2022) even delve into travel behaviour at the scale of individual restaurants. Interestingly, contrasts in travel behaviour emerge when comparing different urban contexts. For instance, Ravalet (2007) reveals that affluent peripheral municipalities in Lyon, France, exhibit atypical motorisation patterns. More than half of the households in these areas are multi-motorised, starkly contrasting the less than 20% observed in other selected zones. This disparity underscores the importance of local context in shaping travel behaviour. From a psychological perspective, Ababio-Donkor et al. (2020) explores the impact of affect on commuting mode choice. Affect, defined by Baumeister and Bushman (2007) as an automatic response to positive or negative experiences, plays a crucial role in shaping travel decisions. Human memory of experiences appears disproportionately influenced by the most intense moments and final impressions in a sequence of events. Consequently, any prominent user experience with a particular travel mode, positive or negative, can significantly impact future behaviour. This nuanced understanding of travel behaviour, encompassing temporal patterns, local contexts, and psychological factors, offers valuable insights for transportation planners and policymakers. Considering these diverse influences, more effective strategies can be developed to manage urban mobility, especially in the Festival of Lights in Lyon context.

1.1.1.2 COMMERCIAL PEDESTRIAN SOFTWARES

In crowd organisation and event management, careful planning is crucial for success. While traditional methods, such as rules of thumb or empirically refined processes, are often used, there is also a growing interest in integrating insights from public research and advanced tools. For instance, software like *Iventis*, from Cusdin (2015), has been utilised in events such as the Dubai Expo 2020, an international exhibition held in Dubai from 1 October 2021 to 31 March 2022. *Iventis* assists organisers by enabling the creation of site maps, positioning infrastructure, and planning for multiple sites, which helps ensure comprehensive planning. The software offers approximate crowd densities and visitor flow rate calculations to help identify potential bottlenecks. Users can customise parameters like average pedestrian size (modelled as disks), walking speeds for specific areas, initial positions, and destinations. By assuming a constant walking speed along pedestrian paths, *Iventis* can estimate travel times. It also calculates flow rates using standard fundamental diagrams (i.e., the relationship between density and flow rate) as the one illustrated in Fig. 1.3. This static modelling approach provides an efficient and cost-effective way to test scenarios and make real-time adjustments. However, cautiously approaching claims about effectiveness cautiously is essential, as practical experiences may vary significantly from theory and rule of thumb.

Vadere is an open-source framework from Kleinmeier et al. (2019), designed to simulate microscopic pedestrian and crowd dynamics. It offers generic model classes, visualisation, and data analysis tools for two-dimensional systems. *Vadere* supports various locomotion models, including the Optimal Steps model from Seitz and Köster (2012) and Social Force models (Köster et al., 2013). Rather than being a model itself, *Vadere* serves as a simulation platform that incorporates these models. It is crafted to be lightweight and user-friendly, making it appealing for applications in crowd management.

By utilising tools like *Iventis* and *Vadere*, event organisers can enhance planning processes, encourage

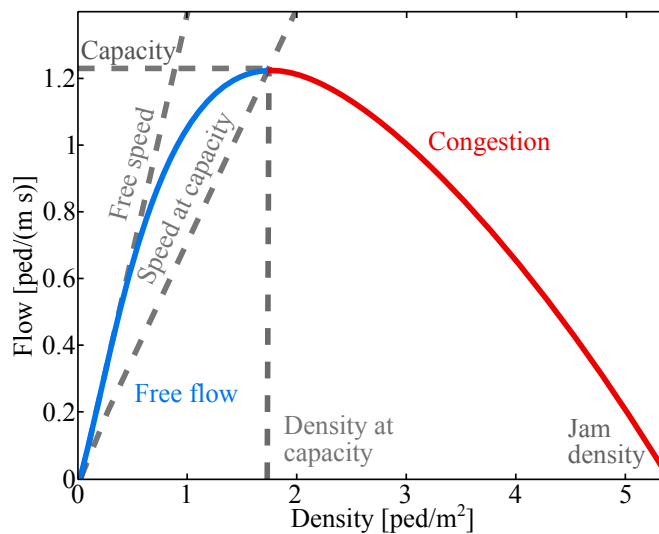


FIGURE 1.3: Scheme, adapted from Feliciani (2017), which illustrates common vocabulary in traffic flow for both vehicles and pedestrians. The curve is divided into two sections. **Free Flow:** Individuals move with minimal interaction, and increased density leads to higher flow. **Congestion Phase:** Beyond a certain density, additional people reduce flow. The slope of a line through the origin indicates velocity at the density point where it intersects the flow-density curve, as flow is expressed as $\rho v(\rho)$. For uniform flow, the curve's peak, known as capacity, represents the maximum flow for a given corridor setup, aiding in safer design.

collaboration, and proactively address crowd management challenges. Nonetheless, these tools have certain limitations, such as the need for more precise dynamic modelling and improved real-time data integration. Addressing these limitations through further research and development could significantly enhance their utility in planning and managing large-scale events, contributing to a safer and more successful experience for attendees.

1.1.2 ROUTE CHOICE (TACTICAL LEVEL)

Below the planning scale lies the tactical scale, which focuses on understanding pedestrian route choices during events such as the Festival of Lights. This involves analysing how pedestrians decide between different paths to the same activity. For example, in the *Parc de la Tête d'Or* during the festival, multiple paths—such as asphalt roads and natural soil trails—lead to the same attraction. The implicit rules influencing route choices can differ between these environments. On asphalt roads, pedestrians are likely to consider factors like distance, crowdedness, and travel time when choosing their routes. In contrast, when navigating trails in the park, factors like scenery, terrain, and proximity to attractions may guide their path selection. By understanding pedestrian decision-making at this tactical scale, event organisers can better manage crowd flows and enhance the overall experience during the Festival of Lights.

1.1.2.1 HUMAN TRAIL SYSTEMS IN PARKS

Helbing et al. (1997) developed an active walker model to explore the evolution of trails in urban green spaces. The image used to describe the model is a hiker traversing a virgin jungle. The first hikers use machetes to progress and build paths. They move slowly. However, this progress is capitalised upon and extended by subsequent hikers, who can then widen the path, lay stones, gravel, and finally, asphalt. In this model, each pedestrian evolves at a desired speed, the orientation of which results from a weighted sum of a term related to the target and a term related to their interaction with the

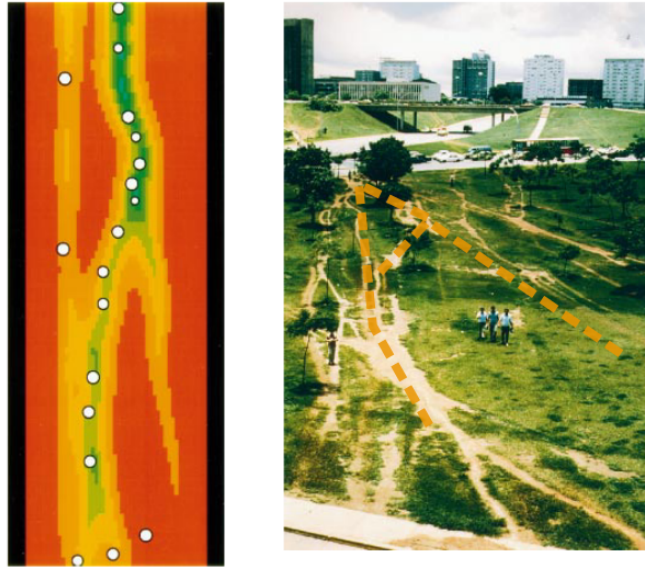


FIGURE 1.4: Similarity between the simulation result (**left**) and the trail system on the university campus of Brasilia (**right**), adapted from Helbing et al. (1997).

environment expressed as the gradient of a potential. The potential used is a smoothed version of a field $G(\mathbf{r}, t)$ expressing the gain of being at a particular position at time t . Physically, this smoothing can be seen as an imprecise visibility of the environment surrounding the pedestrian. The critical equation describing the evolution reads:

$$D_t [G(\mathbf{r}, t)] = \frac{G_0(\mathbf{r}) - G(\mathbf{r}, t)}{T(\mathbf{r})} + I(\mathbf{r}) \left[1 - \frac{G(\mathbf{r}, t)}{G_{\max}(\mathbf{r})} \right] \sum_{\alpha \in \{\text{pedestrians}\}} \delta(\mathbf{r} - \mathbf{r}_\alpha(t)) \quad (1.1)$$

where D_t denotes the material derivative, $G(\mathbf{r}, t)$ stands for the ease of motion at position \mathbf{r} and time t , $T(\mathbf{r})$ is a parameter reflecting the durability of paths against erosion (the larger T , the more established the path, i.e., the easier it is to reach the destination), $G_0(\mathbf{r})$ is the base ease of motion, $G_{\max}(\mathbf{r})$ is the maximum possible ease and $I(\mathbf{r})$ reflects the influence of footsteps on modifying the ease of motion. The first term is a relaxation term accounting for spatial inhomogeneities such as obstacles, hills, or trees. The second term reflects the tendency to prefer places already trodden by other pedestrians. After simulating the model numerous times, one can obtain a set of trajectories. When these trajectories are averaged spatially, they produce a density map that closely resembles the actual path map, as shown in Fig. 1.4.

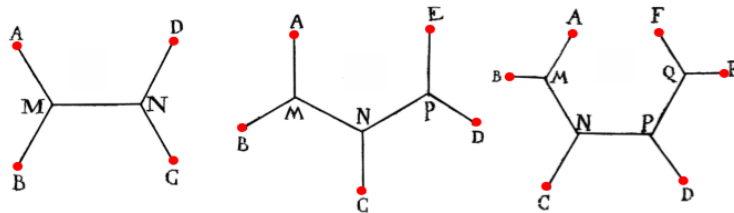


FIGURE 1.5: Examples of minimum Euclidian Steiner Trees, adapted from Brazil et al. (2014). The red dots are the terminal points, i.e. the starting and destination points.

Goldstone and Roberts (2006) extended that previous work by developing a virtual platform to explore how decentralised social groups differ from minimal Euclidean Steiner Trees, also known as cheapest

path networks. See Fig. 1.5 for examples. These trees, as explained by [Robins and Zelikovsky \(2008\)](#), are designed to minimise the total path length, calculated as the sum of all edge weights in the tree.

1.1.2.2 NAVIGATION FIELD AS A STANDARD TOOL

These field patterns are analogous to navigation maps, delineating potential pathways by considering various activity points and their sequential order. Their effectiveness stems from their comprehensive integration of multiple planning aspects. This holistic approach has made them particularly popular in robotics, enabling autonomous movement in robots, as elucidated by [Latombe \(1991\)](#) in his seminal work on robot motion planning. In this context, the robot is represented as a point in configuration space, reacting to an artificial potential generated by the target and the obstacles. The target creates an attractive potential, drawing the robot towards the goal, while the obstacles create a repulsive potential, pushing it away. The negative gradient of the total potential is interpreted as an artificial force guiding the robot. The robot moves systematically towards the lowest values of the global potential. For a visual representation of the navigation field, including obstacles, please refer to Fig. 1.6.

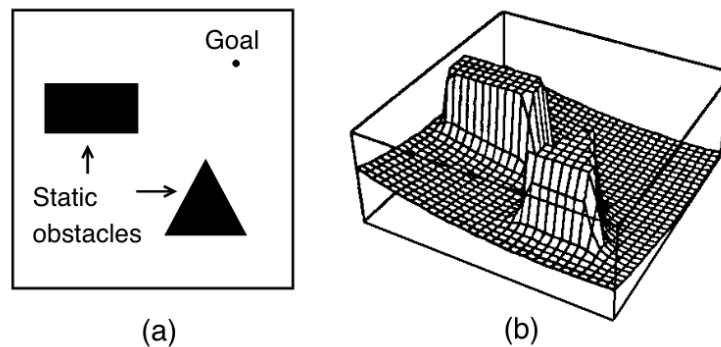


FIGURE 1.6: Global potential field (b) associated with the environment (a), taken from [Soulignac and Taillibert \(2006\)](#).

1.1.2.3 SHORTEST PATH IN CITIES

An experiment by [Seneviratne and Morrall \(1985\)](#), in downtown Calgary, Alberta, Canada, aimed to evaluate the factors influencing pedestrians' route choices within the city's central business district. Researchers conducted an origin-destination survey interviewing 2900 pedestrians at 32 downtown locations over nine consecutive work days. Interviewers asked pedestrians about their current trip, including origin, destination, route taken, and the primary factor influencing their route choice from a list of 10 options, such as shortest route, least crowded, and most attractions. As a result, the most significant factor influencing route choice was the shortest route between origin and destination, cited by 50.7% of respondents. Habitual behaviour was the second most common factor, with 21.7% of respondents consistently using the same route out of habit. Secondary considerations included factors like congestion level, safety, and visual attractions. Specific groups, like shoppers, valued routes with more attractions, while commuters preferred direct routes.

To model such pedestrian behaviour, a potential field approach can be employed, where the field values represent the shortest distance to the target destination, calculated using [Dijkstra \(2022\)](#)'s algorithm on a graph representation of the environment. The potential field values increase as the distance from the target increases, creating a gradient that guides pedestrians toward their destination, as illustrated in Fig. 1.6. A repulsive term can be introduced to account for obstacles and walls, exponentially increasing

as the distance from the obstacle decreases. This repulsive term ensures that pedestrians avoid colliding with obstacles and walls while following the general direction towards the target, as the potential field gradient dictates.

In most cases, the pedestrian reaches its goal without any issues. However, in specific situations, a pedestrian may become trapped in a local minimum or need to cross a virtual barrier, such as close walls (as discussed by [Soulignac and Taillibert \(2006\)](#)). To address this problem, [Dorst and Trovato \(1989\)](#) proposed the so-called wavefront expansion method. The idea is first to discretise the space into a grid and then calculate the potential field values locally. This expansion begins by defining the target cell as 0. Then, each closest neighbour (adjacent cells which are situated in the four cardinal directions) of the goal cell is defined as 1; then, each closest neighbour of the cells with value 1 is defined as 2 (if it has not been evaluated before); and so on. The first three steps of the wavefront expansion are illustrated in Fig. 1.7. By construction, each cell labelled by $i > 0$ has a neighbour with a lower potential: the one labelled $i - 1$. Thus, there are no local minima.

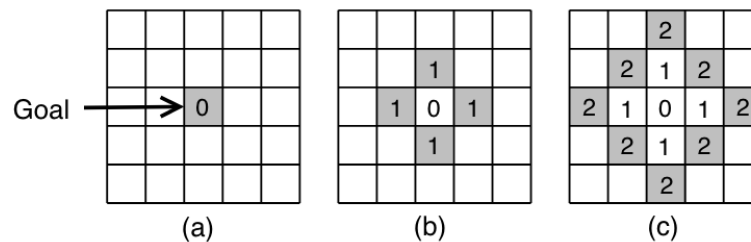


FIGURE 1.7: Evolution of the potential field wavefront (cells filled in grey). Cell labels represent potential field values (undefined in empty cells), extracted from [Soulignac and Taillibert \(2006\)](#).

More complex but crucial situations in high-density environments arise when, instead of walls, one encounters rows of stationary pedestrians, who are not considered obstacles. This type of configuration requires both operational-level anticipation and planning on a more global scale. The coupling between these two levels—operational and tactical—remains a challenge for which no simple solution has yet been found.

1.1.2.4 FASTEST PATH IN CITIES

In the presence of dynamic obstacles like crowds, pedestrians may not choose the shortest path due to the risk of being trapped within the crowd. Instead, their behaviour may be to select a path that minimises travel time. This route choice mechanism is implemented in dynamic floor field models, as demonstrated by [Höcker et al. \(2010\)](#) in their work on efficient navigation methods for microscopic pedestrian simulations. A straightforward approach is to replace the edge weight of a graph representation of the environment, which is typically the distance between two vertices of an edge, with the travel time. These travel times are updated in real-time based on pedestrian local density near the edge, affecting walking speed and travel time. Fig. 1.8 illustrates an example of a dynamic floor field that utilises travel times to guide pedestrian movement.

1.1.2.5 REAL-LIFE SITUATIONS THAT REQUIRE MORE GENERAL ROUTE CHOICE MODELS

We have seen that pedestrians choose their route in cities primarily based on distance and travel time. However, [Chen et al. \(2023\)](#) from Purdue University noticed that subtle incentives in the urban landscape (called nudges), such as sidewalk colour, as shown in Fig. 1.9, could significantly change path choices.

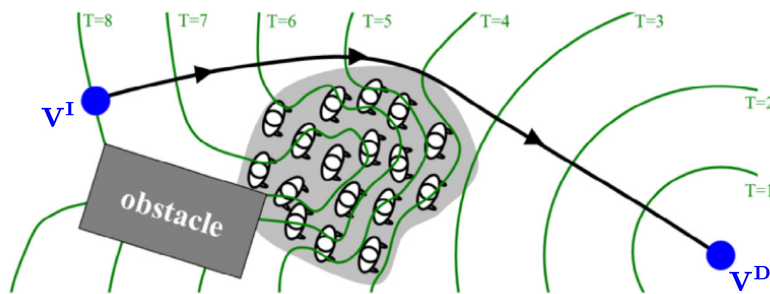


FIGURE 1.8: This figure, adapted from Höcker et al. (2010), illustrates a dynamic navigation field that calculates pedestrian travel times from the initial vertex V^I to the destination vertex V^D . The most direct route is obstructed by a crowd, which would significantly slow movement compared to unoccupied areas. As a result, the optimal path circumvents the group of pedestrians to minimise travel time.

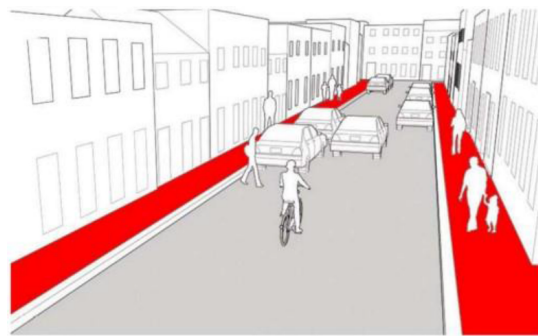


FIGURE 1.9: In the experiment conducted by Chen et al. (2023), subjects were shown a virtual red sidewalk as part of the study. Indeed, participants experienced this virtual environment from the perspective of their virtual apartment. As they prepared to leave, a message on the door informed them: "When the distance is less than 2.5 miles, 3 out of 4 people (75 %) choose to walk rather than use motor traffic." This scenario was designed to influence the subjects' route choices, encouraging them to walk when deciding how to reach a destination.

To test the effectiveness of nudges, the researchers designed an online experiment involving 1984 participants recruited via MechanicalTurk (2005) (a web-based micro-work platform that aims to have humans perform more or less complex tasks online for compensation). Participants had to imagine themselves as tourists in a virtual fictional city and react to different scenarios involving three types of nudges:

Sidewalk colour Comparison between uncoloured sidewalks and sidewalks painted red (energising) or blue (calming).

Priming with images of walking shoes Exposing some participants to images of shoes before answering questions about their interest in walking.

Descriptive norms Messages indicating that 75 % of tourists chose to walk rather than use motorised transport.

The results revealed significant effects of these nudges:

Colored sidewalks, whether red or blue increased the appeal of walking by about 32 % compared to uncoloured sidewalks, with no significant difference between red and blue.

Priming with images of shoes increased interest in walking by about 20 %.

Normative messages positively encouraged participants to choose walking when informed that most other tourists walked.

Another situation where pedestrian behaviour is more complex than merely optimising travel time is when navigating a geometrically complex environment with obstacles like a pillar. Gabbana et al. (2022) demonstrate that pedestrians tend to choose routes that minimise their perceived travel time rather

than the overall travel time computed for all pedestrians combined. This individual optimisation can lead to a sub-optimal traffic distribution from a system-wide perspective, deviating from what would be considered optimal for global welfare. The distinction between optimising individual travel time (user equilibrium) and global travel time (system optimum) is crucial in understanding these dynamics.

1.1.2.6 MORE GENERAL STATEMENT OF THE ROUTE CHOICE PROBLEM

It appears that path choice is influenced not only by the minimisation of distance or travel time but also by psychological factors. This concept is supported by a more comprehensive theory of path choice, which draws inspiration from the utility theory, introduced by [Von Neumann and Morgenstern \(1947\)](#), and the prospect theory, proposed by [Kahneman and Tversky \(1979\)](#), in decision-making. Deterministic utility models, such as the one proposed by [Bovy and Stern \(2012, Chap. 5.3\)](#), assume travellers have perfect information and choose the route that maximises their utility. The utility of route i is typically expressed as:

$$V_i = \beta_1 X_{i1} + \beta_2 X_{i2} + \dots + \beta_n X_{in} \quad (1.2)$$

where V_i represents the deterministic utility, X_{ij} denotes the attributes of route i (e.g., estimated distance, estimated travel time - see Fig. 1.10 for the relation between subjective and objective travel time while performing motor tasks such as walking and cognitive tasks like mental calculations), and β_j are the corresponding coefficients. The route with the highest utility is chosen with certainty. These models are simple to implement but do not account for perception errors or taste variation among travellers. They tend to assign all traffic to a single best route between an origin-destination pair, which is usually unrealistic.

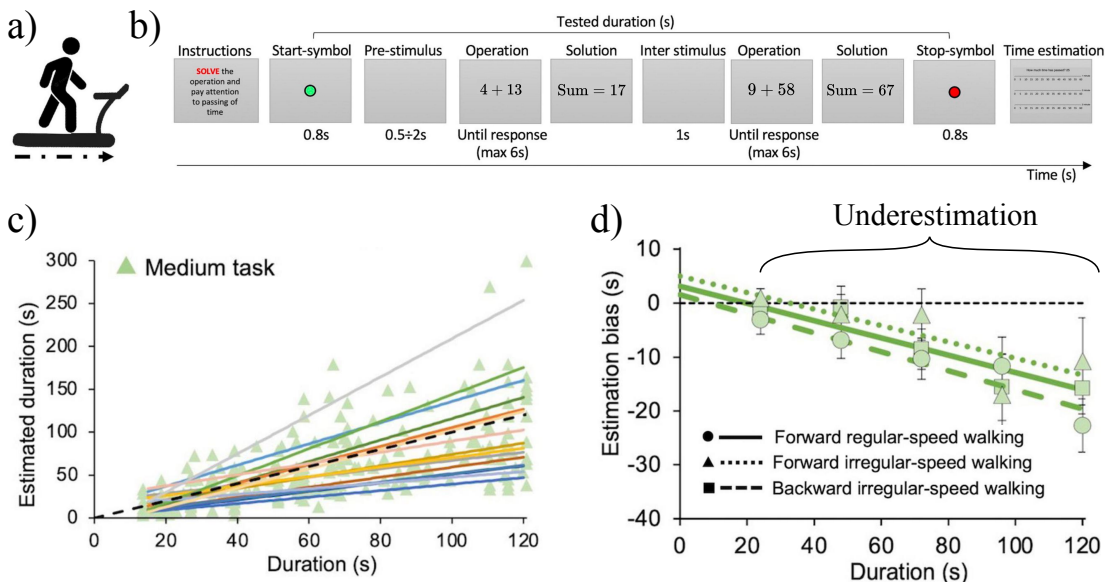


FIGURE 1.10: (a) Illustration of the experiment with a pedestrian walking at different speeds on a treadmill while looking at a screen displaying instructions. (b) Example of the screen display during the duration of a trial. (c) Estimated duration versus actual duration, adapted from [D'Agostino et al. \(2023\)](#). Each coloured fit line represents the average time estimate for an individual participant. Triangles indicate the forward irregular-speed walking condition on a treadmill. The medium-difficulty task involved solving simple arithmetic problems, specifically adding a 1-digit number to a 2-digit number (e.g., $4 + 13$), while walking. The sum of these operations never exceeded 100. (d) Averaged estimation bias (bias = mean(estimate - actual duration)) computed over 21-second intervals, along with their best-fit curves. Error bars represent the standard error across participants. On average, participants overestimated shorter durations and underestimated longer durations. That cognitive bias is widespread in cognitive psychology when you ask someone to estimate a positive quantity, as evidenced by the experimental findings of [Izard and Dehaene \(2008\)](#) and the theoretical framework proposed by [Petzschner et al. \(2015\)](#).

Unlike deterministic utility models, random utility models incorporate uncertainty in route utilities, which accounts for imperfect information, perception errors, and taste variation. This probabilistic framework, pioneered by [Becker et al. \(1963\)](#) and further developed by scholars like [Loomes and Sugden \(1995\)](#) and [Bovy and Stern \(2012\)](#), provides a more nuanced representation of traveller decision-making. The utility of route i is expressed as:

$$U_i = V_i + \epsilon_i \quad (1.3)$$

where V_i is the deterministic component and ϵ_i is a random error term. The probability of choosing route i is then given by:

$$P(i) = \text{Prob}(U_i > U_j \text{ for all } j \neq i) \quad (1.4)$$

Common forms include logit ([Berkson, 1944](#)) and probit ([Finney, 1947](#)) functions. Some models, such as the one proposed by [Hoogendoorn and Bovy \(2004\)](#), incorporate randomness directly into potential trajectories using optimal control formalism. This approach yields more realistic results, particularly in congested networks. While these random utility models offer enhanced accuracy, they are generally more complex to define and implement.

1.1.3 OPERATIONAL LEVEL

We can study the motion of crowds on an even smaller scale by looking at the walking behaviour of pedestrians. When organising events such as the Festival of Lights, it is essential to understand how people interact physically and far from each other to prevent disastrous events. The main models used at the operational level are macroscopic, microscopic, and mesoscopic (see [Fig. 1.11](#) for a visual summary). Macroscopic models describe traffic as a continuum using aggregated quantities like density, flow, and speed fields. They are useful for modelling collective phenomena and situations where heterogeneity is less important. To solve them efficiently, some discrete network-based approach can be built as shown by [Göttlich et al. \(2011\)](#). Microscopic models simulate individual vehicles and drivers, making them suited for heterogeneous traffic, human behaviour analysis, and detailed visualisation. These include follow-the-leader models ([Fehrenbach et al., 2015](#)) and cellular automata ([Schadschneider, 2001](#)). Mesoscopic models are hybrid approaches combining micro and macro elements, such as master equations ([Mahnke and Pieret, 1997](#)) and gas-kinetic models ([Festa et al., 2018](#)). They can be tricky to build and solve. In contrast, macroscopic models often use partial differential equations based on fluid dynamics analogies. Specifically, they typically consist of a continuity equation for mass conservation and a velocity-dependent equation for momentum conservation. On the other hand, microscopic models use ordinary differential equations or discrete update rules to model individual motions. Consequently, the choice of model usually depends on the specific application, available data, and computational requirements. Let's then delve into how macroscopic equations offer valuable insights for understanding and managing crowds at the Festival of Lights. Additionally, we will explore how the complementary use of microscopic equations further enhances these insights in the following sub-subsections.

1.1.3.1 UNIDIRECTIONAL AND BIDIRECTIONAL FLOW SCENARIOS

At the heart of macroscopic models lies the mass conservation equation, commonly called the continuity equation. It establishes a relationship between the spatial variation of flow, denoted as $\mathbf{Q} \doteq \rho\mathbf{v}$, and the temporal variation of density. This relationship ensures the conservation of density over time, as expressed by the following equation:

$$\frac{\partial \rho}{\partial t} + \text{div}(\mathbf{Q}) = 0 \quad (1.5)$$

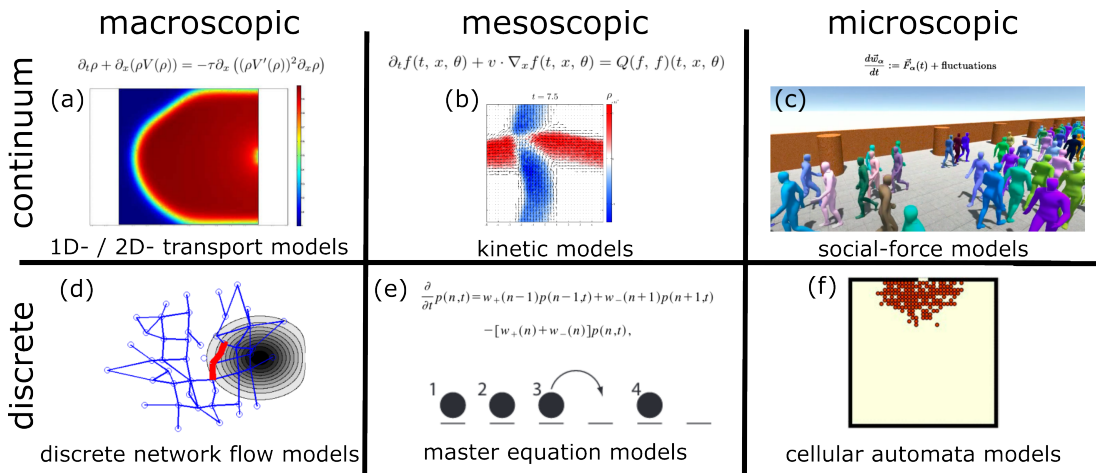


FIGURE 1.11: Schematic classification of pedestrian models at the operational level with examples. Continuum models refer to approaches that are continuous in time and space, while discrete models refer to those that are discrete in either time or space.

<p>(a) Continuous models Equation: Tordeux et al. (2018) Figure: Coscia and Canavesio (2008)</p>	<p>(b) Kinetic models Equation and Figure: Festa et al. (2018)</p>	<p>(c) Force-based models Equation: Helbing and Molnar (1995) Software, Figure: Pettore (2024)</p>
<p>(d) Macroscopic models Figure: Göttlich et al. (2011)</p>	<p>(e) Stochastic models Equation: Mahnke and Pieret (1997) Figure: Schadschneider et al. (2010)</p>	<p>(f) Cellular automata Figure: Burstedde et al. (2001)</p>

The relationship between flow and density, or equivalently between velocity and density, can be measured experimentally¹ and is known as the fundamental diagram. Examples of fundamental diagrams are shown in Fig. 1.12.

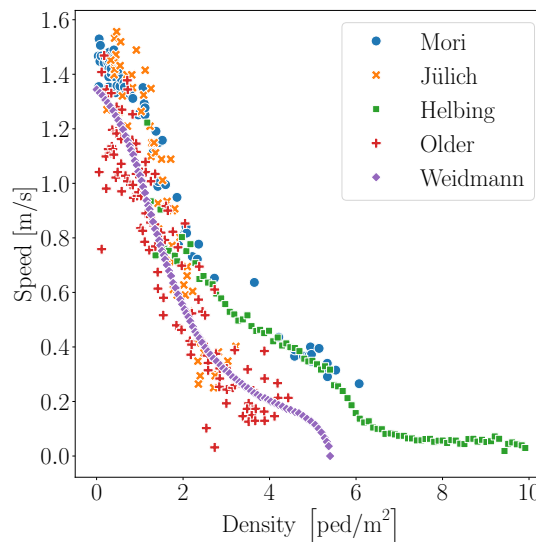


FIGURE 1.12: Examples of empirical fundamental diagrams for unidirectional flow along a corridor with a periodic length of $L_X = 16$ m and a width of $L_Y = 3$ m ([Möri and Tsukaguchi, 1987](#); [Zhang et al., 2011](#); [Helbing et al., 2007](#); [Older, 1968](#); [Weidmann, 1993](#)).

¹In the experiment, a specific section of the corridor where pedestrians move is selected for observation. The average density in this section is measured at least every two seconds to ensure the measurements remain uncorrelated throughout the experiment. Depending on the authors' methodology, averages may then be calculated for each density bin.

From a modelling perspective, this relationship can be represented by determining a close relation between velocity and density. These models are referred to as first-order models because the velocity profile adjusts immediately to changes in the density profile. In contrast, second-order models couple acceleration with density rather than just velocity. Depending on the specific situation being modelled, different choices can be made regarding this relationship, as described by [Coscia and Canavesio \(2008\)](#):

Models of the first kind These models are associated with low-density scenarios where the speed v (the magnitude of the velocity \mathbf{v}) depends solely on density: $v(\rho)$. The direction of movement is determined by the position of pedestrians and their targets.

Model of the second kind These models apply to high-density scenarios where speed depends on the density and its spatial gradient: $v(\rho, \nabla\rho)$. Consequently, the magnitude of the velocity can vary based on local density variations, introducing anisotropy into pedestrian behaviour. Pedestrians are considered anisotropic pedestrians if they are not equally affected by stimuli from all directions. In this context, it refers to walkers who follow a straight line towards their target but whose velocity amplitude changes as the density in their neighbourhood changes.

Model of the third kind These models are particularly relevant in high-density scenarios, where pedestrian behaviour becomes more complex. In such situations, the local density and spatial gradient influence the magnitude and direction of pedestrian velocity: $\mathbf{v}(\rho, \nabla\rho)$. This approach reflects the tendency of pedestrians to navigate towards their destination while simultaneously seeking paths of least resistance. Rather than following strictly linear trajectories, individuals may be drawn to routes with lower-density gradients, resulting in more organic and fluid movement patterns.

First-order models can also handle obstacles by splitting the velocity vector into two contributions: one directed towards the target and the other repelled by the obstacles. However, these models require a specific fundamental diagram for each situation, making them impractical for diverse and complex environments. Consequently, first-order models are primarily suited for describing well-defined and simple scenarios.

1.1.3.2 UNDERGROUND SCENARIO

To model a more general situation, such as a crowd leaving an underground station like the one shown in [Fig. 1.13](#), one can use a second-order model ([Bellomo and Dogbe, 2008](#)) which includes, in addition to a continuity equation for the density, an equation representing the Newton's Fundamental Principle of Dynamics:

$$D_t[\rho(\mathbf{r}, t)\mathbf{v}(\mathbf{r}, t)] = \mathbf{F}[\rho, \mathbf{v}, \nabla] \quad (1.6)$$

where D_t stands for the material derivative and \mathbf{F} characterises both the internal driving force or motivation and external forces applied to the elementary block of individuals in volume $dx dy$ that depends in principle on the local crowd density, the velocity, and their derivatives. Similarly to the first-order model, one can distinguish three kinds of second-order models depending on the dependencies of \mathbf{F} and, therefore, depending on the phenomenology one would like to describe. Therefore, one can describe the repulsive action of obstacles using a pressure-like term in \mathbf{F} ; see the article from [Piccoli and Tosin \(2009\)](#) for more details.

At an even deeper level, [Bruno et al. \(2011\)](#) incorporated non-locality in both space and time into pedestrian behaviour models to account for the fact that visual perception enables pedestrians to gather and synthesise non-local information about their surroundings, a concept already widely explored in medical ([Patla, 1997](#)) and cognitive psychology research ([Gibson, 1950](#); [Kosslyn, 1978](#)).

Non-locality in space Each pedestrian has a defined sensory region essential for perception, evaluation, and reaction, enabling them to perceive and respond to conditions beyond their immediate

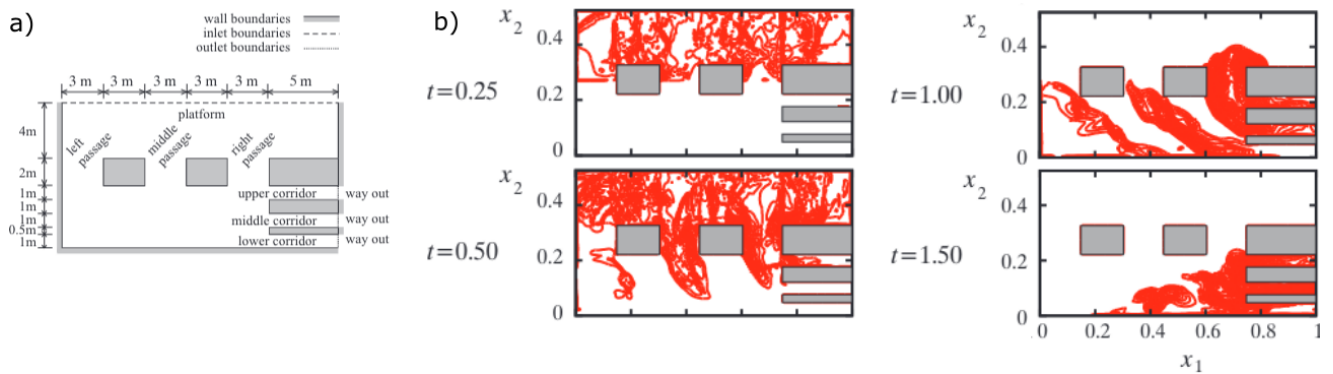


FIGURE 1.13: (a) Map of the underground station used for numerical simulations. Pedestrians arrive from above (inlet boundaries) and exit to the right (outlet boundaries). The grey blocks represent pillars. (b) Instantaneous crowd density fields (times row-wise), adapted from Bruno et al. (2011).

vicinity. They assess the perceived density as a weighted average over their entire sensory region, with greater emphasis on the frontal area, modelling curious pedestrians who perform an ensemble evaluation of their surroundings.

Non-locality in time The model combines two time delays: a reflex time delay for quick reactions and a volitional time delay for more complex evaluations. This approach makes pedestrian reactions non-local in time, accounting for both immediate and delayed responses.

1.1.3.3 STOP-AND-GO WAVES IN QUEUES

Macroscopic equations provide valuable insights into various traffic phenomena, including phantom jams or stop-and-go waves in vehicular traffic (Sugiyama et al., 2008), congestion patterns in pedestrian movement (Ziemer et al., 2016), and solitons or kinks in mathematical models (Komatsu and Sasa, 1995), (Nagatani, 1998a). Stop-and-go waves are self-organised phenomena that emerge directly from the system's dynamics rather than from external factors such as lane changes or pedestrian accidents². These waves are characterised by alternating cycles of movement and stoppage within a flow of pedestrians or vehicles, resulting in waves of congestion propagating through the crowd. They manifest as periods of forward motion followed by sudden halts, creating a ripple effect that travels upstream against the direction of traffic flow. Refer to Fig. 1.14 for a visual representation of stop-and-go waves in the context of car traffic.

Lighthill and Whitham (1955) developed a first-order macroscopic model for traffic flow, which is characterised by its use of a single partial differential equation to describe the dynamics of traffic density. As discussed in Sec. 1.1.3.1, the first-order model assumes that the traffic speed is a function of vehicle concentration, typically expressed as an equation like $v(t) = V[\rho(t)]$, where v is the traffic speed and ρ is the vehicle density. Assuming a traffic hump as the initial condition, the model effectively predicts the motion of traffic humps, the formation of density shock waves at bottlenecks, and the behaviour of traffic near junctions. However, when both the density and velocity are initially uniform, the model does not spontaneously generate shock waves. While the model is interesting, it cannot replicate Sugiyama et al. (2008) experiment.

Conversely, Bain and Bartolo (2019) developed a second-order model to describe velocity waves in a marathon. They incorporated a dependence of the force field \mathbf{F} on a polarization field \mathbf{p} , which accounts

²Other self-organised phenomena have been observed, and a classification based on the place and the context has been proposed by Chen et al. (2018). Please refer to Fig. A.4 in App. A.2.

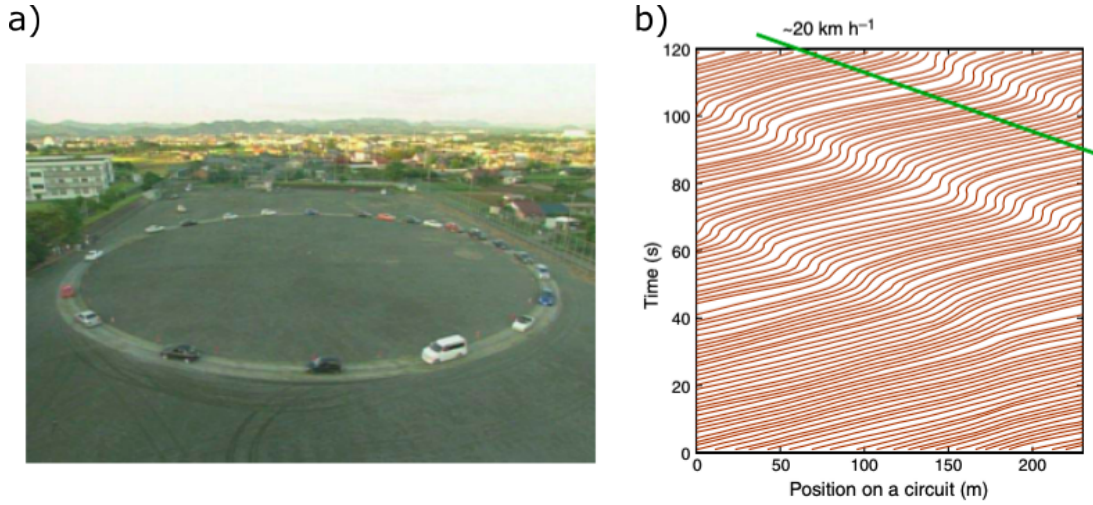


FIGURE 1.14: Experimental setup and results of traffic jam formation on a circular road, adapted from Sugiyama et al. (2008). (a) Snapshot of 22 vehicles on a 230 m circular track. (b) Vehicle trajectories over two minutes show the emergence of a traffic jam cluster and its backward propagation at approximately 20 km/h.

for local alignment between individuals, thereby providing a more comprehensive representation of their local interactions.

Other researchers sought to examine in greater detail the impact of local interactions between pairs of individuals on the emergence of stop-and-go waves at a large scale. To achieve this, they developed microscopic models. For instance, Newell (1961) proposed the Optimal-Velocity Model (OVM) for a single car file, described by the following equation of motion:

$$\frac{dx_j(t + \tau)}{dt} = V(\Delta x_j(t)) \quad (1.7)$$

where $x_j(t)$ represents the position of car j at time t , while $\Delta x_j(t)$ denotes the headway of car j at time t . The parameter τ is a time delay, and $V(\cdot)$ is the optimal velocity function. This model describes how a driver adjusts his velocity based on the observed headway to the car in front. The driver aims to achieve an optimal velocity $V(\cdot)$ that depends on the current headway. This velocity function can be empirically fitted to fundamental diagrams that relate traffic density to flow. The time-delay τ accounts for the driver's reaction time and the car's mechanical response, representing the lag between observing a change in headway and adjusting the velocity accordingly. Interestingly, by setting $\tau = 0$ in Eq. (1.7) and taking the hydrodynamic limit to derive a macroscopic equation, one can obtain the model proposed by Lighthill and Whitham (1955), which cannot reproduce the emergence of stop-and-go waves. Therefore, introducing a time delay appears to be a crucial element for accurately describing the traffic dynamic.

Unlike Newell (1961), who studied congestion waves in vehicular traffic, Fehrenbach et al. (2015) focused on congestion waves in a single pedestrian file. They investigated the time delay and another microscopic feature of human behaviour: the tendency to follow the leader's velocity, i.e., the person directly in front. More precisely, the velocity of pedestrian i verifies the following equation:

$$\frac{dv_i}{dt}(t + \tau) = C \frac{v_{i+1}(t) - v_i(t)}{|x_{i+1}(t) - x_i(t)|^{1+\gamma}} \quad (1.8)$$

where $C > 0$, $\tau > 0$, and $\gamma \geq -1$ are modelling constants. Intuitively, Eq. (1.8) describes a two-phase process. In the first phase, a pedestrian observes the leader (the person directly in front of them) and

decides based on the leader’s speed and position. In contrast, in the second phase, the pedestrian adjusts his velocity to comply with this decision. The model incorporates a time delay τ between the decision-making and action phases, representing the time the pedestrian needs to translate his decision into movement.

1.1.3.4 FINDING YOUR WAY ON A CROWD

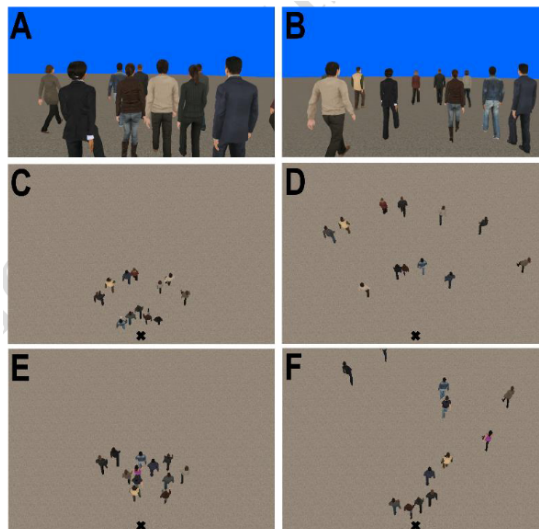


FIGURE 1.15: Virtual crowd display, taken from [Wirth et al. \(2023\)](#). Participant perspectives in high-density (A) and low-density (B) scenarios for the first experiment are shown. Overhead views of high-density (C) and low-density (D) conditions in the first experiment are also provided, along with configurations (E, F) for the second experiment.

Navigating through a crowd during the Festival of Light requires understanding the neighbourhood of interaction in crowd dynamics. Traditionally, two primary models have been proposed to describe how individuals in a crowd influence each other: the metric neighbourhood model ([Cucker and Smale, 2007](#)) and the topological neighbourhood model ([Ballerini et al., 2008](#)), initially used in the study of self-organised patterns in animals such as birds and fish. The metric model suggests that all neighbours within a fixed physical distance influence an individual. In contrast, the topological model posits that an individual is influenced by a fixed number of nearest neighbours, regardless of their physical distance. However, recent experimental studies involving pedestrians navigating through crowds ([Meerhoff et al., 2018](#); [Wirth et al., 2023](#); [Dachner et al., 2022](#)) in both natural and **Virtual Reality (VR)** environments (as illustrated by Fig. 1.15), have provided compelling evidence that neither of these models fully captures the dynamics of human crowd behaviour. These studies suggest that a more accurate model may be needed to account for the complexities of human interactions in crowds. Instead, the visual neighbourhood model has emerged as the most accurate representation. This model is based on the visual information available to individuals, such as their neighbours’ optical motions and visibility, as shown in Fig. 1.16. It suggests that individuals control their movement by responding to visual cues from their neighbours.

In this context, visual cues are optical signals that individuals gather through their sense of sight, helping them navigate and interact with their environment. They adjust their walking speed and direction to cancel out their neighbours’ average angular velocity and optical expansion or contraction (optical size). These adjustments are weighted based on visibility. As a result, a neighbour’s influence diminishes with distance, following optical principles, and is further reduced by visual obstruction from closer individuals.

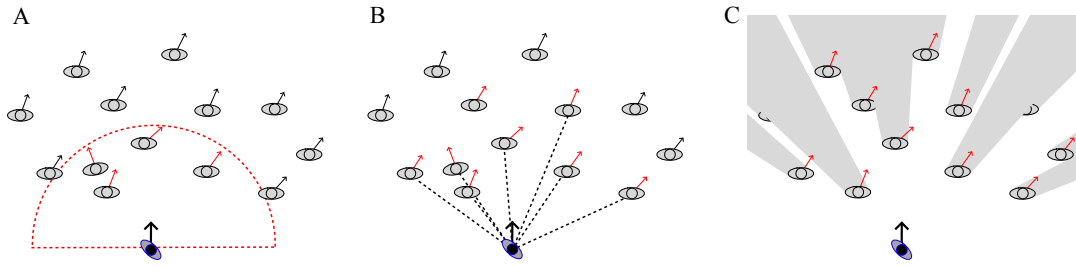


FIGURE 1.16: Three ways of describing the neighbourhood pedestrian interaction. **(A) Metric neighbourhood:** In this case, pedestrians interact with others within a specific radius. The influence of these interactions decreases exponentially as the head-to-head distance increases. **(B) Topological neighbourhood:** This model incorporates topological relationships. Pedestrians interact with their seven nearest neighbours, some of whom may be outside the metric distance threshold. The choice of seven neighbours is not random; it comes from psychological studies such as that of [Miller \(1956\)](#). **(C) Visual neighbourhood interaction:** This model considers a pedestrian's field of vision. Interactions occur with individuals within the pedestrian's line of sight, accounting for occlusion. The scheme is adapted from [Wirth et al. \(2023\)](#).

1.1.3.5 FROM MICROSCOPIC DESCRIPTION TO MACROSCOPIC

When dealing with pedestrians, transitioning from a microscopic to a macroscopic description is usually possible. Various techniques can be employed depending on the macroscopic aspects you want to emphasise or the microscopic details you wish to abstract. This section will explore the two main approaches used in pedestrian dynamics. To illustrate these methods, a slightly modified version of Eq. (1.7), introduced in Sec. 1.1.3.3, will be used. This modification involves linearising the time delay τ dependence through a first-order Taylor expansion in τ and rewriting the equation in terms of Δx_i and Δx_{i+1} for consistency in notation. The modified equation reads:

$$\frac{d^2 \Delta x_i}{dt^2}(t) = a \left[V(\Delta x_{i+1}(t)) - V(\Delta x_i(t)) - \frac{d \Delta x_i}{dt}(t) \right] \quad (1.9)$$

COARSE-GRAINING APPROACH The coarse-graining approach, as suggested by [Lee et al. \(2001\)](#), involves defining macroscopic quantities such as density ρ and flow q as integrals over microscopic variables using a kernel function ϕ . This method smooths out microscopic fluctuations to obtain continuous macroscopic fields. The coarse-grained density and flow are defined as follows:

$$\begin{aligned} \rho(x, t) &= \int dx' \int dt' \phi(x - x', t - t') \hat{\rho}(x', t') \\ q(x, t) &= \int dx' \int dt' \phi(x - x', t - t') \hat{q}(x', t') \end{aligned} \quad (1.10)$$

where $\hat{\rho}(x, t)$ is the micro density: $\hat{\rho}(x, t) = \sum_i \delta(x_i(t) - x)$, $\hat{q}(x, t)$ is the microscopic flow: $\hat{q}(x, t) = \sum_i \frac{dx_i}{dt}(t) \delta(x_i(t) - x)$ and $\phi(x, t)$ is the coarse-graining kernel function that, depending on its chosen shape, obscures specific microscopic details. This method transitions from discrete pedestrian behaviours to continuous macroscopic fields. By averaging over small spatial and temporal scales, it captures overall motion patterns while smoothing out the fine details of individual interactions.

NONLINEAR ANALYSIS The core idea of this method lies in deriving a continuous approximation of the discrete solution at large time and space scales³. A critical question arises: where should this approximation be made? More specifically, which set of initial parameters is most revealing?

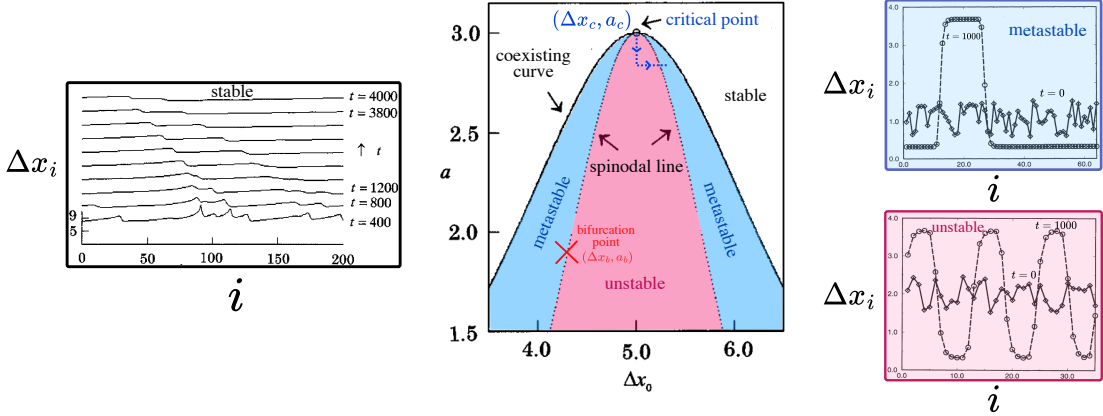


FIGURE 1.17: In the centre, the phase diagram is obtained from simulations of Eq. (1.9). Three distinct regions in the traffic flow are identified: the **stable region** (white) above the coexistence curve, the **metastable region** (blue) between the spinodal and coexistence curves, and the **unstable region** (red) below the spinodal line. The points $(\Delta x_b, a_b)$ and $(\Delta x_c, a_c)$ represent bifurcation points, with $(\Delta x_c, a_c)$ specifically denoting a critical point. Simulation results for each of these three regions are provided, starting from initial configurations where spacings are perturbed by white noise. It is important to note that the simulations corresponding to the red and blue panels (right) were not performed using exactly the same potential. The parameters a and Δx have been chosen such that: in the red region, a homogeneous initial state is linearly unstable, and in the blue region, a homogeneous initial state is linearly stable. The dashed path illustrates the trajectory followed in our approximation. The graphs are adapted from Nagatani (2000); Komatsu and Sasa (1995).

It's particularly intriguing to examine solutions near a bifurcation point - a point in parameter space where a slight change in parameters can lead to dramatically different qualitative behaviours. Linear stability analysis can be employed to identify such a point, providing insight into the linearised system's behaviour. When applied to Eq. (1.9), this analysis reveals that for an initial mean spacings Δx_0 (or equivalently an initial global density) satisfying: $V'(\Delta x_0) > \frac{a}{2}$, the system will diverge. The curve representing the boundary of that unstable state in the $(\Delta x_0, a)$ space is depicted by the dotted black line in Fig. 1.17 (middle panel). Simulation of Eq. (1.9) in the unstable state reveal a spacing profile exhibiting a kink-antikink structure, as shown in Fig. 1.17 (red panel).

While approximate solutions can be sought anywhere in principle, the most exciting cases lie near a specific kind of bifurcation point: a critical point denoted $(\Delta x_c, a_c)$ i.e. a point located at the frontier (between stable and unstable state). Therefore, let's focus on finding an approximate solution near such point as illustrated in Fig. 1.17 by the blue dashed path. The process involves several key steps:

- Define a small parameter to control our approximation.
- Change scale (note that without changing scale, we would merely be performing linear stability analysis).
- Change variables by defining a continuous variable from the discrete one as a perturbation around the solution at the critical point.
- Combine all elements, substitute and expand in order of the small parameter.

Now, let's look at each stage in details:

Introduce a small parameter Define a small parameter, ϵ , to measure the distance from the bifurc-

³For an alternative explanation of this method in the context of pattern formation in particle assemblies, refer to the work of Bena et al. (1993).

ation point. For instance, express this as $a = a_c(1 - \epsilon^\delta)$, where δ is an exponent that varies depending on the scale of interest. Visually, this is analogous to following the blue dashed vertical path depicted in Fig. 1.17.

Change scale Introduce slow spatial and temporal variables to capture the long-wavelength behaviour, i.e. the slow and global dynamics near the bifurcation point:

$$X \doteq \epsilon^\alpha(i + bt), \quad T \doteq \epsilon^\beta t \quad (1.11)$$

where i is the discrete index to identify a car, t is time, and b defines the shift to a moving coordinate system (i.e. the speed in the stationary state at the bifurcation point from which the perturbation is performed, $b = V'(\Delta x_c)$ in our case), α, β are other scaling exponents.

Define a continuous variable Express the dynamical variable as expansion in ϵ around their value at the critical point. For example:

$$\Delta x_i(t) = \Delta x_c + \epsilon^\gamma R(X, T) \quad (1.12)$$

where γ is another scaling exponent, and $R(X, T)$ is the new spacing field.

Determine the exponents introduced in the previous definitions To determine the scaling exponents, one can decompose in Fourier modes the solution of Eq. (1.9), denoted as $\Delta x_i(t)$. We express it as:

$$\Delta x_i(t) = \Delta x_c + A e^{jki + \omega t} \quad (1.13)$$

where A is a real constant known as the amplitude of the Fourier mode assumed very small of order ϵ^γ , j is the imaginary unit, k is a real number referred to as the wave number or spatial growth rate, and ω is a complex number called the pulsation or temporal growth rate. By substituting this mode into Eq. (1.9) and solving for ω in the limit of large spatial scales (i.e., small wave-number), we obtain the so-called dispersion relation (Komatsu and Sasa, 1995):

$$\omega(k) = \frac{a_c}{2}jk + \frac{a_c - a}{4}k^2 - \frac{a_c}{12}jk^3 - \frac{a_c}{16}k^4 + O(k^5) \quad (1.14)$$

The dispersion relation is pivotal in linking wave phenomena' temporal and spatial growth rates. By carefully analysing it, one can identify specific spatial and temporal frequencies one wishes to eliminate or focus on. This analysis also enables the evaluation of scaling exponents that characterise the solution one wants to look for.

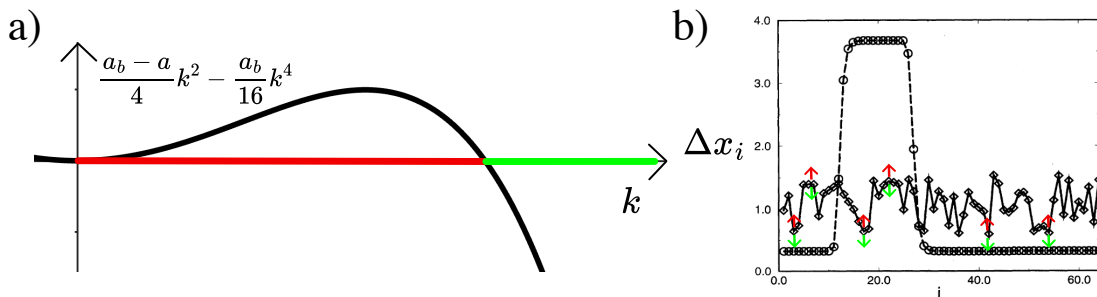


FIGURE 1.18: **a)** Real part of $\omega(k)$, representing the time growth rate of wave modes. Modes with small wave numbers (shown in red) experience growth due to contributions from k^2 , while modes with large wave numbers (shown in green) decay due to contributions from k^4 . **b)** The initial configuration, represented by the solid line, depicts a homogeneous state slightly perturbed by white noise. As time progresses, this configuration undergoes a transformation illustrated by the competition between the little red arrows and the green ones acting on the different modes of the initial state. Ultimately, that initial state evolves into a well-defined soliton structure. This evolution demonstrates the system's tendency to self-organise from a near-uniform state into a localised, stable wave pattern. The figure is adapted from Komatsu and Sasa (1995).

Balancing the right terms in the dispersion relation is crucial for determining the appropriate scaling of space and time. For instance, balancing the second-order and fourth-order terms can help identify the most stable shock waves. In the dispersion relation equation, the real terms (highlighted in colours) govern the growth or decay of the Fourier mode. If only the red term is considered, the Fourier mode will increase. However, if both terms are included and given equal weight, i.e. scaling, small wavenumber modes will grow. In contrast, large wavenumber modes will decay, potentially leading to an interesting soliton solution as illustrated in Fig. 1.18.

To determine the scaling factors, we will follow the blue dashed path illustrated in Fig. 1.17 as an example. If we set $a_c - a$ scales as ϵ^2 , then k should scale as ϵ to balance second order and fourth order term in Eq. (1.14). The scaling of t is determined by the lowest-order term in Eq. (1.14), which is given by a dispersion term proportional to k^3 when we eliminate the propagation term proportional to k by shifting to a moving coordinate system. Thus t scales as ϵ^{-3} . Therefore, $X \sim \epsilon$ and $T \sim \epsilon^3$. To find the scaling of $R(X, T)$, one should decide whether to explore solutions in the unstable or metastable regime, as illustrated in Fig. 1.17. Setting a scaling factor of ϵ is sufficient to explore solutions in the metastable state (as depicted by the blue horizontal dashed path in the middle panel of Fig. 1.17). This leads to the following scalings $X \sim \epsilon$, $T \sim \epsilon^3$, and $R(X, T) \sim \epsilon^{-1}$ or equivalently $\alpha = 1$, $\beta = 3$, $\gamma = 1$, and $\delta = 2$. Ultimately, to effectively observe the emergence of slowly varying shock density waves in the unstable regime, the scaling $R(X, T) \sim \epsilon^{-2}$ would be more suitable.

Substitute, expand and solve Substitute the perturbative expansions into the original discrete equation and expand in powers of ϵ . Collect terms of the same order in ϵ and solve the resulting equations order by order. At the lowest non-trivial order, this yields in our case that **Partial Differential Equation (PDE)** for the perturbation function $R(X, T)$:

$$\frac{\partial R}{\partial T} - \frac{\partial^3 R}{\partial X^3} + \frac{\partial R^3}{\partial X} = 0 \quad (1.15)$$

It turns out that this is the modified **Korteweg-de-Vries (KdV)** equation, which admits soliton solutions, among others, commonly known as stop-and-go waves. As a remark, using an alternative scaling such as $X \sim \epsilon$, $T \sim \epsilon^3$, and $R(X, T) \sim \epsilon^{-2}$ would lead to the **Korteweg-de-Vries (KdV)** equation, whose solutions are also well-known.

It is worth noticing that the linear scaling for which all the exponents are equal to one is nothing more than the **hydrodynamic limit**. As an example, [Tordeux et al. \(2018\)](#) derived in the hydrodynamic limit a macroscopic first-order convection-diffusion flow model from a microscopic follow-the-leader equation with reaction time similar to Eq. (1.7).

1.1.4 DISCUSSION

Three distinct levels have been identified at which authorities can act to understand and manage crowds during the Festival of Lights. While they provide a robust framework for event planning and execution, they have limitations. The **strategic level** focuses on planning schedules, defining possible routes, and determining transportation methods. Although studies exist for the city of Lyon, they remain insufficient to provide a precise global view at this strategic level. This aspect is crucial as it forms the foundation for organising the Festival of Lights. In the future, more comprehensive studies should be conducted to enhance strategic planning.

Upon completion of these strategic tasks, attention shifts to the **tactical level**, which primarily involves route selection. For instance, during the Festival of Lights, a typical path might be the route from the Part-Dieu train station to an Airbnb on the peninsula of Lyon. Predicting the most frequently used paths enables more accessible guidance for individuals, allows for the closure of specific routes

to avoid vehicle interactions, and ultimately enhances the safety of the user experience. To further improve tactical planning, it would be beneficial to conduct surveys on the mindset of Festival attendees beforehand and obtain trajectory data, possibly through drone footage, to identify the most used routes. Such information would provide insights into the most relevant psychological variables influencing route selection.

At a deeper scale, the **operational level** centres on how individuals move along their chosen routes and interact with the environment. This operational aspect is particularly critical as it helps prevent disasters in high crowd density or general panic situations. While macroscopic models are valuable for describing collective phenomena, they have limitations when dealing with heterogeneous crowds that include people on scooters, police officers, and ambulances. Current models do not allow for a simple description of all this variety. Microscopic models are generally more suitable for such scenarios. However, caution should be exercised to avoid over-complicating these models by adding numerous interactions to precisely fit specific situations, as these additional factors may only be relevant to the particular case being studied.

1.2 PHYSICAL MODELLING OF CROWDS AT THE OPERATIONAL LEVEL: INSIGHTS FROM MICROSCOPIC MODELS

1.2.1 THE SOCIAL FORCE MODEL: A PIONEERING APPROACH TO SIMULATING CROWD DYNAMICS

The pioneering microscopic model of crowd dynamics is the **Social Force Model (SFM)** proposed by **Helbing and Molnar (1995)**. Despite its limitations, it is still widely used in pedestrian dynamics software for the general public (see Sec. 1.1.1.2). The **SFM** is a physical framework that describes pedestrian dynamics by positing that individuals are subject to ‘social forces’, which represent internal motivations rather than physical forces directly exerted by the environment. In the **SFM**, pedestrians are modelled as point particles with an ellipsoidal comfort zone they want to preserve. The critical components of the model are:

Driving force This force represents the desire of a pedestrian i to reach a destination at a preferred speed. Mathematically, it is expressed as:

$$\mathbf{F}_i^{\text{des}} = \frac{v_i^{\text{des}} \mathbf{e}_i - \mathbf{v}_i}{\tau} \quad (1.16)$$

where v_i^{des} is the desired velocity amplitude (taken from a normal distribution centred around 1.4 m/s to account for the heterogeneity of people’s behaviour), \mathbf{e}_i is the desired direction pointing toward the destination, \mathbf{v}_i is the current velocity of pedestrian i , and τ is a relaxation time parameter.

Repulsive potential It ensures pedestrians preserve a comfort zone around them from the intrusion of other pedestrians. The repulsive force from another pedestrian j is derived from a potential that represents the comfort zone of pedestrian i . It is given by:

$$\begin{aligned} \mathbf{F}_{ij}^{\text{rep}} &= -\nabla_{\mathbf{r}_i} V_{ij}(b_{ij}) \\ V_{ij} &= V_0 \exp\left(-\frac{b_{ij}}{\sigma}\right) \end{aligned} \quad (1.17)$$

where V_0 is a constant that denotes the strength of the interaction. The equipotential lines of the comfort potential surrounding pedestrian i are depicted as ellipses, with b_{ij} representing the

semi-minor axis, which is given by:

$$b_{ij} = \frac{1}{2} \sqrt{(\|\mathbf{r}_{ij}\| + \|\mathbf{r}_{ij} - \mathbf{v}_i \Delta t\|)^2 - (\mathbf{v}_i \Delta t)^2} \quad (1.18)$$

where $\mathbf{r}_{ij} = \mathbf{r}_i - \mathbf{r}_j$. The ellipse is oriented in the direction of motion and intersects with pedestrian j , as illustrated in Fig. 1.19. The characteristic length scale of the comfort potential is denoted by σ . Notably, the scalar field is significantly influenced by the anticipated position of pedestrian i after a short time interval Δt , assuming constant velocity, reflecting a form of proactive avoidance. This anticipation allows pedestrians to preemptively adjust their path to maintain a comfortable distance from others, thereby minimising potential close encounters. This force can be adapted to the walls and boundaries of the space in which pedestrians move by

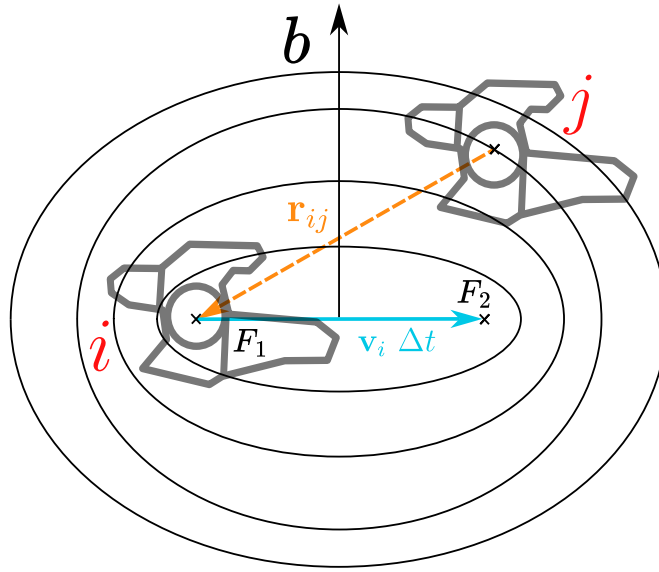


FIGURE 1.19: Illustration of the elliptical personal field equipotentials of pedestrian i . The distance between the two foci of each ellipse is $\|\mathbf{v}_i \Delta t\|$, approximately equal to the length of one step of pedestrian i . The scheme is adapted from Johansson et al. (2007).

using the following potential:

$$U_{io} = U_0 \exp\left(-\frac{\|\mathbf{r}_{io}\|}{R}\right) \quad (1.19)$$

where U_0 is a constant representing the strength of the repulsive interaction from the obstacle, $\|\mathbf{r}_{io}\|$ is the distance between pedestrian i and the nearest point B on the obstacle denoted as o , and R is a characteristic length scale of the repulsion from the obstacle.

Attractive potential towards a group of people, or objects An attractive interaction, denoted as $\mathbf{F}_{ia}^{\text{att}}$, can be introduced between pedestrian i and pedestrian a to model attractions to other pedestrians or objects, such as friends or points of interest. The associated potential is given by:

$$W_{ia} = -A \exp\left(-\frac{\|\mathbf{r}_{ia}\|}{B}\right) \quad (1.20)$$

where A is a constant representing the strength of the attractive interaction, $\|\mathbf{r}_{ia}\|$ is the distance between pedestrian i and the attractive point a , and B is a characteristic length scale of the attraction.

The resulting equation of motion for a pedestrian i of mass m_i is:

$$m_i \frac{d\mathbf{v}_i}{dt} = \mathbf{F}_i^{\text{des}} + \sum_{j \in \{\text{other pedestrians}\}} \mu_{ij} \mathbf{F}_{ij}^{\text{rep}} + \sum_{o \in \{\text{obstacles}\}} \mu_{io} \mathbf{F}_{io}^{\text{rep}} + \sum_{a \in \{\text{other pedestrians}\}} \mu_{ia} \mathbf{F}_{ia}^{\text{att}} \quad (1.21)$$

where μ_{ij} is a constant accounting for the pedestrian's field of vision. It is equal to 1 when individual j is in the pedestrian i field of view of angular size 2ϕ centred around the direction of the desired velocity \mathbf{e}_i and c a positive constant strictly less than 1 otherwise (a similar definition holds for μ_{io} and μ_{ia}). Therefore, they can still interact with a pedestrian behind them, but less strongly than with a pedestrian in front of them.

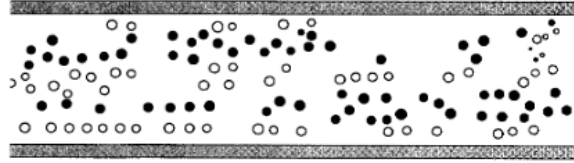


FIGURE 1.20: Above a critical pedestrian density, spontaneous lane formation emerges, with pedestrians moving uniformly in the same direction within each lane. The diameters of the circles are a measure of the actual velocity of motion. Empty circles represent pedestrians with a desired direction of motion opposite to pedestrians symbolised by full circles. The figure is reproduced from [Helbing and Molnar \(1995\)](#).

The **Social Force Model (SFM)** can reproduce the self-organisation of pedestrians into lanes of uniform walking direction, especially in high-density situations as seen in Fig. 1.20. This emergent behaviour significantly reduces the frequency of avoidance manoeuvres, thereby enhancing the overall efficiency of pedestrian traffic flow. Furthermore, the model accurately reproduces oscillatory changes in the direction of pedestrian flow at narrow passages, a phenomenon observed in real-world settings ([Hoogendoorn and Daamen, 2005](#)). This occurs as groups of pedestrians alternately pass through the bottleneck from opposite directions. While the **SFM** has been successful in reproducing many collective phenomena, it has several limitations:

No proper mechanical layer The original **SFM** does not include proper physical interactions accounting for how pedestrians push, fall, deform and shudder, which is critical in high-density scenarios. A significant step was made by [Helbing et al. \(2000a\)](#) with the introduction of normal and tangential contact forces, which enhanced the realism of pedestrian dynamics simulations in escape panic scenarios.

Lack of cognitive and decision-making processes The **SFM** does not incorporate higher-level decision-making processes that influence pedestrian behaviour:

Memory The model does not account for previous experiences, which can influence future behaviour. Indeed, a defining feature of living pedestrians is their capacity to assimilate information, process it, and modify their decisions accordingly, with memory playing a crucial role in this adaptive process. In particular, [Danny Raj and Nayak \(2022\)](#) focus on developing a **SFM** that incorporates a pedestrian's short-term memory of recent movements, allowing it to evaluate its performance in achieving desired velocity and adjust its tactics in response to immediate environmental changes.

Anticipation Pedestrians in the model cannot predict their trajectory or that of others to avoid collisions or choose faster routes. They also cannot rotate to anticipate possible collisions. This lack of anticipation leads to unrealistic oscillatory movements, which occur when pedestrians try to avoid each other, as shown by [Kretz \(2015\)](#). [Karamouzas et al. \(2009\)](#) make a step towards collision avoidance with their **Predictive-Avoidance Model (PAM)**, which is an enhanced version of the **SFM**. This approach enables each simulated pedestrian to anticipate potential collisions within a specified anticipation time as illustrated

in Fig. 1.21. Rather than relying on current positions, PAM calculates ‘evasive forces’ based on the projected locations of pedestrians at the predicted moment of collision. Unlike

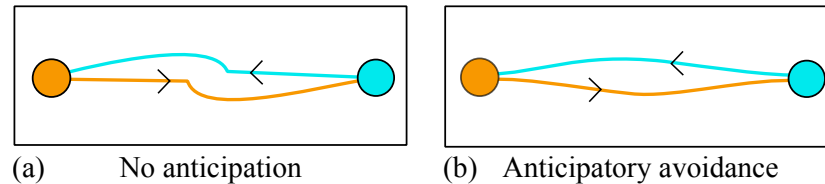


FIGURE 1.21: The **Social Force Model (SFM)** and the **Predictive-Avoidance Model (PAM)** demonstrate distinct pedestrian behaviours in simulated scenarios: (a) In the **SFM** simulation, two pedestrians approach each other on a collision course. The pedestrian on the left, aiming to move right, maintains a straight path until collision is imminent. Only then does he attempt evasive action by swerving around the other pedestrian. (b) The **PAM** simulation of the same scenario reveals more realistic behaviour. Both pedestrians adjust their trajectories well before a collision, exhibiting anticipatory movement. This proactive avoidance reflects the model’s incorporation of pedestrian foresight. The picture is adapted from [Guy and Karamouzas \(2019\)](#).

[Karamouzas et al. \(2009\)](#), who introduced new forces to account for anticipation, [Hu et al. \(2023\)](#) makes slight modifications to **SFM** by increasing the size of the ellipse, specifically by significantly enlarging the ellipse’s anticipation time Δt . This approach is akin to using multiple steps instead of a single step to determine an individual’s comfort zone, from which repulsion forces are calculated. The study quantifies how much the presence of anticipation, represented by Δt in the interaction ellipse, improves predictions of evacuation times, social gathering behaviours, and other dynamics. The results show that improvements are noticeable as long as $\Delta t \sim 20$ s is not too large. Beyond this threshold, the impact of anticipation saturates and does not significantly change outcomes.

Navigation (connecting tactical and operational levels): The model assumes that pedestrians always move towards their destination, which may not be true in complex environments such as labyrinths. This simplification ignores the dynamic decision-making processes involved in navigation as mentioned in Sec. 1.1.2.2 and Sec. 1.1.2.4. Readers interested in enhanced **SFM**, including navigation fields, are encouraged to consult the work of [Jiang et al. \(2017b\)](#).

Brain constraints The model cannot accurately represent situations where pedestrians may react more slowly due to divided attention or distractions, such as using a phone, being exposed to loud noise, listening to music, being lost in thought, or conversing with someone else. Additionally, the model does not account for biases in visual and cognitive processing, which is especially relevant when the individual is covered in information because that’s when most of his actions will be the result of automatic decision-making processes and will not be the result of the deliberate decision-making process as is the case in a supermarket or the middle of a crowd. For example, [Kremer et al. \(2021\)](#) develop a model to account for variation in attention starting from the **PAM**.

Limited representation of group behaviour The original **SFM** does not adequately capture the dynamics of pedestrian groups moving together. In particular, it does not account for adult-child pairs, friendship, or couple interactions, which are common in real-world scenarios. For instance, [Moussaïd et al. \(2010\)](#) demonstrates that social interactions among group members generate typical walking patterns, such as side-by-side and V-like formations, significantly impacting overall crowd dynamics.

Difficulty in parameter calibration One of the weaknesses of the social force model is the abstract nature of its parameters, which makes them neither directly nor easily measurable. Furthermore,

these parameters must be systematically adjusted to replicate a specific situation⁴, meaning they are inherently dependent on the context being studied. Their proliferation also complicates identifying their precise role within the overall dynamics. Efforts are being made to develop models (Echeverría-Huarte and Nicolas, 2023) with measurable parameters no longer tied to specific scenarios. Such models could then be used not only to replicate scenarios but also to make predictions.

The original SFM has undergone numerous refinements and expansions to address its limitations and broaden its applicability across diverse scenarios. For a comprehensive overview of direct improvements to the SFM, readers are directed to Chen et al. (2018). The following two subsections delve into critical mechanical and decision-making factors to enhance crowd management at Lyon’s Festival of Lights.

1.2.2 MECHANICAL ASPECTS

1.2.2.1 VELOCITY-BASED MODEL

The mechanical characteristics of crowd dynamics are fundamentally related to how individual components, particularly pedestrians, respond to stress. To illustrate this concept, consider the analogy of a football released onto a wooden floor. Upon impact, the ball bounces, and an analysis of the velocity of its centre of mass over time reveals discontinuities at the points of contact. Consequently, employing Newton’s equation incorporating a first-order derivative with respect to velocity can be neither straightforward nor mathematically intuitive for modelling such interactions. Given these complexities, a more accessible method for mathematically defining contact involves utilising zero-order models associated with velocity, known as velocity-based models. These models offer a simpler yet effective approach to capturing the essence of crowd dynamics without the need for a complex theory of contact and deformation. They can be expressed as follows:

$$\mathbf{v}_i(t) = \mathbf{V}_i(t, \{\mathbf{q}_j(t)\}_{j \in [1, N]}, \{\mathbf{v}_j(t)\}_{j \in [1, N]}) \quad (1.22)$$

with N the number of pedestrians, \mathbf{V}_i the velocity function of pedestrian i that may depend on time, and the position and velocities of pedestrians, pedestrian i included, making the model implicitly defined. Maury and Venel (2011) developed a collision-free velocity-based model to handle highly packed crowd situations where individuals are represented as disks. Their model is based on two key principles:

- First, they define a spontaneous velocity for each individual, representing the velocity they would prefer in the absence of others. This is typically done using a floor field that indicates desired directions of motion, which slightly differ from those described in Sec. 1.1.2.2. In this case, the spontaneous velocity is proportional to the gradient of the floor field rather than the acceleration, as illustrated by Fig. 1.22.
- Second, they compute the actual velocity by projecting Euclidianly the spontaneous velocity onto the set of admissible velocities denoted C that do not violate non-overlapping constraints between individuals. Therefore, the positions of all the pedestrians verify the following equation:

$$\frac{d\mathbf{q}}{dt} = \mathcal{P}_C(\mathbf{U}(\mathbf{q})) \quad (1.23)$$

denoting $\mathbf{q} \in \mathbb{R}^{2N}$ the position of the N pedestrians, $\mathbf{U}(\mathbf{q})$ the desired velocity field, and \mathcal{P}_C the

⁴A tentative listing of the various base case scenarios that all models should be capable of qualitatively replicating is provided in Fig. A.5, as referenced in App. A.3.

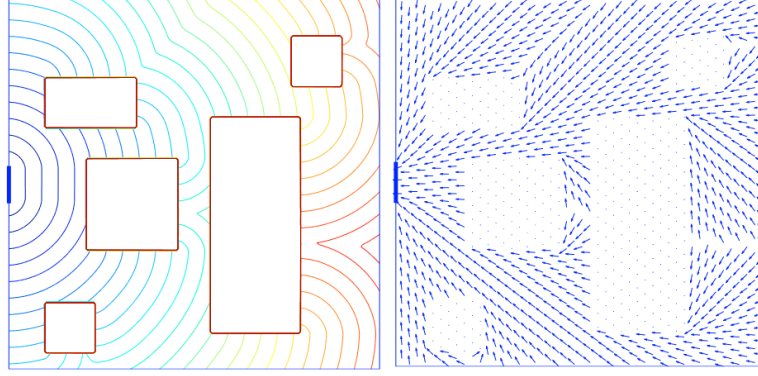


FIGURE 1.22: **Left:** Contour levels of the geodesic distance \mathcal{D} which is the floor field. **Right:** Velocity field $\mathbf{U}(\mathbf{q}) = -s\nabla\mathcal{D}(\mathbf{q})$. The figure is reproduced from [Maury and Venel \(2011\)](#).

Euclidian projection onto C . Intuitively, this projection operation serves as a dynamic constraint, ensuring minimal deviation from the primary goal of reaching the target.

Numerically, Eq. (1.23) can be discretised in time by linearising the constraints on the set of admissible velocities. Denoting by \mathbf{q}_n the position vector at time t_n of all pedestrians, the discretised scheme consists in computing the next velocity \mathbf{v}_{n+1} as:

$$\mathbf{v}_{n+1} = \arg \min_{\mathbf{v} \in C_{\Delta t}(\mathbf{q}_n)} \frac{1}{2} |\mathbf{U}(\mathbf{q}_n) - \mathbf{v}|^2 \quad (1.24)$$

where Δt is the simulation time-step, representing the time interval between two consecutive decisions, $|\cdot|$ is the Euclidean norm such that $|\mathbf{v}|^2 = \mathbf{v}^T \mathbf{v}$, and $C_{\Delta t}(\mathbf{q}_n)$ defines the set of feasible velocities:

$$C_{\Delta t}(\mathbf{q}_n) = \{\mathbf{v} \in \mathbb{R}^{2N} : \forall i < j, D_{ij}(\mathbf{q}_{n+1}) \underset{\text{linearisation}}{\simeq} D_{ij}(\mathbf{q}_n) + \Delta t \mathbf{G}_{ij}(\mathbf{q}_n) \cdot \mathbf{v} \geq 0\} \quad (1.25)$$

This set represents the discrete collection of velocities that ensure no overlap between pedestrians after a small movement. Specifically, it includes all candidate velocities \mathbf{v} such that the distance between any pair of pedestrians i and j remains non-negative after moving for a small time step Δt with the candidate velocity \mathbf{v} .

The minimisation is then computed using the method of Lagrange multipliers generalised to inequality constraints ([Kuhn and Tucker, 1951](#)). Interestingly, these multipliers can be interpreted as interaction pressures between individuals, similar to concepts in thermodynamics. That approach allows the model to replicate commonly observed collective behaviours, such as forming lanes in crowded spaces and forming arch-like structures near exits during evacuations. One of the model's strengths lies in its versatility. It adeptly handles complex geometries, enabling simulations of intricate scenarios like multi-floor building evacuations. Moreover, the model provides valuable insights into potential safety risks. Analysing pressure maps offers a method to estimate the local risk of casualties in various scenarios.

Nevertheless, that model only considers circular shapes. [Narang et al. \(2017\)](#) addressed this limitation by introducing the **Elliptical Optimized Reciprocal Collision Avoidance (EORCA)** model, which represents pedestrians as ellipses or polygonal approximations of ellipses for computational efficiency ([Best et al., 2016](#)). In this model, each agent selects an optimal velocity from a convex set of permissible velocities that allow collision avoidance while staying as close as possible to their preferred velocity. Unlike the approach in [Maury and Venel \(2011\)](#), where minimization is performed collectively across all agents, the **EORCA** model applies individual minimization for each agent. This enhancement allows for more realistic crowd simulations by enabling body rotations to avoid collisions, as illustrated in Fig. 1.23.

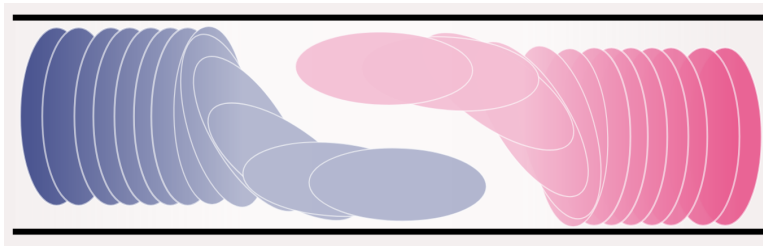


FIGURE 1.23: In a narrow passage, two ellipses approach each other in a confined hallway. To pass safely, each ellipse must rotate. Such behaviours, like shoulder turning, are not possible with disc-shaped agents. The figure is taken from [Best et al. \(2016\)](#).

1.2.2.2 PRESSURE WITHIN THE CROWD

Crowd density is a critical factor in determining the level of danger within a gathering, but it is not the only consideration. When crowd density exceeds six pedestrians per square meter, turbulence can create unpredictable high velocity and pressure zones ([Helbing et al., 2007](#)). These conditions can dynamically lead to thoracic injuries due to compression and asphyxiation when the pressure from surrounding bodies becomes so intense that individuals cannot expand their chests to breathe.

It is essential to examine the role of pressure in crowd disasters. Previous simulations have provided detailed pressure maps ([Maury and Venel, 2011](#)) but lack comparative data to assess potential lethality at specific points within these simulations. A few studies, though still limited in number, have attempted to address this gap in the literature. For instance, [Smith and Lim \(1995\)](#) indicate that humans can tolerate forces exerted on the upper body ranging from 116 N to 774 N for a few seconds, potentially varying results based on sex, age, and weight.

In contrast to these tolerance studies, [Lobdell et al. \(1973\)](#) and [Kroell et al. \(1974\)](#) conducted research on the human body's resistance to brief impacts that transfer kinetic energy. These impacts are similar to what a pedestrian might experience in a concert when pushed by a fast-moving person. This study allowed researchers to explore the mechanical properties of the human body and measure the stress-strain relationship between applied pressure and deformation as illustrated in [Fig. 1.24](#). They determined that a force of 3000 N from a mass moving at about 23 km/h is sufficient to fracture human ribs. From these data, a mechanical model could be developed to reproduce such stress-strain behaviour.

1.2.2.3 PEDESTRIANS AS DEFORMABLE GRAINS

To incorporate the considerations described in the theory of pedestrian plasticity into a pedestrian model such that the deformation of the human body, a more directed approach would be to work with a second-order model, such as the social force model, rather than a first-order model like the one proposed by [Maury and Venel \(2011\)](#). However, it is still possible to reconcile both approaches. Interestingly, by subtracting by \mathbf{v} and dividing by the simulation time step Δt , which can be interpreted as a relaxation time denoted τ_{mech} , each side of [Eq. \(1.24\)](#), one gets an explicit Euler discretisation of the second order differential equation:

$$\dot{\mathbf{v}} = \frac{1}{\tau_{\text{mech}}} \left(\arg \min_{\mathbf{v} \in C} \left\{ \frac{1}{2} |\mathbf{U}(\mathbf{q}) - \mathbf{v}|^2 \right\} - \mathbf{v} \right) \quad (1.26)$$

Importantly, it should be noted that the equation [Eq. \(1.24\)](#) is not equivalent to the equation [Eq. \(1.26\)](#), as a first-order model is, by definition, not a second-order model. What is presented here is merely a method to increase the order of the first-order model, effectively promoting it to a second-order model

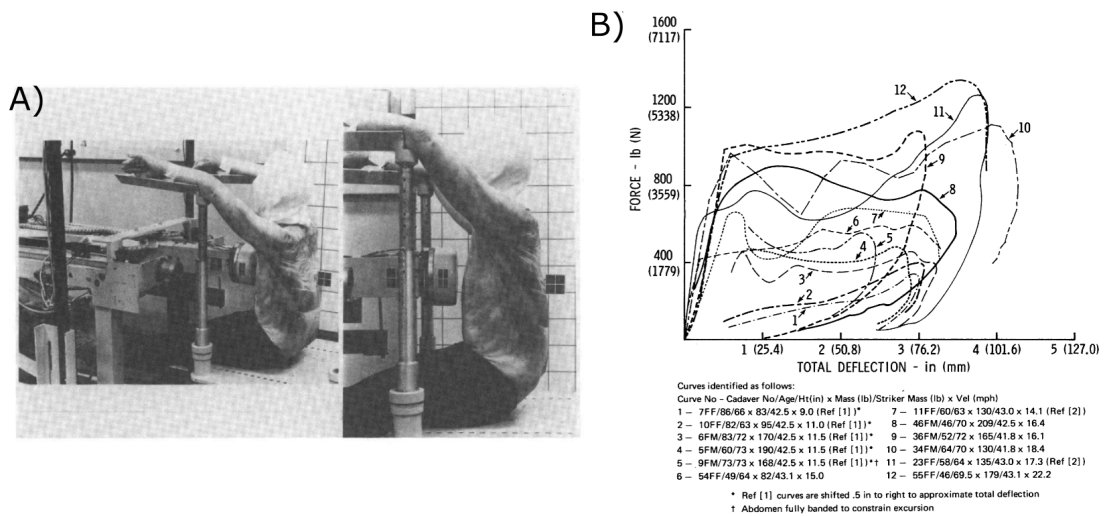


FIGURE 1.24: (A) Experimental setup: The experimental setup utilises unembalmed human cadavers subjected to an anteroposterior blunt force applied to the thorax. This method ensures that only kinetic energy is transmitted over a very short duration, distinguishing it from typical plasticity measurements that involve vertical quasi-static experiments with the transmission of potential energy. Specifically, a wooden log with a diameter of 15.24 cm serves as the impacting mass. This log travels at a constant speed and strikes the sternum directly. To ensure stability during the experiment, the legs of the corpses are secured to horizontal support with adhesive tape. At the same time, the arms are raised and extended to rigid horizontal supports, also secured with adhesive tape, as illustrated in the setup photos. The experiment is conducted after the dissipation of rigor mortis but before the onset of decomposition to ensure the cadavers are in an optimal state for testing. High-frequency cameras are employed to measure the body's deflection, and pressure sensors are used to measure the force applied to the sternum. This equipment enables the measurement of stress-strain curves (or force-deflection curves equivalently). **(B) Force-deflection curves:** The force versus total deflection for a load of different masses travelling at various velocities is plotted. Initially, the force-deflection curve exhibits a linear region where the force increases with deflection. This linear region ends at a point typically referred to as the 'yield point' in material science. Beyond this point, the curve enters a plateau or plastic region where the force levels off, indicating significant deformation of the body part without a corresponding increase in force. Drops within this region can be interpreted as plastic events, such as rib fractures. Finally, the force falls in the discharge zone when the load is removed. The fact that the total deflection does not return to zero indicates that the thorax has undergone irreversible transformations, such as fractures. The figures are reproduced from Kroell et al. (1974).

by introducing a new relaxation parameter, τ_{mech} , which is related to inertia and thus to the mass of pedestrians. In this second-order modelling approach, pedestrians no longer change their velocity instantaneously. Instead, the situation resembles being on an ice rink: even if pedestrians want to change direction, they cannot do so instantaneously due to inertia.

Finally, pedestrian dynamics can also be conceptualised as a system where individuals are subject to a relaxation force that guides them towards an optimal velocity. This velocity is selected through anticipatory collision avoidance, where each pedestrian continually recomputes their direction of motion to minimise their distance toward their destination while minimising potential conflicts with others. While this approach can be applied collectively to all pedestrians using the variable \mathbf{v} , it can be refined by introducing heterogeneity in behaviour using \mathbf{v}_i , potentially reflecting varying degrees of self-interest among individuals, which is essential in describing pedestrian behaviour (see Sec. 1.1.2.5). This refinement, however, may compromise the collision-free nature of the model. Incorporating mechanical forces similar to Newton's equation in granular material physics can address this issue. The resulting framework (Korbmacher et al., 2023) consists of two distinct layers. A decision-making layer involves the minimisation of a cost function to determine optimal velocities that guide towards the destination, minimising the possible future collision. A mechanical layer applies Newton's second law to govern the physical interactions between pedestrians. This dual-layer approach allows for a more nuanced representation of pedestrian behaviour, capturing cognitive decision-making processes

and physical constraints. The following set of equations governs it:

$$\begin{aligned}
 & \textbf{Decision-Making Layer:} \\
 & \mathbf{v}_i^{\text{des}} = \arg \min_{\mathbf{v}_{\text{candidate}} \in \mathbb{R}^2} \mathcal{E} \left(t, \{\mathbf{q}_j(t)\}_{j \in [1, N]}, \{\mathbf{v}_j(t)\}_{j \in [1, N]}, \mathbf{v}_{\text{candidate}} \right) \\
 & \textbf{Mechanical Layer:} \\
 & \frac{d\mathbf{v}_i}{dt} = \frac{\mathbf{v}_i^{\text{des}} - \mathbf{v}_i}{\tau_{\text{mech}}} + \frac{1}{m_i} \sum_{x \in \{\text{neighbours and obstacles}\}} \mathbf{F}_{x \rightarrow i}^{\text{mech}}
 \end{aligned} \tag{1.27}$$

where \mathcal{E} denotes the cost function, $\mathbf{v}_{\text{candidate}}$ is a dummy variable, \mathbf{v}_i is the translational velocity, and τ_{mech} is a relaxation time, indicating that achieving a decision requires some time and is not instantaneous.

1.2.2.4 NON-CIRCULAR PEDESTRIAN SHAPES

Various shapes have been used to model solid objects in discrete element simulations, depending on the dimension and complexity of the model, as illustrated in Tab. 1.1. Comprehensive reviews of particle

TABLE 1.1: Non-exhaustive solid shapes in discrete element simulations

Dimensionality	Shapes
3D	<ul style="list-style-type: none"> • Spheres (Lubachevsky et al., 1996) • Ellipsoids (Lin and Ng, 1997) • Superquadrics (Williams and Pentland, 1992) • Spherocylinders (Kidokoro et al., 2015) • Composite of spheres (Pöschel and Buchholtz, 1995)
2D	<ul style="list-style-type: none"> • Disks (Haff and Anderson, 1993) • Ellipses (Rothenburg and Bathurst, 1991) • Polygons (Hopkins, 1992) • Polar forms (Hogue and Newland, 1994) • Association of disks (Gallas and Sokolowski, 1993)

shapes can be found in Dziugys and Peters (1998). Despite extensive scientific literature on grain dynamics, few pedestrian models accurately incorporate a mechanical layer with non-circular shapes⁵. The model developed by Echeverría-Huarte et al. (2020) simulates evacuation using self-propelled spherocylindrical pedestrians in two dimensions. It incorporates self-propulsion forces, granular-type interactions, and self-alignment torques, all governed by Newtonian mechanics. The model employs a first-order derivative of the velocity equation alongside an angular momentum equation to describe the evolution of pedestrian translation and orientation. The simulations explore the impact of desired speed, obstacle distance from the exit, and angular strength on evacuation dynamics. It reveals the complex interplay between flow and clogging dynamics, demonstrating that optimal obstacle placement can significantly enhance evacuation efficiency by reducing clog formation. Conversely, excessive alignment strength can impede flow.

⁵Chraïbi et al. (2010) introduced a generalised centrifugal force model for pedestrian dynamics that uses elliptical volume exclusion to simulate pedestrian movement more realistically. While this model provides valuable insights into pedestrian behaviour across various geometries, it diverges from traditional mechanical models by focusing on inertial forces rather than mechanical elements like damped springs to describe mechanical interactions.

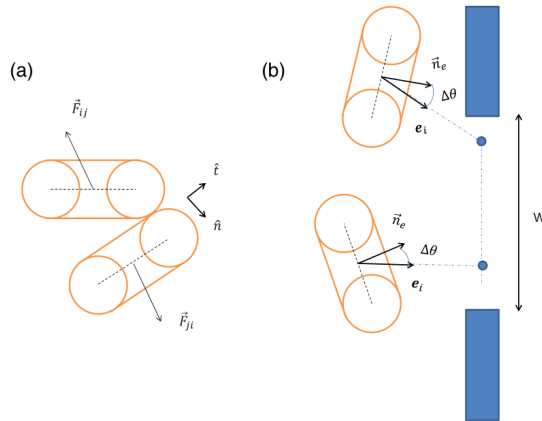


FIGURE 1.25: Sketch illustrating (a) the contact interaction between two spherocylinders; and (b) the orientation of the acting direction, i.e. of the driving force. The blue dots indicate the endpoints of the target segment that pedestrians aim to reach. The scheme is reproduced from [Hidalgo et al. \(2017\)](#).

Unlike [Echeverría-Huarte et al. \(2020\)](#), who incorporated obstacles, [Hidalgo et al. \(2017\)](#) proposed a numerical framework to simulate pedestrian dynamics under highly competitive conditions without the use of obstacles, as illustrated in Fig. 1.25. Their model aimed to understand the relationship between competition (modelled as changes in desired velocity) and evacuation time. Increasing the desired velocity (representing higher competitiveness) led to lower evacuation flow rates, consistent with the **Faster-is-Slower Effect (FSE)**. Additionally, higher desired velocities result in more significant flow interruptions and longer evacuation times, particularly in the steady-state phase. The model produced power-law tail distributions of time lapses between consecutive individuals passing through the exit, matching experimental findings in both sheep dynamic ([Zuriguél et al., 2014](#)) and pedestrian dynamic ([Garcimartín et al., 2016](#)).

A significant limitation of these models is their inability to adapt to different pedestrian scenarios. In these models, orientation changes occur only through mechanical contact, not anticipation. For instance, applying this model to the Festival of Lights would result in people colliding at wall corners or barriers while attempting to navigate around them. The decision layer, detailed in the next section Sec. 1.2.3, primarily addresses these collision anticipation issues.

1.2.3 DECISION-MAKING LAYER

Let's take another look at the first part of Eq. (1.27), which we'll recall for convenience:

$$\mathbf{v}_i^{\text{des}} = \arg \min_{\mathbf{u} \in \mathbb{R}^2} \mathcal{E} (t, \{\mathbf{q}_j(t)\}_{j \in \llbracket 1, N \rrbracket}, \{\mathbf{v}_j(t)\}_{j \in \llbracket 1, N \rrbracket}, \mathbf{u}) \quad (1.28)$$

The decision is embedded within the first part with the cost function \mathcal{E} , which encompasses all cognitive, psychological and biological constraints — essentially, all non-mechanical contact effects. Consequently, all elements of anticipation are naturally contained within this function. The anticipation process involves estimating its position and velocity as well as those of its neighbours imprecisely over a given duration or time horizon. This horizon may be influenced by various factors, such as physical constraints (like their working memory capacity) and learning. Neuroscience research has long focused on the intricacies of visual input processing and estimation. As explained by [Fishburn et al. \(1979\)](#), traditional decision-making models often assume unlimited time, knowledge, and computational power, allowing for infinite future pedestrian state estimations without temporal constraints. However, real-world scenarios, such as navigating a crowded festival amidst visual noise, impose significant limitations on

these resources.

In response to these constraints, some researchers like [Todd and Gigerenzer \(2000\)](#) propose that humans rely on simple, fast, and frugal heuristics to make effective decisions quickly with minimal information. Individuals may employ straightforward rules of thumb to guide their behaviour in crowd situations as demonstrated by [Seitz et al. \(2016\)](#) in Fig. 1.26 instead of minimising a cost function. Two prominent

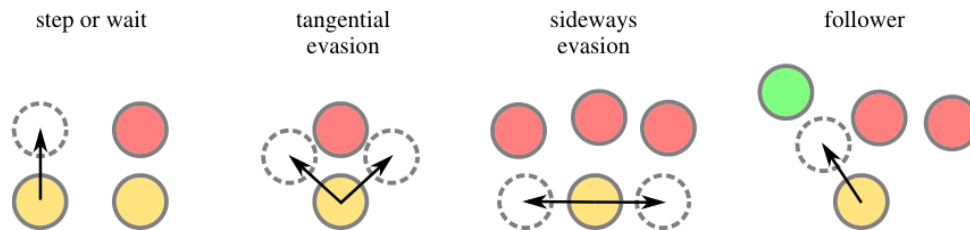


FIGURE 1.26: The illustration depicts four pedestrian movement heuristics, showcasing how individuals navigate in crowded spaces. A pedestrian, represented by a yellow circle at the bottom, interacts with other pedestrians (solid circles) as they all attempt to move upward. Dashed circles indicate potential steps based on each heuristic. The **step-or-wait heuristic** involves moving forward or pausing if the desired space is occupied. **Tangential evasion** allows pedestrians to sidestep around others to avoid collisions. The **sideways evasion heuristic** directs pedestrians to their respective sides when the path ahead is blocked. Lastly, the **follower heuristic** encourages mimicking the movement of another pedestrian heading in the same direction, illustrated by a green circle moving towards the upper left. These cognitive shortcuts help model complex pedestrian behaviours in various crowd scenarios, from normal foot traffic to emergency evacuations. The schemes are reproduced from [Seitz et al. \(2016\)](#).

heuristics are:

Follow the majority Individuals mimic the actions of the surrounding crowd ([Evans et al., 2021](#)).

Follow the leader Leaders significantly influence the behaviour of individuals within a group. The concept of a leader can vary, encompassing those perceived as most successful or confident ([Popper, 2014](#)), or even the nearest neighbour in the field of view ([Zhao and Zhang, 2017](#)).

These heuristics leverage the ‘wisdom of the crowd’ principle, assuming that collective behaviour is most of the time beneficial. These strategies lead to effective outcomes in various situations, such as locating exits or avoiding obstacles. Consequently, individuals can make rapid and beneficial decisions without extensive analysis, resulting in adaptive behaviour. Interestingly, a similar phenomenon occurs in sheep herds as explained by [Gómez-Nava et al. \(2022\)](#). Although sheep adopt a ‘follow the leader’ heuristic, the leader changes frequently. As a result, the herd efficiently locates grazing areas, demonstrating collective intelligence. However, the application of these heuristics is not without risk. Certain scenarios, particularly emergencies, can lead to sub-optimal or dangerous outcomes. For instance, during an evacuation, people might instinctively follow the largest flow of individuals, even if it doesn’t lead to the safest or most efficient exit route as shown by [Lin et al. \(2020\)](#) using **Virtual Reality** environment. The efficacy of these heuristics depends heavily on context. While they often simplify decision-making in complex environments, they can also result in overlooking potentially superior alternatives. Therefore, understanding when and how to apply these heuristics is crucial for optimising crowd management and safety in various situations of the Festival of Lights.

Other models, more fundamental and based on neural coding and decoding ([Ganguli and Simoncelli, 2014](#)), suggest that individuals use more complex cognitive processes than simple heuristics. For instance, individuals first encode information in their brains by constructing a mental representation of visual input data. This representation translates visual input into a language that can be interpreted and usable by the brain, specifically as a certain statistic of neuronal spikes, mathematically represented as a random variable. It is now established that information is intrinsically encoded in the statistics of spikes rather than in the spikes themselves. Therefore, measuring the state of a single neuron does not provide

meaningful information about the processed data, much like how measuring a single bit in a computer does not reveal the information being processed. Individuals make decisions based on this mental representation, such as selecting a desired velocity. This step is called decoding. Computational or resource constraints can be applied to encoding, decoding, or both. This can be framed mathematically as an optimisation problem where the mental representation and decision are optimally computed under biological constraints. Certain heuristics can be retrieved by structuring the problem that way, as demonstrated in research on cognitive biases (Petzschner et al., 2015; Dufour, 2021).

This model formulation in terms of constrained optimisation, similar to Eq. (1.27), bears a striking resemblance to statistical physics approaches that seek to minimise energy while adhering to entropy constraints. It also shares intriguing parallels with game theory formulations in the context of robot motion (Lavage, 1996). As a result, interest in this type of model has been steadily growing among researchers. Its appeal lies in its ability to provide a unified framework for examining diverse phenomena across various situations, offering a powerful tool for interdisciplinary analysis and problem-solving. Let's explore the main ingredients recently implemented in this cost function.

1.2.3.1 BIOMECHANICAL COST

Walking is a complex, multi-causal process involving coordinated movements and muscle activation to achieve a specific goal. It can be divided into two main phases according to Kibushi et al. (2018): stance and swing (see Fig. 1.27 for an illustration). The stance phase, which makes up about 60 % of the gait cycle, includes four sub-phases: loading response (foot flat), mid-stance, late stance, and pre-swing. During this phase, the foot is in contact with the ground, supporting the body weight. In contrast, the swing phase, comprising the remaining 40 % of the gait cycle, involves the advancement of the non-weight-bearing leg from its position behind the body to its position in front of the body, preparing for the next heel strike. Biomechanically, the human body can be modelled as a system of body segments linked at joints. Therefore, human locomotion can be analysed in terms of kinematic (relative motion between segments), kinetic (forces and moments enabling centre of mass motion), and energetic (energy expenditure of motion).

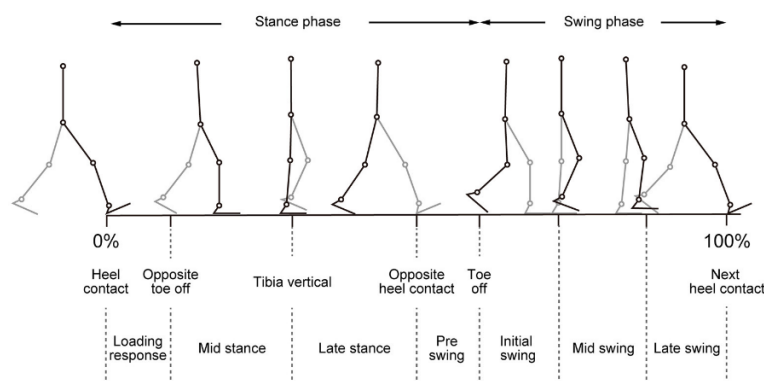


FIGURE 1.27: The gait cycle is depicted through a series of simplified stick diagrams illustrating the key phases of human walking. Each phase is represented by a minimalist human form, with the right leg in black and the left in grey for easy distinction. The cycle begins and ends with the right heel making contact with the ground, encompassing a full stride. The scheme is reproduced from Kibushi et al. (2018).

BIOLOGICAL PERSPECTIVE From a biological perspective, walking requires energy primarily from the metabolic breakdown of fuels such as carbohydrates, proteins, and fats. This process consumes oxygen and produces carbon dioxide as a byproduct. Subsequently, muscles convert this metabolic

energy into mechanical energy to generate forces and facilitate motion. However, this conversion is not perfectly efficient; the metabolic efficiency is typically around 20 – 25 %, with the remainder dissipated as heat. Researchers commonly employ indirect calorimetry techniques to assess energy expenditure while walking. One such method, as described by Hills et al. (2014), measures respiratory oxygen consumption and carbon dioxide production. This approach leverages the direct, linear relationship between oxygen consumption and energy production, which holds at normal walking speeds (between 0.5 and 3 m/s). Specifically, approximately 5 kcal is expended per litre of dioxygen (O_2) consumed. It's important to note that various factors influence energy expenditure during walking. These include walking speed, step size, body weight, and individual characteristics. Interestingly, Cotes and Meade (1960) demonstrated that the energy expenditure of horizontal walking at natural step frequency is linearly related to the square of forward velocity:

$$\mathcal{E}_{\text{speed}} = a + b v^2 \quad (1.29)$$

where a and b are constants that may depend on the type of person considered (age, gender, health). This relationship is illustrated in Fig. 1.28.

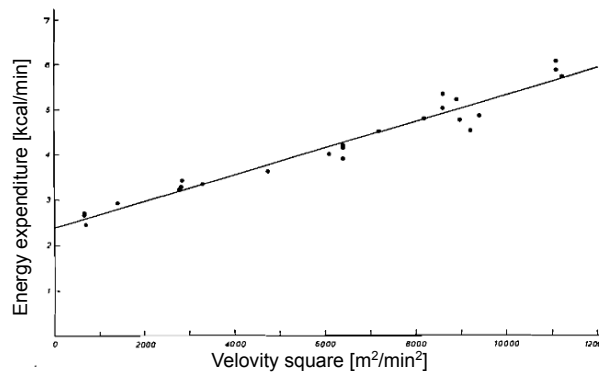


FIGURE 1.28: Energy expenditure as a function of velocity squared for subject walking naturally on a flat surface. The figure is adapted from Cotes and Meade (1960).

MECHANICAL PERSPECTIVE From the mechanical perspective, several models have been developed to explain how humans optimise different mechanical factors to minimise the overall metabolic cost. These include the gait determinants theory, inverted pendulum theory, and dynamic walking theory, as explained by Kuo (2007). A unifying model proposed by Faraji et al. (2018) and illustrated in Fig. A.2 (App. A.1) tries to estimate the metabolic cost of walking from the combination of four primary mechanical components:

Swing and torso dynamics This includes the energy required for leg swing and maintaining torso balance.

Center of mass velocity redirection The energy needed to redirect the **Center of Mass** velocity during step-to-step transitions.

Ground clearance The energy required to lift the foot off the ground during the swing phase.

Body weight support The energy needed to support the body weight during the stance phase.

We have discussed the metabolic cost of translational movement but have yet to address the rotational cost. Although flexible humans can rotate their bodies freely, they are limited by muscle stiffness, joint stiffness, and mobility issues. Consequently, rotating any body part incurs a metabolic and physical cost.

From a **dynamic perspective**, a medical study from Lang et al. (2023) investigated the impact of

upper body movement, particularly torso rotation, on the energy expenditure of runners. That study identified a negative correlation between metabolic cost and the range of torso rotation, indicating that increased torso rotation is linked to lower energy expenditure during running. This counter-intuitive finding suggests that more significant shoulder rotation does not elevate energy costs but reduces them, enhancing running efficiency. Additionally, shoulder and pelvis rotations increase with running speed, highlighting their importance in maintaining balance and efficiency at higher speeds.

From a **static perspective**, [Torén \(2001\)](#) have examined muscle effort using surface **ElectroMyoGraphy**, especially in the external oblique and erector spinae muscles (see [App. A.1](#) for a visualisation), during trunk rotation. It was found that muscle effort remains relatively low up to about a 20-degree twisting angle but increases progressively beyond this point. This indicates that more significant trunk rotation requires higher muscular effort, potentially raising energy expenditure.

Currently, the model may permit a pedestrian to move backwards. Therefore, it is essential to understand how the desired velocity should align with the rest of the body. At first sight, we can assume that a pedestrian's head points toward its desired direction of motion, as turning the head relative to the body incurs a structural cost. However, in some cases, like walking sideways on a familiar path, pedestrians may move without looking ahead, thus avoiding head rotation. This level of detail is not considered. We, therefore, must assess the cost of rotating the head or neck relative to other body parts. This aspect has been explored in studies such as [Liu et al. \(2024\)](#), which examines the mechanical response of the neck during passive motions. In these tests, participants' heads are rotated by a mechanical apparatus while a load cell measures the torque required for this rotation (see [Fig. A.3](#) in [App. A.1](#)).

1.2.3.2 INERTIA

One can incorporate an inertia term into the cost function, which effectively represents the cost of changing the speed between the current moment and a future instant:

$$\mathcal{E}_{\text{inertia}} = K_I \|\mathbf{v}_i(t + \delta t) - \mathbf{v}_i(t)\|^2 \quad (1.30)$$

As [Karamouzas et al. \(2017\)](#) pointed out, incorporating an inertia term to a cost function with a future time δt equal to the simulation time step results in a second-order equation for the desired velocity. Consequently, this approach leads to a set of Newton-like differential equations that describe pedestrian dynamics from both decision-making and mechanical perspectives. Consequently, the resulting trajectory more closely resembles body dynamics, allowing for smooth changes in velocity, such as gradual acceleration or deceleration. This contrasts with first-order models, which assume zero acceleration and constant speed, dependent on pedestrian density.

1.2.3.3 PRIVATE SPACE

[Hall and Hall \(1966\)](#) have explored the role that space plays in human interactions and dynamics. They introduced the concept of proxemics - the study of human use of space as a specialised elaboration of culture. He argues that our spatial perceptions and behaviours are not universal but deeply influenced by cultural and social factors. This understanding is crucial in managing multicultural events such as the Festival of Lights, where cross-cultural interactions are commonplace. To understand how culture may influence proxemics, let's take a look at the human sensory apparatus and its functioning. It includes the sensory organs (eyes, ears, skin, nose, and tongue) and the neural pathways that process sensory information. These systems help us perceive and interact with our environment, including the spatial relationships between ourselves and others. Sensory perception is not just a passive reception of stimuli but an active process influenced by various factors, including cultural

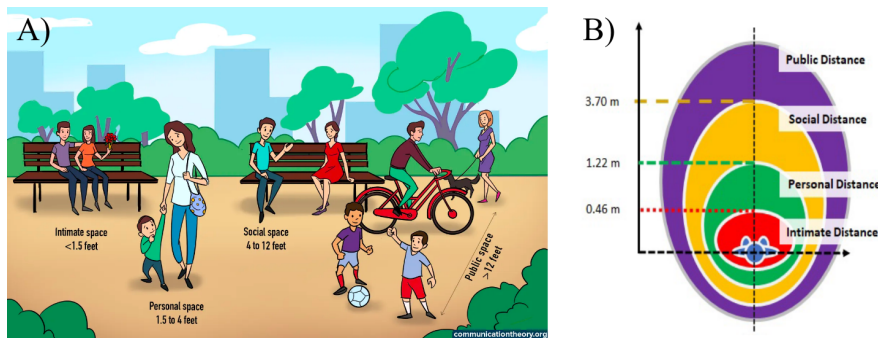


FIGURE 1.29: **Human Interaction Area:** (A) Illustration, from the website [Collective \(2022\)](#), of the interaction distances according to Proxemics. (B) Human interaction area according to Proxemics. The sketch is reproduced from [Patompak et al. \(2020\)](#).

norms and expectations. For instance, [Cao and Gross \(2015\)](#) have revealed that Chinese individuals tend to experience sensory attenuation for sounds produced by others, perceiving them as less intense than their British counterparts. [Hall and Hall \(1966\)](#) identified four primary distance zones in human interactions by measuring the average spacing between individuals across various situations and cultural contexts, as illustrated in Fig. 1.29. These zones - intimate, personal, social, and public - may vary in size depending on cultural factors.

Intimate distance Intimate distance ranges from body contact to approximately 40–50 cm. This zone is typically reserved for close relationships such as couples, parent-child pairs, and close friends. The infringement of this intimate zone by another person can cause discomfort and may even be perceived as painful by people from different cultures who see personal space differently. For instance, [Jourard \(1966\)](#) conducted the so-called coffee study in the U.S., France, the U.K., and Puerto Rico. He watched people sitting in cafes and recorded the rate at which people touched each other in a one-hour sitting. Puerto Ricans touched 180 times, the French 110, the British 0, and the Americans touched twice.

Personal distance Personal distance extends from about 40–50 cm to 120 cm. It includes two phases: **Close phase (50 to 90 cm)** This range allows for physical touch and is common among people who know each other well. It is often referred to as ‘shaking hand distance’. **Far phase (90 to 120 cm)** This range does not permit touch and is typical for interactions where a bit more formality is needed, such as meeting someone unexpectedly on the street. This distance signals readiness for an open and neutral conversation.

Social distance Social distance ranges from approximately 120 cm to 3.5 m. This distance is suitable for casual interactions among acquaintances and strangers. It is common in business meetings, classrooms, and other impersonal social affairs. At this distance, the tone of the conversation is typically polite and professional.

Public distance Public distance is anything beyond 3.5 m and is usually observed between foreigners or in public speaking scenarios. This distance is ideal for lectures, speeches, and other forms of one-way communication to a larger audience.

Proxemic zones play a key role in nonverbal communication, influencing how we interact with others based on our relationships and cultural backgrounds. Recognising and respecting these distances can help prevent discomfort and potential conflicts that could lead to an overreaction, which could propagate through the crowd and lead to an unexpected crowd disaster during the Festival of Lights. In Fig. 1.30, five different shapes of proxemic zones are illustrated, highlighting the complexity and variability of this concept. The precise shape of an individual’s comfort zone remains a subject of debate, as it appears to be influenced by many factors. These include the nature of the interaction, the motion of the individuals involved, and the presence or absence of significant social signals like eye

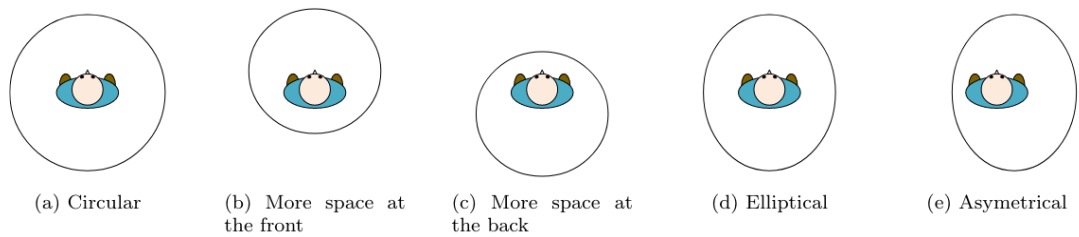


FIGURE 1.30: **Different representations of personal space.** (a) Circular shape (Hall and Hall, 1966), (Hecht et al., 2019), (b) More space at frontal zone (Hayduk, 1981), (Patompak et al., 2020) (c) More space at rear zone (Newman and Pollack, 1973), (d) Elliptical shape (Helbing and Molnar, 1995), (e) Asymmetrical shape (Gérin-Lajoie et al., 2008). The sketch is adapted from Patompak et al. (2020).

contact. While these various models offer insights, further research is needed to fully understand how these elements interact and shape personal space across diverse situations and over time.

One approach to reconciling these different perspectives is to conceptualise proxemic zones in terms of a comfort field surrounding an individual. This can be visualised as a series of concentric barriers emanating from the person, as depicted in part B of Fig. 1.29 and in Fig. 1.19. The lines in these illustrations represent thresholds of decreasing comfort as one is closer to the central individual. To explore this concept experimentally, participants can be asked to rate their comfort on a scale from 1 (minimal comfort) to 10 (maximal comfort) as another person stands at different distances and angles relative to them. By collecting data across a range of positions, researchers can map out a comprehensive field of comfort around an individual. Building on this idea, in the context of interaction between humans and robots, Neggers et al. (2022) proposed to fit this comfort field with an inverted Gaussian function of the polar coordinates as illustrated in Fig. 1.31.

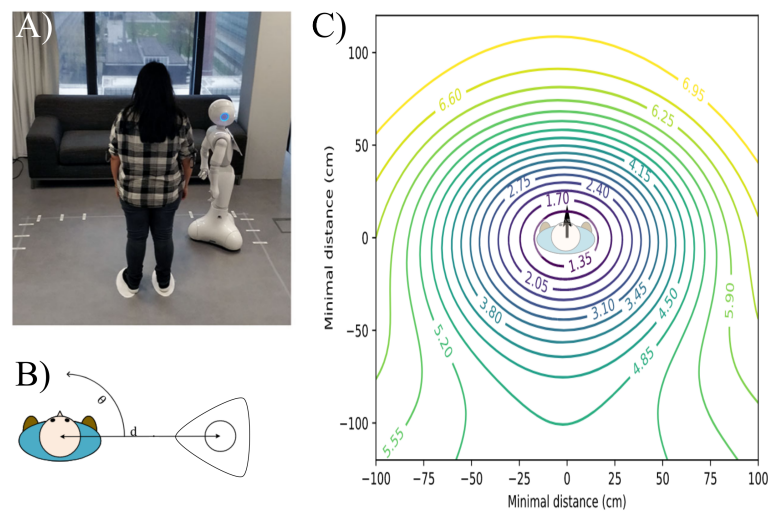


FIGURE 1.31: (A) Picture of the experimental set-up. (B) Schematic overview of distance d and angle θ . Distance d represents the centre-to-centre distance between the human and the robot, and angle θ represents the polar angle of this point. (C) Fitted contour field of comfort space of a **static** human. The arrow represents the orientation of a human, with the front directed to the top of the figure. Axes represent the position in centimetres from the centre of the human. The scale has been intentionally adjusted from that used in the article to ensure it is orthonormal. Comfort is lower at the back of a person. The figures are adapted from Neggers et al. (2022).

We can express some criticisms regarding the employed methodology by Neggers et al. (2022). Based on psychological research and standard survey design practices, individuals generally find it easier to assess discomfort than comfort. This tendency is linked to a greater awareness and sensitivity towards negative experiences, commonly called negativity bias. When using rating scales, people often prefer

to quantify varying levels of discomfort (ranging from mild to severe) over comfort levels. Additionally, no information is provided on how the relative orientation of nearby pedestrians affects the shape of this scalar field.

1.2.3.4 TIME TO COLLISION

The Festival of Lights draws large crowds, with people manoeuvring to avoid bumping into one another. To navigate this bustling environment safely, pedestrians likely anticipate potential collisions and adjust their speed accordingly. [Karamouzas et al. \(2014\)](#) developed a method for calculating a collision avoidance potential based on collision anticipation, known as the **Time To Collision (TTC)** potential. This method is derived from empirical data. To compute the **TTC**, one extrapolates the trajectories of

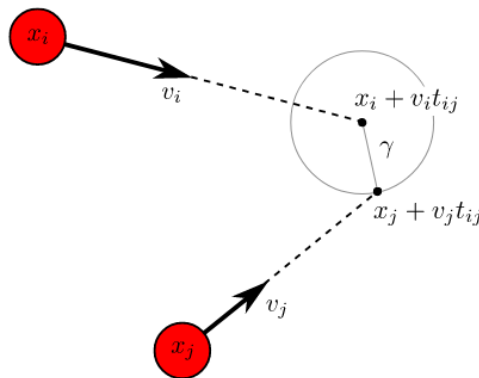


FIGURE 1.32: Calculation of the time to a collision between two pedestrians represented as disks with radius R . The minimum separation distance is $\gamma = 2R$. The scheme is reproduced from [Festa et al. \(2018\)](#).

nearby pedestrians based on their current velocity, as illustrated in Fig. 1.32. This approach utilises the radial distribution function and its relationship to pair potential energy in dilute systems. The pair correlation function, also known as the radial distribution function, is a fundamental measure of spatial particle distribution in a system. It quantifies the probability of finding particle pairs separated by a distance r relative to a random distribution. Typically calculated as the ratio between the histogram of inter-particle distances and that of randomly positioned particles (ideal gas), this function offers a standardised method to compare spatial distributions across different materials. This function provides valuable insights into a material or system's structure and interactions as illustrated in Fig. 1.33. Solid materials exhibit sharp peaks corresponding to atomic lattice positions. It can reveal information about orientation and spatial relationships for pedestrian dynamics, particularly when modelling pedestrians as non-spherical entities like spherocylinders.

Interestingly, expressing this density as a function of **TTC** rather than distance r appears more relevant in pedestrian modelling as outlined by [Karamouzas et al. \(2014\)](#). Indeed, incorporating walking direction into the calculation via **TTC** enables a collapse of different pair distributions computed for various velocity norms as shown in Fig. 1.34. This suggests that **TTC** could be a key variable in describing pedestrian 'material' and measuring potential interactions between its components. It's worth noting that for dilute systems, it's possible to relate the potential interaction energy to the pair correlation function as follows⁶:

$$g(\tau) = \exp\left(-\frac{E(\tau)}{E_0}\right) \quad (1.31)$$

where E_0 is a characteristic pedestrian energy, whose value is scene-dependent. Then [Karamouzas](#)

⁶Physicists refer to this as the reversible work theorem. See [Chandler \(1987\)](#), p. 201 for a proof.

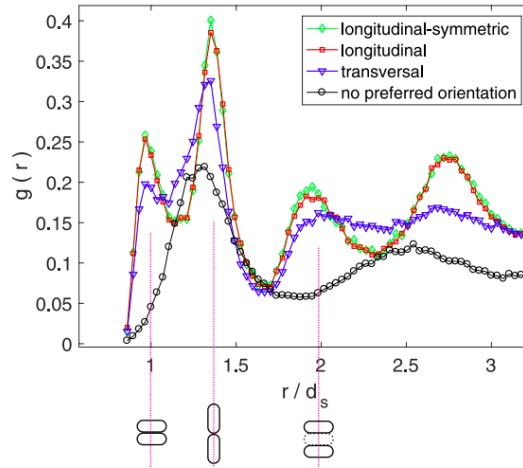


FIGURE 1.33: The pair correlation function $g(r)$ is plotted for active particles similar to pedestrians within a 2 m radius from the exit as they flow through a bottleneck of width $W = 0.7$ m at a propulsion velocity $v_p = 1.0$ m/s. $g(r)$ is displayed for three distinct orientations of the propulsion velocity with respect to the main axis of the spherocylinder, as well as the special case of no preferred orientation for comparison. The distance r is normalised by the particle's short diameter d_s . The figure is reproduced from [Parisi et al. \(2018\)](#).

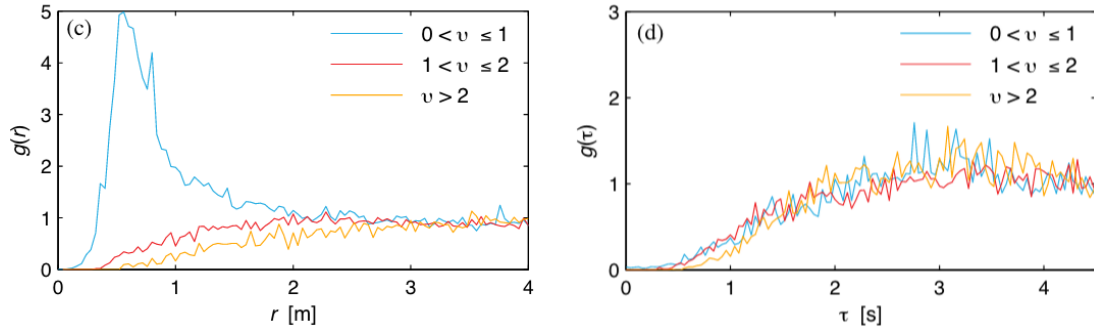


FIGURE 1.34: The pair distribution function g , when plotted versus the inter-pedestrian distance r , exhibits significantly different behaviours for pedestrian pairs with varying velocities in modulus, where v is measured in meters per second. In contrast, when g is calculated as a function of the time-to-collision τ , the curves for different speeds v converge and collapse onto each other, indicating a universal behaviour independent of the speed. The figures are reproduced from [Karamouzas et al. \(2014\)](#).

[et al. \(2014\)](#) propose a functional form for $E(\tau)$ that fits the observed data:

$$E(\tau) \propto \frac{\exp\left(-\frac{\tau}{\tau_{CA}}\right)}{\tau^2} \quad (1.32)$$

where τ_{CA} denotes the time of collision anticipation, also referred to as horizon time. This is typically on the order of seconds (e.g., 3 seconds, as noted by [Karamouzas et al. \(2014\)](#)). Beyond this period, the pedestrian can no longer anticipate a collision, causing the potential to drop sharply. A closed-form formula exists for simple shapes like disks to express the time to a collision between pedestrians, given their positions and velocities. However, it is important to note that no general formula exists for more complex geometries, making it challenging to numerically determine if two pedestrians will collide. Additionally, **Time To Collision** values can exhibit significant discontinuities at the boundary between non-collision and collision scenarios. These discontinuities pose challenges for motion analysis when using differential equations, as they result in sharp discontinuities in the resulting force. To address this issue, it is necessary to smooth these discontinuities, as highlighted by [Karamouzas et al. \(2017\)](#).

1.2.4 DISCUSSION


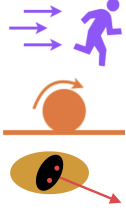


Cost function terms	Description	Illustration
Static floor field	This term accounts for the goal of reaching a specific destination given already known static obstacles.	
Biomechanical	<p>Speed: Represents the metabolic cost required to achieve a specific translational velocity.</p> <p>Inertia: Refers to the cost associated with changes in velocity over time, helping to reproduce the smoothness of data trajectories.</p> <p>Desired direction-body misalignment: Prevent the pedestrian from continuously moving backwards. At first sight, we assume that a pedestrian's head points toward its desired direction of motion, as turning the head relative to the body incurs a structural cost.</p>	
Private	This term captures the desire to maintain one's personal comfort space. While its shape may vary in different situations and with changes in velocity (Patompak et al., 2020), we assume it remains constant due to a lack of experimental data. This assumption is crucial for identifying stationary patterns, such as people waiting during events like the Festival of Lights.	
Time-to-collision	Focuses on avoiding collisions of comfort spaces while walking.	

TABLE 1.2: Components of the decision-making cost function. All have already been introduced into Echeverría-Huarte and Nicolas (2023) model for circular-shaped pedestrians except the desired direction-body misalignment term. The mathematical expressions of the biomechanical cost and Static Floor Field term, which do not depend on the pedestrian shape, are presented in App. C.2.1 and App. C.2.2 respectively and summarised in App. C.2.3.

A portion of the literature on crowds has chosen to describe their behaviour microscopically, that is, by imposing rules on the individuals' dynamics, distinguishing two stages in the dynamics. The first stage involves selecting a desired speed based on minimising a cost function that includes various terms accounting for the desire to reach the target via a floor field and the inherent constraints of being human. These constraints (summarised in the Tab. 1.2) include biomechanical limits related to our muscles and joints, cognitive constraints related to our ability to extract and use information from the surrounding environment, and more psychological factors (at a slightly higher cognitive level than the processing of external stimuli) such as the desire to preserve comfort space and avoid collisions.

It is essential to note that these cost terms are largely well-grounded in experimental evidence and are not merely arbitrary rules. They depend on parameters that can be measured experimentally, which is a strength, in contrast to the classic Social Force Model, whose parameters heavily depend on the specific scenario encountered.

A preliminary pedestrian model attempting to compile some of these elements for circular pedestrian forms was developed by Echeverría-Huarte and Nicolas (2023), but its extension to arbitrary shapes has not yet been achieved and is the subject of Chap. 3 of this thesis.

CHAPTER 2

A MULTI-SCALE FIELD STUDY AT THE FESTIVAL OF LIGHTS IN LYON

In recent years, numerous pedestrian models have been developed, with parameters calibrated using databases of high-density trajectories collected under controlled laboratory conditions. However, this approach has limitations in real-world applications. Here, I present one of the first comprehensive field-collected datasets of pedestrian trajectories and meta-information that has been led to address this gap. This extensive dataset spans several hundred square meters and captures densities reaching up to 4 pedestrians per square meter. Furthermore, this valuable dataset will serve to calibrate the two-dimensional model presented in Chap. 3, enhancing its real-world applicability. The data collection occurred during the 2022 edition of the Festival of Lights in Lyon as part of the Franco-German MADRAS project. The dataset encompasses a wealth of information, including up to 7000 trajectories, Global Positioning System (GPS) data, and contact information. Moreover, it identifies rare events and phenomena of interest, providing a comprehensive view of pedestrian behaviour in complex, real-world scenarios. The methods used for data collection are presented, ensuring transparency and reproducibility of the research.

This chapter's content has been adapted from the article (Dufour et al., 2024f), submitted to Scientific Data. In this work, I personally organised the data collection in Lyon, manually tracked LargeView trajectories, gathered and analysed contact numbers, GPS tracks, and LargeView trajectories. Additionally, I contributed to the description and methodology for the Festival of Lights, calibrated LargeView cameras, and contributed to building an interactive app for data exploration. The data can be accessed through the following links, each providing specific types of information:

Dataset Dufour et al. (2024a) Offers TopView trajectory data, capturing multidirectional flow patterns and paths from a bird's-eye perspective.

Dataset Dufour et al. (2024b) Provides GPS data, offering precise location tracking and mapping information.

Dataset Dufour et al. (2024c) Contains geometric data relevant to the study, detailing spatial configurations and measurements.

Dataset Dufour et al. (2024d) Comprises TopView trajectory data at smaller densities.

Dataset Dufour et al. (2024e) Includes survey data, which encompasses responses and feedback collected during the research.

2.1 INTRODUCTION

Large gatherings raise challenges regarding public safety and flow management. Religious festivals, music concerts, and significant outdoor events are particularly concerning due to their history of inadequate crowd management, which, in the worst instances, has led to deadly stampedes or crowd crushes (Helbing et al., 2007; Sieben and Seyfried, 2023; Feliciani et al., 2023; Sharma et al., 2023b). These accidents are documented in the timeline in Fig. 2.1. Beyond the rules of thumb that have been refined over the years, a deeper fundamental understanding of the dynamics of dense crowds will be instrumental for more efficient event planning and crowd management. Here, a crowd will be described as dense if its density exceeds the arbitrary threshold of 1.5 or 2 ped/m², thus falling in Fruin (1970) ’s Level of Service F; critical conditions with extreme densities (say, above 8 ped/m²), which must be avoided in practice, are left out of the scope.

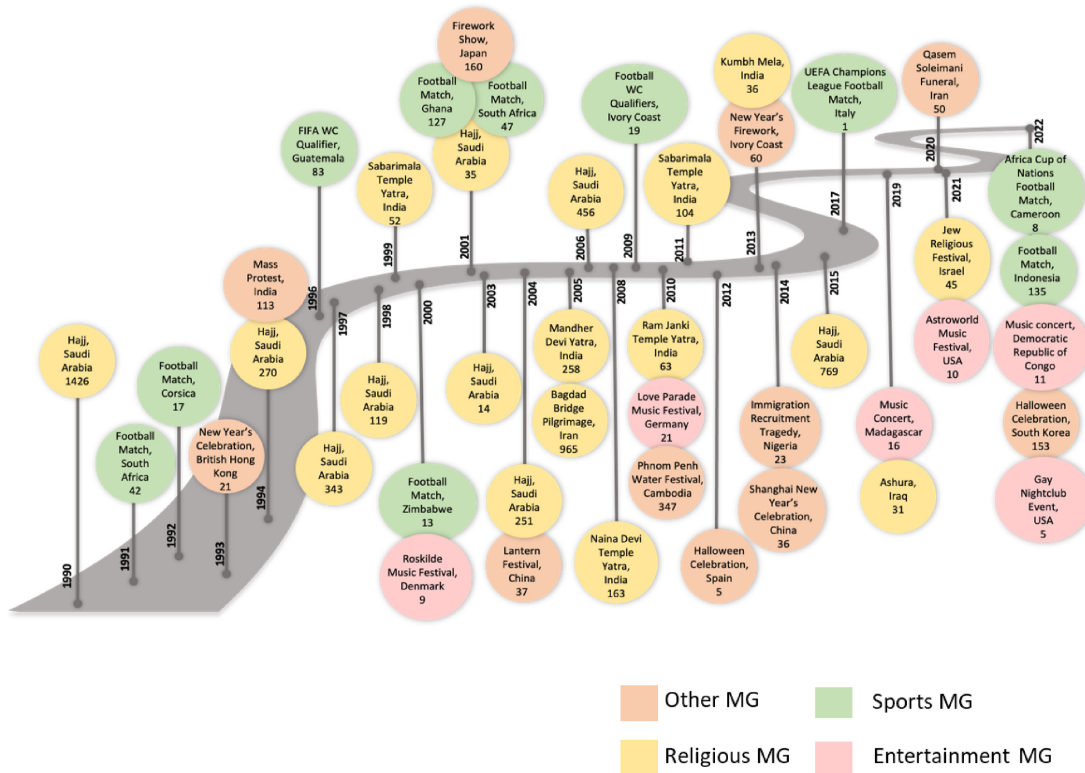


FIGURE 2.1: Deaths and injuries resulting from crowd crush at mass gathering events, 1990–2022. The scheme is taken from Sharma et al. (2023a).

2.1.1 CONTROLLED EXPERIMENTS IN THE REAL WORLD

The current theoretical understanding of crowd dynamics in high-density scenarios primarily stems from controlled experiments conducted in idealised environments, such as the ones performed in large sheds by teams from the Forschungszentrum Jülich (2020) research centre. These experiments allow researchers to precisely control parameters and observe a range of uncommon scenarios, such as emergency evacuations with high-density crowds, bidirectional flows, unidirectional flows, and pedestrian dynamics at intersections (Zhang and Seyfried, 2014; Cao et al., 2017). Let us also mention

the datasets collected by the groups of [Haghani et al. \(2020\)](#) and [Pastor et al. \(2015\)](#) to explore crowd dynamics during emergency evacuation drills, [Murakami et al. \(2021\)](#) to probe the emergence of unidirectional and bidirectional pedestrian flows or those of [Nicolas et al. \(2019\)](#) dedicated to the response of crowds to the crossing of intruders. However, these highly controlled environments often fail to reflect the full complexity of real-world situations accurately. Experimental conditions can differ significantly from reality, and laboratory experiments frequently struggle to capture the complete context in which behaviours occur. Factors such as social desirability bias and the artificial nature of the lab setting can lead participants to alter their behaviour, thus affecting the validity of the results.

2.1.2 CONTROLLED EXPERIMENTS IN VIRTUAL REALITY

In recent years, [Virtual Reality \(VR\)](#) platforms have gained popularity as tools for studying crowd behaviours due to their ability to provide low-cost, precise control over experimental conditions in scenarios that are difficult or unethical to replicate in real life, such as emergency evacuations due to fire ([Lin et al., 2020](#)). Locomotion trajectories in [VR](#) are qualitatively similar to reality but exhibit quantitative differences as shown by [Shipman et al. \(2024\)](#), [Yin et al. \(2022\)](#) and [Olivier et al. \(2014\)](#). The interaction loop in [VR](#) affects user behaviour, introducing perception and motion generation biases. Needed visual feedback in [VR](#) generally enables participants to make realistic navigation decisions but with some limitations, such as delayed collision information and slight positional offsets. Locomotion interfaces induce various biases, including altered walking speeds, modified personal space sizes, and increased gait instability.

2.1.3 FIELD DATA

Meanwhile, the thirst for **field data** to train data-based methods, such as machine learning algorithms, remains unquenched for dense crowds because field studies usually involve situations of low density. The primary datasets are listed in [Tab. 2.1](#). For instance, the widely used [Eidgenössische Technische Hochschule \(ETH\)](#) dataset and [University of Cyprus \(UCY\)](#) dataset, which originate from surveillance videos, capture pedestrian scenes at density $0.1 - 0.5 \text{ ped/m}^2$, with many pedestrian avoidance situations. In this density range, the pedestrian dynamics are governed by different mechanics than at higher density ([Fruin, 1970](#); [Best et al., 2014](#); [Cordes et al., 2024](#)). Often, empirical datasets encompass a heterogeneous mixture of road users, as in the [Stanford Drone \(SD\)](#) dataset, which includes pedestrians, cyclists, skateboarders, cars, and buses. While these datasets capture small scenes, the [Grand Central Station \(GCS\)](#) dataset covers a vast area in a train station in New York. Although one scene can contain hundreds of pedestrians, the average density is below 0.2 ped/m^2 due to the size of the area. Also worth mentioning is the [Edinburgh Informatics Forum \(EIF\)](#) dataset, which provides trajectories of 92 000 people in a university playground from an overhead camera. The data cover 118 days of observation with very low average densities and, most of the time, just a few pedestrians in one scene. Studies on mass gatherings that utilise a sparse sample of smartphone signals also exist ([Wirz et al., 2013](#)). More extensive reviews of field studies on pedestrian trajectories can be found in ([Amirian et al., 2020](#); [Haghani, 2020](#); [Korbmacher and Tordeux, 2022](#)).

2.1.4 SCIENTIFIC CONTRIBUTION

The present work aims to compensate for the lack of field data on dense crowds by providing a comprehensive picture of pedestrian flows at a large gathering around a major culture and entertainment event. For this purpose, we collected various types of data relevant to pedestrian dynamics and crowd management at the Festival of Lights (2022), which took place in the city of Lyon, France, in December. These data cover an extensive range of length scales, from the global flow picture and contextual elements down to individual pedestrian trajectories and some statistics on physical contacts. In the following, an emphasis shall be placed on all observations that depart from what is typically prescribed or observed in controlled experiments, thus further underlining the added value of actual field data.

TABLE 2.1: Summary of pedestrian field datasets

Dataset name	Density [ped/m ²]	Description	References
ETH	0.1 – 0.5	Captures pedestrian scenes with many avoidance situations	(Pellegrini et al., 2009)
UCY	0.1 – 0.5	Captures pedestrian scenes with many avoidance situations	(Lerner et al., 2007)
SD	< 0.1	Includes pedestrians, cyclists, skateboarders, cars, and buses in small scenes	(Robicquet et al., 2016)
GCS	< 0.2	Covers a large area at the Train Station in New York with many pedestrians	(Zhou et al., 2012)
EIF	< 0.01	Provides trajectories of 92 000 people in a university playground over 118 days	(Majecka, 2009)

2.1.5 LYON’S FESTIVAL OF LIGHTS

Lyon’s yearly Festival of Lights is a four-evening event (from December 7 to 11 in 2022, mostly from 7 pm to 11 pm) wherein the city is lit up remarkably. Originally a religious tribute to the Virgin Mary, it has become a massive international festival renowned for its innovative light shows and artistic projections on historic buildings. The event attracts millions of local and international visitors, more than 2 million officially in 2022, according to a newspaper article published in *Le Progrès* (12 Dec. 2022). Key attractions include *Place des Terreaux* and *Place Saint-Jean*, where light shows were reported to be watched by 150 000 and 80 000 spectators every night, respectively, in 2022 as mentioned in the newspaper article in *Le Progrès* (12 Dec. 2022). Quite interestingly, managing the associated crowd flows is one of the most prickly issues for the event organisers to ensure smooth flows and reasonable delays for a pleasant experience, but above all, to ward off crowd accidents, especially after a difficult situation witnessed in the 2000s¹ and the tragedies that have occurred in massive entertainment events around the world, e.g. at the Love Parade in Duisburg, Germany, in 2010 (Sieben and Seyfried, 2023) or during Halloween on the streets Seoul, Korea, in 2022 as illustrated in Fig. 2.1. This is achieved by regulating flows at different scales: **macroscopically**, by suggesting routes through the city to visit the multiple light installations, for instance, starting at *Place Bellecour*, moving to *Place des Terreaux*, and then exploring *Vieux Lyon*, especially near Saint-Jean Cathedral; **mesoscopically**, by installing barriers and safety agents, particularly near *Place des Terreaux*, and imposing unidirectional flows in many streets to ease congestion **microscopically** by continuously monitoring the event with CCTV. Our methodology explores these three scales for crowd flows, focusing on the microscopic one at the central location of *Place des Terreaux*. The crowd’s movement was notably monitored with strategically placed cameras, as depicted in Fig. 2.3.

¹Private communication with the organisers of the event.

2.2 METHODS

2.2.1 GENERAL ORGANISATION OF THE DATA COLLECTION CAMPAIGN

Data collection was planned to capture a complete picture of pedestrian motion during the Festival of Lights. For that purpose, we combined various methods targeting different scales. **Macroscopically**, we inspected the broad patterns of macroscopic crowd flows on the ground around *Place des Terreaux* and recorded the scene with a broad overview. We surveyed passers-by near the square and asked them the following questions:

- "How many people were with you?"
- "How many children were with you?"
- "What was the last screening you attended before the one at *Place des Terreaux*?"
- "What screening do you plan to attend next? (You can answer that you don't know)"

We tried to limit bias in the selection of the 79 respondents by making no distinction as to general or physical appearance and by ensuring that we interviewed a sample from around the square and not limited to a single street. **Mesoscopically**, we recruited participants willing to share their **GPS** data and record how often they bumped into other people. **Microscopically**, we installed several cameras filming specific zones from the top (with all required authorisations to ensure privacy preservation). Below, we make a distinction between *TopView* cameras (labelled 1, 2, 3, 5, 6, 7, 8) and *LargeView* camera (labelled 4). An overview of the data collected in this study is shown in Fig. 2.2.

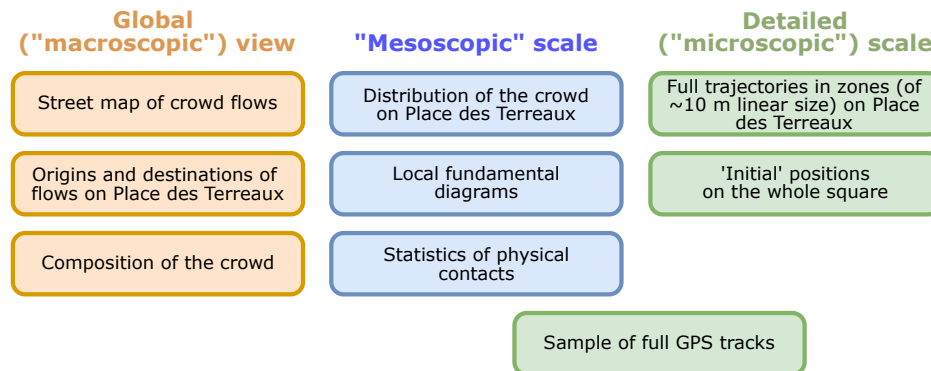


FIGURE 2.2: Scales probed in this manuscript and summary of the data collected at each scale.

2.2.2 GPS DATA OF RECRUITED PARTICIPANTS AND COLLISION COUNTS

A group of 24 undergraduate and doctoral students from the **Institut Lumière Matière (ILM)** in Lyon were invited to participate in the field study. More precisely, they were asked to follow a general route (starting from the queue at the entrance to the square, on *Rue du Président Edouard Herriot* to the exit on *Rue Lanterne*, following the flow of the crowd), behaving as a standard spectator. Meanwhile, their smartphones recorded their **GPS** positions using the *GeoTracker* application. Although the accuracy of the measurements varied from phone to phone, the trajectories obtained were generally reliable, with a margin of error of around 10 meters. Besides, each participant used a stopwatch on their smartphone to record each moment they collided with another pedestrian. Upon synchronisation with the **GPS** data, this method enabled us to determine precisely the time and the location of the collisions. Every participant was taught what to consider a collision. Minor rubbing of clothing was therefore not recorded. We also tried to involve spectators on site, explaining the instructions and procedures, but none managed to send us **GPS** data. Over the 24 students involved in that experiment, 16 provided us

with a detailed list of physical contacts, among which 8 could be coupled to GPS data.

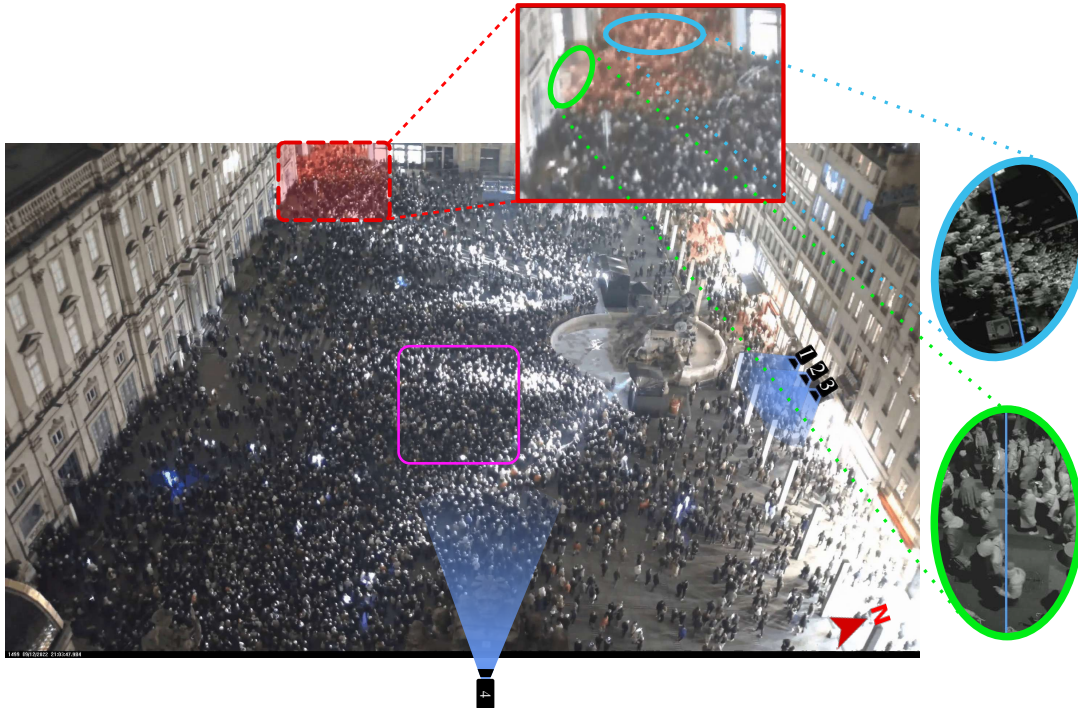


FIGURE 2.3: A dense crowd gathered in and around *Place des Terreaux* following a light show on 12 December 2022, at 9 : 41 pm (Additional Video). The fields of view from our cameras are marked in blue, while the square pink area represents the portion of the camera’s four field of view we tracked precisely. **Inset**: A zoomed-in view shows two exit streets where we monitored the outflow.

2.2.3 VIDEO PROCESSING AND PEDESTRIAN TRACKING FOR THE *TOPVIEW* CAMERAS

To get a finer view of pedestrian trajectories, we deployed lightweight *SjCAM A10* cameras, selected for their night vision capabilities and long battery life, at strategic locations around *Place des Terreaux*. These cameras filmed the scene from a zenithal perspective. Three cameras, labelled 1, 2, and 3 in Fig. 2.4, were positioned on the north side of *Place des Terreaux*, protruding from the windows of an *Airbnb* apartment and a restaurant on the second floor. They captured the bidirectional movement of pedestrians below. Another camera, numbered 8, was mounted atop an existing post at the square’s southeast corner to monitor incoming flows; however, its nighttime footage was unusable due to lighting issues. Two additional cameras, numbered 5 and 6, were placed on *Rue Constantine*, one of the main exits after the light show, hanging from the balconies of an *Airbnb* apartment to film pedestrian egress from above. A final camera numbered 7 was temporarily held at the end of a stick at the southwest corner to provide a closer view of the pedestrian outflow. The portable *SjCAM A10* cameras recorded nearly 200 GB of video at 30 frames per second.

From the collected footage, pedestrian trajectories were extracted from 10 excerpts (see Tab. 2.4), using the PeTrack software (Boltes and Seyfried, 2013a,b). This software is commonly employed for detecting and tracking pedestrians’ heads in controlled experimental settings. The process notably involves calibrating the cameras to match pixel coordinates with real-world coordinates, split into two distinct phases: intrinsic and extrinsic calibration. **Intrinsic calibration** corrects the optical distortions specific to each camera lens by determining the optimum parameters to transform a reference pattern, such as a checkerboard, into its recorded image (see App. B.2 for a detailed explanation). Then, **extrinsic calibration** yields the conversion between real-world coordinates and pixel coordinates using three

successive operations: a rotation and a translation of the reference frame, followed by a projection to move from the camera frame to the screen frame (see App. B.1 for a detailed explanation). The parameters of these operations minimise the differences between the known real-world coordinates of objects (here, staff members) positioned at predefined positions (here, at regularly spaced positions on a virtual *grid*) and the associated pixel coordinates. Such calibration is only an approximation if the people who are filmed are of unequal heights, especially without a stereoscopic camera to reconstruct the scene in three dimensions². The inaccuracy decreases as the camera positions higher and films from a zenithal viewpoint. In this setup, the maximum uncertainty due to differences in height is expected to be approximately 22 cm for the **CCTV** footages and 8 cm for the *SjCAM* footages (look at App. B.3 for a detailed explanation). Additionally, there are uncertainties in detecting the central point on the head (approximately $\lesssim 5$ cm) and errors arising from the fact that not all individuals stand perfectly upright. After the calibration step, pedestrians are detected and tracked in the videos from the *SjCAM* footage using a semi-automatic process with the PeTrack software. In contrast, **CCTV** footages are tracked manually. Compared to controlled experimental conditions, several challenges were encountered, primarily due to lighting conditions. To address this, pedestrian heads were initially detected manually and then tracked frame-by-frame using the extended pyramidal iterative Lucas-Kanade feature tracker (Bouguet, 2004) integrated into PeTrack. Although this method is notably robust, manual corrections are frequently necessary when illumination shifts abruptly from dark to bright areas.

2.2.4 VIDEO PROCESSING AND PEDESTRIAN TRACKING FOR THE *LARGEVIEW* CAMERAS

In addition to the previously mentioned *TopView* cameras, we have gathered extensive *LargeView* video footage from cameras that offer a bird’s-eye view of the entire square. Two of these cameras are located at *Place Saint-Jean*. In contrast, another camera (numbered 4 in Fig. 2.4) captures *Place des Terreaux* from the City Hall tower, approximately 48 meters above ground level (Archives Municipales de Lyon, 2024). Although all recordings are accessible, only the videos from *Place des Terreaux* have undergone thorough analysis and are discussed in this report. The expansive view provided by the camera, numbered 4, along with variations in lighting, prevents the automation of tracking using PeTrack, necessitating a semi-manual approach. Intrinsic calibration was deemed unnecessary as the camera lens exhibited minimal optical distortion, verified by the straightness of lines in the video footage. Comprehensive extrinsic calibration was conducted by positioning a staff member at 32 predefined, evenly spaced points across the square (as illustrated in Fig. B.3) and applying the geometric transformations outlined below. The resulting accuracy for *absolute* positions, assessed using independently collected positions (either of the same staff member or others), ranged from 10 cm to approximately 2 meters at the farthest end of the square, over 80 meters from the camera horizontally. Given that this inaccuracy is primarily geometric, the *relative* positions between pedestrians and their neighbours are expected to be significantly more precise.

Initially, we manually identified the positions of all individuals across the entire square at a specific moment, occasionally reviewing video frames to locate pedestrians temporarily obscured from view. This was done after a show cycle, as people began to exit, on Thursday, December 8. Subsequently, we tracked a random sample of approximately 270 individuals over several seconds, with around 100 of them being tracked for a duration of 20 seconds. Finally, we focused on a specific area of interest where opposing flows of people intersect. This area is square-shaped (before correcting for geometric distortion) and is located near the fountain, a critical convergence point with high density. We used custom Python-based software to manually track the trajectories of all visible individuals in

²For more detailed information on stereographic cameras, including the calculations between image coordinates and the corresponding 3D points in real space, please refer to the work by Mussabayev et al. (2018).

this area over approximately 30 seconds, typically pointing at a rate of two frames per second. Linear interpolation allowed us to increase the sampling rate of the trajectories to 10 Hz before exporting them as *CSV* files.

It should be noted that the resolution and quality of these videos are inferior to those of other videos. This, combined with varying illumination, impeded the detection of some individuals, especially children and shorter people, in specific frames. Consequently, while these trajectory sets may exhibit imperfections compared to those extracted from the *TopView* cameras, they remain accurate, nearly comprehensive, and address more complex flow scenarios than the *TopView* cameras.

2.2.5 CONVERSION INTO GLOBAL COORDINATES

All trajectories were converted into global coordinates using the *RGF-93* Lambert-93 coordinate reference system (*EPSG:2154*) for precise global positioning. This transformation involved adjusting the positions of several landmarks visible in the videos and satellite imagery. The geometric shapes and locations of all obstacles in the square, including the fountain, temporary crowd barriers surrounding it, bollards, and Buren columns, were determined through direct measurements, satellite imagery, and photographs taken on-site; they are provided as an external dataset.

2.2.6 QUANTITATIVE INDICATORS

Relevant static and dynamic indicators can be computed using the detailed pedestrian trajectories.

Flow rate. The outflow rate during the egress from *Place des Terreaux* was measured by virtually drawing cross-section lines at the two main exits, as shown in Fig. 2.3. The number of people crossing these lines was manually counted by reviewing the recorded videos.

Density field. To be useful, the extracted microscopic trajectories often need to be smoothed into continuous fields. Specifically, the local density field, denoted as $\rho(\mathbf{r}, t)$ (Johansson et al., 2008), is derived by computing the convolution of the microscopic particle density $\rho_\mu(\mathbf{r}, t) = \frac{1}{A} \sum_j \delta(\mathbf{r} - \mathbf{r}_j(t))$ —where $\delta(\cdot)$ is the Dirac delta function and A is the surface area—with a Gaussian kernel $\phi_\xi(\mathbf{r}) \propto \exp\left(-\frac{\mathbf{r}^2}{2\xi^2}\right)$ whose integral is normalised to 1, for a chosen half-width ξ , viz.:

$$\rho(\mathbf{r}, t) = \int_{\mathcal{A}} \rho_\mu(\mathbf{r} - \mathbf{r}') \phi_\xi(\mathbf{r}') d^2\mathbf{r}' \quad (2.1)$$

For further smoothing, the time dependence can also be coarse-grained by averaging the field over a short time window Δt :

$$\bar{\rho}(\mathbf{r}, t) = \frac{1}{\Delta t} \int_{t-\frac{\Delta t}{2}}^{t+\frac{\Delta t}{2}} \rho(\mathbf{r}, t') dt' \quad (2.2)$$

Velocity field. Similarly, the microscopic velocities $\mathbf{v}_j(t) = \frac{1}{\delta t} \cdot [\tilde{\mathbf{r}}_j(t + \delta t) - \tilde{\mathbf{r}}_j(t)]$, estimated from the vector difference between two positions of pedestrian j over a small time interval δt (with $\delta t = 0.5$ or 1 second in this context), can be coarse-grained. The trajectories are initially smoothed using a second-order Butterworth low-pass filter. Trajectories that are too short for effective filtering remain unfiltered (which represents 9% of the total number of trajectories). Near the start (t_s) and end (t_e) of each trajectory, linear interpolation is applied between the raw trajectory \mathbf{r} and the filtered trajectory $\tilde{\mathbf{r}}$ to address the Butterworth filter's limitations when past or future data points are absent. This interpol-

ation is expressed as³ $\tilde{\mathbf{r}}_j(t) \leftarrow \alpha(t)\mathbf{r}_j(t) + [1 - \alpha(t)]\tilde{\mathbf{r}}_j(t)$, where $\alpha(t) = \max\{e^{-(t-t_s)}, e^{-(t_e-t)}\}$. Subsequently, the trajectories are converted into a velocity field through Gaussian convolution:

$$\mathbf{v}(\mathbf{r}, t) = \frac{\sum_j \mathbf{v}_j(t) \phi_\xi(\mathbf{r} - \tilde{\mathbf{r}}_j(t))}{\sum_j \phi_\xi(\mathbf{r} - \tilde{\mathbf{r}}_j(t))} \quad (2.3)$$

The resulting field exhibits abrupt variations due to many individuals deviating from, or walking counter to, the primary local flow direction. Like the density field, the velocity field can be averaged over a finite time interval Δt to smooth out these variations:

$$\bar{\mathbf{v}}(\mathbf{r}, t) = \frac{1}{\Delta t} \int_{t-\frac{\Delta t}{2}}^{t+\frac{\Delta t}{2}} \mathbf{v}(\mathbf{r}, t') dt' \quad (2.4)$$

The coarse-grained picture given by the smooth velocity field masks possible counterflows and fluctuations, whose presence can be ascertained by computing a *variance* field:

$$\text{Var}_{\mathbf{v}}(\mathbf{r}, t) = \frac{\int_{t-\frac{\Delta t}{2}}^{t+\frac{\Delta t}{2}} \sum_j \phi_\xi(\mathbf{r} - \mathbf{r}_j(t')) \|\mathbf{v}_j(t') - \bar{\mathbf{v}}(\mathbf{r}, t)\|^2 dt'}{\int_{t-\frac{\Delta t}{2}}^{t+\frac{\Delta t}{2}} \sum_j \phi_\xi(\mathbf{r} - \mathbf{r}_j(t')) dt'} \quad (2.5)$$

Trajectories of counter-walking pedestrians j significantly deviate from the continuous flow, thus exhibiting a large variance relative to the velocity field, denoted as $\text{Var}_{\mathbf{v}}^j$. More precisely, the variance is computed by averaging the squared difference between pedestrian j 's velocity $\mathbf{v}_j(t)$ and the coarse-grained velocity $\bar{\mathbf{v}}(\mathbf{r}_j(t), t)$ at that position, over the entire duration of pedestrian j 's trajectory, i.e. $\text{Var}_{\mathbf{v}}^j = \langle \|\mathbf{v}_j(t) - \bar{\mathbf{v}}(\mathbf{r}_j(t), t)\|^2 \rangle$.

Fundamental diagram. The fundamental diagram is obtained by relating the instantaneous pedestrian speeds $\|\mathbf{v}_j(t)\|$ to the local density ρ (binned in cells of linear size 0.25 m and duration 0.5 s).

2.3 DATA DESCRIPTION

2.3.1 SIZE OF THE CROWD AND FLOW DIRECTIONS

Place des Terreaux is centrally located in Lyon and serves as a key attraction during the Festival of Lights. Pedestrian traffic around the square is regulated: spectators enter from the southeast via *Rue du Président Edouard Herriot*, typically remain in the square for the duration of one show (6 minutes and 30 seconds), sometimes two, and then exit either to the southwest via *Rue Constantine* or to the northwest via *Rue d'Algérie*, as illustrated in Fig. 2.4 b.

Field surveys conducted around 11 pm on Friday revealed that most spectators had previously watched light animations just south of the square. Upon entering *Place des Terreaux*, many were uncertain about their next destination or planned to head home. These large-scale origin-destination flows are depicted in Fig. 2.4 a. Spectators usually belong to social groups of two to four people; larger groups, up to ten people, also exist but are less frequent. Most groups do not include children, although groups with one or two children were observed, as shown in Fig. 2.5.

The entrance to *Place des Terreaux* is managed by gatekeepers who ensure the square does not exceed approximately two-thirds capacity. They restrict access by closing a barrier before the start of each

³At the start ($t = t_s$) and end ($t = t_e$) of the trajectory, α is close to 1, giving more weight to the original data. This helps preserve the trajectory's endpoints. In the middle, α decreases, giving more weight to the smoothed data. The beginning and end of the raw trajectories are thus preserved, reducing artefacts from filtering.

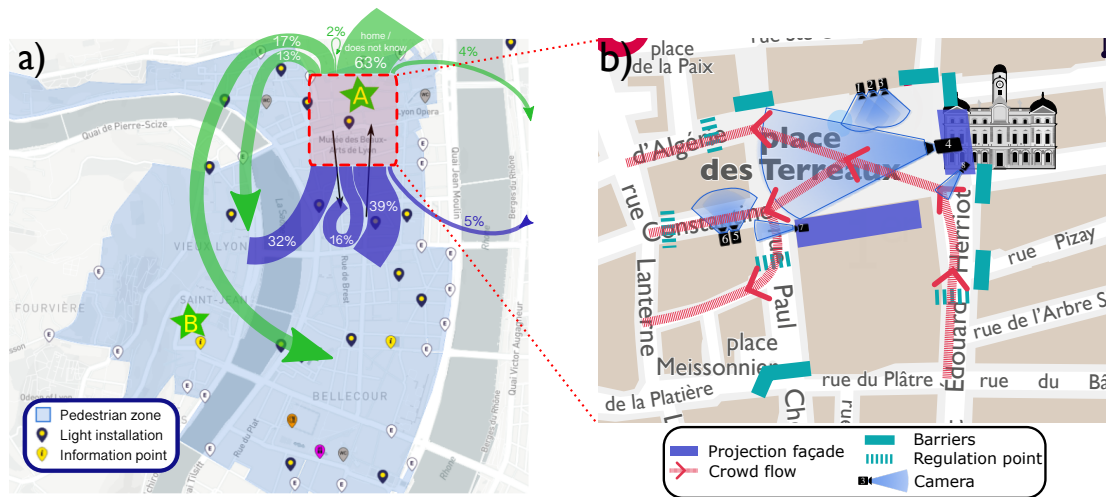


FIGURE 2.4: Maps of the macroscopic crowd flows during the Festival. (a) Pedestrian zone for the Festival (adapted from the official map) indicating the distribution of origins (in blue) and destinations (in green) of around 300 people, just before and just after the show on *Place des Terreaux*, obtained by surveying 79 passers-by around 11 pm on Friday, December 8, 2022. (b) Local map showing the imposed flow directions around *Place des Terreaux*. All figures are oriented to the North unless otherwise shown in the figure.

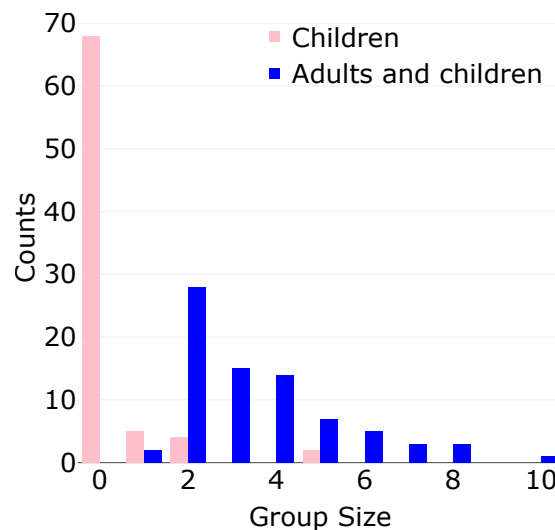


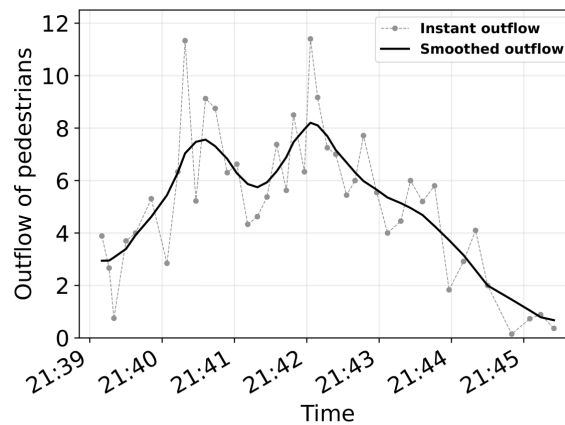
FIGURE 2.5: The histogram illustrates the sizes of social groups, both adults and children (in blue), and only children (in pink), as reported by survey respondents around 10 : 30 pm to 11 pm on Friday 9 December 2022. These groups were part of the crowd preparing to enter *Place des Terreaux*. The counts refer to the number of groups. It is important to note that these self-reported values indicate a significantly higher number of groups with at least four members compared to estimates made by the authors through direct street observations.

show, leading to a queue of people standing on *Rue du Président Edouard Herriot* that can stretch over several blocks. During a light show, the number of people in *Place des Terreaux* can significantly exceed 4000, as determined by manually detecting the initial positions of the entire crowd on video (refer to Tab. 2.2). This number is corroborated by the cumulative pedestrian outflow measured at both exits, *Rue Constantine* and *Rue Paul Chenavard*, at the end of a show, from 9 : 38 pm to 9 : 45 pm on 9 December 2022 (see Sec. 2.2). The total evacuation time was approximately 6.5 minutes.

The evolution of pedestrian outflows over time is illustrated in Fig. 2.6. This figure presents both the raw, instantaneous values (depicted by dashed black lines) and the smoother curves (solid black line) obtained by applying a Gaussian filter with a kernel standard deviation of 2.0. The maximum outflow exceeded 11 ped/s on *Rue Constantine* and nearly reached 10 ped/s on *Rue Paul Chenavard*. In total,

3833 pedestrians were counted, with 1803 on *Rue Constantine* and 2030 on *Rue Paul Chenavard*. These figures correspond to a global density below one pedestrian per square meter. However, as we will observe, the global average is not particularly insightful due to significant spatial heterogeneity. It is important to note that both counting methods tend to underestimate the actual numbers, as not all individuals were manually counted in the snapshots, and some remained in the square after the show. Despite the regulated inflow, variations in the number of attendees occur during each cycle. Remarkably, visual inspection of the entrance and egress flow points reveals a high degree of regularity in these flows across cycles. Notably, obstacles and prohibited areas (marked in blue in Fig. 2.8) visibly alter the flows, creating a confluence zone between the fountain and the northern building, along with congestion points on the opposite side of the fountain. In contrast, the crowd moves almost freely along the southern side, which is less attractive to spectators during the show, as projections are primarily displayed on the facade of the south building.

(a) *Rue Constantine*



(b) *Rue Paul Chenavard*

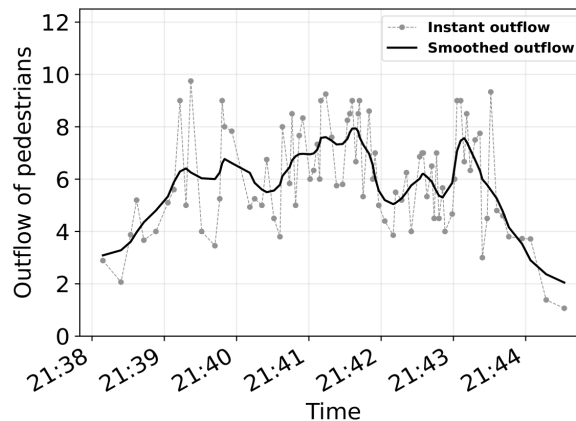


FIGURE 2.6: Pedestrian outflows, measured in pedestrians per second, during a cycle on 10 December 2022 (a spatio-temporal diagram used to compute the outflow is available in App. B.4).

The GPS trajectories collected from informed participants, as depicted in Fig. 2.7, illustrate potential routes from the square’s entrance to its exit and beyond. By synchronising these trajectories with the reported times of pushes and strong contacts, we can identify where these interactions occurred; their locations are marked as stars on the figure. Notably, the number of such pushes varies significantly among participants, ranging from nearly zero to approximately 100 throughout the trajectory, as noticeable in Fig. 2.7. These variations highlight the heterogeneity of the crowd packing, the diversity of individual behaviours, and, plausibly, different appraisals of what should be counted as a push. Still, the order of magnitude of the frequency of strong contacts questions the collision-free navigation hypothesis

at the heart of some models based on velocity obstacles (Van Den Berg et al., 2011; Karamouzas et al., 2017), but also, at the other pole, the strong role played by contact forces at densities below 4 ped/m^2 in some force-based models.

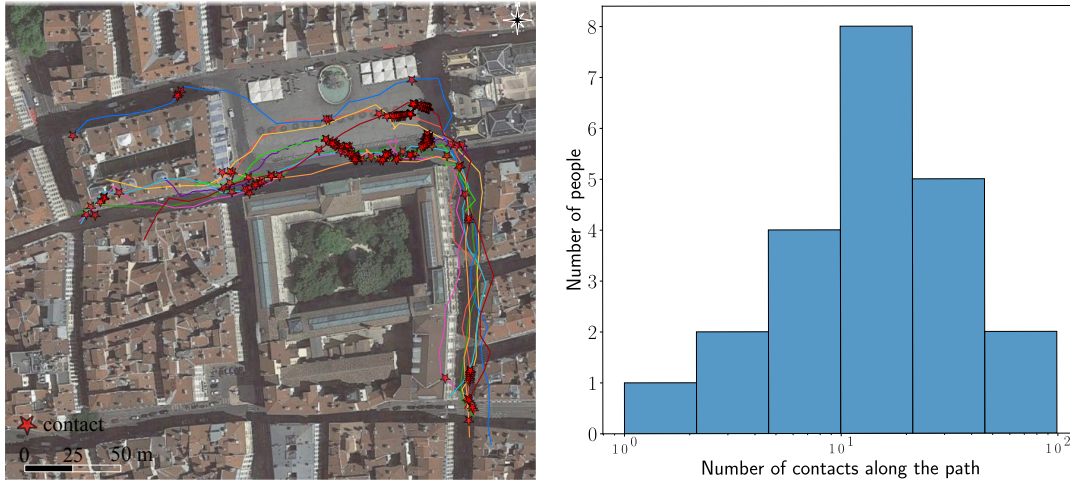


FIGURE 2.7: **Left panel:** Ten GPS tracks are paired with contact data, with each contact marked by a red star. Clusters of red stars appear at the entrance and exit of Place des Terreaux. Note that the satellite view timing does not match the data, and some GPS tracks overlap buildings due to varying GPS precision across devices, providing a general idea of contact locations. **Right panel:** A histogram showing the distribution of contact counts along the path on a logarithmic scale, incorporating data from the left panel and additional entries without GPS tracks.

2.3.2 GLOBAL VIEW OF THE FLOW PATTERNS ON PLACE DES TERREAUX

To better understand the crowd distribution and flow patterns during the evacuation of the square after a show, we analyzed the *LargeView* video recordings. From a snapshot captured at the start of the repeated evacuation process, we manually extracted the positions of all visible heads in the crowd. These positions are represented as small red disks in Fig. 2.8 a, along with the accessible geometry of the square. The heterogeneous spatial distribution is manifest and becomes even more pronounced in the corresponding density field shown in Fig. 2.8 b, where local densities range from nearly 0 ped/m^2 to 4 ped/m^2 . The trajectories of approximately 100 randomly sampled pedestrians tracked over about 20 seconds and shown in Fig. 2.8 a (also see [Supplementary Video](#)), further exhibit marked heterogeneity, with a significant portion of pedestrians halted and some moving counter to the flow. To get a broader perspective on this heterogeneity, we measured the initial velocities, defined as the speeds of individuals when instructed to exit the square at the end of the light show, for a larger sample of 270 people over a few seconds, as shown in Fig. 2.8 b. Plotting these initial speeds against the local density provides the fundamental diagram presented in Fig. 2.9 (left). In comparison to conventional fundamental diagrams (Vanumu et al., 2017), typically derived from controlled environments. The data presented here exhibit significantly more variability. Precisely, while the highest speeds observed at a given density align broadly with Weidmann’s empirical formula (Wirz et al., 2013) $v(\rho) = v_0 \cdot \left[1 - \exp \left(-\gamma \cdot \left(\frac{1}{\rho} - \frac{1}{\rho_{\max}} \right) \right) \right]$, many speed data points fall between 0 m/s and this envelope. These points often represent individuals strolling, possibly due to social interactions within their groups or because they are stationary. This observation parallels the debate in vehicular traffic studies about a unique relationship between speed and density, with some advocating for a

fundamental diagram that spans a two-dimensional region⁴ (Jiang et al., 2014). Despite this variability, discernible flow patterns emerge during the evacuations of *Place des Terreaux*. Most pedestrians move westward towards the two main exits at the top of Fig. 2.8. Between the fountain and the northern building (right side of the figure), flows predominantly head west through a convergence zone, which will be examined in more detail later. Along the road adjacent to the southern building, most trajectories extend linearly from East to West under near free-flow conditions. In contrast, trajectories closer to the fountain are notably shorter over the same time interval, indicating congestion and a greater diversity of movement, with many individuals at a standstill.

File	Date [UTC+1]	Duration	# Initial Positions	# Long (~ 20 s) Trajectories / All	Mean / Median Speed [m/s]
<i>LargeView</i>	8 December 2022 20 : 13	20 s	4081	114 / 277	0.44 / 0.36

TABLE 2.2: Basic statistics for the *LargeView* inspected over the whole square.

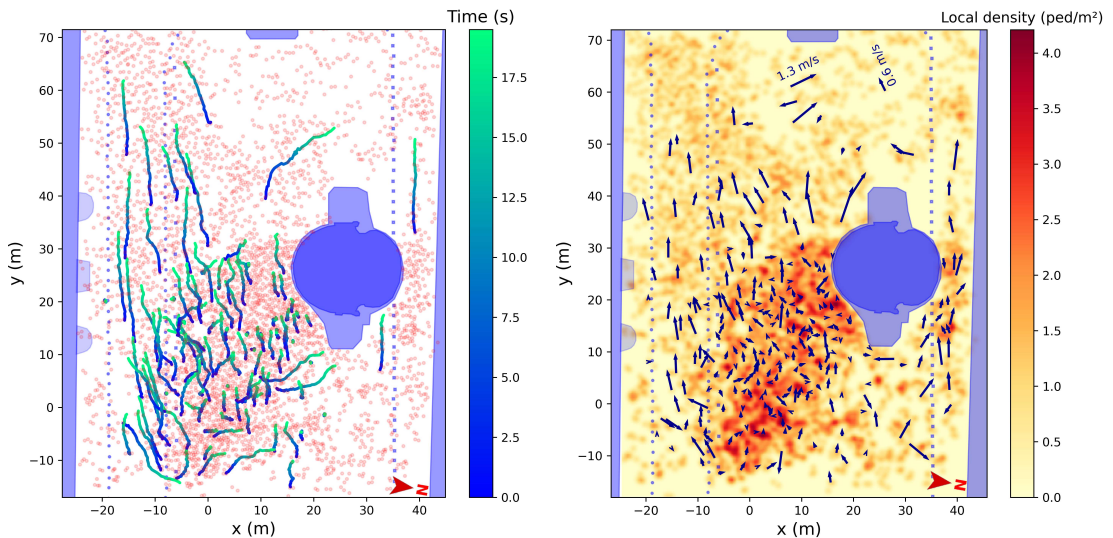


FIGURE 2.8: A comprehensive overview of the crowd’s positions and dynamics on *Place des Terreaux* is presented. **Left Panel:** This panel illustrates the trajectories of approximately 100 pedestrians tracked over a span of 20 seconds. Small red disks mark the initial positions of all individuals in the square. Various obstacles, such as fountains, buildings, bollards, and barriers, are shaded in blue. **Right Panel:** This panel displays the initial velocities of around 270 pedestrians, computed with a time step of $\Delta t = 1$ s. The background features a heat map representing the initial density field, computed using a Gaussian kernel with a half-width of $\sigma = 0.5$ m.

2.3.3 COMPLEX FLOW IN A REGION OF HIGH DENSITY NEAR THE CENTRE OF THE SQUARE

Let’s delve deeper into the pedestrian flows by examining the central zone, highlighted by the pink rounded square in Fig. 2.3. This area, measuring 15 meters by 25 meters, exhibited complex patterns and high densities during two distinct periodic egresses. We endeavoured to track all pedestrians within this zone semi-manually, limited by the video resolution and occasional occlusions (see Sec. 2.2 for details). The extracted trajectories can be used to construct and animate a *digital twin* of the crowd, providing a direct visualisation of the crowd flow. This animation does not account for the heterogeneous sizes of pedestrians, representing all agents as standard adults, nor does it consider their social relationships.

⁴as a heatmap visualising time against local density, with speed indicated by colour. It effectively allows to discriminate between stationary individuals and dynamic instabilities, such as stop-and-go waves.

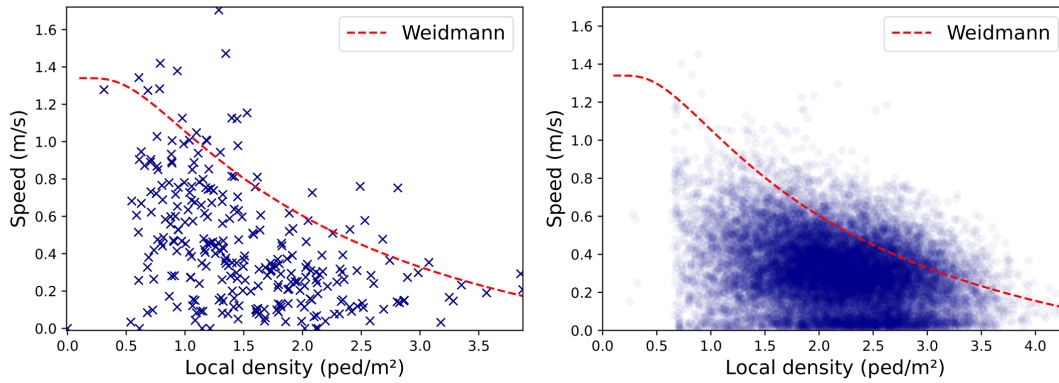


FIGURE 2.9: The fundamental diagrams illustrate the relationship between pedestrian speed and local density. The left panel depicts this relationship across the entire *Place des Terreaux*, using a sample of initial velocities as shown in Fig. 2.8 (right panel). The right panel focuses on a central region of the square, where pedestrians were exhaustively tracked for approximately 20 seconds (see Fig. 2.10). The dashed red lines represent Weidmann’s empirical formula: $v(\rho) = v_0 \cdot \left[1 - \exp\left(-\gamma \cdot \left(\frac{1}{\rho} - \frac{1}{\rho_{\max}}\right)\right)\right]$ with parameters $v_0 = 1.34$ m/s, $\gamma = 1.9$ m⁻², and $\rho_{\max} = 5.4$ ped/m².

At first glance, there is a noticeable overall flow towards the West (the top of the image). However, the flow pattern is non-uniform, featuring counter-flows, individuals squeezing through the crowd, and others moving slowly.

These complex features that obscure the general characteristics can be simplified by coarse-graining trajectories into smooth density and velocity fields, as illustrated in the left panels of Fig. 2.10 and Fig. 2.11. These smooth fields reveal noticeable density heterogeneities, but the flow pattern is more streamlined: most velocity vectors are aligned, directed towards the top of the figure, and rarely exceed half a meter per second. A slight tendency to navigate around densely populated areas is still observable. These coarse-grained fields can be interpreted as the underlying base flow. On top of this base flow, the variability of trajectories can be reintroduced by calculating local velocity variances, as shown in the right panels of Fig. 2.10 and Fig. 2.11, highlighting trajectories that significantly deviate from the base flow (see Sec. 2.2). This distinction between a smooth, streamlined base flow and counter-walking agents may be beneficial from a modelling perspective, allowing for advancements beyond the homogeneous flows predicted by macroscopic models.

The fundamental diagram relating the velocity magnitude $\|\mathbf{v}\|(\mathbf{r}, t)$ to the local density $\rho(\mathbf{r}, t)$ (with time binned into intervals of 0.5 seconds) is presented in Fig. 2.9. It is essentially similar to that obtained for a sample of pedestrians across the entire square; the maximum speed observed at a given density exhibits a downward trend with increasing density, but all speeds below this upper bound are represented.

File	Start [UTC+1]	Duration	# trajectories	Mean density [ped/m ²]	Mean / median speed [m/s]	Median / Mean trajectory duration [s]
<i>LargeView</i>	8 December	20 s	740	1.92	0.30 / 0.29	17.50 / 17.98
<i>Zoom_A</i>	2022 20 : 16					
<i>LargeView</i>	9 December	45 s	726	1.85	0.29 / 0.27	33.21 / 41.7
<i>Zoom_O</i>	2022 21 : 05					

TABLE 2.3: Basic statistics for the exhaustive trajectory dataset extracted from an area of interest in the *LargeView* videos.

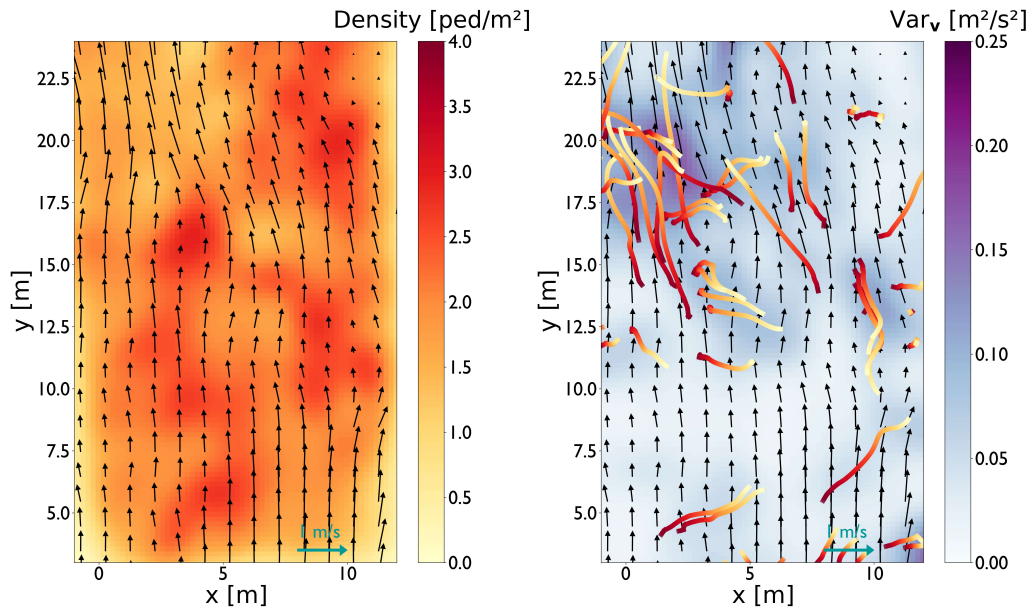


FIGURE 2.10: Continuous description of the complex flow at the centre of the *Place des Terreaux* at 20 : 15, recorded with a *LargeView* camera. **Left panel:** Local density field averaged over the time window of 10 s in our local coordinate system. **Right panel:** Variance field $\text{Var}_v(\mathbf{r})$. The displayed trajectories (coloured from red to yellow as time moves on) are those of *counter-walking* pedestrians, i.e., those who significantly deviate from the continuous velocity field by $\text{Var}_v^i \geq 0.12 \text{ m}^2/\text{s}^2$. The arrows represent the continuous velocity field over the same time window of 10 s. All fields have been smoothed with a characteristic length-scale $\xi = 0.75 \text{ m}$.

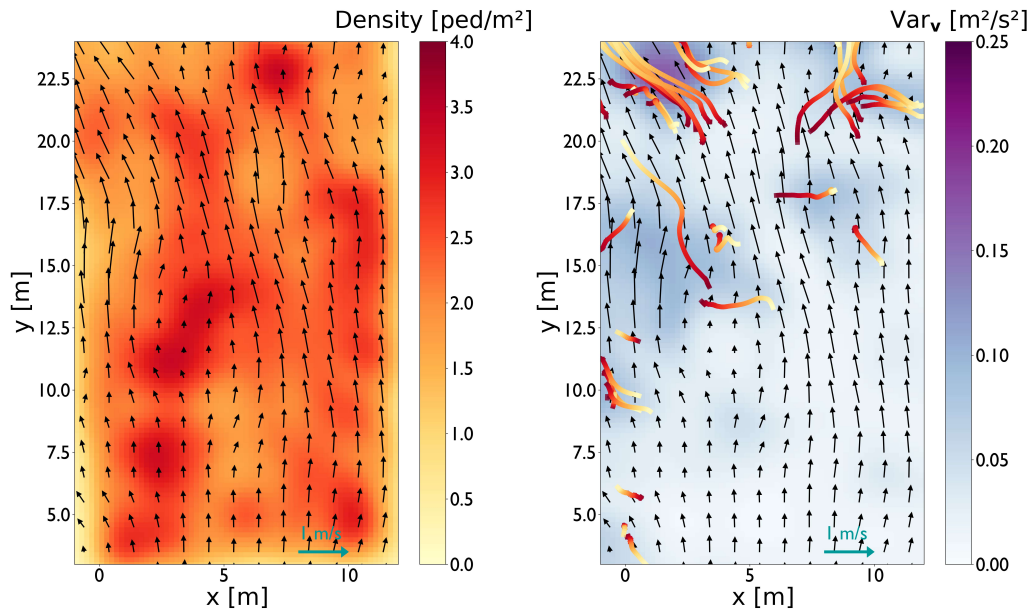


FIGURE 2.11: Continuous description of the complex flow at the centre of the *Place des Terreaux* at 21 : 05, recorded with a *LargeView* camera. Refer to Fig. 2.10 for the rest of the caption.

2.3.4 UNIDIRECTIONAL AND BIDIRECTIONAL FLOW AT DIVERSE DENSITIES ALONG THE NORTHERN BUILDING

The flow pattern along the northern building of *Place des Terreaux* (see Fig. 2.3) appears less intricate compared to the central region. Movement predominantly follows an East-West direction. Additionally, the resolution and orientation of the *TopView* camera 2 provide higher-quality microscopic data for these trajectories. Despite this apparent simplicity, the crowd flows deviate from the idealised unidirectional and bidirectional flows observed in controlled experiments, albeit to varying degrees.

To gain a comprehensive understanding, the fundamental diagram is presented in Fig. 2.12, which averages the speed of the trajectories and the global density level in one-second intervals. The scatter in this relationship is significantly reduced compared to measurements taken in the centre of *Place des Terreaux* (see Fig. 2.9). Furthermore, Tab. 2.4 provides basic statistics for each of the nine trajectory datasets, with three sequences specifically selected for detailed analysis.

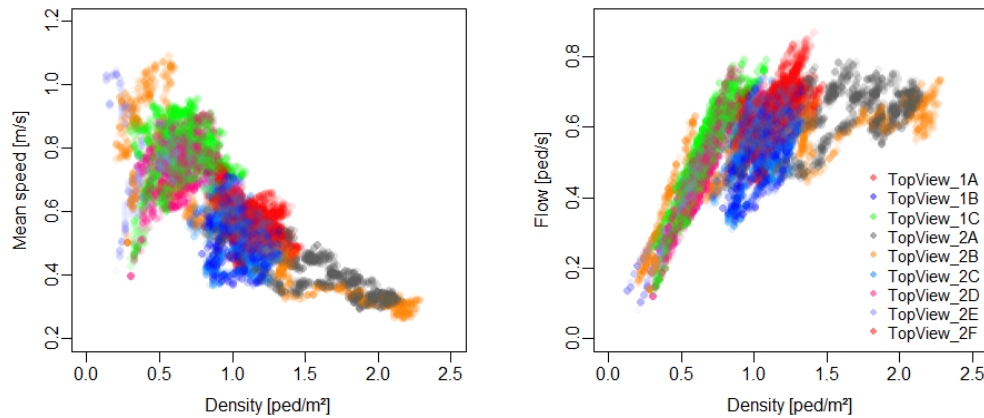


FIGURE 2.12: The fundamental diagram obtained by averaging the speed of the trajectories and the global density level in the scene in time steps of one second is shown for the *TopView* datasets. The diagrams closely resemble those from Feliciani (2017) for multidirectional flow, as illustrated in Fig. B.11 of the App. B.5.

File	Start [UTC+1]	End [UTC+1]	# trajectories	Mean density [ped/m ²]	Mean speed [m/s]	Median / Mean trajectory duration [s]
<i>TopView_1A</i>	22 : 40 : 45	22 : 44 : 15	965	1.13	0.57	13.23 / 12.27
<i>TopView_1B</i>	22 : 55 : 06	22 : 57 : 46	685	1.07	0.52	11.76 / 12.64
<i>TopView_1C</i>	23 : 10 : 33	23 : 13 : 58	673	0.65	0.78	9.2 / 9.03
<i>TopView_2A</i>	21 : 26 : 27	21 : 29 : 07	711	1.58	0.41	19.1 / 18.11
<i>TopView_2B</i>	21 : 40 : 39	21 : 43 : 25	612	1.11	0.58	11.17 / 13.18
<i>TopView_2C</i>	22 : 55 : 18	22 : 58 : 20	693	1.06	0.54	11.96 / 12.94
<i>TopView_2D</i>	23 : 10 : 16	23 : 12 : 57	529	0.64	0.75	8.83 / 8.96
<i>TopView_2E</i>	23 : 24 : 59	23 : 26 : 11	218	0.57	0.75	8.83 / 8.63
<i>TopView_2F</i>	23 : 54 : 59	23 : 56 : 30	183	0.37	0.95	6.8 / 6.92
Total			5269	0.96	0.63	10.63 / 12.22

TABLE 2.4: Basic statistics for the exhaustive trajectory datasets extracted from *TopView* videos.

2.3.4.1 UNIDIRECTIONAL PEDESTRIAN FLOW (TOPVIEW_2B)

In the *TopView_2B* video recording, unidirectional flow prevails. Among the 612 trajectories collected, 496 pedestrians move from right to left, 60 from left to right, 46 from bottom to top, and 10 from top to bottom. In the left panel of Fig. 2.13, trajectories are colour-coded based on their entry and exit points: green for entry on the left and exit on the right, grey for entry on the right and exit on the left, red for entry from the bottom and exit at the top, and blue for entry from the top and exit at the bottom. Despite the prevailing unidirectionality, it is noteworthy that the streamlines are not strictly parallel in this essentially unconstrained geometry, even when focusing solely on the grey trajectories. Examining the density and speed profiles, computed using Gaussian-kernel filters (see Eq. (2.3) and the documentation in Mohcine and Dufour (2024) and Schrödter, Tobias and The PedPy Development Team (2023)), Fig. 2.13 (right panel) reveals that they are relatively uniform, except for a few pedestrians standing in the upper left of the scene, which results in density peaks.

Finally, Fig. 2.14 presents a time series of various global indicators. The cumulative inflows from the four directions confirm the dominance of pedestrians moving to the right. Interestingly, there is a noticeable evolution of density over time. From $t = 30$ s onward, the density steadily increases from 0.4 to 2.2 ped/m², as observed in the snapshots in Fig. 2.15. The average speed in the area mirrors this trend, decreasing steadily from about 1 to 0.3 m/s. These trends align with expectations based on existing literature on unidirectional flow in controlled experiments. The reduced average speed at low density can be attributed to static individuals and the presence of social groups, which are known to reduce walking speed (Nicolas and Hassan, 2023).

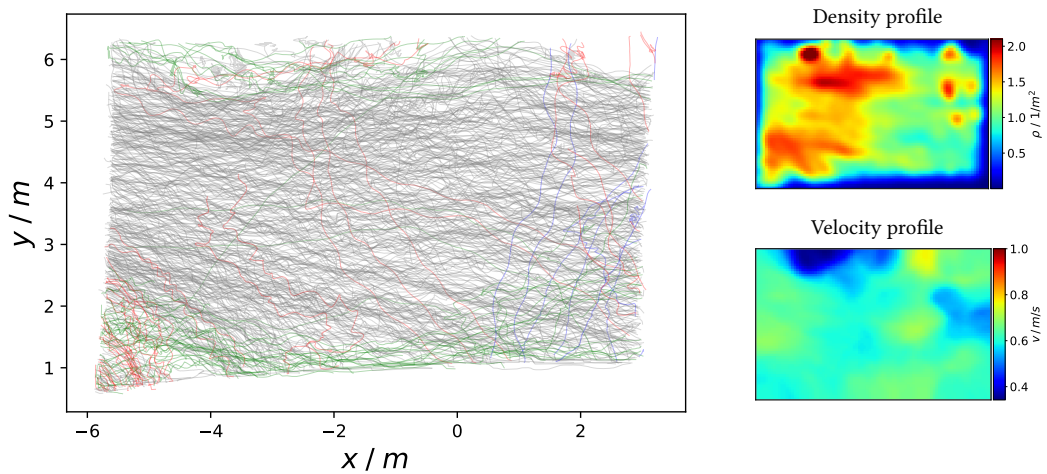


FIGURE 2.13: Trajectories (left panel) with density and speed profiles (right panels) for the *TopView_2B* video recording showing predominantly unidirectional pedestrian dynamics.

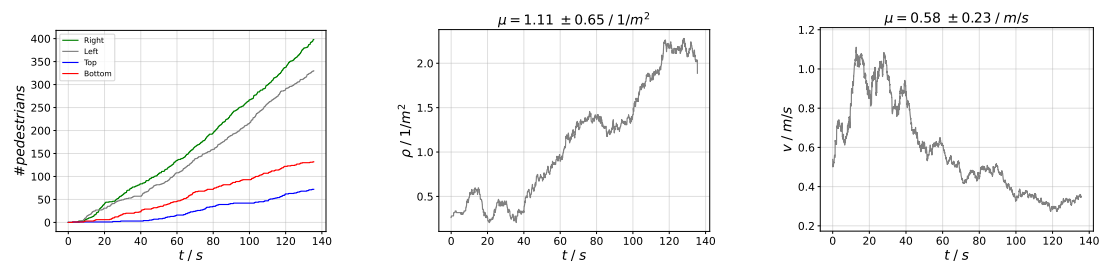


FIGURE 2.14: Cumulative flow, density and mean-speed time series for the *TopView_2B* video recording. The density increases over time for this video recording while the speed decreases.

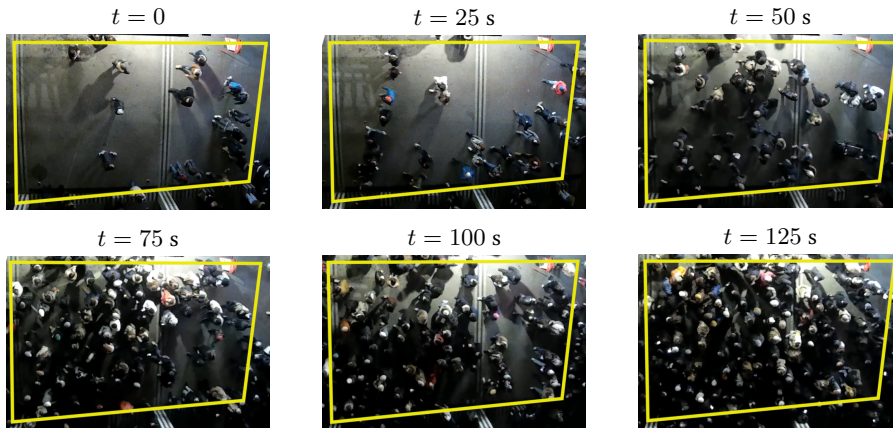


FIGURE 2.15: Snapshots of the *TopView_2B* video recording at different times.

2.3.4.2 UNIDIRECTIONAL FLOW WITH STANDING PEDESTRIANS AS OBSTACLES (TOPVIEW_2C)

The *TopView_2C* sequence, captured in the same area, introduces an additional perturbation: a group of pedestrians standing in the upper left part of the scene. Out of the 693 trajectories recorded, 603 pedestrians move to the left, 68 to the right, 15 upward, and 7 downward, indicating a predominantly unidirectional flow. However, the presence of the static group significantly impacts the trajectories, compelling other pedestrians to navigate around it and causing congestion in the flow dynamics (see Fig. 2.16, left panel).

The density and speed profiles reveal two congested queues with reduced speed around the stationary group (see Fig. 2.16, right panels). The situation remains stationary over time, with global density fluctuating between 0.8 and 1.3 ped/m² and average speed ranging from 0.4 to 0.7 m/s (see Fig. 2.17). The snapshots corroborate this in Fig. 2.18, which depicts similar crowding conditions.

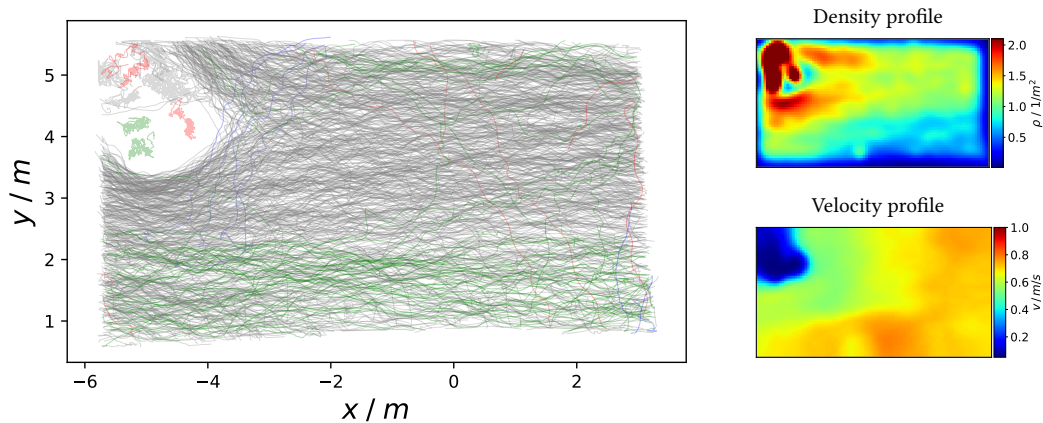


FIGURE 2.16: Trajectories (**left panel**) with density and speed profiles (**right panels**) for the *TopView_2C* video recording. The pedestrian dynamics are predominantly unidirectional, while the scene includes standing pedestrians in the upper left corner, initiating avoidance behaviour and queuing.

2.3.4.3 UNBALANCED BIDIRECTIONAL FLOW (TOPVIEW_2D)

The last recording that we describe, *TopView_2D*, contains 529 pedestrian trajectories, including 396 trajectories to the left, 109 to the right, 13 up and 13 down (see Fig. 2.19, left panel). The counter-walking pedestrians can no longer be neglected. They generate a substantial counter-flow with lane

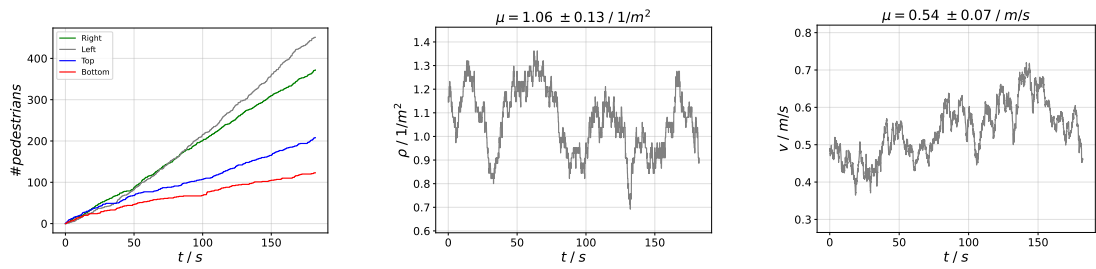


FIGURE 2.17: Cumulative flow, density and mean-speed time series for the *TopView_2C* video recording. The situation is relatively stationary in time.

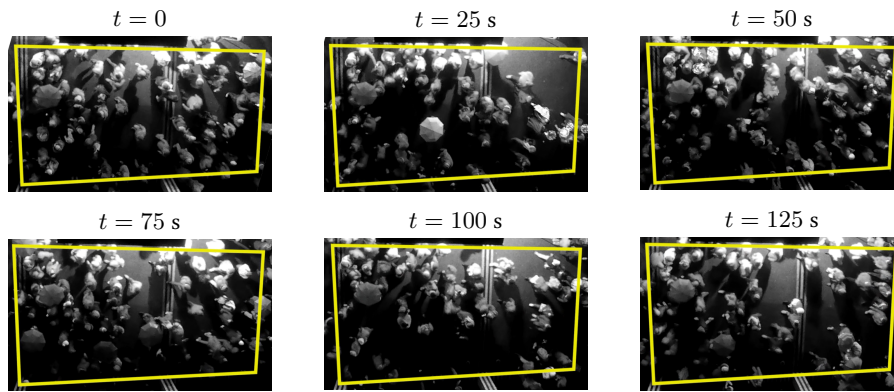


FIGURE 2.18: Snapshots of the *TopView_2C* video recording at different time instants.

formation by direction, separated by a group of standing pedestrians in the centre right of the scene. Accordingly, we are dealing with an unbalanced (75 % : 21 %) bidirectional flow. The density and speed profiles are relatively homogeneous, although the flow to the left is slightly more congested (see Fig. 2.19, right panels). Again, the state is stationary in time, with a global density fluctuating between 0.4 and 1 ped/m² and a mean speed between 0.5 and 0.9 m/s (see Fig. 2.20). The snapshots show the crowd is sparser than the previously presented video recordings (see Fig. 2.21).

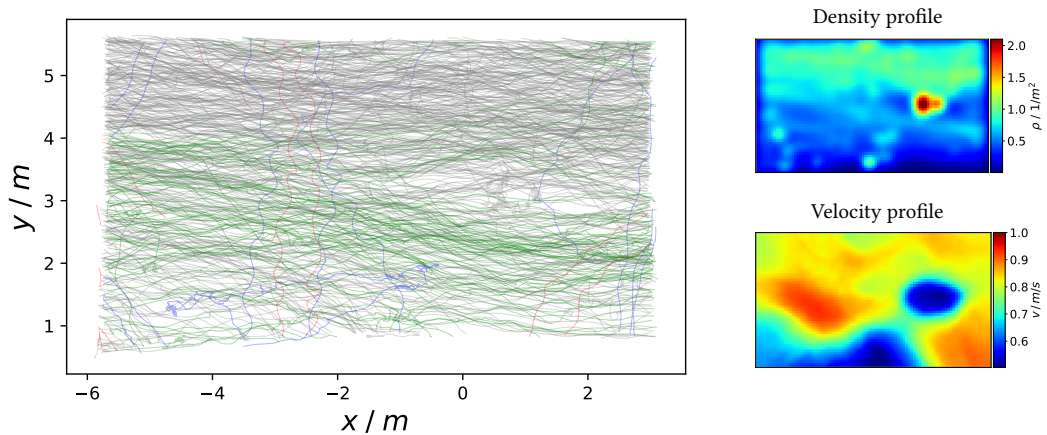


FIGURE 2.19: Trajectories (**left panel**) with density and speed profiles (**right panels**) for the *TopView_2D* video recording (counter-flow pedestrian dynamics with lane formation).

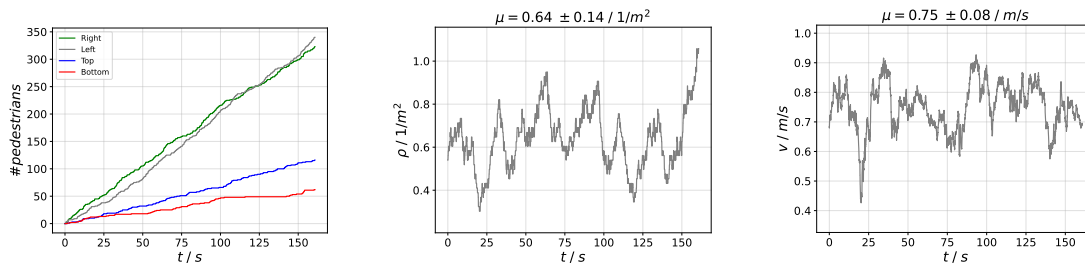


FIGURE 2.20: Cumulative flow, density and mean-speed time-series for the *TopView_2D* video recording. The situation is relatively stationary in time.

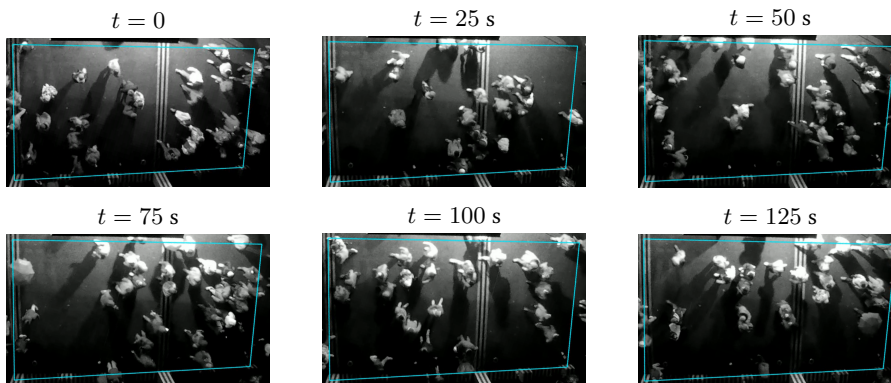


FIGURE 2.21: Snapshots of the *TopView_2D* video recording at different times.

2.3.5 IDENTIFICATION OF SINGULAR QUALITATIVE PHENOMENA

In this section, we highlight key features passively observed during the real-world Festival of Lights, a complex scenario that significantly diverges from controlled settings. Many of these features arise from the multi-directional nature of the flow or, more broadly, the diverse objectives of the pedestrians within the crowd. These features notably include:

- temporarily static groups of people around which pedestrians are forced to navigate
- pronounced density variations
- repeated movement patterns of groups following each other through the crowd, resembling snakes (referred to as *crossing channels* in the controlled experimental study by Wang et al. (2023))
- various non-standard pedestrians, such as individuals pushing strollers or pulling luggage
- a complex geometry of the premises that cannot be strictly reduced to two dimensions
- ambulances crossing the square

Depending on their prevalence and impact on pedestrian flow, these effects may need to be incorporated into models to achieve convenient applications. We categorise these distinctive features into three groups: **(i) non-standard geometry of the premises**, **(ii) diversity of goals and speed preferences**, **(iii) heterogeneity of the crowd composition**. Additionally, we identify the video recordings and specific times when these features can be observed.

2.3.5.1 NON-STANDARD GEOMETRY OF THE PREMISES

In contrast to the common reliance on a binary geometry, which distinguishes between accessible and inaccessible spaces, the square in question exhibits regions of varying attractiveness. Notably, the vicinity of the walls where shows are projected is visibly less appealing to the crowd. Some modelling

File	Start	End	Description
<i>TopView_1B</i>	0 : 00	2 : 40 (end)	a 7-people group standing on the right side. People are sometimes heckling or fighting, which makes the shape evolve (around 0 : 45) Between 0 : 53 and 1 : 05, interactions between the standing group and a mobile group of a similar size
<i>TopView_1C</i>	0 : 00	0 : 56	group of 3 people (2 adults and one child) standing in the middle
<i>TopView_1C</i>	0 : 25	0 : 50	group of 3 people stopping, standing and restarting moving in the bottom right side
<i>TopView_1C</i>	0 : 58	1 : 30	group of 2-standing people stopping, standing and restarting on the top side. This group is split by people passing between them
<i>TopView_2A</i>	0 : 00	2 : 41 (end)	group of standing people on the left. The group size evolves from 2 to 8 people
<i>TopView_2B</i>	0 : 00	0 : 22	group of 2 standing people on the left
<i>TopView_2B</i>	0 : 45	1 : 12	a group of 2 walking people stops and stands on the left
<i>TopView_2C</i>	0 : 10	1 : 14	a group of 2 walking people stops and stands on the left
<i>TopView_2E</i>	0 : 00	0 : 35	2 standings groups on the top (with limited impact on flow)
<i>TopView_2F</i>	0 : 00	0 : 53	standing group of 3 people on the left border

TABLE 2.5: Situations of (temporarily) static groups.

approaches have been proposed in the literature to capture this heterogeneity (Helbing et al., 1997; Echeverría-Huarte and Nicolas, 2023). Additionally, the geometry is neither composed of straight borders nor entirely two-dimensional. Knee-high bollards and waist-high steel crowd barriers restrict movement (and are thus associated with lower local density, as shown in Fig. 2.8). Still, they can overlap with pedestrians in three dimensions.

2.3.5.2 DIVERSITY OF GOALS AND SPEED PREFERENCES

We have previously highlighted the complexity and multi-directionality of the flow patterns in some sequences. Here, we focus on the effects and implications of the diverse intentions among spectators, including their varying goals and speed preferences.

STATIC GROUPS OF PEOPLE. First and foremost, numerous temporarily static groups of people can be observed, often forcing passing pedestrians to navigate around them. These groups, typically consisting of 2 to 8 individuals, were found throughout the area of interest in the *TopView* recordings. Two distinct scenarios can be identified: (i) a group moves, stops, and resumes motion; (ii) a group remains stationary for the entire footage duration. The first scenario is particularly intriguing, as it allows us to study the effects of people stopping, standing, and resuming motion over time.

Tab. 2.5 summarises our observations of such static groups, excluding those who stop for less than two seconds. Although these groups are hardly included in controlled experiments of different flow types, they disrupt the base flow, significantly impacting the dynamics. Unlike classical obstacles, these groups are more complex because they are transient, appear and disappear, and fluctuate in size and shape over time. This variability can result from the addition of new members (see Tab. 2.5, *TopView_2A* file) or specific behaviours of group members, such as heckling (see Tab. 2.5, *TopView_1B* file). Additionally, pedestrians splitting a group of stationary people have also been observed (see Tab. 2.5, *TopView_1C* file).

RUNNING PEDESTRIANS Conversely, we noticed that some people were running in the instances listed in Tab. 2.6.

File	Start	End	Nature
<i>TopView_1A</i>	2 : 49	2 : 53	2 people accelerating to reach a speed higher than the main flow from middle to right side
<i>TopView_2B</i>	0 : 09	0 : 14	3 people running from left to right side

TABLE 2.6: Instances of running pedestrians.

2.3.5.3 MARKED DENSITY HETEROGENEITIES

Giant density fluctuations, which far exceed those expected in a physical system at equilibrium, are common in active matter assemblies (Dey et al., 2012; Manning, 2023). In the specific case of pedestrian assemblies, pronounced density heterogeneities are particularly noticeable. Some areas are notably depleted, forming voids, while others are characterised by high-density clusters of tightly packed groups within the same recording (see Tab. 2.7).

File	Start	End	Nature
<i>TopView_1A</i>	1 : 09	2 : 05	gap, high-density in the left

TABLE 2.7: Voids and density heterogeneities.

LINES OF PEOPLE REPEATING THROUGH THE CROWD In dense regions, we have often observed people worming their way through a static or counter-moving crowd and following each other, thus forming 1D snake-like structures (Tab. 2.6). People follow each other along these 1D structures, most probably due to the depleted channels opened in the wake of the predecessors (Nicolas et al., 2019), in addition to their possible social relationships. Similar self-organised structures have been observed in controlled experiments of people crossing static groups and dubbed *cross-channels* (Wang et al., 2023). Still, they have received much less attention than stable lanes in bidirectional flows or the stripes formed at the intersection of two flows. Indeed, their frequency in the empirical dataset seems to owe much to the multiple directions of pedestrians and the non-stationary character of the flow. We hypothesise that the observed transient *snakes* could turn into stable lanes in stationary conditions and with a limited number of directions, with distinct yet unknown consequences on the flow properties.

File	Start	End	Description
<i>TopView_1A</i>	0 : 35	0 : 47	lane formation on both sides
<i>TopView_1A</i>	1 : 11	1 : 28	mini-lanes: 3 people walk counter to the main flow
<i>TopView_1A</i>	1 : 12	2 : 05	serpentine group at the top
<i>TopView_1B</i>	1 : 05	2 : 40 (end)	snake/lane formation from right to left side due to a standing group; quite high density.
<i>TopView_2A</i>	0 : 24	0 : 39	a group of 6 is worming their way through a dense counter-moving crowd.
<i>TopView_2B</i>	0 : 27	0 : 40	a group of 7 is worming their way through a crowd moving in the same direction. The group splits (going from bottom to right side).
<i>TopView_2B</i>	1 : 12	2 : 00	a lane appears on the top, opposite the main flow.
<i>TopView_2C</i>	0 : 27	0 : 40	a serpentine group of 2 – 3 people at moderately high density (from right to left)
<i>TopView_2C</i>	0 : 00	0 : 15	a serpentine group of 9 at medium density (from right to left)

TABLE 2.8: Serpentine groups (people walking counter to the main flow and following each other in line).

2.3.5.4 HETEROGENEITY OF THE CROWD COMPOSITION

SOCIAL GROUPS. Unlike the homogeneous crowds of individual agents traditionally considered by crowd modellers, the crowd at the Festival of Lights primarily consists of social groups. Some of these groups are quite large (see Fig. 2.5), even though they may become separated in practice, and some include families with children. Naturally, this composition is expected to influence the microscopic dynamics at play.

PUSHCHAIRS AND BIKES. Moreover, not all pedestrians fit the standard image of a typical pedestrian. Some navigate through crowds of varying densities while pushing strollers, while others manoeuvre their bicycles (Tab. 2.9). Consequently, the shape of the agent to be modelled varies significantly from that of a standard pedestrian. Additionally, the density tends to be higher in front of strollers than behind them, prompting pedestrians behind the *pushers* to frequently attempt to overtake them.

File	Start	End	Nature
<i>TopView_1B</i>	0 : 01	0 : 13	pedestrian with a bike
<i>TopView_1B</i>	1 : 33	1 : 48	pushchair
<i>TopView_1C</i>	3 : 05	3 : 16	pushchair
<i>TopView_2A</i>	1 : 25	1 : 53	pushchair
<i>TopView_2A</i>	2 : 33	2 : 41	pushchair
<i>TopView_2B</i>	0 : 49	1 : 12	pushchair
<i>TopView_2E</i>	0 : 36	0 : 50	pushchair
<i>TopView_2F</i>	0 : 59	1 : 06	pedestrian with a bike

TABLE 2.9: Non-standard pedestrians (pushchairs, bikes, etc.).

AMBULANCES. Finally, we observed instances where an ambulance needed to navigate through the crowd. In response, the crowd opened a pathway ahead of the vehicle to facilitate its passage.

2.4 TECHNICAL VALIDATION

2.4.1 TRAJECTORY DATASETS FOR THE *TOPVIEW* RECORDINGS.

All trajectory datasets were visually inspected and manually corrected where necessary. In addition, comparing the overlapping time series of density and mean speed obtained from the *TopView_1B* and *TopView_2C* video recordings, on the one hand, and the *TopView_1C* and *TopView_2D* videos, on the other hand, further validated the results (Fig. 2.23). The fields of view of these cameras are similar (see Fig. 2.22), and their recordings overlap in time (see Tab. 2.4). We find a relatively small root-mean-square differences (from 5 to 10 %) between overlapping sequences, both for the mean speed and for the density (see Tab. 2.10). Nonetheless, a systematic bias is observed in opposite directions for *TopView_1B/TopView_2C* and *TopView_1C/TopView_2D*. These biases may be explained by perspective effects and partly biased correction of optical and geometric distortions.

File	RMSD Mean Speed [m/s]	RMSD Density [ped/m ²]
<i>TopView_1B / TopView_2C</i>	0.02	0.05
<i>TopView_1C / TopView_2D</i>	0.05	0.07

TABLE 2.10: **Root Mean Square Differences (RMSD)** between the pedestrian mean speed and density time series for the *TopView_1B* and *TopView_2C* video recordings and the *TopView_1C* and *TopView_2D* video recordings, as shown in Fig. 2.23.

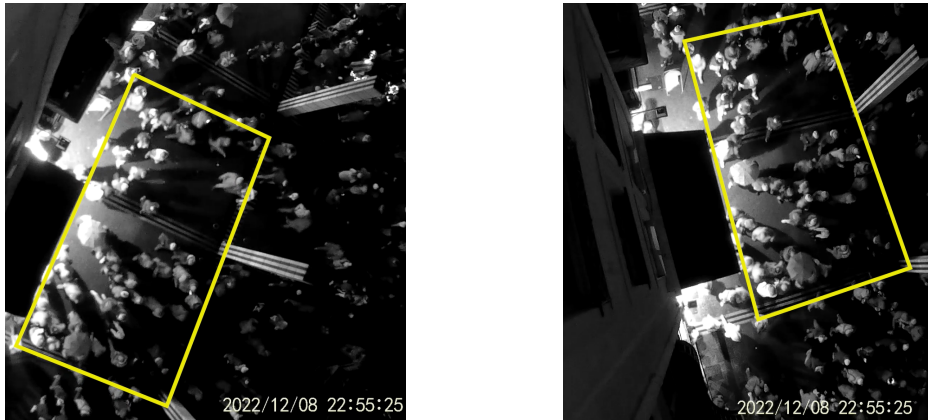


FIGURE 2.22: Point of view for the *TopView_1* and *TopView_2* camera videos, which capture the same scene from different locations and angles.

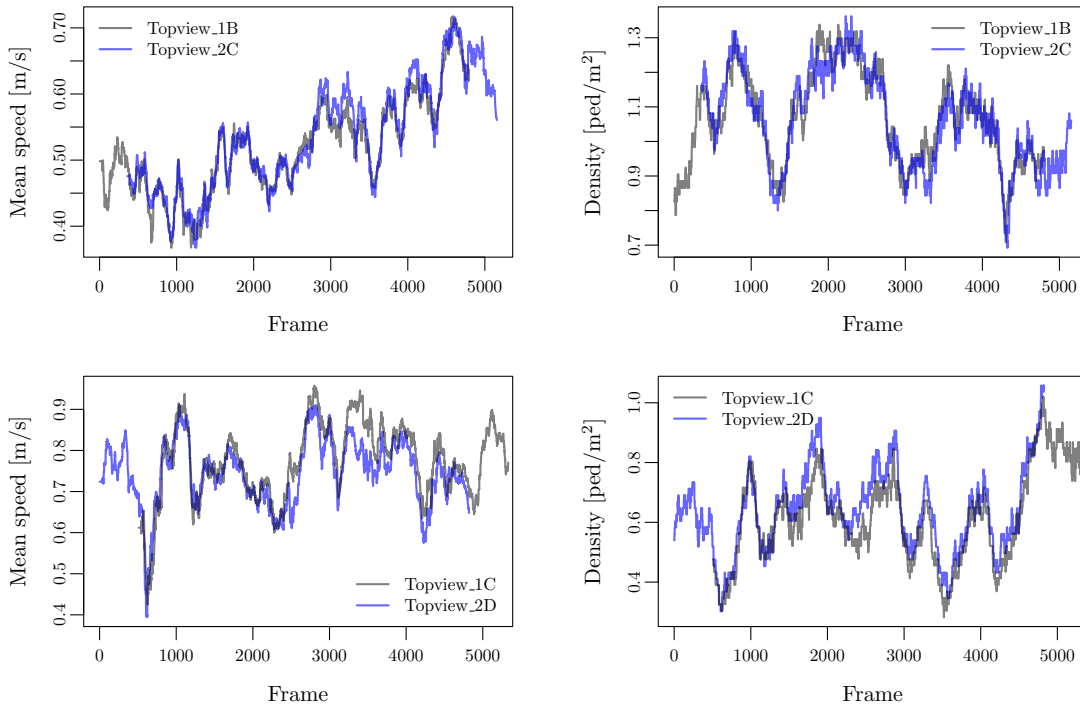


FIGURE 2.23: Superposition of the pedestrian mean speed (**left panels**) and density (**right panels**) time series for the *TopView_1B* and *TopView_2C* video recordings (**upper panels**) and for the *TopView_1C* and *TopView_2D* video recordings (**lower panels**), which capture the same scene from different locations and angles of view, and which partly overlap in time.

2.4.2 TRAJECTORY DATASETS FOR THE *LARGEVIEW* RECORDINGS

As mentioned above, owing to the lower resolution of the *LargeView* recordings, the quality of the extracted data is not quite as good. Occasionally, we may have failed to detect shorter individuals or swapped intersecting trajectories. Despite these challenges, two staff members (called ‘coders’) independently extracted trajectories from different recordings and then analysed each other’s work. The coders largely agreed on the extracted data, although there were occasional disagreements or uncertainties regarding some data points. The common trends observed in the density and velocity

fields, as shown in Fig. 2.10 - Fig. 2.11, which correspond to different days of recording, further support the robustness of the presented data.

To further validate the *LargeView* trajectory dataset, possible detection or tracking errors were analyzed jointly by the two coders in a second stage. Errors were categorised as either major or minor. Major errors included omissions of clearly visible pedestrians and the creation of non-existent ones. Minor errors involved misidentifying or possibly swapping pedestrians as well as slightly inaccurate clicks on a pedestrian's head. The joint analysis led to the detection of 10 major errors (1.3%) out of ~ 740 trajectories and 6 minor errors in the *LargeView* Zoom_O dataset, and 3 major errors (0.4%) out of ~ 740 trajectories and 5 minor errors in the *LargeView* Zoom_A dataset, over 10 seconds. (All these errors were corrected in the final dataset.)

In order to assess errors on the local densities, two sub-regions of rectangular shape were defined at distinct locations in time and space, each measuring $4 \times 6 \text{ m}^2$, and the two coders separately counted all people in these regions, including flickering appearances who were *likely* to be people, even if this was not certain, in order to get an upper bound. Their respective counts typically differed by less than 10%, and exceeded the number of actually tracked pedestrians by 20% to 30% in the *LargeView* Zoom_O dataset and 9% to 12% in the *LargeView* Zoom_A dataset, depending on the location of the rectangle. This leads to the conclusion that the local densities given by our dataset underestimate the actual densities by *at most* by 9% to 30%.

2.4.3 MAPPING TO REAL-WORLD COORDINATES

To map the pedestrian positions in pixel coordinates to real-world coordinates, calibration using people standing at predefined positions was performed; the distances between the predefined positions were carefully measured on the ground. In the most distant part of the square, the calibration error on the real-world coordinates (but not the *relative* positions) may reach a couple of meters. Then, after conversion, we successfully checked the compatibility of the crowd positions with the geometry of the premises obtained from *Google Earth* data and our independent positioning of obstacles.

2.4.4 SURVEYS

Six distinct staff members gave out oral surveys about origins, destinations, and group sizes. In addition to the collected statements, group sizes were also passively observed on the field.

CHAPTER 3

MODELLING 2D PEDESTRIAN DYNAMICS WITH NON-CIRCULAR COMFORT & PHYSICAL SPACES

Research is expected to alternate between theoretical models and experimental data, creating a dynamic interplay that advances understanding. Initially, general experimental data serve as a foundation for developing preliminary models. These models, in turn, enable predictions about pedestrian behaviour in various situations. Subsequently, experiments are designed to validate or invalidate these predictions. By analysing the results of new experiments, researchers can uncover novel aspects to incorporate into the models. This iterative process not only refines the models but also provides forecasts that guide the design of future experiments. Thus, the continuous dialogue between experimentation and theory significantly advances research on crowd dynamics.

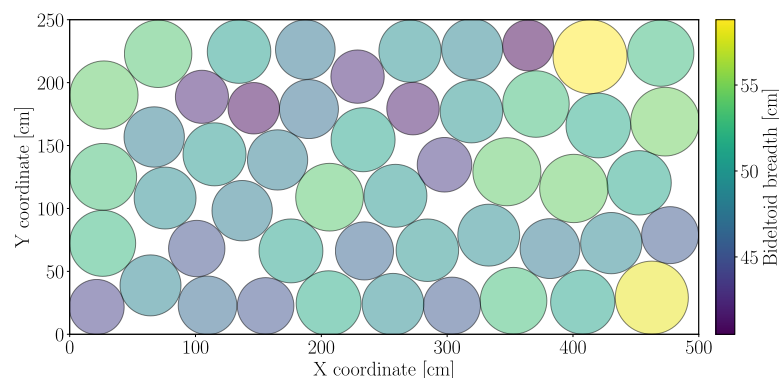


FIGURE 3.1: Tight random packing of pedestrians using disks, achieving a density of $4.0 \text{ pedestrians/m}^2$. Details of the algorithm used can be found in App. C.1.1. The diameters of these disks are drawn from the empirical *bideltoid breadth* distribution of a portion the US population, as documented in the ANthropometric SURvey 2 (ANSURII) database from Gordon et al. (2012a). Both the disk diameters and the empirical *bideltoid breadths* have a mean of 49 cm and a standard deviation of 4 cm. For further information on the definition of these measurements, please refer to Fig. 3.2.

Our work is no exception to these challenges. Specifically, the previously studied Festival of Lights field experiment was conducted due to the lack of field data in medium to high-density, heterogeneous situations involving ambulances, scooters, strollers, suitcases, children, and babies. The analysis of these data highlighted certain aspects of crowd dynamics that current two-dimensional pedestrian models do not yet account for.

Most existing models (Echeverría-Huarte and Nicolas, 2023) represent pedestrians as disks. However, when *bideltoid breadth* is used as the disk diameter, a tight random arrangement of a real population only reaches densities of about four pedestrians per square meter. This is far below the maximum densities observed during the Festival of Lights, where **peaks significantly exceed 4 people per square meter**, although people are not very tightly packed. Note that much higher densities (sometimes above 8 ped/m²) have been reported in various situations (Helbing et al., 2007; Pastor et al., 2015; Nicolas et al., 2019).

Some would argue that reducing the disk diameter based on chest depth could replicate observed densities. However, in addition to failing to replicate a realistic shape, this would fail to replicate a critical feature: the number of neighbouring contacts. A disk-shaped model inherently limits the maximum number of contacts to six, whereas the later proposed elongated shape allows for up to eight contacts. This higher number of contact is observed in high-density evacuation scenarios, as demonstrated by Garcimartín et al. (2013).

Moreover, sneaking behaviours were observed: pedestrians moving out of a dense group would **rotate their chest to make their way**. At lower densities, pedestrians adopt this behaviour to avoid potential collisions. Although one might assume that a pedestrian would rather change direction, it appears more accessible, or less mentally taxing, to **pivot the torso when a collision is imminent**. The goal is to develop a crowd dynamics model incorporating these three critical observations from the Festival of Lights.

Decision-Making Layer:

$$(\mathbf{v}_i^{\text{des}}, \omega_i^{\text{des}}) = \arg \min_{(\mathbf{u}, \omega) \in \mathbb{R}^2 \times \mathbb{R}} \mathcal{E}(\mathbf{u}, \omega)$$

Mechanical Layer:

$$\frac{d\mathbf{v}_i}{dt} = \frac{\mathbf{v}_i^{\text{des}} - \mathbf{v}_i}{\tau_{\text{mech}}} + \frac{1}{m_i} \sum_{x \in \{\text{neighbours and obstacles}\}} \mathbf{F}_{x \rightarrow i}^{\text{mech}} \quad (3.1)$$

$$\frac{d\omega_i}{dt} = \frac{\omega_i^{\text{des}} - \omega_i}{\tau_{\text{mech}}} + \frac{1}{I_i} \sum_{x \in \{\text{neighbours and obstacles}\}} \tau_{G_i, x \rightarrow i}^{\text{mech}}$$

As explained in Chap. 1, a practical approach to modelling pedestrian behaviour relies on a coupling between a decision-making component that determines a desired speed and a mechanical layer that confronts this decision with reality - a coupling summarised by Eq. (3.1) where \mathcal{E} may depend on time, position and velocity of neighbouring agents such as pedestrians, and obstacles. This choice is based on the theoretical foundations discussed in Chap. 1.

The desired speed aims to achieve a goal while respecting metabolic, physical, and psychological constraints as much as possible. This desired speed then serves as input to a Newtonian set of mechanical equations, which account for the relaxation of the real pedestrian speed towards the desired speed within the order of reaction time and potential mechanical contact forces with obstacles or other pedestrians. A decision is made at each reaction time interval δt . Various constraints can be integrated into the decision-making layer, solidly grounded in experimental data for a large part (Chap. 1). This

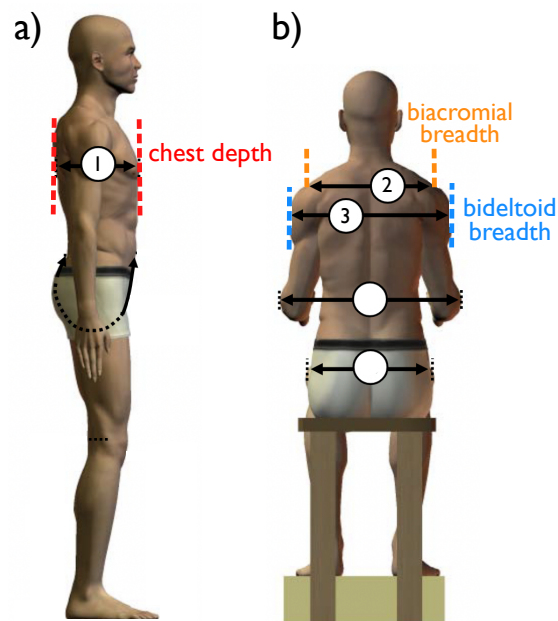


FIGURE 3.2: Illustration of anthropometric measurements, adapted from [Gordon et al. \(2012b\)](#), highlighting the anatomical landmarks used for standardised assessment. It specifically focuses on *chest depth* (a), *biacromial breadth* and *bideltoid breadth* (b). More precisely, the **biacromial breadth** denotes the distance between the acromion points at the top of the shoulder blades, measured with a firm chest while seated to ensure accuracy.

dichotomy is also practical because it allows for a unified description of seemingly diverse situations, as illustrated by the following examples:

Decision-making layer illustration Consider a pirate ship at sea in the well-known dangerous Singapore Strait ([Liss, 2003](#)) aiming to intercept a cargo vessel. Instead of immediately steering directly towards the target, the pirate ship first anticipates the vessel's future position. It then adjusts its rudder and speed to approach the target as quickly as possible.

Mechanical layer illustration In contrast to the decision-making layer, which relies on long-range interactions by anticipating potential collisions and the behaviour of nearby individuals, the mechanical layer focuses on direct contact interactions. Specific scenarios heavily rely on physical contact, such as the *wall of death*, a game where two walls of people collide at concerts. You can view an example of this in action via this [video link](#). In this game, participants lose the ability to move freely and experience a sense of losing control, leading to a dissociation between the mind and body. In such situations, interaction with the environment occurs solely through physical contact.

However, existing models ([Echeverría-Huarte and Nicolas, 2023](#)) that incorporate this coupling rely on circular shapes to represent pedestrians, resulting in the issues mentioned above. Consequently, this chapter seeks to establish the foundation for a model that considers the inherently anisotropic nature of pedestrians' shapes. By *shape*, we refer to both the **physical form** (handled by the mechanical layer), which is assumed to be impenetrable yet deformable, and the decision-making shape, or **comfort zone**, that individuals wish to preserve from intrusion by obstacles or neighbouring pedestrians. This comfort zone decays relatively smoothly away from the pedestrian and it is penetrable.

3.1 MECHANICAL LAYER

3.1.1 PHYSICAL SHAPE

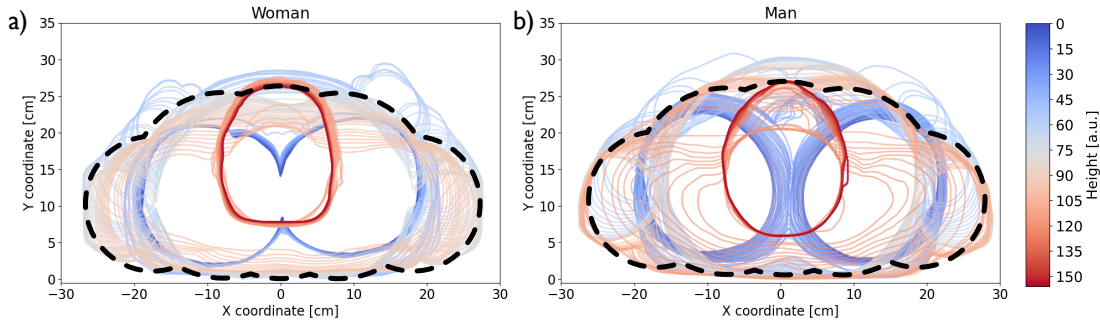


FIGURE 3.3: Superposition of the cross-sectional contours of two cryogenic bodies at different altitudes. The two bodies belonging to a woman on the **left** and a man on the **right** have significant body fat fractions (compared to people in the [ANSURII](#) database from [Gordon et al. \(2012a\)](#)). The contours were obtained by processing each section’s images of the dataset from the [U.S. National Library of Medicine \(1994, 1995\)](#). The upper body displays a reddish hue, while the lower part appears bluish. The contours of the head and legs, where the hands rest, are visible. The abdomen is discernible at the centre, with the shoulders at the extremities. The dotted outline represents the chosen shape to model a 2D pedestrian.

To analyse pedestrians’ shapes, we studied the cross-sections of two cryogenically preserved middle-aged (man and woman) cadavers from the [U.S. National Library of Medicine \(1994, 1995\)](#). This project, initiated by the [National Library of Medicine](#), offers a freely accessible library of images of cryosections, [Computed Tomography \(CT\)](#) scans, and [Magnetic Resonance Imaging \(MRI\)](#) of cadavers (see Fig. 3.4 for an example of a man torso section).

To model the shape of a 2D pedestrian, we consider the exterior contour formed by the union of all superimposed contour sections of male and female cryogenic bodies, as illustrated in Fig. 3.3 excluding hand movements and respiratory deformations. We choose to represent this rounded contour using five overlapping disks to cover this area: two for the shoulders, two for the pectorals, and one for the belly, as shown in Fig. 3.3. Interestingly, this contour closely matches the thoracic section of Fig. 3.4, with the only difference being the circle in the middle representing the belly.

3.1.2 CREATING A SYNTHETIC CROWD

Having chosen the shape, the next step is to expand it to an entire real population, creating a synthetic crowd. This crowd can be utilised further in models and will possess the physical characteristics representative of the chosen real population. Using five disks to model a pedestrian’s shape—two for the shoulders, two for the chest, and one for the abdomen—enables easy adaptation to the diverse morphologies found within a population. The [ANSURII](#) database from [Gordon et al. \(2012a\)](#) is utilised to achieve accurate modelling, offering a standardised and comprehensive range of measurements. This database includes 93 different metrics collected for 6000 [US](#) Army personnel, comprising 4082 men and 1986 women. While the sample does include women, it does not perfectly represent the civilian [US](#) population, which, according to the [National Health and Nutrition Examination Surveys \(NHANES\)](#) database from [Cd et al. \(2012\)](#), has a higher proportion of women¹. The [NHANES](#) database provides only statistical summaries for a limited set of measurements across the entire [US](#) population. Notably,

¹This can be attributed to the fact that women generally in the [US](#) have a higher life expectancy than men.

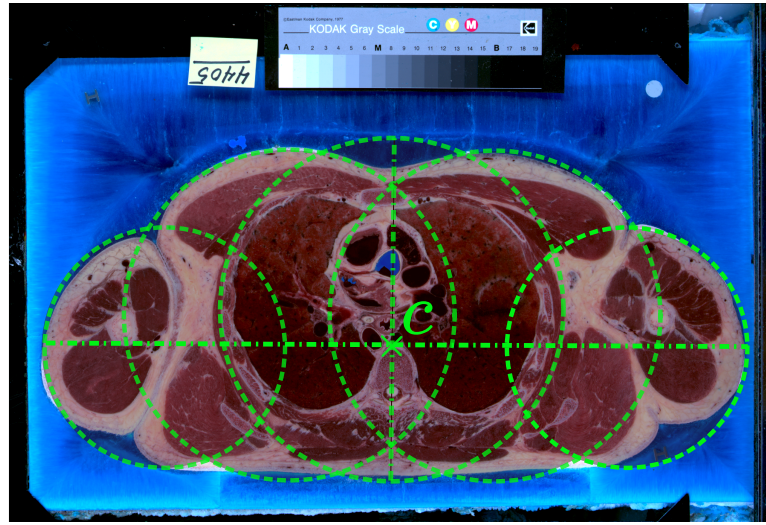


FIGURE 3.4: Torso section of a cryogenic man, slice number 4405, from the [U.S. National Library of Medicine \(1994, 1995\)](#) database, covered with five disks. The cross c represents the centre of the neck, which is used as the centre of homothety. This allows us to adjust the standard shape to accommodate various measurements across a real-world population from the [ANSURII](#) database ([Gordon et al., 2012a](#)). The ‘Kodak Q-13 Gray Scale’ ruler measures 20.3 cm by 2.5 cm.

it does not include specific measurements such as *chest depth* and *bideltoid breadth*. Interestingly, the *biacromial breadth* measurement is equal in both datasets, suggesting some consistency in skeletal dimensions (refer to Fig. 3.2 for a visualisation of these measurements).

The discrepancy in the male-to-female ratio in the [ANSURII](#) database is not an issue for us: we can adjust the gender proportion in our synthetic crowd by randomly removing men to achieve the desired balance, ensuring a more representative model.

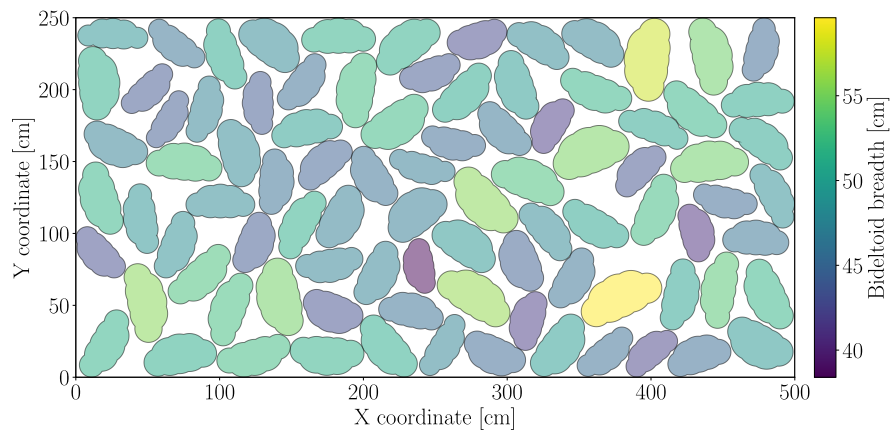


FIGURE 3.5: Tight random packing of pedestrians without a preferred orientation using an arrangement of five disks, achieving a density of **7.2 pedestrians/m²**. Details of the algorithm can be found in App. C.1.1. Both the sample from the [ANSURII](#) database ([Gordon et al., 2012a](#)) and our model database exhibit a mean *bideltoid breadth* of 49 cm and a mean *chest depth* of 25 cm. For more information on the definition of these measurements, please refer to Fig. 3.2.

To preserve the overall shape, we use a homothety (or homogeneous dilation). Specifically, we apply a homothety centred at c (as illustrated in Fig. 3.4) to the chosen shape contour, with a particular scale factor to align with the empirical *chest depth* measurement. Another homothety also centred at c but with a different scale factor, is used to modify the circle centres, ensuring that the *bideltoid breadths* match. This sequence of two homotheties—one altering the original shape contour and the other the

circle centres—does not perfectly preserve the initial shape (shown in Fig. 3.3) but achieves a realistic approximation.

Consequently, we can create a synthetic two-dimensional pedestrian population with *chest depth* and *bideltoid breadth* measurements that precisely match those from the ANSURII database while also maintaining similar shapes. This model enables us to simulate a tight random arrangement of individuals within a specified area shown in Fig. 3.5. The chosen shapes support the high pedestrian densities observed near the fountain in *Place des Terreaux* during the Festival of Lights.

3.1.3 MECHANICAL INTERACTIONS

Now that we have established a population of 2D shapes, we can explore the interactions that may occur between these shapes upon contact. While constructing a specific particle shape is relatively straightforward, determining the contact interactions is significantly more complex, with several issues arising in this context:

Definition of contact

Firstly, it is crucial to define what contact means. Contact between two 2D shapes occurs when two shapes interpenetrate or bond together. For disks, determining interpenetration and bounding is straightforward. However, more sophisticated algorithms are necessary for other shapes, as explained by Dziugys and Peters (1998) in his comprehensive review of granular material simulations.

Definition of contact surface

If contact, specifically interpenetration, is detected, the next step is determining the contact surface, which will define the direction of the associated contact forces. This surface is the line that models the real contact between the objects, as in reality, objects cannot interpenetrate but only deform. Modelling the contact surface for disks of the same radius is relatively simple. However, when the radii differ, multiple definitions arise as illustrated in Fig. 3.6 a). Defining the contact surface becomes even more intricate for more complex shapes, such as polygons, as shown in Fig. 3.6 b). A mere 10° deviation in determining the normal to the contact surface can result in unrealistic particle movements as outlined by Hogue and Newland (1994).

Definition of contact point

Once the contact surface has been established, and consequently the direction of potential contact forces, it is necessary to determine the point of application for these forces. For disk-shaped particles, contact points can be defined either as the centre of the overlap area or as the midpoint of the line connecting intersection points as illustrated in Fig. 3.6 a). The latter approach can lead to errors during collisions with walls, as it assumes no wall deformation—an assumption only valid for perfectly rigid walls. We will, therefore, stick to the definition of the centre of the contact area.

Mechanical interaction law

The final challenge involves determining the mechanical interaction law, which governs the deformation and contact of the colliding materials. We first review the techniques used in granular material studies to derive these interaction laws for pedestrians and obstacles. The elegant work of Popov and Heß (2015) is discussed in the App. C.1.2, revisiting the expressions initially derived by Hertz (1882) for a normal contact between two spheres and by Mindlin (1949) for a tangential contact using a foundation of springs.

Although relationships between stress and deformation specific to the human body exist (see Fig. 1.24) and exhibit a linear regime for small deformation, the nature of contact between different humans is

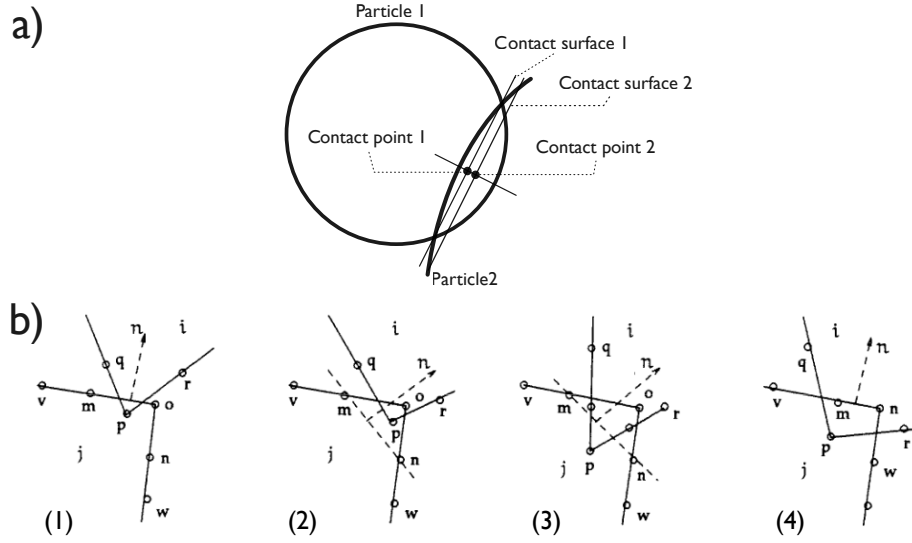


FIGURE 3.6: Surface Contact and contact point definition problem. **For disks (a)**, two primary methods are used to define contact surfaces and points. **Bisector Method:** The contact surface is defined as the bisector of the shortest line segment connecting the centres of two disks or a disk and a wall. The contact point is the centre of this bisector (**point 2**). **Intersection Method:** The contact surface is the line connecting the intersection points of the disks. The contact point is the midpoint of this line (**point 1**). This method can lead to inaccuracies when a particle collides with a wall, as it assumes the wall is infinitely rigid and does not deform. The diagram is adapted from [Dziugys and Peters \(1998\)](#). **For polygons (b)**, the definitions of contact surfaces and points can vary significantly for polygonal contacts as illustrated in the following scenarios: (1) One-point contact on flat surfaces (2) One-point contact on corners (3) Multiple-point contact with polygon i inside polygon j (4) Multiple-point contact with polygon j inside polygon i . These schemes are adapted from [Hogue and Newland \(1994\)](#).

not yet well understood. Contact may occur at various points as hands may also be involved. Therefore, we model the interaction in the simplest way we find appropriate, using a single-damped spring as illustrated in Fig. 3.7.

The motion equation for the centre of mass of pedestrian i , with mass m_i , is given by the following expression. Technical details are available in App. C.1.3, and a comprehensive overview of notations, definitions, and mathematical expressions can be found in App. C.1.5:

$$\begin{aligned} \frac{d\mathbf{v}_i}{dt} = & \frac{\mathbf{v}_i^{\text{des}} - \mathbf{v}_i}{\tau_{\text{mech}}} + \frac{1}{m_i} \sum_{(j1, i1) \in \mathcal{C}_i^{\text{(ped)}}} \left(\mathbf{F}_{j1 \rightarrow i1}^{\parallel \text{contact}} + \mathbf{F}_{j1 \rightarrow i1}^{\perp \text{contact}} \right) \\ & + \frac{1}{m_i} \sum_{(w, i1) \in \mathcal{C}_i^{\text{(wall)}}} \left(\mathbf{F}_{w \rightarrow i1}^{\parallel \text{contact}} + \mathbf{F}_{w \rightarrow i1}^{\perp \text{contact}} \right) \end{aligned} \quad (3.2)$$

where a pair $(j1, i1)$ belongs to the set $\mathcal{C}_i^{\text{(ped)}}$ if and only if the pedestrian components $i1$ (a part of pedestrian i) and $j1$ are in contact. Similarly, a pair $(w, i1)$ is included in the set $\mathcal{C}_i^{\text{(wall)}}$ if and only if the wall segment w is in contact with component $i1$ ². The symbol \parallel indicates a force tangential to the contact surface, while \perp signifies a force orthogonal to the contact surface. As these forces act on the contact centre and not directly on the centre of mass, they may introduce torque into the dynamic. Additionally, to incorporate decision-making, a restoring force is applied to steer the pedestrian toward

²The summation encompasses all components of neighbouring shapes of pedestrian i . The notation $i1$ (for a component of pedestrians i) should not be mistaken for i_1 , which typically refers to the first vertex of a polygonal shape i .

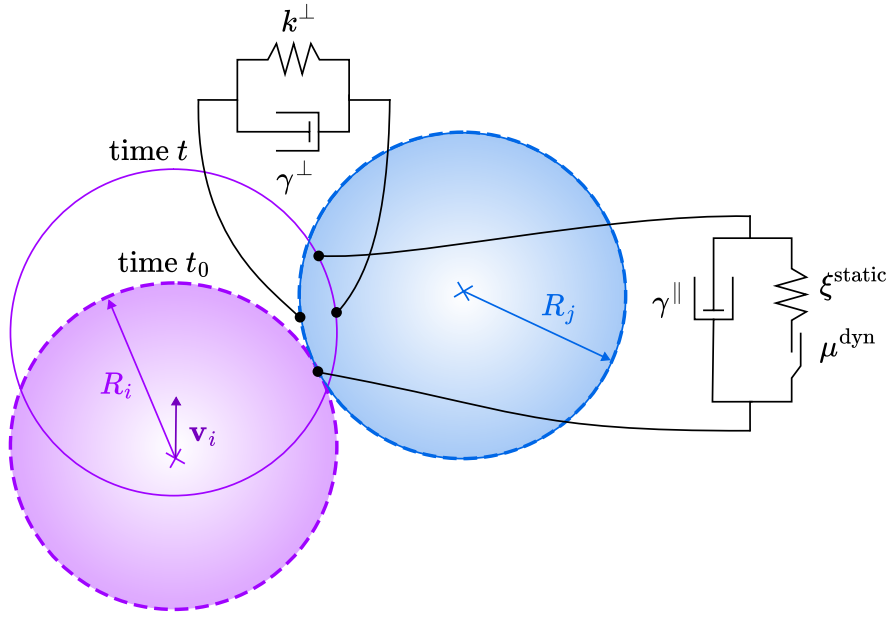


FIGURE 3.7: The interactions between two composite disks, with radii R_i and R_j , belonging to pedestrians i and j , can be modelled using a combination of mechanical elements. Pedestrian i moves with velocity \mathbf{v}_i , while pedestrian j remains stationary ($\mathbf{v}_j = \mathbf{0}$). In the normal direction (orthogonal to the contact surface), the interaction is described by a spring in parallel with a dashpot, capturing both elastic effect and energy dissipation. In the tangential direction (parallel to the contact surface), the interaction is modelled by a spring in series with a slider, in parallel with a dashpot. The slider represents a threshold-based element that resists motion until a certain force is applied, after which it slips or ‘yields’ at a constant force. This models plastic deformation in granular materials, where grains rearrange permanently once a critical stress is exceeded. Here, it refers to the Coulomb’s law: initially, the tangential force is proportional to the extension of the spring, but once a threshold—is reached, a constant force proportional to the normal force is applied modelling sliding of the contact. The dashed line represents the configuration of the composite disks at the onset of contact (at time t_0). Refer to App. C.1.3 for all technical details.

its desired angular velocity. Following this, the rotational dynamics are governed by:

$$\frac{d\omega_i}{dt} = \frac{\omega_i^{\text{des}} - \omega_i}{\tau_{\text{mech}}} + \frac{1}{I_i} \sum_{(j1, i1) \in \mathcal{C}_i^{(\text{ped})}} \tau_{G_i, j1 \rightarrow i1} + \frac{1}{I_i} \sum_{(w, i1) \in \mathcal{C}_i^{(\text{wall})}} \tau_{G_i, w \rightarrow i1} \quad (3.3)$$

where I_i represents the moment of inertia of pedestrian i in its principal inertia frame, projected along the z -axis (the out-of-plane axis). ω_i denotes the angular velocity of pedestrian i . The term $\tau_{G_i, j1 \rightarrow i1}$ refers to the torque at the centre of mass G_i of pedestrian i , resulting from pedestrian-pedestrian interaction forces. A similar expression applies to torques arising from pedestrian-wall interactions. The details on the numerical integration method can be found in App. C.1.6.

3.2 DECISION-MAKING LAYER

Each pedestrian makes a decision periodically every δt , which represents the time needed to gather and process environmental information—essentially, their reaction time. This decision-making process, whether conscious or unconscious, involves selecting an optimal desired translational velocity (\mathbf{v}^{des}) and rotational velocity (ω^{des}) from a set of alternatives. This selection is mathematically represented by the following equation:

$$(\mathbf{v}^{\text{des}}, \omega^{\text{des}}) = \arg \min_{(\mathbf{u}, \omega) \in \mathbb{R}^2 \times \mathbb{R}} \mathcal{E}(\mathbf{u}, \omega) \quad (3.4)$$

whose minimization is performed using a Nelder-Mead algorithm³ (Olsson and Nelson, 1975). The cost function aggregates various components using a weighted sum as follows:

$$\mathcal{E}(\mathbf{u}, \omega) = \mathcal{E}^{\text{Biomecha}}(\mathbf{u}, \omega) + \mathcal{E}^{\text{SFF}}(\mathbf{u}) + \mathcal{E}^{\text{TTC}}(\mathbf{u}, \omega) + \mathcal{E}^{\text{privacy}}(\mathbf{u}, \omega) \quad (3.5)$$

where:

- $\mathcal{E}^{\text{Biomecha}}(\mathbf{u}, \omega)$ denotes the **biomechanical cost**,
- $\mathcal{E}^{\text{SFF}}(\mathbf{u})$ denotes the **static floor field cost**,
- $\mathcal{E}^{\text{TTC}}(\mathbf{u}, \omega)$ denotes the **time to collision cost**, and
- $\mathcal{E}^{\text{privacy}}(\mathbf{u}, \omega)$ denotes the **privacy cost**.

All these components are illustrated in Fig. 3.8. For a detailed explanation of each term, refer to Tab. 1.2. Depending on the value of the coefficients, each cost component can become significant, reflecting diverse motivations.

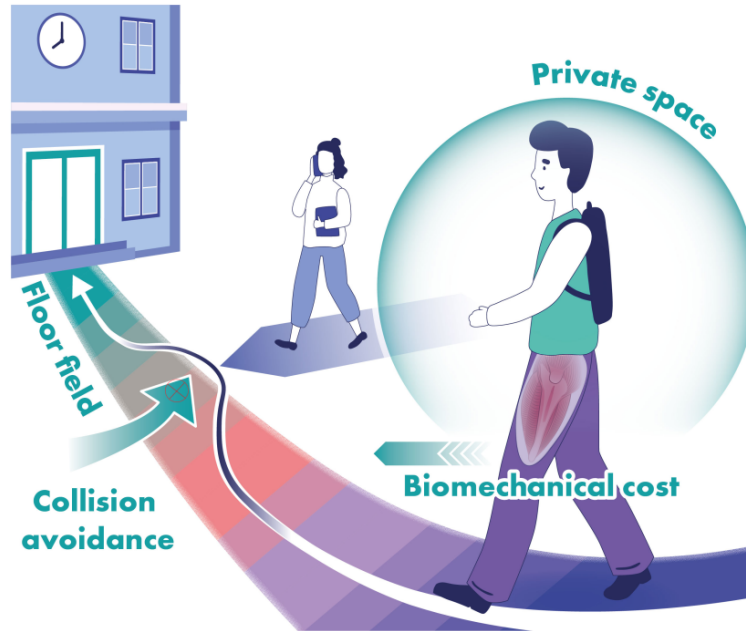


FIGURE 3.8: Sketch illustrating the diverse contributions to the cost function optimised in the decision-making layer. Illustration by [Émilie Josse \(2024\)](#) / Graphics for Science.

Among these components, only the privacy and TTC terms are affected by the shape of the comfort zone. Therefore, we will concentrate on these two terms in the following sections.

3.2.1 PROXEMICS

We propose that individuals have a personal comfort zone, which can be visualised as a series of protective barriers where personal comfort is prioritised. The height of each barrier indicates the level of discomfort experienced when someone enters that space. Thus, the farther someone is from you, the more comfortable you feel with their presence, as shown in Fig. 3.9 (left panel).

³Although the Melder-Mead method is a local minimum solver, it performs quite well with an appropriate initial guess. However, it is somewhat slow; the minimization method will, therefore, require refinement in the future to effectively handle huge crowds.

This comfort zone can be represented as a field in a continuous space. We depicted its isolines using star-convex polygons⁴ instead of continuous smooth curves. This representation simplifies the derivation of expressions for the **Time To Collision (TTC)** and privacy cost terms, making them numerically computable. It enhances both simplicity and computational efficiency. Consequently, these isolines can be non-convex and adaptable to various unexplored situations, such as discomfort fields for an adult with a bicycle or a pushchair (see an illustration of such a star-convex shape in App. C.2.5).

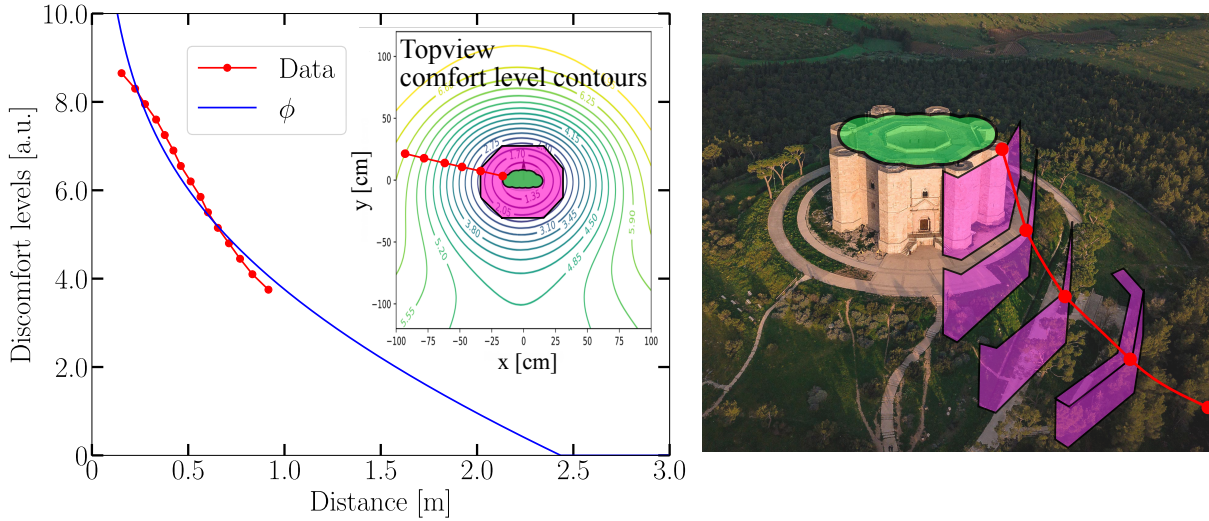


FIGURE 3.9: **Left:** The inset provides a top view of the pedestrian’s scalar comfort field, with the physical form shown in green at the centre. The 2.40 comfort level is approximated by an 8-sided polygon with unequal sides. The field is assumed to be isotropic at each polygon vertex, allowing comfort levels to be examined in one direction and applied similarly in others despite differences between the pedestrian’s front and back. As discussed in Sec. 1.2.3.3, focusing on discomfort rather than comfort levels is preferable because individuals tend to discern negative scenarios more effectively due to negativity bias. To convert comfort to discomfort, we used the formula $discomfort = 10 - comfort$, where 10 represents the maximum comfort level in the experiment’s questionnaire. These data are fitted with a ϕ function, shown in blue, effectively capturing the pedestrian’s discomfort levels as they decrease and reach zero at a certain distance. These discomfort levels can be schematically visualised as castle walls, as illustrated on the right side of the figure. The inset is adapted from [Neggors et al. \(2022\)](#). **Right:** This section presents an artistic illustration of a comfort zone. The interior of the keep symbolises the human body, while the height of the surrounding walls represents a specific level of discomfort related to someone’s presence on these walls. As a person moves further from the keep, their presence-related discomfort diminishes, leading to a decrease in wall height. The photo is adapted from [Daria and Roberto \(2024\)](#).

As shown by [Neggors et al. \(2022\)](#), the comfort level contours close to the pedestrian tend to be relatively homogeneous in shape (see the inset of Fig. 3.9). Therefore, our approximation appears effective, particularly in areas not too distant from each pedestrian. The amplitude of the contours is well-matched with a one-dimensional function, ϕ , which increases as it approaches the body shape and diminishes at greater distances as illustrated in Fig. 3.9 (right panel):

$$\phi(\|\mathbf{r}\|) = \max\left(0, A \cdot \frac{1 - \frac{\|\mathbf{r}\|}{R_{CT}}}{\left(\frac{\|\mathbf{r}\|}{R_{CT}}\right)^{1/4}}\right) \quad (3.6)$$

where $A = 2.62$ and $R_{CT} = 2.43$ m.

⁴In geometry, star-convexity generalises the notion of convexity.

3.2.2 TIME TO COLLISION COST

Let's examine the **Time To Collision (TTC)** cost denoted as V_{ij}^{TTC} . While the concept of **TTC** dates back to earlier works referenced in e.g. [Olivier \(2008\)](#)'s thesis, it was [Karamouzas et al. \(2014\)](#) who demonstrated its empirical relevance in natural conditions. This concept pertains to collisions between physical shapes and is mathematically represented as:

$$V_{ij}^{\text{TTC}} = K_{\text{TTC}} \frac{\exp\left(-\frac{\tau_{ij}}{\tau_{\text{CA}}}\right)}{\tau_{ij}^2} \quad (3.7)$$

where τ_{ij} is the **TTC** between pedestrians i and j , τ_{CA} is the characteristic time of collision anticipation which was set to 3.0 s and K_{TTC} is a parameter that adjusts the relative importance of this cost in comparison to the other terms within the cost function. This formulation raises challenges for numerical cost minimisation. A minor variation in the candidate velocity \mathbf{u} can result in avoiding a collision entirely, leading to a zero cost in energy. This creates discontinuities in the energy landscape, which are notoriously difficult to handle numerically and probably unrealistic for pedestrians.

However, to address that issue of discontinuities, instead of considering collisions between physical shapes, one can focus on the possible collisions between comfort spaces or, more specifically, discomfort fields (then, rather than discussing a physical collision, we address an intrusion into a comfort zone.) This approach is akin to a pedestrian calculating the **TTC** potential for each wall of the 'castle' of [Fig. 3.9](#) and then averaging them. This process effectively acts as a convolution between the discomfort field and the **TTC** potential over the variable $\|\mathbf{r}\|$, which represents the distance from the castle tower (or swelling η when referring to the $\|\mathbf{r}\|/R_{\text{CT}}$ variable as mentioned in [Eq. \(3.6\)](#)). For mathematical simplicity, we will primarily use the swelling variable η to describe a specific discomfort level contour in the following discussion.

This formulation allows us to rewrite the **TTC** term as a convolution over the swelling ratio of the two interacting pedestrians as follows:

$$\mathcal{E}^{\text{TTC}}|_{ij}(\mathbf{u}, \omega) = \int_0^{+\infty} K(\eta) V_{ij}^{\text{TTC}}[\tau_{\eta}(\mathbf{u}, \omega)] d\eta \quad (3.8)$$

where $K(\eta) = \phi(\eta R_{\text{CT}})$ is a compactly supported kernel. Notably, with this definition of η , any discomfort level contour associated with a swelling η greater than 1 will not contribute to the integral, as the kernel value will be zero. With this in mind, one can forget the discomfort field and instead consider the polygonal shape as a simple pedestrian shape that can vary in size according to η . This perspective simplifies the concept.

However, to compute this integral, we still need to understand the relationship between τ and η . Although deriving an analytical expression is challenging, this relationship can be determined numerically at a low cost. The approach is to let the two pedestrians in interaction evolve, as illustrated in [Fig. 3.10 a](#)). At each time step of this evolution, we determine the minimal swelling ratio η^* that leads to an overlap between the two contours. The polygonal nature of the discomfort level contours makes this calculation feasible with low computational cost (refer to [App. C.2.6](#) for detailed technical information). This process establishes a relationship between η^* and τ . To ensure that each η^* is mapped onto a unique **TTC** value, we choose the minimum **TTC** from the calculated swelling ratios as illustrated in [Fig. 3.10 b](#)). This approach reflects the idea that pedestrians are more sensitive to imminent collisions than those that might occur later. More precisely, η^* is related to η as follows:

$$\eta(\tau) = \min \{ \eta^*(\tau') : \tau' < \tau \} \quad (3.9)$$

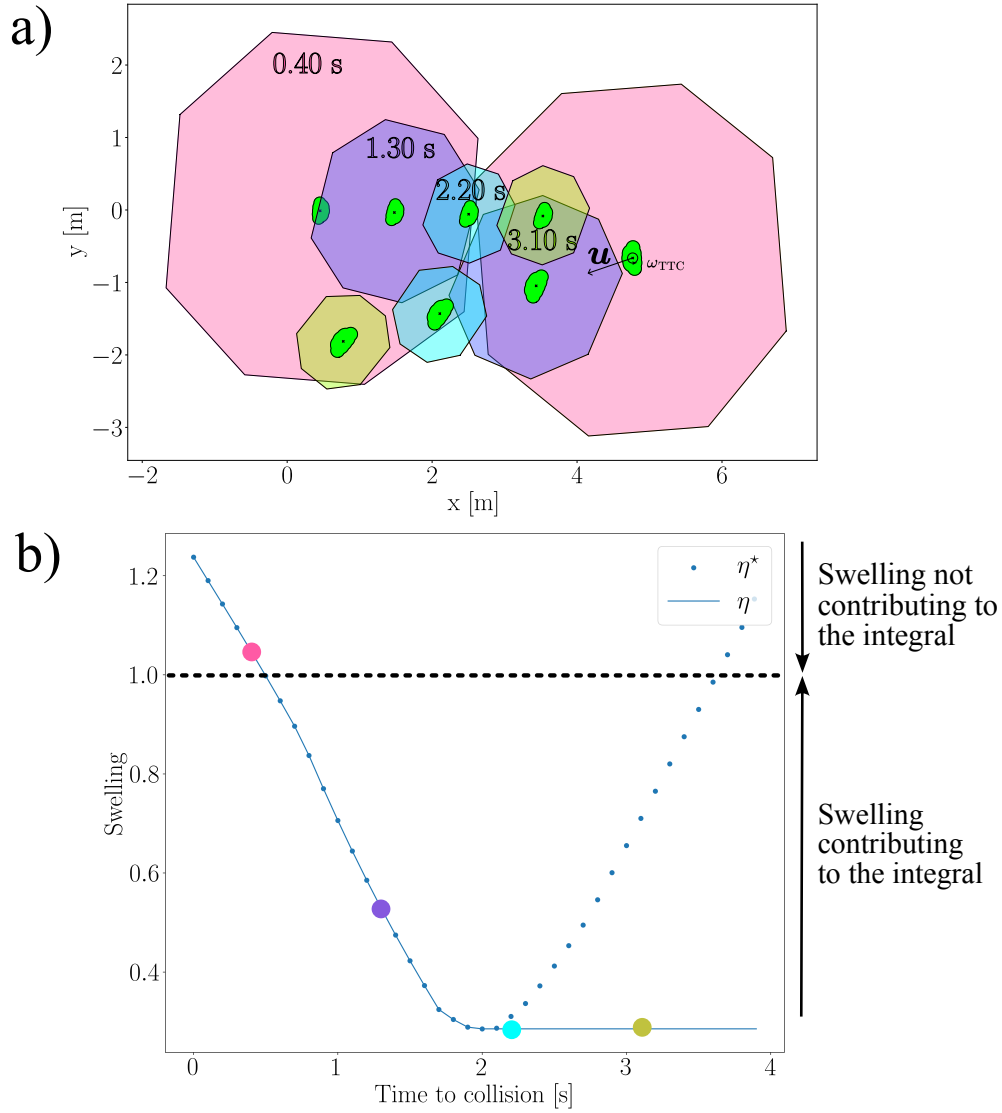


FIGURE 3.10: **a)** Illustration of the swelling ratio η leading to an overlap between two contours at different times in the forecast future. The left agent moves with its translational velocity (at time t) and a rotational velocity $\omega_{TTC} = \omega(t) \exp(-t/\tau_{CT})$, which decreases exponentially over time, with a cut-off time τ_{CT} set to 1 s, reflecting that pedestrians do not behave like spinning tops. The right agent moves with a candidate translational velocity \mathbf{u} , and a rotational velocity that also decreases exponentially, depending on its candidate rotational velocity. The future is discretised into time steps Δt_{TTC} set to 0.1 s. **b)** The relationship between swelling and the **Time To Collision** is depicted. At time $t=0$, the swelling is initialised at a large value such that it touches the opposite wall, corresponding to a zero **TTC**. This process is iterated to generate data points (dots on the graph). To ensure a one-to-one relationship, only the minimal swelling ratio observed up to each point in time is considered. This selection results in the smooth curve (solid line) displayed on the graph. The solid line represents η , while the dashed line represents η^* . Swelling values above one do not contribute to the integral, as the kernel for these values equals zero.

Using a Riemann scheme (as detailed in App. C.2.7), one can then compute numerically Eq. (3.8). Furthermore, assuming that a pedestrian primarily interacts with the individual with whom a collision is most imminent, the total **TTC** interaction potential affecting pedestrian i is determined by the maximum value among all neighbours:

$$\mathcal{E}^{TTC}|_i(\mathbf{u}, \omega) = \max_{j \in \mathcal{N}_i} \mathcal{E}^{TTC}|_{ij}(\mathbf{u}, \omega) \quad (3.10)$$

where \mathcal{N}_i refers to the neighbours of i . Pedestrians and obstacles are considered neighbours if they fall within a 70° half-angle visual cone and are less than 7 meters apart. Furthermore, obstacles are automatically considered neighbours if they are within a 2-meter radius around pedestrian i . More precisely, the distance between two pedestrians is measured from their respective centre of mass. For obstacles, the distance is defined as the shortest Euclidean distance from the pedestrian's centre of mass to the obstacle.

As a side remark, when two individuals are very close, their comfort zones overlap. In such scenarios, the integral (Eq. (3.8)) yielding the **TTC** cost is limited to a tiny interval in η , between η_{\min} and η_{\max} (with transparent notations), regardless of direction. Consequently, the integral takes a negligible value. This isn't problematic because this term is only significant at greater distances. In this context, the relevant factor is the privacy cost, which will be explained next.

3.2.3 PRIVACY COST

In contrast to the **TTC** term, the privacy term depends on the pedestrian's final (contemplated) position, i.e., at time $t + \delta t$. Similar to the time-to-collision interaction potential, a repulsive interaction potential can be defined for privacy interactions. Between pedestrian i and pedestrian j , this potential is denoted as $\mathcal{E}^{\text{privacy}}|_{ij}$. It represents a smooth version of a discontinuous interaction potential, which imposes a cost when the private spaces of two pedestrians overlap at the next decisional time step. This overlap is then smoothed out using the kernel $K(\eta)$. Consequently, $\mathcal{E}^{\text{privacy}}|_{ij}$ depends only on the overlap at the next decisional time step, i.e., $\eta(\tau = \delta t)$ leading to:

$$\mathcal{E}^{\text{privacy}}|_{ij}(\mathbf{u}, \omega) = \zeta K[\eta(\delta t)] \quad (3.11)$$

Finally, the total short-term repulsion interaction potential affecting pedestrian i is simply the sum over all its neighbours:

$$\mathcal{E}^{\text{privacy}}|_i(\mathbf{u}, \omega) = \sum_{j \in \mathcal{N}_i} \mathcal{E}^{\text{privacy}}|_{ij}(\mathbf{u}, \omega) \quad (3.12)$$

Decision-making layer		
δt	Decisional time step, i.e. the time interval between two consecutive decisions	0.1 s
R_{CT}	Cutoff radius of ϕ the discomfort field	2.43 m
A	Amplitude of ϕ the discomfort field	2.62
τ_{TTC}	Time of forecasting in Time To Collision interaction term	4 s
τ_{CA}	Time of collision anticipation (Karamouzas et al., 2014)	3 s
τ_{CT}	Cutoff time in the angular velocity used during the evolution of interacting shape in the computation of the Time To Collision cost	1 s
Δt_{TTC}	Time step of the evolution of interacting shape in the computation of the Time To Collision cost	0.1 s
u^∞	Preferential speed (free-walking speed)	$\mathcal{N}(1.4, 0.2)$ m/s
d_c	Characteristic repulsion length of walls	20 cm
Mechanical layer		
Δt_{mech}	Simulation time step for the mechanical layer	10^{-6} s
m_i	Mass of pedestrian i (kg)	-
I_i	Moment of inertia of pedestrian i (kg m ²)	-

TABLE 3.1: Known parameters of the model. Importantly, the **Static Floor Field** coefficient is not included because it can be substituted with the free walking speed, as demonstrated in App. C.2.4. To account for heterogeneity in free walking speed within our synthetic crowd, we employ a normal distribution with a mean of 1.4 m s^{-1} and a standard deviation of 0.2 m s^{-1} , as referenced in (Chandra and Bharti, 2013). The mass for each pedestrian is already given in our synthetic crowd. The moment of inertia for each pedestrian is calculated as detailed in App. C.1.4

Decision-making layer	
K_I	'Inertial' coefficient (kg s^{-1})
K_{Tor}	'Torsion' coefficient (J/rad^2)
ζ_{body}	Repulsive coefficient for personal space (body-body interaction) (J)
ζ_{wall}	Repulsive coefficient for personal space (body-wall interaction) (J)
$K_{\text{body}}^{\text{TTC}}$	Time-to-collision coefficient (body-body interaction) (kg m^2)
$K_{\text{wall}}^{\text{TTC}}$	Time-to-collision coefficient (body-wall interaction) (kg m^2)
Mechanical layer	
τ_{mech}	Relaxation time (s)
$\xi_{\text{body}}^{\text{static}}$	Body stiffness of tangential spring to prevent slip (static) (kg/s^2)
$\mu_{\text{body}}^{\text{dyn}}$	Dynamic friction coefficient for pedestrian-pedestrian contact (dynamic) (dimensionless)
$\gamma_{\text{body}}^{\parallel}$	Damping coefficient for tangential contact force (parallel) (kg s^{-1})
k_{body}^{\perp}	Body stiffness for orthogonal contact force (perpendicular) (N m^{-1})
$\gamma_{\text{body}}^{\perp}$	Damping coefficient for orthogonal contact force (perpendicular) (kg s^{-1})
$\xi_{\text{wall}}^{\text{static}}$	Wall stiffness of tangential spring to prevent slip (static) (kg/s^2)
$\mu_{\text{wall}}^{\text{dyn}}$	Dynamic friction coefficient for pedestrian-wall contact (dynamic) (dimensionless)
$\gamma_{\text{wall}}^{\parallel}$	Damping coefficient for tangential contact force (parallel) on wall contacts (kg s^{-1})
k_{wall}^{\perp}	Wall stiffness for orthogonal contact force (perpendicular) on wall contacts (N m^{-1})
$\gamma_{\text{wall}}^{\perp}$	Damping coefficient for orthogonal contact force (perpendicular) on wall contacts (kg s^{-1})

TABLE 3.2: Unknown parameters that need to be fit to experimental data.

3.3 NUMERICAL RESULTS

With our theoretical model setup, the next step is determining its parameters. Refer to Tab. 3.1 for the parameters with known values and Tab. 3.2 for those with unknown values. We will then assess its ability to replicate scenarios in controlled settings.

3.3.1 QUALITATIVE REPLICATION OF SIMPLE SITUATIONS

We first assessed the orders of magnitude of these parameters by considering simple situations:

Starting and stopping: An unaccompanied pedestrian must start moving and be able to stop at the target in a reasonable amount of time ($K_I \sim 10^{-2}$, $\tau_{\text{mech}} \sim 0.5$).

Turning towards a target: A pedestrian must be able to turn to face a target ($K_{\text{Tor}} \sim 0.1$).

Maintaining one's comfort zone: A pedestrian close to a static agent wishes to maintain their comfort zone by moving away ($\zeta_{\text{body}} \sim 0.1$). The same applies when a wall is nearby ($\zeta_{\text{wall}} \sim 0.1$).

Collision avoidance: When a pedestrian must go around another stationary pedestrian ($K_{\text{body}}^{\text{TTC}} \sim 10^{-2}$), or around an obstacle as illustrated in Fig. 3.11 ($K_{\text{wall}}^{\text{TTC}} \sim 10^{-2}$).

Frontal collision: When an agent approaches a static pedestrian, they must not interpenetrate or bounce off each other as though they were billiard balls ($k_{\text{body}}^{\perp} \sim 10^6$, $\gamma_{\text{body}}^{\perp} \sim 10^4$). The equivalent scenario with a wall involves $k_{\text{wall}}^{\perp} \sim 10^6$ and $\gamma_{\text{wall}}^{\perp} \sim 10^4$.

Rotational collision: A pedestrian next to another one with a fixed centre of mass tries to turn without bouncing off like a billiard ball ($\xi_{\text{body}}^{\text{static}} \sim 10^5$, $\gamma_{\text{body}}^{\parallel} \sim 10^4$). In a similar situation, the pedestrian must induce rotation in its neighbour by rotating himself ($\mu_{\text{body}}^{\text{dyn}} \sim 0.1$). Equivalent scenarios when interacting with a wall have also been simulated ($\xi_{\text{wall}}^{\text{static}} \sim 10^5$, $\gamma_{\text{wall}}^{\parallel} \sim 10^4$, $\mu_{\text{wall}}^{\text{dyn}} \sim 0.1$).

We then tried to replicate more complex experimental scenarios in controlled settings. The focus was put on scenarios where collective dynamics are at play and are expected to be highly sensitive to pedestrian (physical and private-space) shapes. Significant practical properties such as the fundamental diagram (in the sparse to moderately dense regime) had already been replicated by the simple circular specification of the model (Echeverría-Huarte and Nicolas, 2023), for both unidirectional and bidirectional flows, as

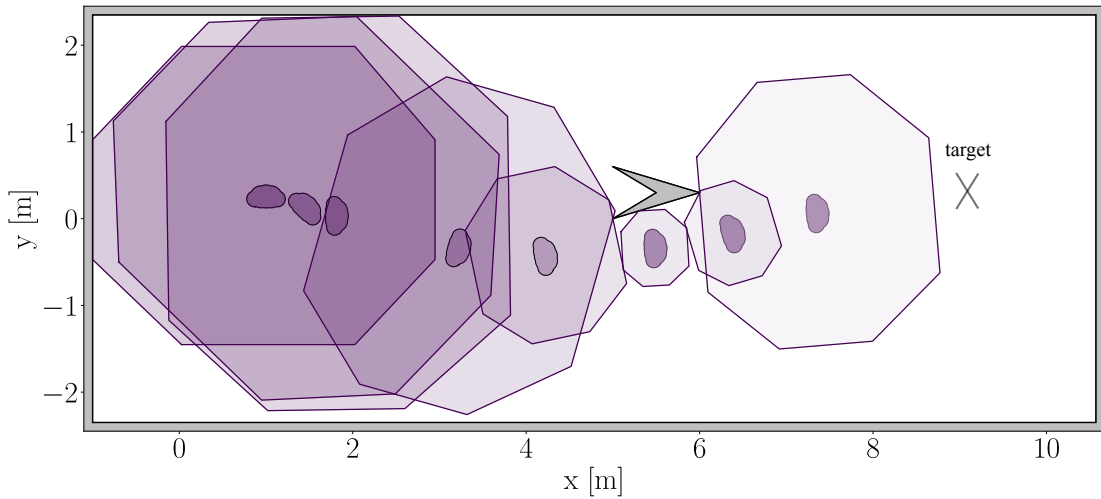


FIGURE 3.11: In this test scenario, a pedestrian must walk toward a target while navigating around a non-convex obstacle. The initial body orientation is fixed arbitrarily, so that the pedestrian starts rotating as soon as the simulation begins. Transparency increases over time.

summarised in Fig. 3.12; they will not be further discussed here.

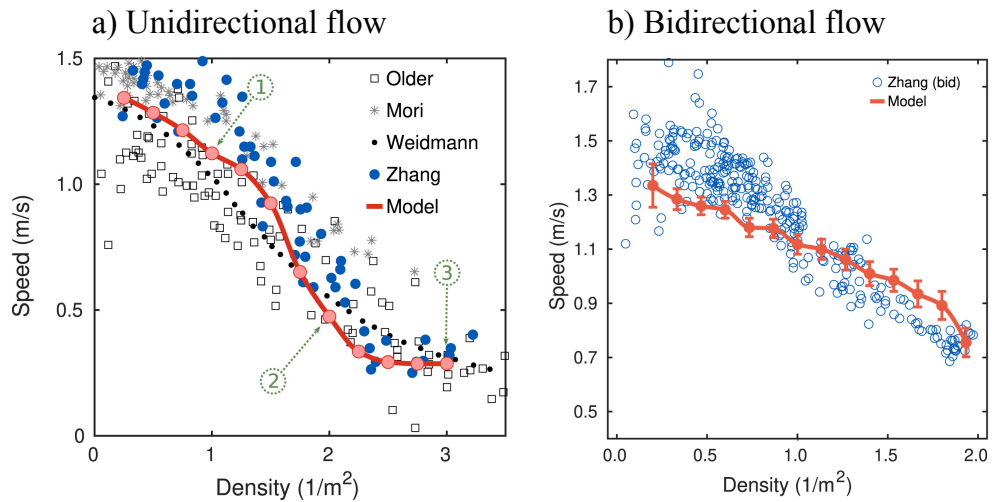


FIGURE 3.12: Fundamental diagrams relating the average pedestrian speed to the mean density for (a) a unidirectional flow along a corridor with periodic length $L_X = 16$ m and width $L_Y = 3$ m. The variation of the simulated mean speed with the density is shown along with various experimental data sets (Older, 1968; Mōri and Tsukaguchi, 1987; Weidmann, 1993; Zhang et al., 2011). (b) A bidirectional flow in a corridor. The figure is adapted from Echeverría-Huarte and Nicolas (2023).

3.3.2 FORWARD PROPAGATION OF A PUSH THROUGH A ROW OF PEOPLE

We began with an experiment involving the propagation of a push through a line of people from Feldmann and Adrian (2023). Fourteen volunteers, aged 19 to 55, participated. Five participants stood in front of a punching bag, facing a wall within a 3-by-5 meters area as shown in Fig. 3.13. The last person in line was pushed forward with the punching bag, manually operated by an experimenter.

Various spatial configurations were tested by adjusting the distance between subjects and their proximity to the wall. The bag was pushed with three different intensity levels, and the pressure was measured using a sensor on the back of the person as shown in Fig. 3.14. Another pressure sensor was placed on the wall to capture additional data. The initial arm position was also varied: arms along the body,

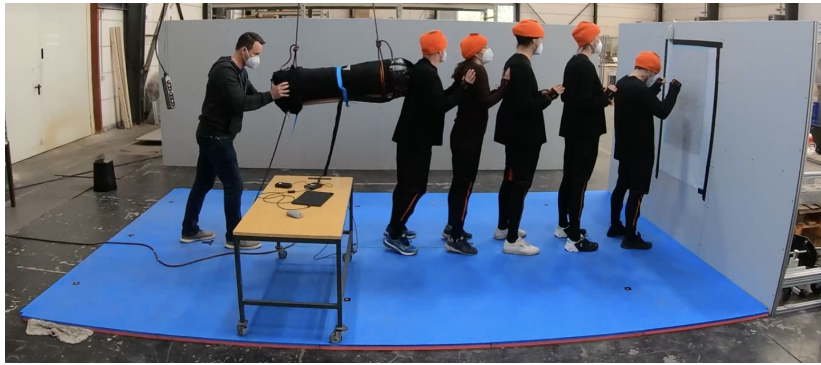


FIGURE 3.13: Setup of the experiments. The experimental area covered with mats has a size of $3\text{ m} \times 5\text{ m}$. On the left side, a punching bag is suspended from the ceiling. A solid wall limits the right side of the area. Five people lined up in a queue and are pushed forward in a controlled manner. The picture is taken from [Feldmann and Adrian \(2023\)](#).

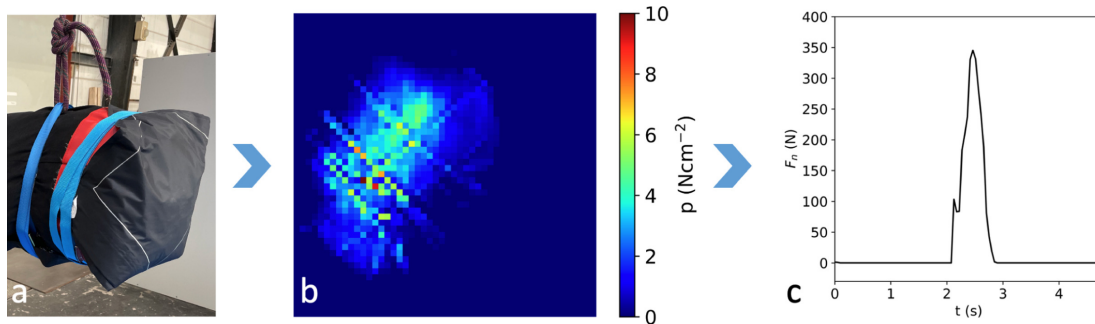


FIGURE 3.14: (a) A pressure sensor measures the pushing intensities at the punching bag. (b) Spatial image of a single time frame recorded by the pressure sensor. (c) Time series of the normal force. The figure is taken from [Feldmann and Adrian \(2023\)](#).

at shoulder level (to expedite recovery during the push), or in an intermediate position. Nevertheless, pedestrians still had the right to use their hands to protect themselves and prevent injury.

To replicate this scenario using our model, we selected individuals from our synthetic population whose mass closely matched that of the experimental subjects. We set each pedestrian's decision-making speed to zero to reflect their intention not to move from their initial position. The initial arm position was simulated by appropriately adjusting the coefficient of the force normal to the contact surface k_{body}^{\perp} and the damping normal coefficient $\gamma_{\text{body}}^{\perp}$. The optimal parameters of the mechanical layer minimised the mean quadratic difference between the data trajectories (cut at the moment pedestrians started to go back to their initial position) and the simulated ones for each experiment. Fig. 3.15 illustrates two simulations compared with data, showcasing good agreement. The experimental trajectory appears somewhat jittery because it records the movement of the head. In contrast, our model replicates the overall body movement, ensuring it halts at the correct moment.

3.3.3 COMPETITIVE EGRESS OF PEDESTRIANS

Evacuation scenarios where mechanical contacts significantly influence outcomes warrant further investigation. In particular, the *faster is slower* effect, linked to varying levels of competitiveness during an evacuation, was observed in an experiment conducted at the University of Navarra by [Garcimartín et al. \(2013\)](#). In this study, 93 to 98 volunteers participated in an evacuation exercise held in an indoor gym. Participants were instructed to exit through a door 69 cm wide under three different competitiveness conditions: low (no intentional contact), medium (soft contact allowed), and high

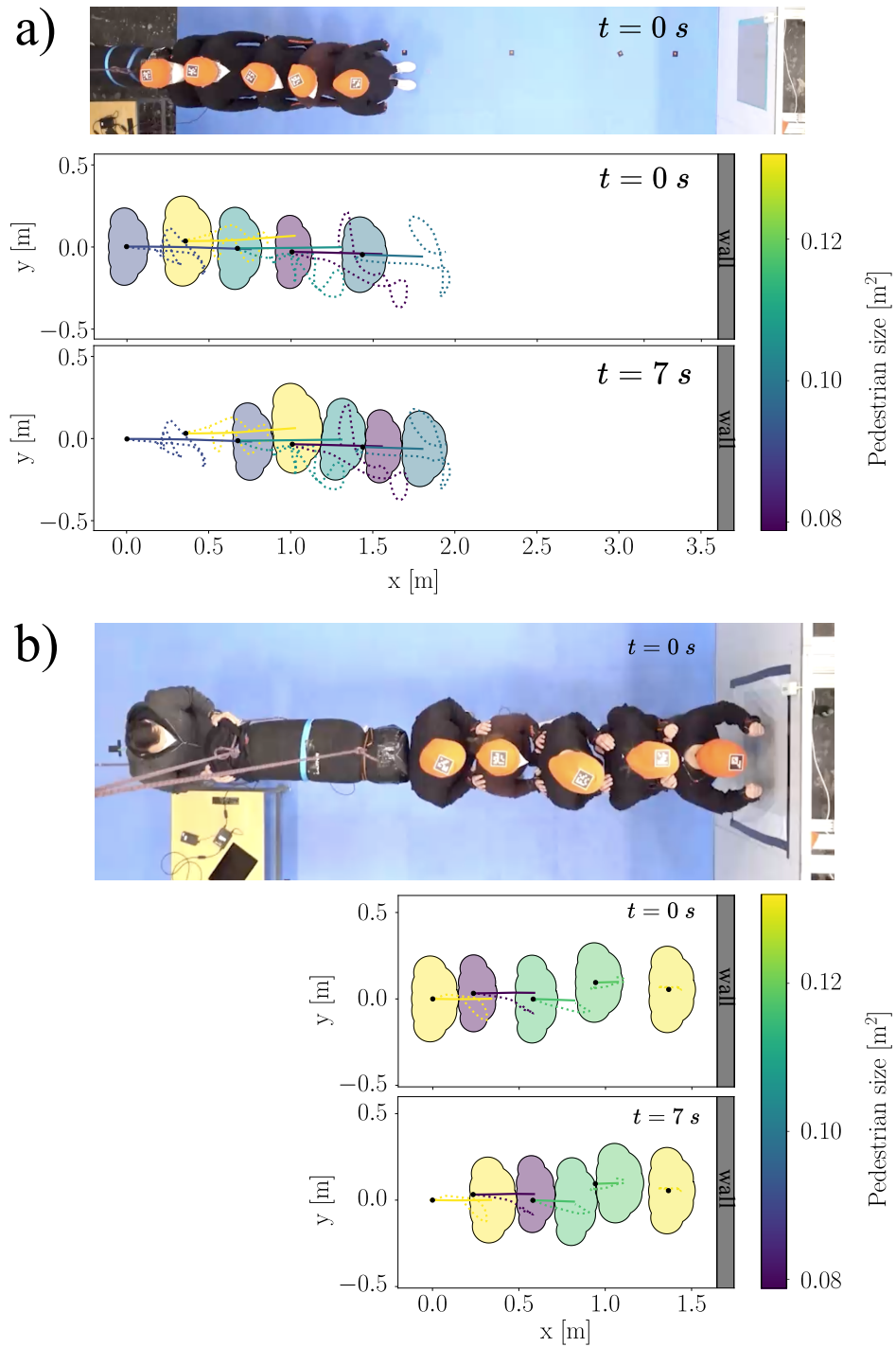


FIGURE 3.15: **(a)** The top panel provides a top-view photo of the experiment's initial setup. The middle panel shows their starting positions in the simulation, while the lower panel displays their positions at the end. Initially, the pedestrians have their arms along their bodies. At $t = 0.05$ s, a force starts to apply to the leftmost pedestrian. The solid lines depict the simulated trajectories of each pedestrian, while the dotted lines represent the experimental trajectories of their heads. **(b)** Simulation of a scenario where pedestrians are closer to the wall. The force starts to apply at $t = 2.2$ s. Additionally, each pedestrian starts with their hands on the shoulder blades of the person in front. The pedestrian closest to the wall places their hands on the wall itself.

(moderate pushing permitted). By adjusting the preferential velocity of each pedestrian u^∞ according to the level of competitiveness allowed during the experiment, our model successfully replicates this phenomenon as illustrated in Fig. 3.17.

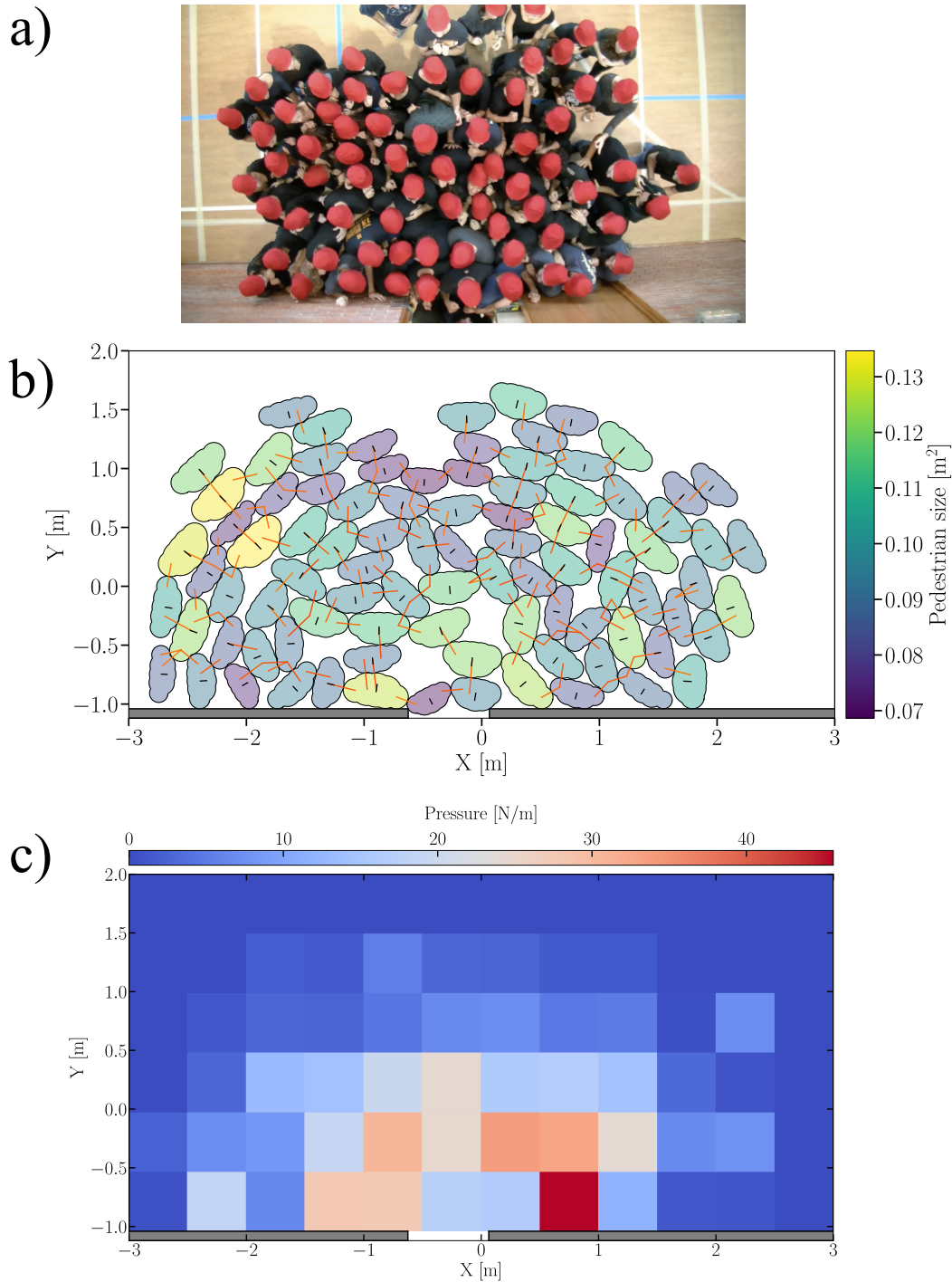


FIGURE 3.16: **(a)** A snapshot depicting an evacuation drill under highly competitive conditions, as described by [Garcimartín et al. \(2013\)](#). **(b)** Similarly to above, a snapshot illustrating the egress of 93 individuals evacuating through a narrow doorway measuring 69 cm in width. **(c)** A pressure map created by binning the space into squares with a side length of 0.5 m and averaging the measured pressure across the entire simulation duration. In this context, ‘pressure’ refers to the average magnitude of normal forces measured within a specified spatial bin divided by the perimeter of the physical body. This average is calculated over time and includes the two pressures measured during physical contact.

A simulation snapshot is also presented in Fig. 3.16 b). The contacts between the different shapes are represented by rods, highlighting the formation of contact arches that constrain the flow. By averaging the magnitude of the pressures associated with these contacts over time and space, a pressure map can

be drawn, shown in Fig. 3.16 c). This map reveals shapes similar to concentric semicircles of equal pressure, representing these contact arches.

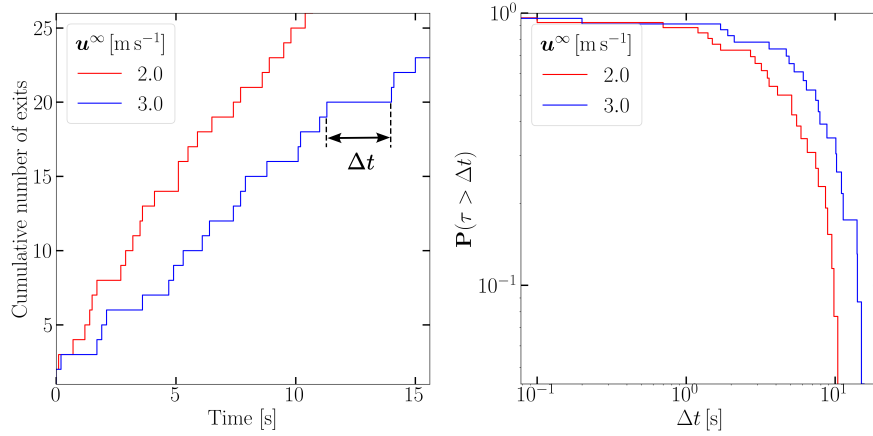


FIGURE 3.17: **Left** The cumulative number of exits as a function of time for two different mean preferred speeds, u^∞ , demonstrating the *faster is slower* effect. **Right** Survival function $\mathbf{P}(\tau > \Delta t)$ of time gaps between successive egresses.

3.3.4 TWO PEDESTRIANS PASSING EACH OTHER IN A CORRIDOR

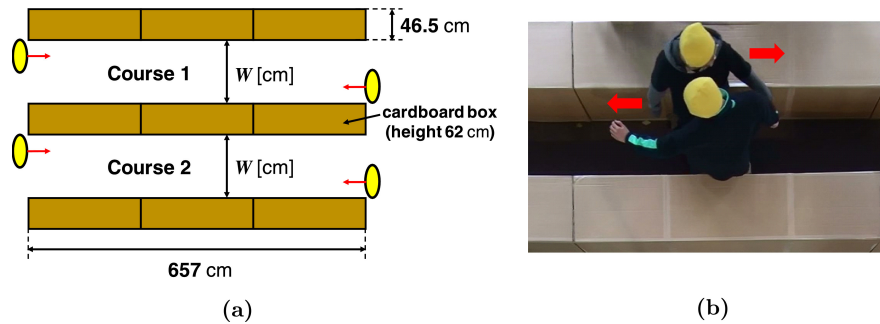


FIGURE 3.18: **(a)** Scheme of the experimental setup. Two courses are created using cardboard boxes. Four participants, represented by yellow ellipses, were positioned at the ends of these courses. Upon receiving a cue, they walked to the opposite ends. The side on which they would pass each other was specified to them before each trial and their initial position. **(b)** Experiment Snapshot for a corridor width of 60 cm. The image shows two participants passing each other by rotating their bodies. The figure is taken from Yamamoto et al. (2019).

With the parameters of the mechanical layer specified, we can focus on experiments where decision-making aspects play a crucial role while mechanical aspects do not. Specifically, we explored scenarios in corridors where individuals initially positioned on opposite sides attempt to cross without making contact with someone approaching from the opposite direction. During their journey, pedestrians adjust their position and orientation to avoid collisions. The experiment involved four male participants aged 18 to 25 and was conducted at The University of Tokyo. Two courses were constructed using cardboard boxes to form corridors with widths ranging from 60 to 140 cm as illustrated in Fig. 3.18. Participants were positioned at opposite ends of the corridor and instructed to walk towards each other, passing midway. They wore tablets equipped with gyroscope sensors to record body rotations.

An illustrative simulation where two pedestrians navigating a corridor by rotating to avoid each other is shown in Fig. 3.19. By adjusting the parameters $K_{\text{body}}^{\text{TTC}}$, ζ_{body} , and ζ_{wall} , we can replicate the experiment qualitatively, as shown in Fig. 3.20.

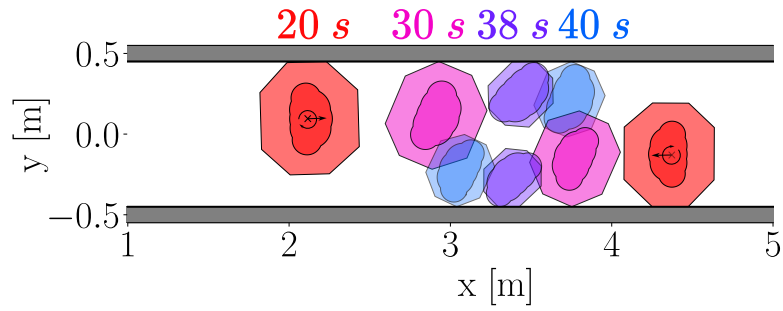


FIGURE 3.19: Simulation of two pedestrians passing each other in a 90 cm wide corridor. The pedestrians’ physical bodies are depicted in a darker colour, while their maximum comfort contour space is shown in a more transparent shade. The transparency increases over time. It evidences that the pedestrians rotate their bodies to avoid collisions.

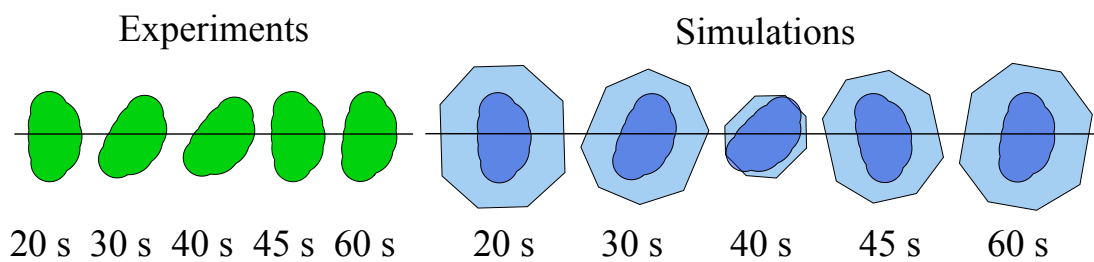


FIGURE 3.20: Comparison of the previous simulation results (Fig. 3.19) for the subject moving from left to right with the measured experimental data.

CHAPTER 4

A NOISE-INDUCED KAPITZA'S PENDULUM INSTABILITY TO ACCOUNT FOR STOP-AND-GO DYNAMICS IN TRAFFIC

The scenarios considered so far do not consider flow instabilities. However, such instabilities are well documented in pedestrian dynamics, as illustrated in Fig. 4.1, where alternating patterns of stalled and moving phases emerge.



FIGURE 4.1: Crowd moving to the right during the Hajj in 1426H (January 12, 2006). The movement displayed alternating patterns of jammed and moving sections, also known as *stop-and-go waves* in two dimensions. Moving parts are highlighted in green, while stationary parts are shown in grayscale. The full video is available on the **Fouloscopie** *YouTube* channel at the following [link](#).

To investigate this phenomenon, [Ziemer et al. \(2016\)](#) conducted a one-dimensional experiment where individuals moved along an elliptical path (see Fig. 4.2). By varying the pedestrian density, they

observed that when the density exceeded a critical threshold, stop-and-go waves began to emerge. Remarkably, even the slightest perturbation in this high-density regime was sufficient to trigger these waves, highlighting their sensitivity to small perturbations.

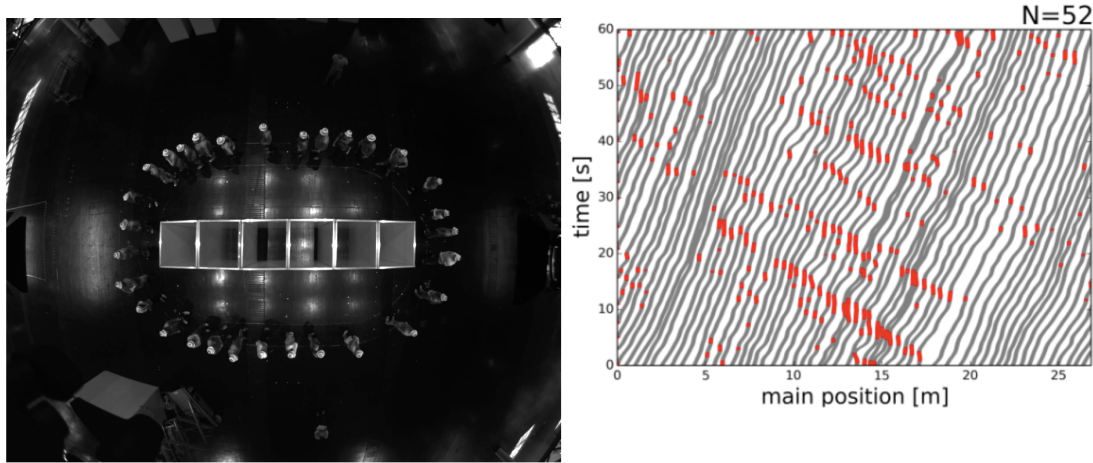


FIGURE 4.2: Snapshot from a video showing pedestrians moving on an ellipsoidal shape. The trajectories of the pedestrians are displayed on the right. Red segments indicate moments when pedestrians are stationary, while gray segments represent movement. The figure is adapted from [Ziemer et al. \(2016\)](#).

Such instabilities are also commonly seen in single-lane traffic, as demonstrated by ([Sugiyama et al., 2008](#)) in an experiment involving cars on a circular track. At first glance, the phenomenon appears similar to that observed in pedestrian dynamics and can be approximately described using a linear collective instability induced by delays and lags in the system’s dynamics.

However, such a modelling framework fails to account for the fluctuations observed during transition periods in experimental settings ([Sugiyama et al., 2008](#)). The present study shows that an alternative stochastic modelling approach can accurately reproduce the formation of stop-and-go dynamics. Unlike classical methods, this new framework is unconditionally linearly stable. However, the introduction of noise leads to a non-linear instability, resulting in the emergence of waves and oscillations within the dynamics. This is akin to Kapitza pendulum ([Butikov, 2017](#)).

The content of this chapter is adapted from the articles ([Dufour et al., 2024g](#)) (in preparation for submission), for the physical interpretation, and ([Ehrhardt and Tordeux, 2024](#)) (submitted to the Franklin Open journal), which addresses the mathematical aspects. My primary contributions were in formulating the problem, designing and carrying out numerical simulations, analysing the results, and clarifying the physical origin of the observed phenomena.

CONTEXT

Determining the stability of many-body systems, particularly those with three or more components, is often a complex challenge. This complexity is exemplified by the enduring question of the solar system’s stability ([Moser, 1978](#); [Villani, 2012](#)). The situation becomes even more intricate when deterministic equations of motion fail to adequately describe a system’s dynamics ([Gardiner, 2021](#)). A prime example of this complexity can be seen in vehicular traffic. Drivers are well-acquainted with stop-and-go waves on highways, where traffic jams—sometimes referred to as phantom jams—emerge without any apparent cause, compelling drivers to alternately slow down and speed up. The physical origins of these phenomena remain a topic of debate, even in scenarios involving single-file traffic. This ongoing debate has significant practical implications for both safety and congestion management. Recently,

these issues have gained renewed attention due to instabilities observed in platooning experiments involving **Adaptive Cruise Control (ACC)** vehicles (Stern et al., 2018; Gunter et al., 2020; Makridis et al., 2021).

Many factors can destabilise traffic flow, as reaction times, delays, and inaccurate perceptions or responses influence vehicle control and environmental perception. Some of these factors can be included deterministically in equations of motion. Specifically, finite response times and latency in vehicle control (Nagatani and Nakanishi, 1998; Orosz et al., 2004, 2010; Wilson and Ward, 2011; Tordeux et al., 2012, 2018) can be modelled using inertial ordinary differential equations (Komatsu and Sasa, 1995) and delayed linear equations (Nagatani and Nakanishi, 1998). These have traditionally been identified as causes of linear instabilities that disrupt the uniform, steady flow of a vehicle platoon or string. Theoretical analyses, such as those by Pipes (1953); Kometani and Sasaki (1958); Chandler et al. (1958); Herman et al. (1959); Komatsu and Sasa (1995). Additionally, numerical studies by Bando et al. (1995, 1998) provide foundational insights into these instabilities. When response times are too slow, the underlying dynamics can lead to the emergence of stop-and-go waves. These dynamics replicate the amplification of spontaneous perturbations observed in experiments with **Adaptive Cruise Control**-equipped vehicles. This phenomenon is particularly evident in finely-tuned non-linear models, which accurately replicate experimental observations (Treiber et al., 2000; Tomer et al., 2000; Jiang et al., 2001; Tordeux et al., 2010).

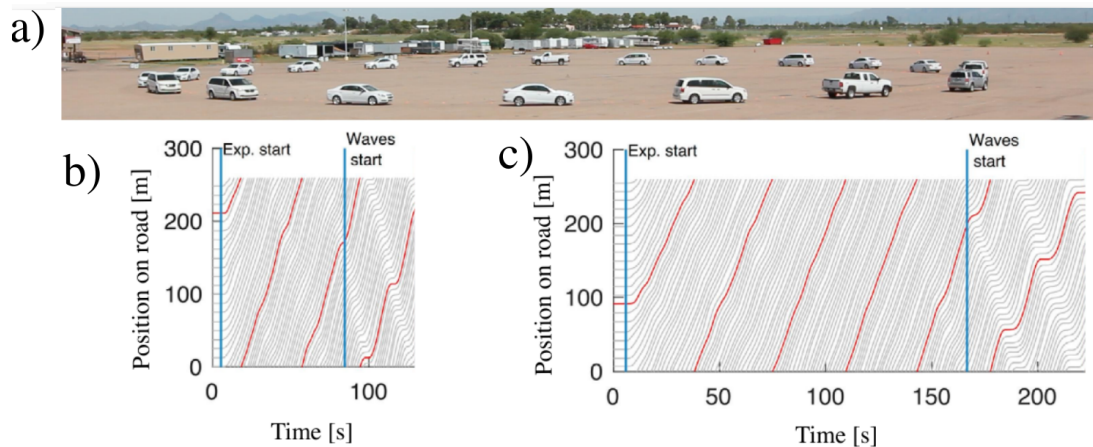


FIGURE 4.3: **a) Ring of Vehicles:** At the initial time, all vehicles are equally spaced and moving at the same speed. **b) Vehicle Trajectories:** The trajectories of all vehicles are shown, with one vehicle's trajectory highlighted in red. Two distinct phases can be observed: the first phase is a homogeneous state lasting approximately 90 seconds, followed by a second phase characterised by stop-and-go waves. **c) Trajectories from Another Trial:** In this trial, the phase with stop-and-go waves begins much later, around 170 seconds. The diagrams are adapted from Stern et al. (2018).

For cars without **ACC**, it has been argued that delay-induced instabilities fail to capture critical features observed in empirical single-file traffic or controlled experiments with vehicle platoons. Tian et al. (2016) highlight these discrepancies in empirical settings, while controlled experiments by Jiang et al. (2018) and Tian et al. (2019) further emphasise the limitations of these models. In experiments involving cars on a ring, such as those conducted by Sugiyama et al. (2008); Tadaki et al. (2013); Stern et al. (2018), around twenty human-driven vehicles followed each other on a single-file loop. Above a specific vehicular density, fully developed stop-and-go waves were observed but only after long transition times, ranging from one to several minutes (as depicted in Fig. 4.3).

The irregular emergence of stop-and-go waves at high densities seems incompatible with linear instabilities, which would cause these waves to occur systematically in the same manner and at consistent time. Instead this phenomenon suggests a metastable state, as discussed by Nakayama et al. (2009) and

Schadschneider et al. (2010, Chapters. 6.3, 6.5) with experimental data and by Wilson (2008) with a deterministic non-linear model. Linearly unstable systems that directly link speed and spacing through an optimal velocity function also fail to explain the concave growth of speed fluctuations observed in a platoon of cars following a leader travelling at a constant speed on open roads (Fig. 4.4), as noted by Treiber and Kesting (2017); Jiang et al. (2018); Tian et al. (2019). This latter phenomenon can be accurately reproduced by car-following models incorporating deterministic action points, where a response is triggered only when the stimulus exceeds a finite threshold, as Treiber and Kesting (2017) highlighted.

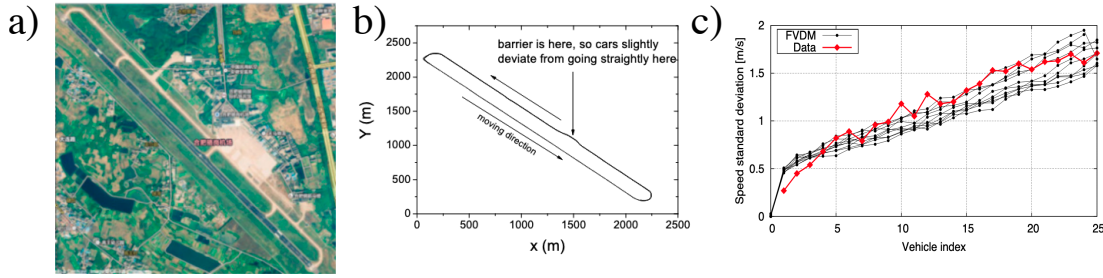


FIGURE 4.4: **a) Airport Map:** The map illustrates how cars are moving in a manner that approximates an open road (Jiang et al., 2017a). **b) Path Scheme:** This diagram depicts the route that cars follow at the airport. GPS devices installed in the cars enable the measurement of their trajectories (Jiang et al., 2017a). **c) Velocity Analysis:** The red line represents the standard deviation of each car's velocity along the platoon, averaged over specific time intervals. In contrast, the black line shows simulations based on the full velocity difference model with additive white noise. The model exhibits a convex behaviour, whereas the actual data demonstrates a concave behaviour (Tian et al., 2019).

A realistic outcome can be achieved by augmenting the equation of motion with a stochastic term. This approach is expressed in the following 1D equation:

$$dv_n(t) = A(\Delta x_n(t), v_n(t), v_{n+1}(t)) dt + \sigma dW_n(t) \quad (4.1)$$

Here, the stochastic noise term σdW_n represents the influence of numerous degrees of freedom not captured by the deterministic response A . The function A is dependent on several factors, including the gap $\Delta x_n = x_{n+1} - x_n - \ell$, where x_n is the position of the n -th car and $\ell \geq 0$ is the length of the vehicles. It also depends on the speed $v_n = \dot{x}_n$, among other variables. The significant impact of noise in systems that exhibit linear instability within specific parameter ranges is well understood by physicists and does not come as a surprise.

In physical systems, especially near dynamical instabilities, stochastic noise can lead to the so-called *noisy precursors* of instability, such as sustained oscillations (Wiesenfeld, 1985). These phenomena should not be confused with genuine instabilities.

It is well-established that **additive** noise does not impact the stability of a stochastic differential equation, such as Eq. (4.1), at the linear level. However, certain parameter settings may reveal a linear instability. To identify a *bona fide* noise-induced instability, Ngoduy (2021) introduced a **multiplicative** noise, which increases with relative speeds. This approach significantly amplifies the noise as the system deviates from steady flow, potentially driving it into instability through a positive feedback mechanism. Multiplicative noise can be studied perturbatively by linearizing the response function A . Specifically, it can modify an existing criterion for linear instability in the deterministic response A . Hidden degrees of freedom, such as inaccurate driver perceptions or responses represented by dW_n , can indeed amplify or *anticipate* the existing linear instability.

In this work, we propose that a simple additive noise can significantly impact and destabilise a car-

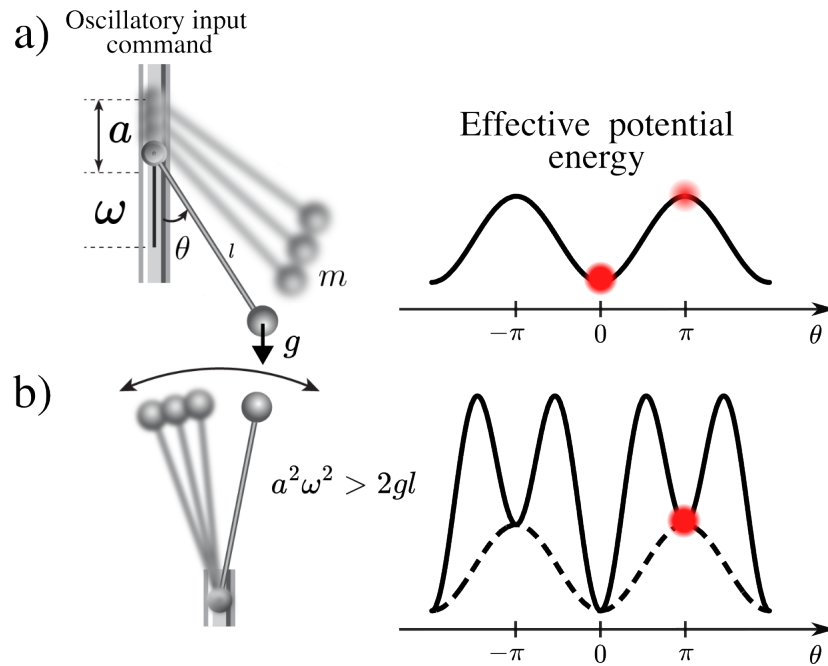


FIGURE 4.5: The Kapitza pendulum’s equilibrium position is determined by the vertical oscillatory input command, which varies in frequency and amplitude. **a)** When the input amplitude and frequency are sufficiently small, the equilibrium position is at $\theta = 0$. The right side illustrates the effective potential energy landscape (obtained by averaging the dynamic over the fast oscillations of the input oscillatory command, refer to [Golovinski and Dubinkin \(2022\)](#) for technical details), indicating that the mass, depicted in red, can achieve different energy levels depending on the amplitude of its oscillations. **b)** As the input frequency increases, the energy landscape through which the mass moves is altered, rendering the position at $\theta = \pi$, which was previously unstable, now metastable. It is important to note that the condition for observing the inversion of stability at $\theta = \pi$ is applicable when the pivot amplitude is small and the pivot frequency is large. This is because the effective energy is derived by separating the fast and slow components of the pendulum’s motion. Improved criteria can be established to observe an inversion of stability at $\theta = 0$ as well ([Butikov, 2017](#)). This scheme is adapted from [Bukov \(2018\)](#). For a visualisation of its movement, visit the [animation](#) from [Gereshes \(2019\)](#) and the interactive [app](#) from [Neumann \(2001\)](#).

following model that is otherwise unconditionally stable in the deterministic limit. This finding highlights an alternative source of traffic instabilities independent of factors like response delays and reaction times. This role of random noise had only been glimpsed in cellular automaton models for traffic, where vehicles may randomly brake relative to their desired acceleration at each time step. Similar effects have been noted in continuous space models ([Krauß et al., 1996](#); [Jost and Nagel, 2005](#)).

We show that this alternative, non-perturbative stochastic route to instability arises from the excitation of *non-linearities* in the response term A . Unlike traditional non-linear hydrodynamic instabilities ([Bergé, 1976](#)), the resulting stop-and-go dynamics require the continuous noise action to be sustained, yet they closely resemble empirical observations. The crucial role of non-linearities complicates analytical progress; however, drawing an analogy with the Kapitza pendulum (illustrated in Fig. 4.5) — where stable and unstable positions swap due to vertical oscillations—provides valuable insights into the observed phenomena.

Specifically, using this analogy, we heuristically explain our findings by decomposing the noise’s effect into a finite periodic (oscillatory) driving component and a stochastic triggering perturbation. The periodic component stimulates the system’s non-linear response and controls the gap necessary to trigger instability. When this gap reaches zero, the system loses stability against minor perturbations. Consequently, the complex noise-induced non-linear instability simplifies to the more manageable problem of determining the asymptotic stability of a periodic orbit under vanishing noise.

4.1 CAR-FOLLOWING MODELS AND STOCHASTIC TERMS

Traffic problems have given rise to models galore, likely due to their practical applications and geometric simplicity. Insight into metastable states has been partially achieved through the use of cellular automata and interacting particle systems (Barlovic et al., 1998; Ke-Ping and Zi-You, 2004; Kaupužs et al., 2005; Huang et al., 2018), (Schadschneider et al., 2010, Chap. 8.1). However, our focus is on continuous car-following models that follow the generic structure of Eq. (4.1), whether they are deterministic (with $dW_n = 0$) or include a stochastic component. Among the existing models, we single out four models:

Stochastic Optimal Velocity (SOV) model (Wagner, 2011; Treiber and Helbing, 2009; Wang et al., 2020; Friesen et al., 2021)

$$dv_n = \left(\frac{V(\Delta x_n) - v_n}{T_1} + \frac{\Delta v_n}{T_2} \right) dt + \sigma dW_n \quad (4.2)$$

where $V : \mathbb{R} \mapsto \mathbb{R}_+$ is a sigmoid-like **Optimal-Velocity (OV)** function as described by (Bando et al., 1995; Jiang et al., 2001; Treiber and Helbing, 2009). This function depends on the spacing Δx_n , while T_1 and T_2 (both greater than zero) represent the relaxation times for optimal velocity and speed alignment, respectively.

Inertial Car-Following (ICF) model (Tomer et al., 2000)

$$dv_n = K \cdot \left(1 - \frac{2v_n T + \ell}{\Delta x_n + \ell} \right) dt + \frac{Z^2(-\Delta v_n)}{2\Delta x_n} dt - 2Z(v_n - v_0) dt + \sigma dW_n \quad (4.3)$$

where $Z(x) = (x + |x|)/2$ denotes the positive part of x , $T > 0$ represents the desired time gap, and $\ell_{g_e}0$ indicates the vehicle length.

Stochastic Intelligent Driver (SID) model (Treiber and Kesting, 2017)

$$dv_n = a \left(1 - \left(\frac{f_n}{\Delta x_n} \right)^2 - \left(\frac{v_n}{v_0} \right)^4 \right) dt + \sigma dW_n \quad (4.4)$$

where $f_n = s_0 + T v_n - v_n \Delta v_n / (2\sqrt{ab})$, a and b (both greater than zero) are the desired acceleration and maximum deceleration parameters, respectively, s_0 represents the minimal gap and $T > 0$ the desired time gap.

Stochastic Adaptive Time Gap (SATG) model

$$dv_n = \frac{1}{T_n^\varepsilon} (\lambda (\Delta x_n - T v_n) + \Delta v_n) dt + \sigma dW_n \quad (4.5)$$

where $\lambda > 0$ is a sensitivity parameter, T_n^ε a bounded mollifier of the time gap and T is the desired time gap.

We will primarily simulate these models on a finite loop, employing periodic boundary conditions and a single line of cars (without overtaking) to replicate the experimental conditions described in (Sugiyama et al., 2008; Tadaki et al., 2013). Additional details regarding the simulation settings and the notations used in defining the models are provided in the supplementary material App. D.1.

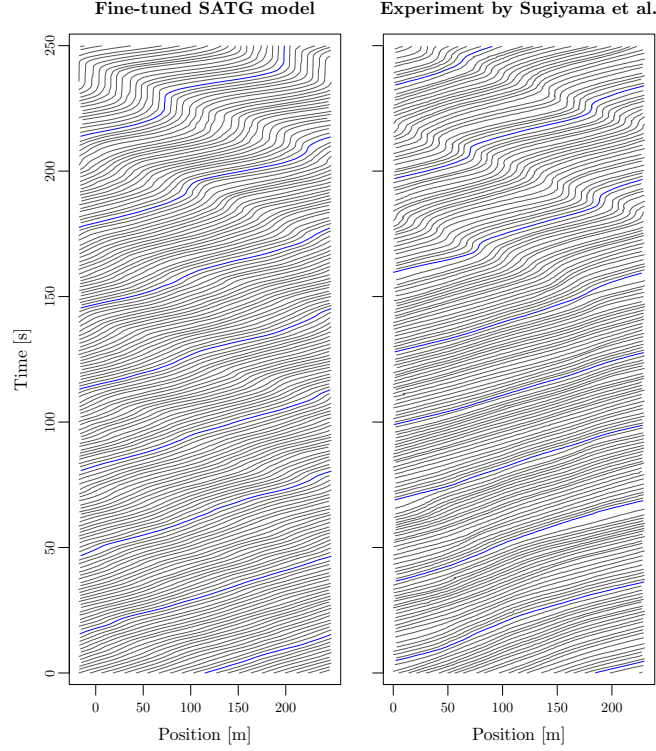


FIGURE 4.6: Trajectories featuring stop-and-go waves in a selected simulation of the finely-tuned **SATG** model, using parameters $T = 0.7$ s and $\lambda = 1/3$ s $^{-1}$ (**left panel**), as well as in the experiment conducted by [Sugiyama et al. \(2008\)](#) (**right panel**).

4.2 NUMERICAL EVIDENCE OF A NOISE-INDUCED INSTABILITY AND ITS EMPIRICAL PLAUSIBILITY

At low car densities and with sufficiently small noise volatility σ , the models mentioned above exhibit stability with linear car trajectories $x_n(t)$. However, as density increases, most models tend to experience a linear instability that leads to stop-and-go waves, at least within certain parameter ranges ([Orosz et al., 2004](#); [Treiber and Kesting, 2017](#)). In contrast, the **Adaptive Time Gap (ATG)** model (i.e., the **SATG** model without stochasticity) is notable for its unconditional linear stability, as demonstrated by linear stability analysis (refer to App. D.2). To validate these analytical predictions, we perform numerical simulations of the models for $N = 22$ cars using an implicit/explicit Euler–Maruyama solver (technical details are provided in the App. D.1). We assess the stability of the base flow by employing a disorder parameter:

$$\phi(t) = \sqrt{\langle \Delta x_n^2 \rangle - \langle \Delta x_n \rangle^2} \quad (4.6)$$

where the angular brackets denote an average over cars n , deviating from zero when stop-and-go waves appear¹. To differentiate between various noise volatilities, one can define an average over time of the simulation order parameter $\langle \phi \rangle$, where the angular brackets indicate a time average of the simulation. Apart from the residual disorder caused by noise, which induces *thermal* vibrations around equilibrium positions, the simulations confirm the predictions, including the stability of the **SATG** uniform flow at sufficiently low σ . However, **SATG** abruptly transitions to a non-uniform state ($\phi \neq 0$) as the noise surpasses a threshold σ^* , as illustrated in Fig. 4.7. This threshold depends on the system size and

¹One may find an example of $\phi(t)$ on App. D.1.

approaches zero as $N \rightarrow \infty$ (see Fig. 4.8). The abrupt and seemingly discontinuous transition in $\langle \phi \rangle$ contrasts with other models' smoother emergence of stop-and-go dynamics. Nonetheless, it coincides with the onset of stop-and-go waves (Fig. 4.6), which, once developed, resemble those found in other models (See App. D.1 to play with an online simulation and see by yourself the trajectories produced by the different models mentioned above). These waves have a wavelength determined by the system size. However, shorter-wavelength modes can also be linearly unstable in optimal velocity models, albeit generally less so than the largest wavelength (Orosz et al., 2004). The jammed phase propagates upstream at a speed of approximately $v_c = -\ell/T \approx -5 \text{ m s}^{-1}$, where ℓ is the vehicle length and T is the desired time gap.

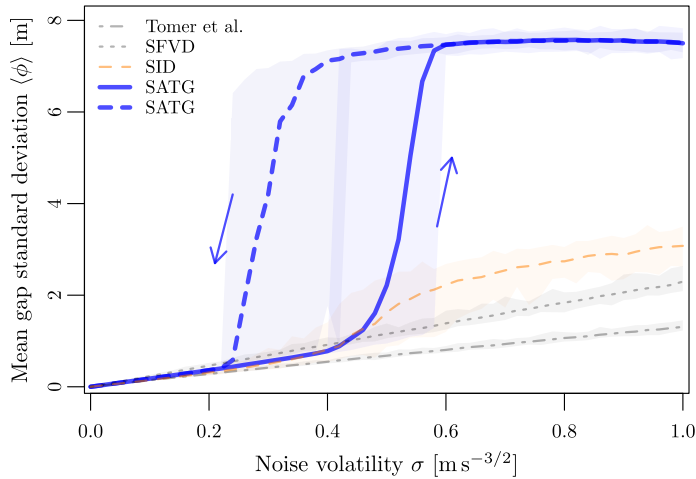


FIGURE 4.7: Standard deviation of the inter-vehicle distances in the stationary state according to noise volatility σ for 22 vehicles with periodic boundaries and uniform initial conditions, as in the experiment by Sugiyama et al. (2008). The continuous lines represent mean values, while the coloured areas indicate the minimum and maximum range (refer to the App. D.1 for simulation details). Near-linear models, such as SOV model Eq. (4.2) and SICF model Eq. (4.3), exhibit no noise-induced instability; the deviation increases linearly with σ . In contrast, non-linear models, SID model Eq. (4.4) and SATG model Eq. (4.5), describe a phase transition to stop-and-go dynamics. The former undergoes subcritical instability, while the latter experiences a non-linear instability. Notably, the non-linear SATG model Eq. (4.5) displays hysteresis: when starting from a jammed initial condition, the noise amplitude threshold is significantly lower.

In contrast to waves arising from linear instability, their emergence occurs erratically after a typically long but highly variable transient period. This behaviour aligns with empirical data from (Sugiyama et al., 2008; Tadaki et al., 2013), where stop-and-go waves do not consistently appear in the same manner at a given car density. These features of the SATG model suggest a first-order transition toward traffic instability, accompanied by metastability, as supported by empirical findings (Nakayama et al., 2009). This is further evidenced by the bimodal distribution of ϕ at the transition, as illustrated in Fig. 4.8. A consequence of this proposed discontinuous transition, with its associated energy barrier, is the presence of hysteresis, a phenomenon commonly observed in traffic systems (Schadschneider et al., 2010, Chapters. 6.5, 8.1, 9.4). Our simulations confirm the emergence of a significant hysteric loop when noise volatility (or car density) is increased into the high-noise region and then decreased, as shown in Fig. 4.7. Notably, stop-and-go waves persist even below the noise level required to destabilise the homogeneous flow.

4.3 RATIONALISATION WITH OSCILLATORY DRIVING

However, the hysteresis loop does not persist without noise ($\sigma = 0$). Even if the system begins in a regime characterised by stop-and-go dynamics, it will revert to uniform flow when the noise level

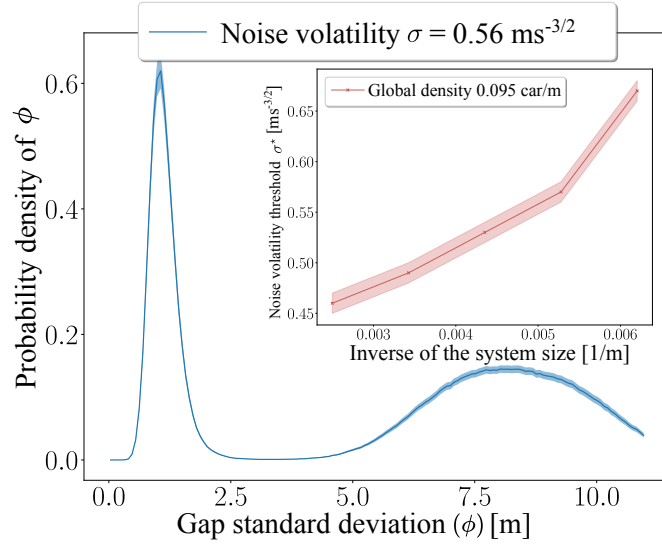


FIGURE 4.8: Probability density of ϕ computed along simulations for a noise volatility of $0.56 \text{ ms}^{-3/2}$. The solid blue line represents the mean, while the shaded area indicates the standard error (see App. D.1 for simulation details). The distribution exhibits bimodality, with one peak corresponding to a uniform flow perturbed by thermal-like fluctuations and another peak associated with stop-and-go waves. Throughout the simulation, the system transitions between these states. The **inset** shows that the threshold transition across the inverse system size exhibits a quasi-affine behaviour with a non-zero y-axis intercept, suggesting that the transition persists in the thermodynamic limit.

becomes sufficiently low (see App. D.1 Fig. D.4 a) for an illustration). In other words, noise is essential for sustaining stop-and-go dynamics, unlike a subcritical hydrodynamic instability where noise triggers a transition to another flow branch. This highlights the unique nature of the SATG behaviour. The destabilisation of uniform flow at a finite σ cannot be attributed to poorly damped perturbations near linear instability, as seen in the SID model (Treiber and Kesting, 2017) because no such instability exists in SATG. Nor can it be attributed to the self-reinforcement of multiplicative noise, as discussed in (Ngoduy, 2021), since SATG only incorporates an additive white noise. Lastly, in the absence of a bifurcation in the deterministic limit, the noise-induced SATG instability does not lend itself to continuation methods (Orosz et al., 2005), nor to a perturbative stochastic stability analysis (Gardiner, 2021).

4.4 STABILITY SWITCH: ANALOGY WITH THE KAPITZA PENDULUM

We hypothesize that the (finite) noise operates like an external driving force whose continuous actions destabilize the (deterministic) fixed point. To bypass issues arising from the stochasticity of the noise, we draw an analogy with the Kapitza pendulum, a rigid pendulum subjected to vertical oscillatory vibrations which may stabilize its ‘inverted’ equilibrium position, here amalgamated to the state with stop-and-go waves. Thus, we split the noise into a controlled part (periodic driving) and an uncontrolled part $d\tilde{W}$ (the residual stochastic perturbation). More precisely, considering a realization of the noise (σdW_n) over a large time interval T , we extract the Fourier components $\{C_n(\omega)\}$, with $|C_n(\omega)|^2 \rightarrow \sigma^2$ in the limit of large T (Wiener-Khinchine relation). We arbitrarily isolate one of these modes and inject it into the deterministic Eq. (4.5) as a (controlled) oscillatory driving $\{C \cos(\omega t + \varphi_n)\}$, with $C > 0$ ²;

²The idea of introducing oscillations also pops up when one writes an amplitude equation in hydrodynamics (Morozov and van Saarloos, 2007), but in that case it helps probe the nonlinear growth of arbitrary perturbations.

the residual signal is handled as perturbative white noise $\tilde{\sigma} d\tilde{W}_n$. Thus, Eq. (4.5) turns into

$$dv_n(t) = F_n(t) dt + C \cos(\omega t + \varphi_n) dt + \tilde{\sigma} d\tilde{W}_n(t), \quad (4.7)$$

where $F_n(t) =: F(\Delta x_n(t), v_n(t), v_{n+1}(t))$.

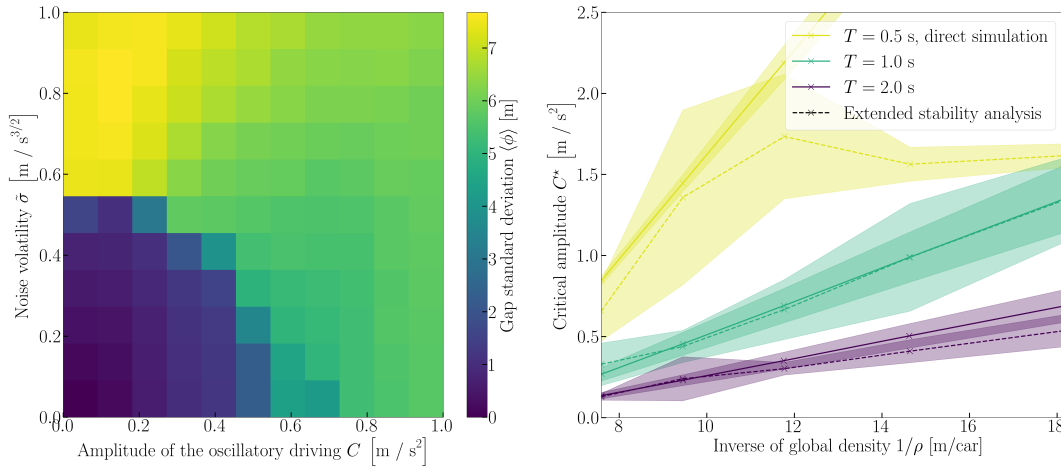


FIGURE 4.9: Left panel: Stability diagram in which the action of the noise is heuristically split into a controlled oscillatory driving (of amplitude C , here asynchronous) and a random residual $\tilde{\sigma}$. Colour overlay: standard deviation of the gaps. In the stop-and-go waves region, two colours are discernible: yellow indicates cars that come to a complete stop for some time, while green represents cars that oscillate back and forth with a net forward movement. For detailed trajectories, please refer to Fig. D.4 b,c in App. D.1. Right panel: Variation of the stability threshold C^* with the car density, computed with agent-based simulations of Eq. (4.7) at a driving frequency of $2\pi 0.05$ rad/s or derived from an extended stability analysis (see main text).

Numerical simulations presented in Fig. 4.9, left panel, confirm that the oscillatory driving facilitates the emergence of stop-and-go waves: the larger the driving amplitude C , the smaller the perturbative noise required to trigger the instability. For strong enough driving $C \geq C^*$, the system becomes even unstable under vanishing noise. The threshold C^* depends on the chosen mode: while it is high (but finite) for synchronous oscillations $\varphi_n = \varphi$ (which maintain the gaps between successive cars), for asynchronous driving C^* reaches a value $C^* \approx 0.5$ (in the conditions of Fig. 4.7) that is very close to the noise instability threshold σ^* of the initial system, with a weak frequency dependence up to $\omega \simeq 2\pi 0.05$. This comparison elucidates the mechanism whereby the instability unfurls in the pristine SATG model: finite noise continuously excites nonlinearities in the deterministic response function F , as does the oscillatory driving, which brings the system to the brink of stability. Accordingly, in contrast with other mechanisms, the instability does not result from *local* properties of F around the state of uniform flow but from *nonlocal* ones.

The oscillatory driving opens the door to a more quantitative rationalization. At zero frequency $\omega = 0$, the driving is equivalent to acceleration offsets $b_n = C \cos(\varphi_n)$ applied to each car. As we show in App. D.3, it turns out that these heterogeneous offsets can make the system linearly unstable for a range of offsets b_n , and implicit analytical expressions can be derived for the growth rates. Let $\nu(\{b_n\})$ be the largest nontrivial growth rate (i.e., the real part of the eigenvalue). If the oscillatory frequency ω is small but nonzero, the driving can be treated as quasi-stationary. Under this approximation, at each time t' , the peak perturbation grows exponentially as $\exp(\nu_{t'} t)$, where $\nu_{t'} = \nu(C \cos(\omega t' + \varphi_n))$.

To go further, since the peak growth mode mostly spans the system size, we overlook the fact that it

may change with time t' , so that the effective growth rate over a period is

$$\begin{aligned}\nu_{\text{eff}}(C) &= \langle \nu_{t'} \rangle_{t'} \\ &\simeq \langle \nu(\{C \cos(x_n)\}) \rangle_x,\end{aligned}\tag{4.8}$$

where the angular brackets denote averages over uniform distributions of t' or $\{x_n\}$. In the last approximation, we replaced the actual phases $\omega t' + \varphi_n$ in the cosines with random ones x_n drawn from a uniform distribution over $]-\pi, \pi]$. This yields decent results, as observed numerically, especially after averaging over the random phases φ_n . The thresholds C^* at which $\nu_{\text{eff}}(C)$ becomes positive are determined by numerically computing the eigenvalues of Eq. (4.8). Remarkably, Fig. 4.9, right panel, proves that C^* , predicted by extended linear stability analysis, accurately reproduce the instability thresholds measured in direct simulations of Eq. (4.7) under oscillatory driving, even at finite frequencies (deviations are observed for small T at low density), and match the noise threshold σ^* at which the genuine SATG model undergoes a transition (Fig. 4.7).

4.5 BACK TO THE FIRST-ORDER LIQUID-GAS TRANSITION ALLUDED TO IN PREVIOUS WORKS

All this bolsters the relevance of the Kapitza analogy. However, despite the singularity of this destabilizing mechanism, from a broader perspective, we find that the general picture of a first-order phase transition established for traffic instabilities (Nagatani, 2002) originating from other processes, e.g., reaction delay (Nagatani, 1998b) or cellular automata simulated in continuous space (Jost and Nagel, 2005), still holds. To clarify the picture, let us map the transition to traffic oscillations onto a liquid-gas transition by likening the noise volatility σ to the temperature and the inverse headway (local density ρ) between cars to the density, i.e., the order parameter. In Fig. 4.10, we plot the ‘phase’ diagram of the disorder parameter ϕ as a function of σ and ρ . A line of discontinuous transitions is clearly observed at intermediate densities for all temperatures’ σ above a critical value, while the homogeneous state remains stable at both low (gas-like) and high (liquid-like) densities. Amusingly, in this liquid-gas analogy, the gas phase begins to boil’ as the temperature σ increases—a counterintuitive phenomenon reminiscent of a paradox found in simple crowd models (Helbing et al., 2000b).

Finally, we use this image to shed a different light on the hysteresis that we have observed. As one varies σ at fixed density, similarly to what is shown in Fig. 4.7, one moves along a vertical line in Fig. 4.10: the system does not transit between two pure states, but from a pure phase into a co-existence region. Starting from the uniform regime, the system may avoid tipping into instability until it hits the spinodal. In contrast, starting from the co-existence region, stop-and-go waves may persist up to a different neutral stability line, the binodal. Interestingly, unlike in a liquid-gas mixture underneath the binodal line, there is no *static* coexistence between the jammed and freely flowing phases in a steady state; instead, the jam moves continuously. Similar transitions into circulating states have recently been identified in other systems with non-reciprocal interactions (Fruchart et al., 2021); this is easily rationalized by considering that each car is tied by a spring to the predecessor, but not to its follower, so that the in and out currents cannot compensate at an interface.

Exploring variations in σ at a fixed density, as shown in Fig. 4.7, involved examining the transition along a vertical line: the system did not shift between two pure states but from a pure phase into a coexistence region. Unlike a liquid-gas mixture, the jammed phase in this region does not coexist with the free phase in a steady state but moves continuously. Similar transitions into circulating states have recently been identified in other systems with non-reciprocal interactions (Fruchart et al., 2021); this can be easily rationalised by considering that each car is connected by a spring to a leader but not to its

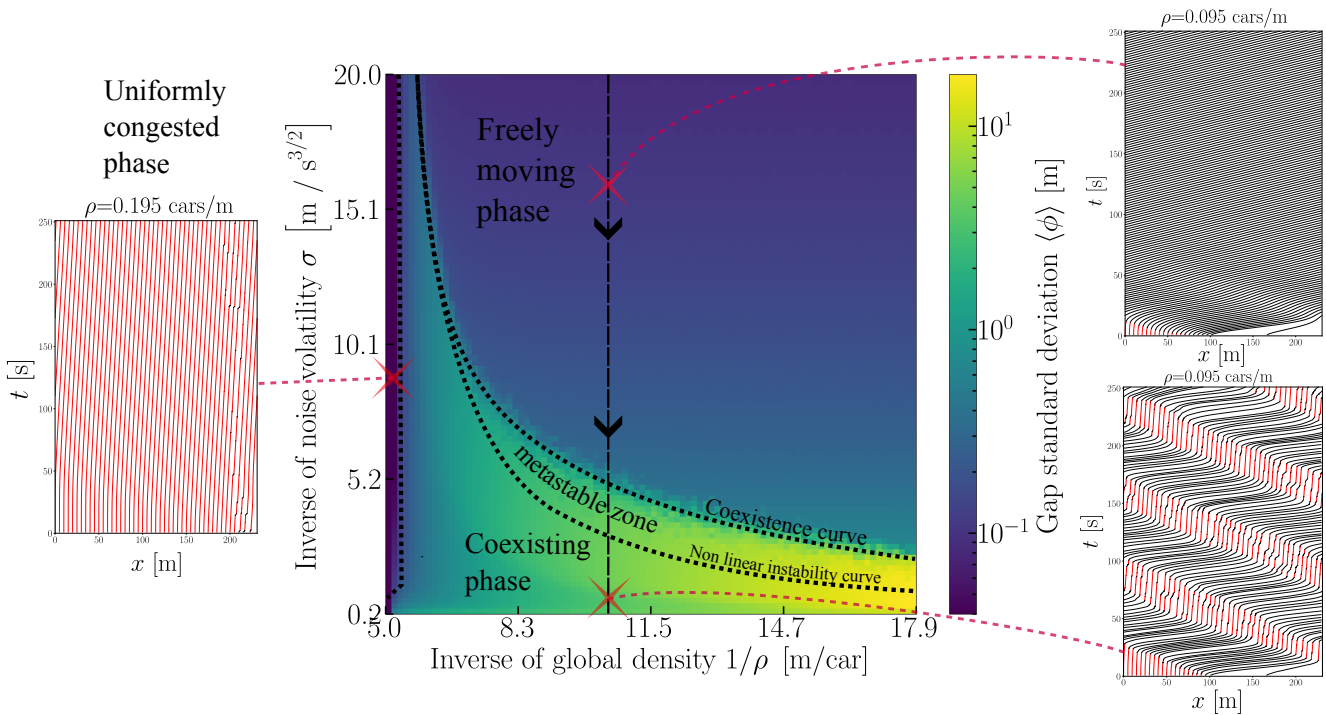


FIGURE 4.10: Heatmap of $\langle \phi \rangle$ representing the gap standard deviation averaged over time as a function of the inverse of σ (acting as a temperature) and the inverse of the global density ρ (acting as a volume) for an initially jammed configuration. One can distinguish the coexistence curve, below which two phases coexist in equilibrium: the **freely moving phase** and the **uniformly congested phase**. In this coexistence region, stop-and-go waves are observed. The nonlinear instability curve delineates the region where, starting from a freely moving phase, the system evolves toward the coexistence phase through the growth of a nonlinear instability. This contrasts with the linear instability curves typically found in phase diagrams, where even a slight disturbance can push the system onto the coexistence region. In this scenario, some noise is still required to activate the nonlinear modes of the system. The side panels show kymographs of trajectories in different regions of parameter space.

successor, preventing compensation in and out currents at an interface.

CONCLUSION

In summary, our study demonstrates that the **Stochastic Adaptive Time Gap (SATG)** model, while exhibiting unconditional linear stability, experiences a sudden transition into a state characterised by stop-and-go waves, closely mirroring the experimental observations of [Tadaki et al. \(2013\)](#), as noise intensity increases. This transition is driven by a mechanism akin to destabilising a pendulum under vibrations, where finite noise excites non-linear modes. This process is reminiscent of barrier crossing observed in liquid-gas phase transitions, albeit with an unsteady coexistence phase. Although the model we examined has unique features, the overall picture of this transition parallels that found in deterministic car-following models with a reaction time (where reaction time acts like temperature) as described by [Nagatani and Nakanishi \(1998\)](#), and even more so in the continuous version of the Nagel-Schreckenberg cellular automaton ([Krauß et al., 1996](#); [Jost and Nagel, 2005](#)), where cars may brake randomly at each time step. Ultimately, our findings reinforce the analogy with classical physical systems and suggest that macroscopic observations alone are insufficient to distinguish between different physical origins of stop-and-go waves. We are planning virtual reality experiments to manipulate these physical factors individually to pinpoint the key elements responsible for stop-and-go waves.

CONCLUSION

With the surge in mass events, crowd dynamics have become an increasingly important subject of study. Understanding how groups move and evolve in space, particularly at medium and high densities, is crucial for organising such events.

The first section of this PhD dissertation presented one of the first field datasets on dense crowds. This dataset includes pedestrian trajectories and meta-information collected during the 2022 Festival of Lights in Lyon as part of the Franco-German MADRAS project. It includes up to 7000 trajectories, GPS data, and contact information. In addition, some rare events have been identified, providing an in-depth description of pedestrian dynamics in complex, real-life scenarios. The collection of contact data has provided insight into the maximum number of contacts a pedestrian might experience during a journey, which can reach around a hundred. The traditional social force model does not accurately represent this. By coupling this data with **GPS** data, I discovered that these contacts are mainly associated with behavioural changes, starting movements, and stopping. Additionally, I observed that the densities recorded could not be replicated using simple disks with diameters equivalent to shoulder width.

Then, I developed a theoretical framework for modelling crowd dynamics that integrates a decision-making component, where pedestrians regularly adjust their desired speed, and a mechanical layer that confronts these decisions with the surrounding physical reality. Most existing models fail to faithfully reproduce mechanical interactions, often relying on idealised interaction forces and simplified circular shapes. Drawing inspiration from the scientific literature on grain dynamics, I integrate more realistic mechanical interactions into the Newtonian equations, using damped springs that are tangential and normal to the contact surfaces. I also use anthropometric data to represent the human contour as faithfully as possible, in two dimensions, rather than using simple disks. This allows me to create a synthetic crowd that incorporates individual heterogeneity.

Regarding decision-making, pedestrians strive to choose a desired speed while adhering to various metabolic, physical, and psychological constraints, largely supported by empirical data. These constraints include:

- ★ A **destination constraint** which considers the goal of reaching a specific location.
- ★ **Biomechanical limits** related to the muscular and articular capacities of pedestrians.
- ★ A cost associated with the **misalignment between the body and the desired direction of movement**.
- ★ A desire to preserve one's **social bubble**, a zone that individuals wish to keep free of any intrusion, whether from obstacles or neighbouring pedestrians.
- ★ An intention to **avoid collisions** or interpenetration of comfort spaces during movement based on the estimation of time to collision.

This comfort space is modelled by a scalar field of discomfort whose contours are not simply circular. The model is implemented in C++ and tested in various scenarios. After validation in simple situations involving pairs of pedestrians or a pedestrian near a wall, I successfully compare the model's predictions with experiments involving the propagation of a push through a row of people, evacuations, and weaving movements between walls and pedestrians. The model successfully reproduces the 'faster is slower' effect during an evacuation. Nevertheless, at this stage, many improvements could be made. During the Festival of Lights, there were not only pedestrians but also strollers, wheelchairs, people with canes, and suitcases—a wide variety of pedestrian shapes that are not accounted for in the model. The decision-making aspect could also be significantly improved, as it does not seem to replicate the observation of the spontaneous emergence of counter-clockwise vortex motion in assemblies of pedestrians within an enclosure (Echeverría-Huarte et al., 2022). Decision-making elements, particularly related to how the brain acquires and processes information, may be the source of this bias. These elements have yet to be incorporated.

Finally, I investigate collective phenomena that occur not only in crowds but also in vehicular traffic, specifically stop-and-go waves resulting from the growth of dynamical instabilities. To better understand these phenomena, I simulate a car-following model that relies on maintaining a constant time gap with the following vehicle. Although the deterministic version of the model is unconditionally stable, introducing noise intriguingly leads to the emergence of stop-and-go waves. I explain this observation using an analogy with the Kapitza pendulum, which develops a new stationary state under strong vibrations. Specifically, discontinuities in a suitably defined order parameter appear when noise or density exceeds a finite threshold, echoing a liquid-gas transition. This noise may stem from inaccuracies in drivers' and pedestrians' observations, difficulties in brain information processing, or unaccounted interactions. I could further explore and attempt to compare the behaviour of cars with that of pedestrians. Despite a noticeable difference in inertia, the nature of their interactions seems fundamentally different. Virtual reality experiments, where it would be possible to impose a reaction time artificially, could help determine whether the reaction time typically used to describe stop-and-go waves in pedestrians and cars is the cause.

My research on crowd dynamics highlights the importance of integrating decision-making processes with mechanical interactions to deepen our understanding of complex collective behaviours, notably in crowded environments.

APPENDIX A

STATE OF THE ART

A.1 BIO-MECHANICAL COST (BACK ON PAGES 36, 37 AND 37)

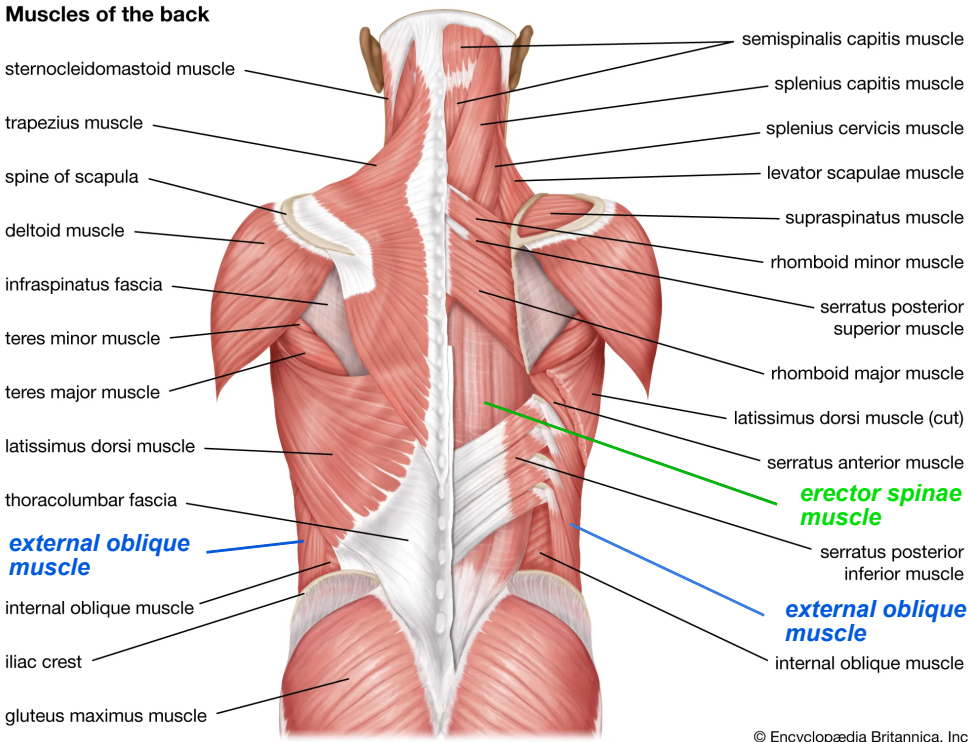


FIGURE A.1: Illustration of the back muscles, adapted from T. Editors of Encyclopædia Britannica (2023).

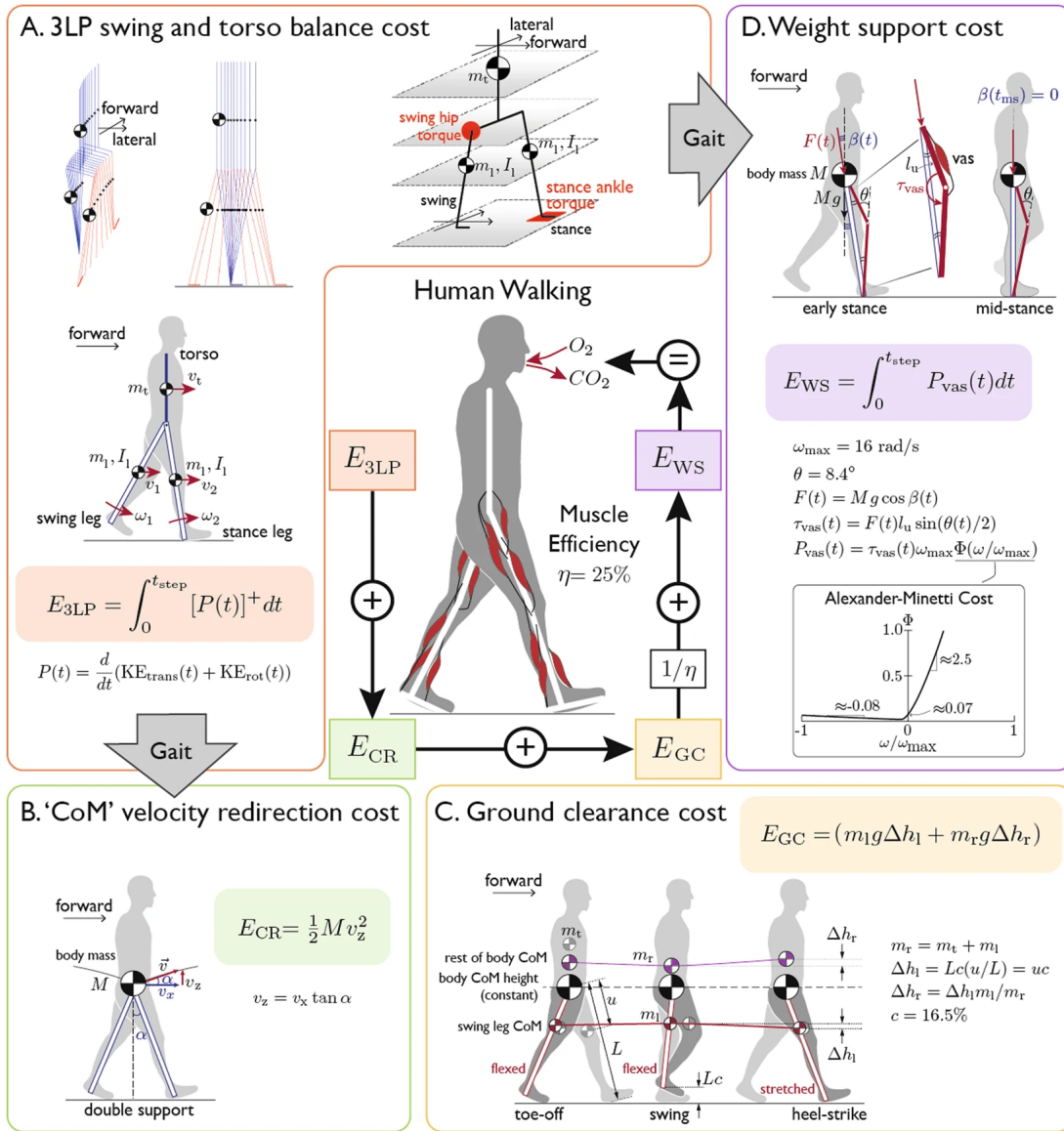


FIGURE A.2: The metabolic cost model for human walking includes four primary energy components according to Faraji et al. (2018): (A) The **Three Linear Pendulum** model incorporates **swing cost** and **torso balance cost**. This model represents the legs and trunk as three linear pendulums. The costs are calculated as the integral of the positive component of the kinetic energy change rate; (B) **Center of Mass velocity redirection cost**, accounting for vertical work to change the centre of mass velocity during step transitions; (C) **Ground Clearance cost**, representing the potential energy needed to lift the leg; and (D) **Weight Support cost**, which involves the metabolic cost of muscles supporting the body during stance. Each component is derived from specific mechanical and physiological parameters to estimate the overall metabolic cost.

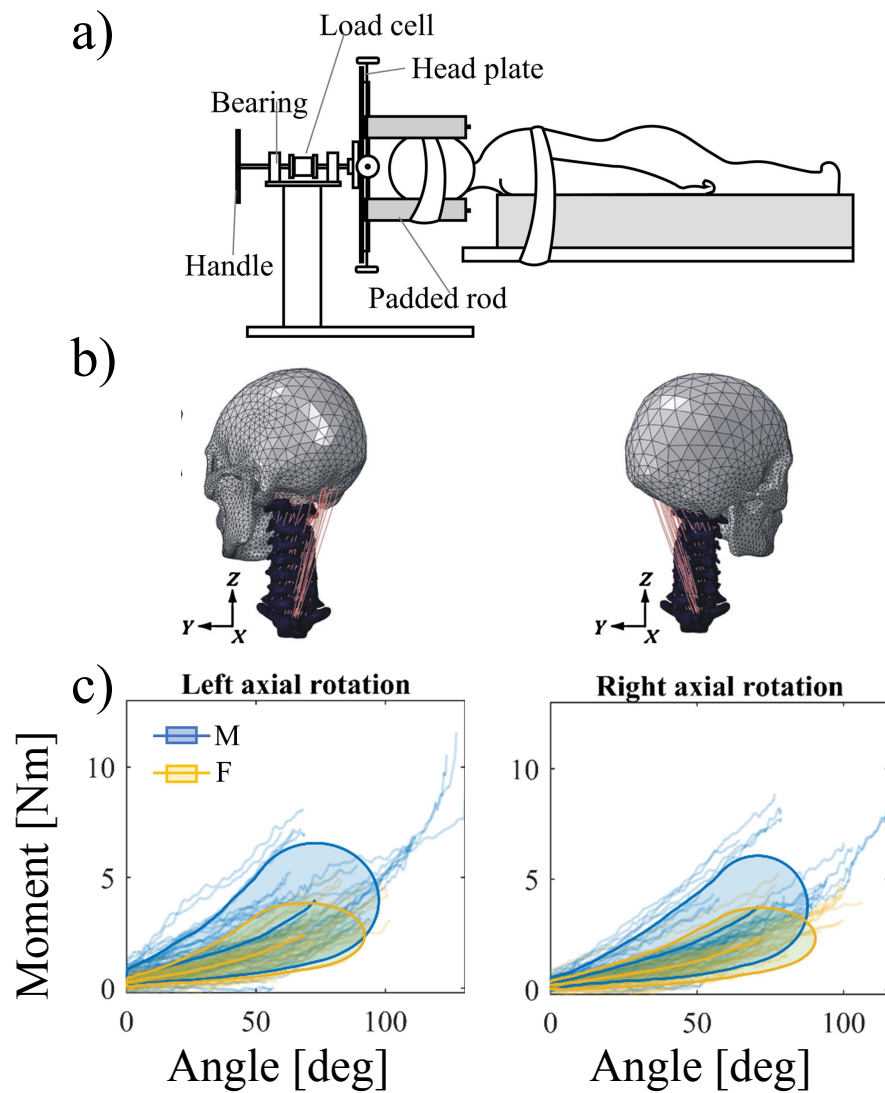


FIGURE A.3: **a)** Scheme of the experimental setup reproduced from [Liu et al. \(2024\)](#). With adjustable padded rods and straps, participants lay prone positions with their heads secured. The head was attached to a head plate, which was axis-symmetric about a shaft supported by two low-friction bearings. The participant's head was rotated at a controlled speed using a handle attached to the apparatus. As the head was rotated, the load cell recorded the applied moment (torque) throughout the motion. **b)** Representation of the maximum head range of motion, adapted from [Wang et al. \(2014\)](#). **c)** Moment-angle plot data is displayed, with men represented in blue and women in orange ([Liu et al., 2024](#)).

A.2 SELF-ORGANISATION PHENOMENA IN CROWD DYNAMICS (BACK ON PAGE 17)

No.	Place	Self-organisation phenomenon	Category	Generation condition	Effect
1	Corridor	Lane formation	Crowd	Higher relative velocity in opposite directions	Minimising the frequency and strength of avoidance manoeuvres
2		Stripe formation	Crowd	Crossing flow in only two directions	Minimising obstructing interactions and maximising the average pedestrian speeds
3		Freezing-by-heating	Evacuation	Driving term and dissipative friction, while the sliding friction is not required	Decreasing the whole speed
4	Bottleneck	Oscillatory flow	Crowd	Simple pedestrian interactions	Reducing frictional effects and delays
5		Zipper effect	Evacuation	Provisions have been made for a decrease in personal space at the bottleneck, either via a decrease in the repulsive forces interpreted by each individual or a decrease in the personal space of each individual at an angle in front of the individual	–
6		Intermittent flow	Evacuation	Pedestrian's impatience and increase of the driving term or desired speed	Emerging of pedestrian queue before the bottleneck
7		Faster=slower	Evacuation	Pedestrian's impatience and increase of the driving term or desired speed	Slowing down crowd motion or evacuation
8		Panic	Evacuation	Pedestrian's impatience and increase of the driving term or desired speed	So high pressures that pedestrians are crushed or falling and trampled
9	Open space	Stop-and-go waves	Evacuation	Relaxation time to adjust the velocity or acceleration	Emerging of the congestion
10		Turbulence	Evacuation	Local force-based interaction	Random and unintended displacements into all possible directions
11	Other	Herding	Evacuation	The influence of the destination and route choices of others on the individual is accounted	Pure herding implies that the crowd is eventually moving into the same and probably congested direction, so that available emergency exits are not efficiently used

FIGURE A.4: **One classification of self-organisation phenomena proposed by Chen et al. (2018).** Self-organization is a fascinating phenomenon that emerges from non-linear interactions among numerous objects or subjects without external intervention. This process often results in various spatial-temporal patterns of motion, as described by Camazine et al. (2020).

A.3 ASSESSMENT OF A PEDESTRIAN MODEL (BACK ON PAGE 28)

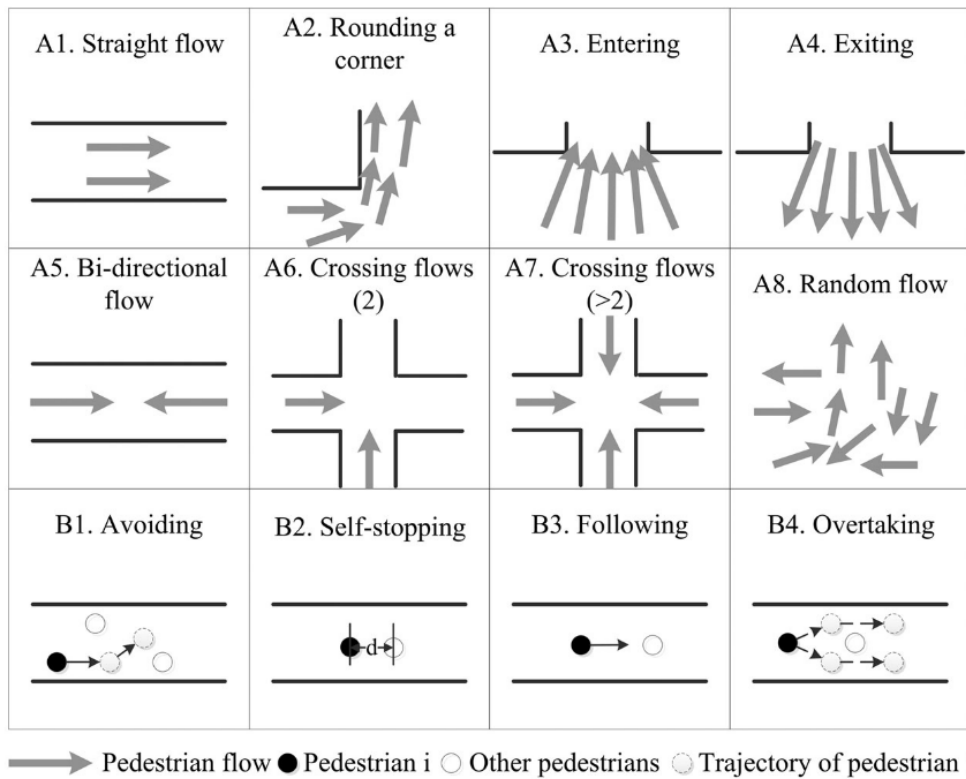


FIGURE A.5: Crowd and individual motion base cases. The schemes are taken from [Chen et al. \(2018\)](#).

APPENDIX B

A MULTI-SCALE FIELD STUDY AT THE FESTIVAL OF LIGHTS IN LYON

B.1 EXTRINSIC AND INTRINSIC CALIBRATION (BACK ON PAGE 49)

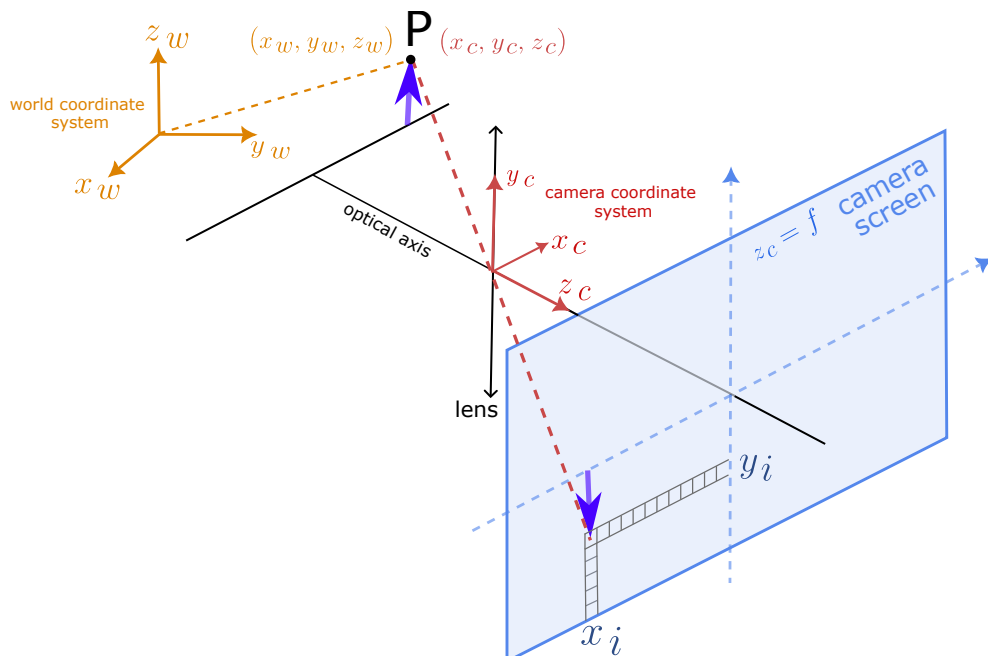


FIGURE B.1: Schematic representation of a point P considered at infinity expressed both in the world coordinate system in yellow (x_w, y_w, z_w) , in the camera coordinate system in red (x_c, y_c, z_c) , in the screen camera coordinate system in blue (x_i, y_i) , and in pixels (u_i, v_i) .

Camera calibration parameters are typically categorized into extrinsic and intrinsic parameters (Heikkila and Silvén, 1997). Extrinsic parameters are essential for converting the world coordinate frame, denoted as $\mathcal{B}_c = (\mathbf{x}_w, \mathbf{y}_w, \mathbf{z}_w)$, into a camera-centered coordinate frame, represented as $\mathcal{B}_w = (\mathbf{x}_c, \mathbf{y}_c, \mathbf{z}_c)$.

This transformation using a pinhole camera model is depicted in Fig. B.1. The pinhole camera model relies on the intercept theorem (*théorème de Thalès* in French), where each point in the world space is projected via a straight line through the projection centre onto the image plane. For now, we will limit our focus to the pinhole camera model; more advanced models that account for camera distortion will be explored later App. B.2. To express an arbitrary world point P located at (x_c, y_c, z_c) in camera

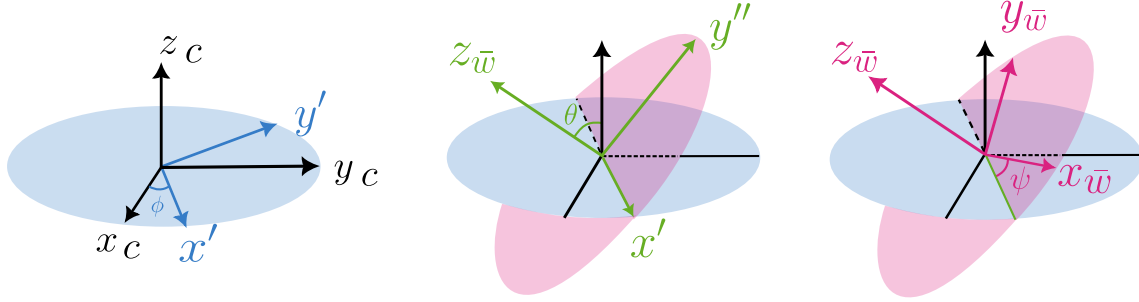


FIGURE B.2: Schematic representation of the three rotations of the Euler-transformation in the x -convention representing a change of basis from \mathcal{B}_c to \mathcal{B}_w .

coordinates, a change of basis is required. To define the orientation and position of one orthonormal basis \mathcal{B}_c with respect to another \mathcal{B}_w , three rotation angles and translation parameters are required. We will use Euler angles in the x -convention: ϕ , θ , and ψ . These angles define a sequence of three elementary rotations as illustrated in Fig. B.2:

First Rotation of angle ϕ around the z -axis transforms the coordinate frame (x_c, y_c, z_c) into (x', y', z_c) .

Second Rotation of angle θ around the x' -axis changes the coordinate frame to (x', y'', z_w) .

Third Rotation of angle ψ around the z_w -axis converts the coordinate frame to (x_w, y_w, z_w) .

Therefore, the transformation of the point P can be performed using the following matrix equation:

$$\begin{aligned} \begin{bmatrix} x_w \\ y_w \\ z_w \end{bmatrix}_{\mathcal{B}_w} &= \begin{bmatrix} \cos(\psi) & \sin(\psi) & 0 \\ -\sin(\psi) & \cos(\psi) & 0 \\ 0 & 0 & 1 \end{bmatrix} \begin{bmatrix} 1 & 0 & 0 \\ 0 & \cos(\theta) & \sin(\theta) \\ 0 & -\sin(\theta) & \cos(\theta) \end{bmatrix} \begin{bmatrix} \cos(\phi) & \sin(\phi) & 0 \\ -\sin(\phi) & \cos(\phi) & 0 \\ 0 & 0 & 1 \end{bmatrix} \begin{bmatrix} x_c \\ y_c \\ z_c \end{bmatrix}_{\mathcal{B}_c} + \begin{bmatrix} t_x \\ t_y \\ t_z \end{bmatrix}_{\mathcal{B}_w} \\ &= \underbrace{\begin{bmatrix} m_{11} & m_{12} & m_{13} \\ m_{21} & m_{22} & m_{23} \\ m_{31} & m_{32} & m_{33} \end{bmatrix}}_{\text{rotation}} \underbrace{\begin{bmatrix} x_c \\ y_c \\ z_c \end{bmatrix}_{\mathcal{B}_c}}_{\text{translation}} + \begin{bmatrix} t_x \\ t_y \\ t_z \end{bmatrix}_{\mathcal{B}_w} \end{aligned} \quad (\text{B.1})$$

where

Coef.	Expression	Coef.	Expression
m_{11}	$\cos(\psi) \cos(\phi) - \sin(\psi) \cos(\theta) \sin(\phi)$	m_{12}	$\cos(\psi) \sin(\phi) + \sin(\psi) \cos(\theta) \cos(\phi)$
m_{13}	$\sin(\psi) \sin(\theta)$	m_{21}	$-\sin(\psi) \cos(\phi) - \cos(\psi) \cos(\theta) \sin(\phi)$
m_{22}	$\cos(\psi) \cos(\theta) \cos(\phi) - \sin(\psi) \sin(\phi)$	m_{23}	$\cos(\psi) \sin(\theta)$
m_{31}	$\sin(\theta) \sin(\phi)$	m_{32}	$-\sin(\theta) \cos(\phi)$
m_{33}	$\cos(\theta)$		

The intrinsic camera parameters typically include the effective focal length f and the image centre, also known as the principal point, denoted as (O_x, O_y) . In computer vision literature, placing the image coordinate system's origin at the image array's upper left corner is standard. The image coordinates are measured in pixels, necessitating coefficients m_x and m_y to convert metric units into pixels. These coefficients are typically found in the camera's data sheets, but with our method, you can independently determine them and verify their accuracy. Using the pinhole camera model, also known as the intercept theorem, the projection of a point (x_c, y_c, z_c) onto the image plane results in the point (x_i, y_i) . This

projection can be expressed as follows:

$$\begin{cases} \frac{y_i}{y_c} = \frac{f}{z_c} \\ \frac{x_i}{x_c} = \frac{f}{z_c} \end{cases} \quad (\text{B.2})$$

The transformation from the projection (x_i, y_i) to the image coordinates in pixels (u_i, v_i) involves scaling and translating the coordinates based on the intrinsic camera parameters. The transformation can be expressed as follows:

$$\begin{cases} u_i = m_x x_i + O_x \\ v_i = m_y y_i + O_y \end{cases} \quad (\text{B.3})$$

In the following discussion, we will incorporate O_x and O_y into u_i and v_i , respectively, without loss of generality. This simplification is justified because a reference point has already been selected when determining the pixel locations of various heads in the calibration image (see Fig. B.3). In our extrinsic



FIGURE B.3: Image used for calibration, reconstructed from excerpts of a *LargeView* camera footage at *Place des Terreaux* in 2023. I positioned myself at each node of the square lattice marked on the ground, where each square has a side length of 640 cm.

calibration process, we use a height of 1.80 meters for z_w , representing the student's height in Fig. B.3. This assumption allows us to simplify the problem by treating all individuals as having the same height. Consequently, we can quickly solve our system of two equations with two variables, enabling us to express x_w and y_w as functions of the pixel coordinates u_i and v_i . To proceed with the solution, we express z_c in terms of z_w and the other relevant parameters as follows:

$$z_c = \frac{z_w - t_z}{\sin(\theta) \sin(\phi) \frac{x_i}{f} - \sin(\theta) \cos(\phi) \frac{y_i}{f} + \cos(\theta)} \quad (\text{B.4})$$

We reinject the expression for z_c into that for x_w and y_w to get:

$$\begin{aligned}
x_w &= \left[\frac{\cos(\psi) \cos(\phi) u_i}{\cos(\theta) f m_x} + \frac{\cos(\psi) \sin(\phi) v_i}{\cos(\theta) f m_y} - \frac{\sin(\psi) \cos(\theta) \sin(\phi) u_i}{\cos(\theta) f m_x} + \frac{\sin(\psi) \sin(\theta)}{\cos(\theta)} \right. \\
&\quad \left. + \frac{\sin(\psi) \cos(\theta) \cos(\phi) v_i}{\cos(\theta) f m_y} \right] \frac{z_w - t_z}{1 + \sin(\theta) \left[\frac{\sin(\phi) u_i}{\cos(\theta) f m_x} - \frac{\cos(\phi) v_i}{\cos(\theta) f m_y} \right]} + t_x \\
y_w &= \left[-\frac{\sin(\psi) \cos(\phi) u_i}{\cos(\theta) f m_x} - \frac{\sin(\psi) \sin(\phi) v_i}{\cos(\theta) f} - \frac{\cos(\psi) \cos(\theta) \sin(\phi) u_i}{\cos(\theta) f m_x} + \frac{\cos(\psi) \sin(\theta)}{\cos(\theta)} \right. \\
&\quad \left. + \frac{\cos(\psi) \cos(\theta) \cos(\phi) v_i}{\cos(\theta) f m_y} \right] \frac{z_w - t_z}{1 + \sin(\theta) \left[\frac{\sin(\phi) u_i}{\cos(\theta) f m_x} - \frac{\cos(\phi) v_i}{\cos(\theta) f m_y} \right]} + t_y
\end{aligned} \tag{B.5}$$

Without loss of generality, let's make a change of variables to simplify the expressions:

$$t_z \rightarrow z_w - t_z \doteq \bar{t}_z \tag{B.6}$$

$$m_x \rightarrow \frac{1}{f m_x \cos(\theta)} \doteq F_x \tag{B.7}$$

$$m_y \rightarrow \frac{1}{f m_y \cos(\theta)} \doteq F_y \tag{B.8}$$

Furthermore, let's denote for the sake of clarity:

$$\gamma \doteq \frac{\bar{t}_z}{1 + \sin(\theta) [\sin(\phi) F_x u_i - \cos(\phi) F_y v_i]} \tag{B.9}$$

We finally get:

$$\begin{aligned}
x_w &= t_x + \tan(\theta) \sin(\psi) \gamma \\
&\quad + \cos(\psi) [\cos(\phi) F_x u_i + \sin(\phi) F_y v_i] \gamma \\
&\quad + \cos(\theta) \sin(\psi) [\cos(\phi) F_y v_i - \sin(\phi) F_x u_i] \gamma \\
y_w &= t_y + \tan(\theta) \cos(\psi) \gamma \\
&\quad - \sin(\psi) [\cos(\phi) F_x u_i + \sin(\phi) F_y v_i] \gamma \\
&\quad + \cos(\theta) \cos(\psi) [\cos(\phi) F_y v_i - \sin(\phi) F_x u_i] \gamma
\end{aligned} \tag{B.10}$$

The relationship between world coordinates and pixel coordinates is therefore determined. As illustrated in Fig. B.3, we have the values for $x_i, y_i, x_w, y_w,$ and z_w for numerous points. The 8 unknown parameters that need to be estimated are $\theta, \psi, \phi, t_x, t_y, \bar{t}_z$ and F_x, F_y . These parameters can be determined by minimising the least squares of the residuals between the world coordinates and the pixels coordinates. This method provides a physical understanding of the process but is computationally inefficient and heavily dependent on the initial parameter guess. A challenge remains: the *LargeView* camera was replaced after I performed its extrinsic calibration but before the recording of the Festival of Lights. Consequently, it is necessary to map the coordinates from Fig. B.3 to those in the *LargeView* camera footage (see Fig. 2.3). Mathematically, this requires transitioning from one projective space (a vector space with a vanishing point) to another. This transition can be accomplished using a homography, denoted as H_1 . Consider a set of corresponding points, x_{i1}^1, y_{i1}^1 from one image, and x_{i2}^1, y_{i2}^1 from the other, as illustrated in Fig. B.4. The homography relates these points, represented in homogeneous coordinates¹, as follows:

$$\begin{bmatrix} x_{i1} \\ y_{i1} \\ 1 \end{bmatrix} = H \begin{bmatrix} x_{i2} \\ y_{i2} \\ 1 \end{bmatrix} = \begin{bmatrix} h_{00} & h_{01} & h_{02} \\ h_{10} & h_{11} & h_{12} \\ h_{20} & h_{21} & h_{22} \end{bmatrix} \begin{bmatrix} x_{i2} \\ y_{i2} \\ 1 \end{bmatrix} \tag{B.11}$$

The homography matrix is a 3×3 matrix with 8 **Degree of Freedom (DoF)**. Each **DoF** can be intuitively interpreted, as detailed in Tab. B.1. These include a rotation parameter, two translation parameters,

¹The passage to homogeneous coordinates allow translation to be expressed as a linear operation involving matrices.

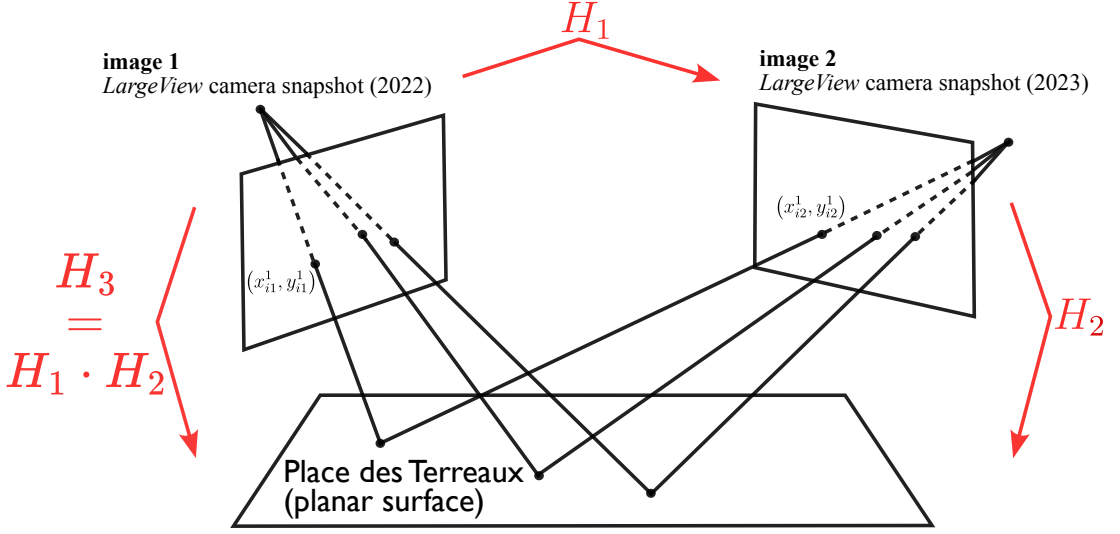


FIGURE B.4: A planar surface is observed from two distinct camera positions. To convert image 1 (see Fig. 2.3), to image 2, used for calibration (see Fig. B.3), apply the homography H_1 . Next, transform image 2 to align with a planar surface at *Place des Terreaux*, which includes the heads of pedestrians standing at a height of 1.8 meters, by applying the homography H_2 . The scheme is adapted from [Christiano Gava \(2011\)](#).

a scale factor, and four shear factors. For computational stability ([Heikkilä and Silvén, 1997](#)), the coefficients are typically normalised such that $h_{00}^2 + h_{01}^2 + h_{02}^2 + h_{10}^2 + h_{11}^2 + h_{12}^2 + h_{20}^2 + h_{21}^2 + h_{22}^2 = 1$. This approach is equivalent to the previous method (see Eq. (B.1) and Eq. (B.3)), where the goal is to map a projective plane of the real world, with the vanishing point at infinity, to the projective space of a camera. This can be framed as a linear algebra problem, solvable using linear algebra techniques. Specifically, determining the homography matrix parameters can be approached as an eigenvalue problem of a specific matrix. To solve for the height unknowns, we require at least four additional equations derived from different sets of corresponding points: x_{i1}^1, y_{i1}^1 (first point in image 1), x_{i2}^1, y_{i2}^1 (corresponding point in image 2), x_{i1}^2, y_{i1}^2 (second point in image 1), x_{i2}^2, y_{i2}^2 (corresponding point in image 2), and so on. Let's organise the full set of remaining equations into:

$$PH = \begin{bmatrix} -x_{i1}^1 & -y_{i1}^1 & -1 & 0 & 0 & 0 & x_{i1}^1 x_{i2}^1 & y_{i1}^1 x_{i2}^1 & x_{i2}^1 \\ 0 & 0 & 0 & -x_{i1}^1 & -y_{i1}^1 & -1 & x_{i1}^1 y_{i2}^1 & y_{i1}^1 y_{i2}^1 & y_{i2}^1 \\ -x_{i1}^2 & -y_{i1}^2 & -1 & 0 & 0 & 0 & x_{i1}^2 x_{i2}^2 & y_{i1}^2 x_{i2}^2 & x_{i2}^2 \\ 0 & 0 & 0 & -x_{i1}^2 & -y_{i1}^2 & -1 & x_{i1}^2 y_{i2}^2 & y_{i1}^2 y_{i2}^2 & y_{i2}^2 \\ -x_{i1}^3 & -y_{i1}^3 & -1 & 0 & 0 & 0 & x_{i1}^3 x_{i2}^3 & y_{i1}^3 x_{i2}^3 & x_{i2}^3 \\ 0 & 0 & 0 & -x_{i1}^3 & -y_{i1}^3 & -1 & x_{i1}^3 y_{i2}^3 & y_{i1}^3 y_{i2}^3 & y_{i2}^3 \\ -x_{i1}^4 & -y_{i1}^4 & -1 & 0 & 0 & 0 & x_{i1}^4 x_{i2}^4 & y_{i1}^4 x_{i2}^4 & x_{i2}^4 \\ 0 & 0 & 0 & -x_{i1}^4 & -y_{i1}^4 & -1 & x_{i1}^4 y_{i2}^4 & y_{i1}^4 y_{i2}^4 & y_{i2}^4 \end{bmatrix} \begin{bmatrix} h_{00} \\ h_{01} \\ h_{02} \\ h_{10} \\ h_{11} \\ h_{12} \\ h_{20} \\ h_{21} \\ h_{22} \end{bmatrix} = \begin{bmatrix} 0 \\ 0 \\ 0 \\ 0 \\ 0 \\ 0 \\ 0 \\ 0 \\ 0 \end{bmatrix} \quad (\text{B.12})$$

where P is not a square matrix and $\|H\|_2^2 = 1$, where $\|\cdot\|_2$ denotes the euclidean vector norm. We can rewrite the expression from Eq. (B.12) as $\|PH\|_M^2 = 0$, where $\|\cdot\|_M$ is the standard matrix norm ($\|A\|_M^2 = A^T A$ with A a square matrix).

This allows us to reformulate the problem as finding H^* such that:

$$H^* = \underset{H: \|H\|_2^2=1}{\operatorname{argmin}} \|PH\|_M^2 \quad (\text{B.13})$$

We want to find H that minimises $H^T P^T P H$ such that $H^T H = 1$. To achieve this, we define a loss

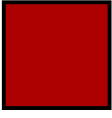
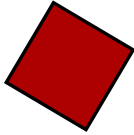

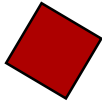

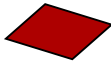

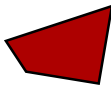
A Square	Transforms Into	Transformation Matrix	Transformation Properties
		$\begin{bmatrix} \cos(\theta) & -\sin(\theta) & t_x \\ \sin(\theta) & \cos(\theta) & t_y \\ 0 & 0 & 1 \end{bmatrix}$	<ul style="list-style-type: none"> • 3 Degree of Freedom (DoF) • Parameters: Translation (t_x, t_y), rotation angle θ • Conservation of shape and area
Euclidean			
		$\begin{bmatrix} s \cos(\theta) & -s \sin(\theta) & t_x \\ s \sin(\theta) & s \cos(\theta) & t_y \\ 0 & 0 & 1 \end{bmatrix}$	<ul style="list-style-type: none"> • 4 DoF • Parameters: All <i>Euclidean</i> parameters, scale factor s • Conservation of shape but not an area
Similarity			
		$\begin{bmatrix} a_{00} & a_{01} & t_x \\ a_{10} & a_{11} & t_y \\ 0 & 0 & 1 \end{bmatrix} =$ $\underbrace{\begin{bmatrix} 1 & \mu_x & 0 \\ \mu_y & 1 & 0 \\ 0 & 0 & 1 \end{bmatrix}}_{\text{Shear in xy-directions}} \underbrace{\begin{bmatrix} s \cos(\theta) & -s \sin(\theta) & t_x \\ s \sin(\theta) & s \cos(\theta) & t_y \\ 0 & 0 & 1 \end{bmatrix}}_{\text{Similarity transformation}}$	<ul style="list-style-type: none"> • 6 DoF • Parameters: All <i>Similarity</i> parameters, shear factor in xy-directions μ_x, μ_y • Preservation of parallelism but not angles or lengths
Affine			
		$\begin{bmatrix} h_{00} & h_{01} & h_{02} \\ h_{10} & h_{11} & h_{12} \\ h_{20} & h_{21} & h_{22} \end{bmatrix} =$ $\underbrace{\begin{bmatrix} 1 & 0 & 0 \\ 0 & 1 & 0 \\ \mu_{z1} & \mu_{z2} & 1 \end{bmatrix}}_{\text{Perspective projection}} \underbrace{\begin{bmatrix} a_{00} & a_{01} & t_x \\ a_{10} & a_{11} & t_y \\ 0 & 0 & 1 \end{bmatrix}}_{\text{Affine transformation}}$	<ul style="list-style-type: none"> • 8 DoF • Parameters: All <i>Affine</i> parameters, shear factors in z-direction μ_{z1}, μ_{z2} • No preservation of parallelism, angles, or lengths • The perspective projection allows <i>parallel lines</i> of the parallelogram to converge at a vanishing point.
Homography			

TABLE B.1: This 2D transformation hierarchy shows how each point (represented in homogeneous coordinates) of the initial square is transformed using the specified transformation matrix. This process can be represented as follows: $[x_{\text{new}} \ y_{\text{new}} \ 1]^T = \text{Transformation Matrix} \times [x_{\text{old}} \ y_{\text{old}} \ 1]^T$. Additionally, the physical properties associated with each type of transformation are described, and some decompositions of the transformation matrix into simpler transformations are proposed. Note that these decompositions are not unique. The table is adapted from Hood (2015).

function using the method of Lagrange multipliers:

$$\mathcal{L}(H, \lambda) = H^T P^T P H - \lambda(H^T H - 1) \quad (\text{B.14})$$

Taking derivatives of $\mathcal{L}(H, \lambda)$ w.r.t H we get:

$$\boxed{P^T P H = \lambda H} \quad (\text{B.15})$$

This is an eigenvalue problem. The solution to the problem is the eigenvector H with the smallest eigenvalue λ of a square matrix $P^T P$, which minimizes the loss function.

The initial method, which was based on a nonlinear estimation of calibration parameters, proved to be less efficient. Therefore, we performed the calibration using the estimation of two homographies, H_1 and H_2 , as illustrated in Fig. B.4. The first homography is used to align the coordinates from the images of the Festival of Lights Fig. 2.3 to the calibration image Fig. B.3. The second homography aligns the calibration image to the real-world coordinates. The estimation of these homographies is very fast and provides excellent results, as demonstrated in Fig. B.5, where the transformed points align with the

target points.

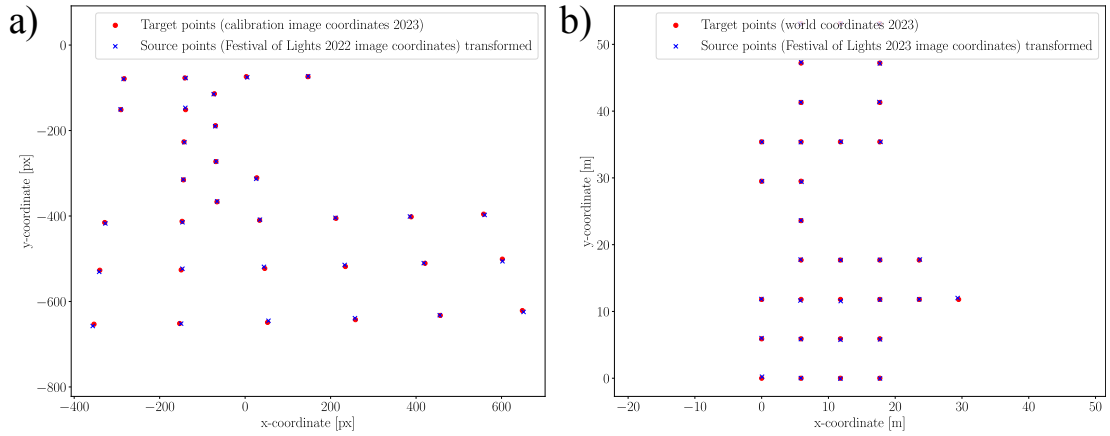


FIGURE B.5: Verification of the calibration procedure. **(a)** We transformed points from the Festival of Lights image coordinates (refer to Fig. 2.3) to the calibration image coordinates (refer to Fig. B.3) using the homography H_1 as shown in Fig. B.4. The lattice nodes on the floor were used to compute this homography. **(b)** Points were transformed from the calibration image coordinates to the world coordinates through the homography H_2 shown in Fig. B.4. The red dots indicate the target points, while the blue crosses represent the transformed points.

B.2 CAMERA DISTORTION IN INTRINSIC CALIBRATION (BACK ON PAGE 48)

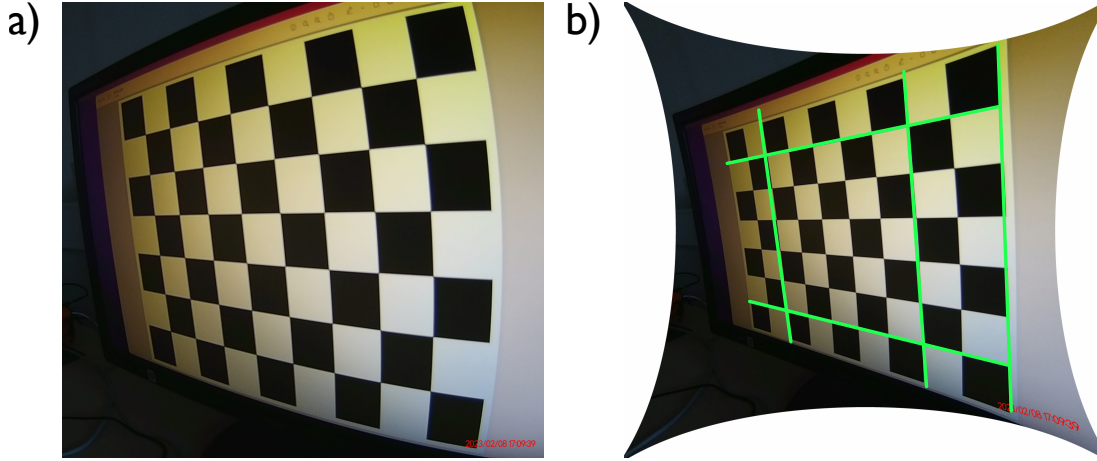


FIGURE B.6: **a)** Image of a planar chequerboard taken with our *SJCAM A10* cameras. The chequerboard is under perspective to notice the distortion variation when the camera-object distance changes. **b)** Image corrected for radial distortion. The curved lines of the chequerboard on the left now appear straight after the correction.

The pinhole camera model is a simplified representation of a camera's projection system, providing a fundamental mathematical framework to describe the relationship between world and image coordinates. While a useful toy, the pinhole camera model lacks the precision required for high-accuracy applications, necessitating more comprehensive camera models. Some advanced models enhance the pinhole approach by incorporating corrections for systematic distortions in image coordinates, which are common due to imperfections in most cameras. Typical issues include internal misalignment within the camera assembly, non-orthogonal alignment of the **CCD** sensing array with the lens's optical axis, and the effects of a thick lens. For example, fish-eye cameras with broad fields of view introduce significant geometric nonlinear distortion, as shown in Fig. B.6. Distortion correction aims to convert the distorted view of wide-angle cameras into a pinhole perspective view. However, this *undistortion* process can result in images with many vacant pixels, which can be addressed using interpolation methods. Optical distortions are generally categorised into two types: **chromatic** and **geometric**. Chromatic aberrations occur when different wavelengths of light, present in white light, fail to converge at a single focal point. This results in colour errors, as illustrated in Fig. B.7. Since chromatic aberration is not a significant issue for tracking pedestrians either on *LargeView* camera footage or in *SJCAM* footage, I will not delve further into this topic. Geometric aberrations, caused essentially by lens curvature and misalignment of the screen concerning the lens, make straight lines appear curved or wavy in images. The two principal forms of geometric distortion considered here are radial and decentering (tangential) distortion. The standard model for the radial and decentering distortion is a mapping U from the distorted image coordinates (x_d, y_d) to the undistorted image coordinates (x_u, y_u) such that:

$$\begin{aligned}
 x_u &= x_d \\
 &+ \underbrace{\overline{x_d} (\kappa_1 r_d^2 + \kappa_2 r_d^4 + \kappa_3 r_d^6 + \dots)}_{\text{radial}} \\
 &+ \underbrace{[p_2 (r_d^2 + 2\overline{y_d}^2) + 2p_1 \overline{x_d} \overline{y_d}] [1 + p_3 r_d^2 + \dots]}_{\text{tangential}} \\
 y_u &= y_d \\
 &+ \underbrace{\overline{y_d} (\kappa_1 r_d^2 + \kappa_2 r_d^4 + \kappa_3 r_d^6 + \dots)}_{\text{radial}} \\
 &+ \underbrace{[p_2 (r_d^2 + 2\overline{y_d}^2) + 2p_1 \overline{x_d} \overline{y_d}] [1 + p_3 r_d^2 + \dots]}_{\text{tangential}}
 \end{aligned} \tag{B.16}$$

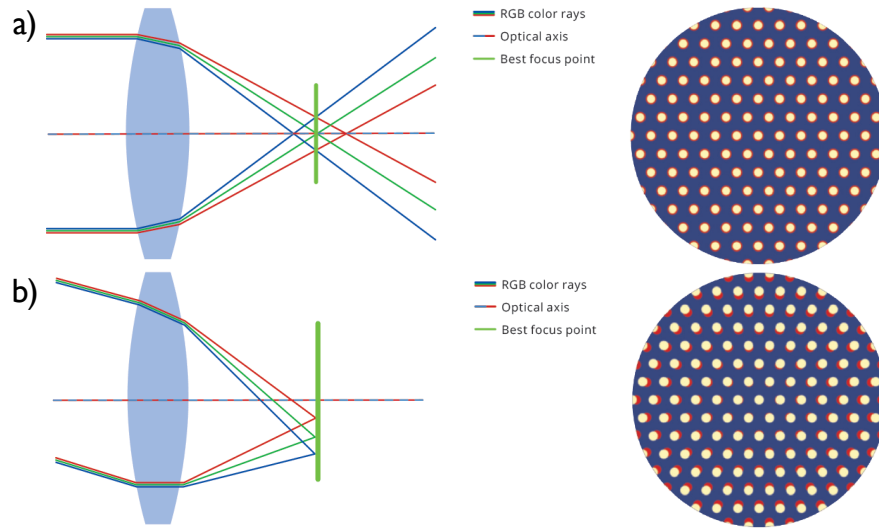


FIGURE B.7: Chromatic aberration can be of two types: longitudinal **a**) and lateral **b**), depending on the direction of incoming parallel rays. On the right side, a set of offset disks allows light to pass through, which is then gathered and focused onto a screen to create an image. Chromatic aberrations cause the iridescent look on the disks. The figure is adapted from [Sedazzari \(2015\)](#).

where $\overline{x}_d = x_d - O_x$, $\overline{y}_d = y_d - O_y$, $r_d^2 = \overline{x}_d^2 + \overline{y}_d^2$, $\kappa_1, \kappa_2, \kappa_3, \dots$ are the coefficients of radial distortion, p_1, p_2, p_3, \dots are the coefficients of the decentering distortion and r_d is the radius of an image point from the distortion centre (O_x, O_y) . For an illustration of the effect of radial and tangential

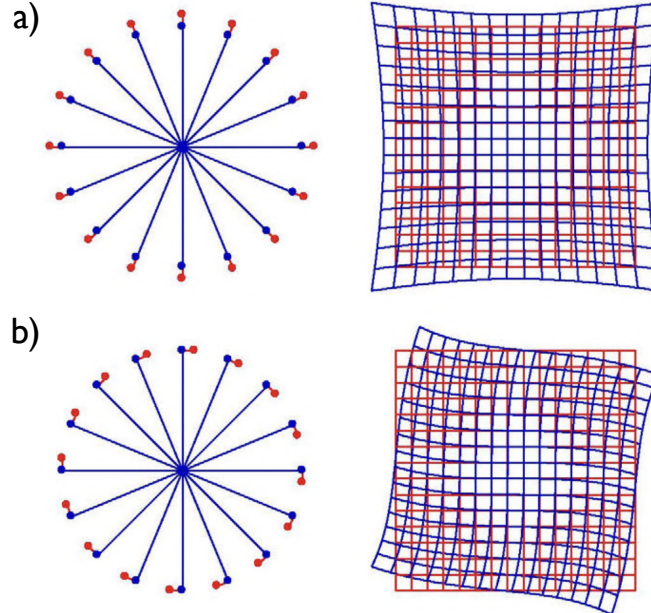


FIGURE B.8: The rotationally invariant cubic distortion function, denoted as U , acts on both a circle and a grid. This function includes coefficients κ_j and p_j , with j ranging up to 3 (see Eq. (B.16)). The distortions are categorised as follows: **a**) radial invariant distortion, **b**) tangential invariant distortion. The deviated pattern is shown in blue, while the undistorted pattern is depicted in red. The figure is adapted from [Ronda and Valdés \(2019\)](#).

distortion on a circle and a square lattice, please refer to Fig. B.8. Eq. (B.16) comes from one model of radial and tangential distortion commonly used and proposed by [Ahmed and Farag \(2005\)](#). Still, many other models exist depending on the computational efficiency, as shown by [Hughes et al. \(2008\)](#).

B.3 UNCERTAINTY DUE TO DIFFERENCES IN HEIGHT (BACK ON PAGE 49)

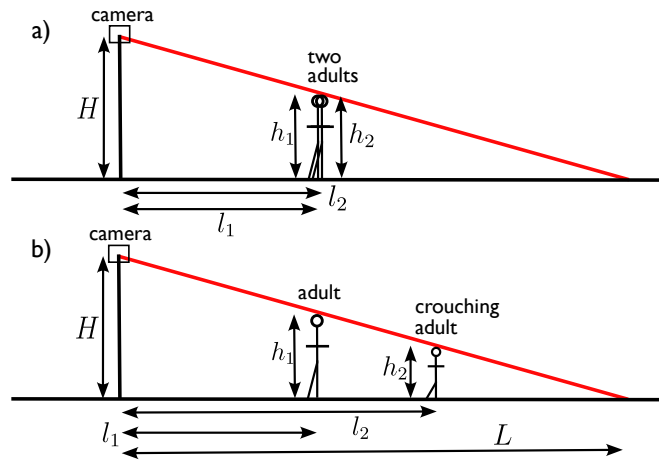


FIGURE B.9: Illustration of the error introduced by assuming uniform height in the calibration procedure. **(a) Scenario with two individuals of equal height:** In this situation, two individuals of the same height appear at the same pixel location in the camera image. **(b) Scenario with one individual crouching:** Here, one individual is crouching yet still appears at the same pixel location in the camera image. However, there is now a spatial separation from the other individual.

The Fig. B.9 illustrates the error introduced by assuming everyone has the same height. In scenario (a), two people of similar height ($h_1 \simeq h_2$) stand close together, like a couple, at nearly the same distance ($l_1 \simeq l_2$) from the camera structure. Their heads appear on almost the same pixel in the camera image. In scenario (b), one person crouches to a child's height at a different distance (l_2), yet their head still appears on the same pixel. In our case, L is of the order of the distance between the camera's base and the fountain in the *LargeView* camera footage of *Place des Terreaux*. We encounter a worst-case error, $\Delta\epsilon$, calculated as $\Delta\epsilon = l_2 - l_1 = \frac{L}{H}(h_2 - h_1)$. With $L \approx 70$ m, $H \approx 48$ m, and $h_2 - h_1 \approx 15$ cm (the height difference between people and a staff reference), the error is about $\Delta\epsilon \approx 22$ cm. For *TopView* cameras, the error is approximately $\Delta\epsilon \approx 8$ cm.

B.4 SPATIO-TEMPORAL DIAGRAM TO COMPUTE OUTPUT FLOW (BACK ON PAGE 53)

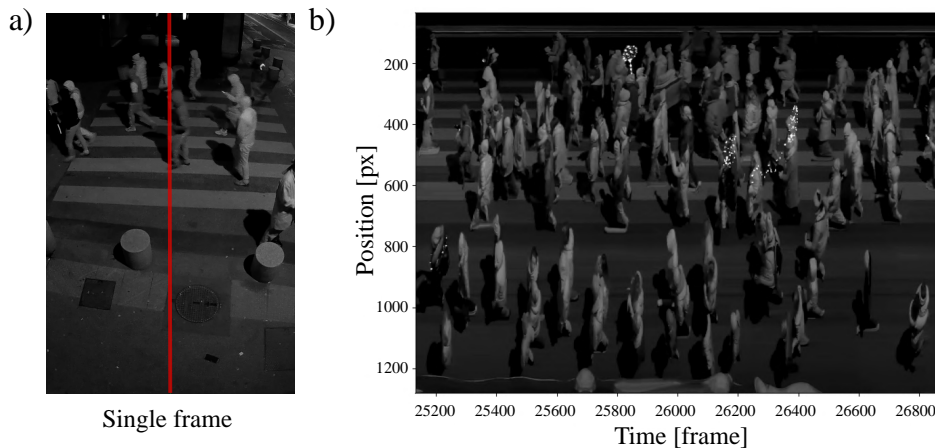


FIGURE B.10: **(a)** A snapshot from Camera 7, located at the exit street *Rue Paul Chenavard* of *Place des Terreaux*, is shown. The red line in the centre indicates the slice position used to construct the spatio-temporal graph **(b)** (pixel versus frame). Only a portion of the complete spatio-temporal graph is displayed.

B.5 REFERENCE FUNDAMENTAL DIAGRAMS (BACK ON PAGE 58)

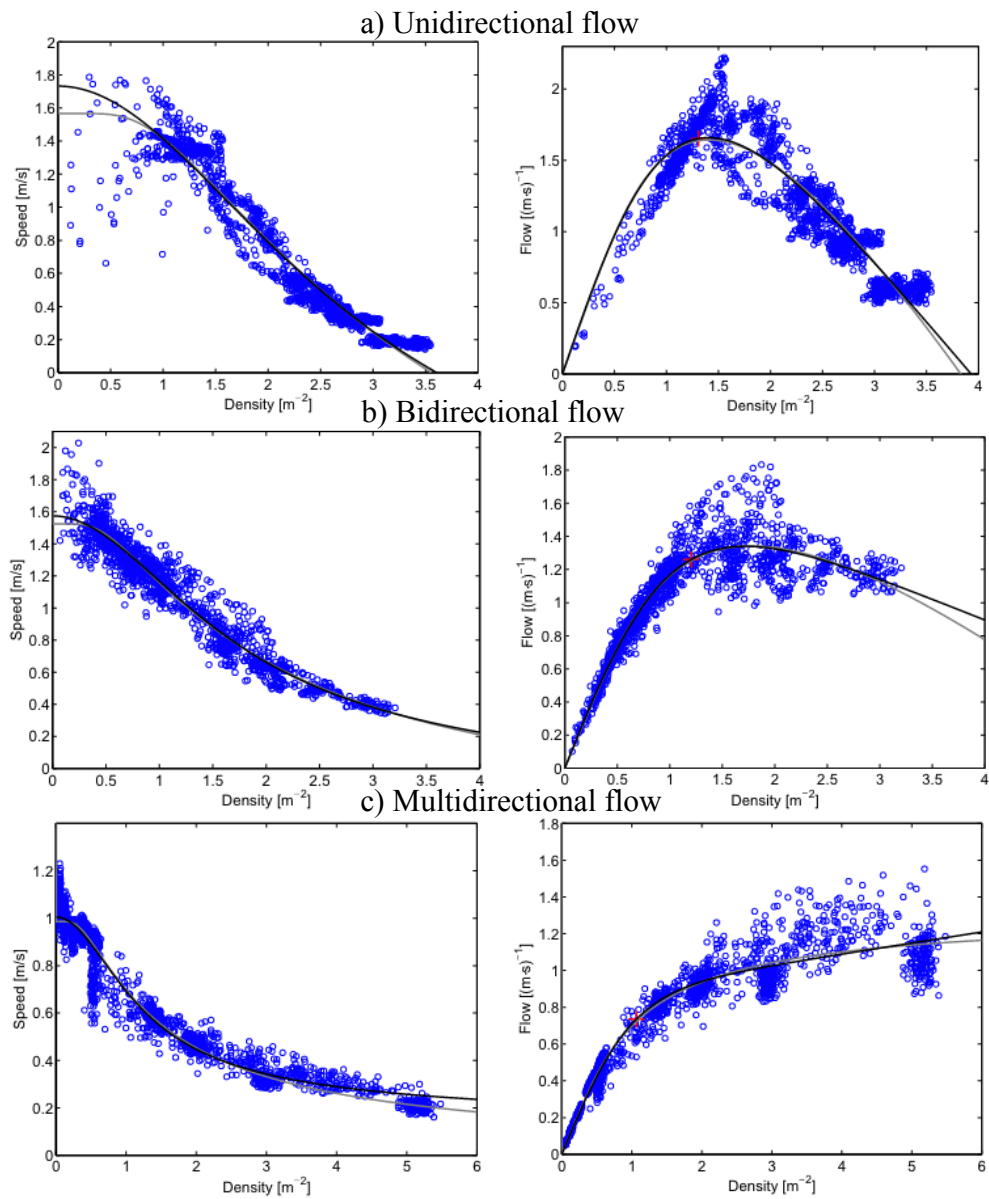


FIGURE B.11: Comparison of fundamental diagrams for various scenarios: unidirectional flow, bidirectional flow, and multi-directional flow (cross intersection). The Weidmann equation (Eq. (2.3.2)) is depicted in grey, while the black line is irrelevant here. The dots indicate data points sourced from the [Forschungszentrum Jülich \(2020\)](#). The figure is adapted from [Feliciani \(2017\)](#).

APPENDIX C

MODELLING 2D PEDESTRIAN DYNAMICS WITH NON-CIRCULAR COMFORT & PHYSICAL SPACES

C.1 MECHANICAL LAYER

C.1.1 COMPACT RANDOM PACKING OF PEDESTRIANS (BACK ON PAGES 69, 73)

Start by selecting several pedestrians from the modelled samples. Place their barycentres uniformly within the designated area. If two pedestrians overlap, they repel each other in a direction perpendicular to the surface of contact, moving a distance proportional to the overlap. If multiple pedestrians overlap, move one in the direction resulting from the sum of the unit vector orthogonal to each of its surface contacts. Repeat this process for all pedestrians.

Apply the same procedure if pedestrians overlap with obstacles, but note that obstacles remain fixed. If there is still available space, repeat the process with a more significant number of pedestrians. If, after several iterations, overlaps persist, this indicates that the number of pedestrians is too high. In such cases, repeat the process with fewer pedestrians until there are no overlaps.

C.1.2 HERTZIAN INTERACTION LAW (BACK ON PAGE 74)

The material is initially approximated as a network of atoms connected by springs. Similarly, the contact interface between two materials can be modelled as parallel linear springs along the interface and springs in series on either side of the interface to represent the contribution of both materials to the formation of the interface as shown in Fig. C.1 in case pedestrians are modelled as disks. Additionally, the materials are assumed to be isotropic, homogeneous, two-dimensional, and characterised by their elastic modulus (E), Poisson's ratio (ν), and shear modulus (G):

Young's modulus (E) describes a material's resistance to longitudinal deformation under tension

or compression. It quantifies the relationship between stress (force per unit area) and strain or deformation in the linear elastic region. It measures how much a material stretches or compresses when pulled or pushed.

Poisson's ratio (ν) characterises the Poisson effect, which is the tendency of a material to expand or contract perpendicular to the direction of applied force. It is defined as the negative ratio of transverse to axial strains. This ratio reveals how much a material's cross-section changes when stretched or compressed lengthwise.

Shear modulus (G) measures a material's resistance to shear deformation. The ratio of shear stress to shear strain quantifies how much a material deforms when subjected to opposing forces parallel to one of its surfaces. It describes a material's stiffness in response to shearing forces.

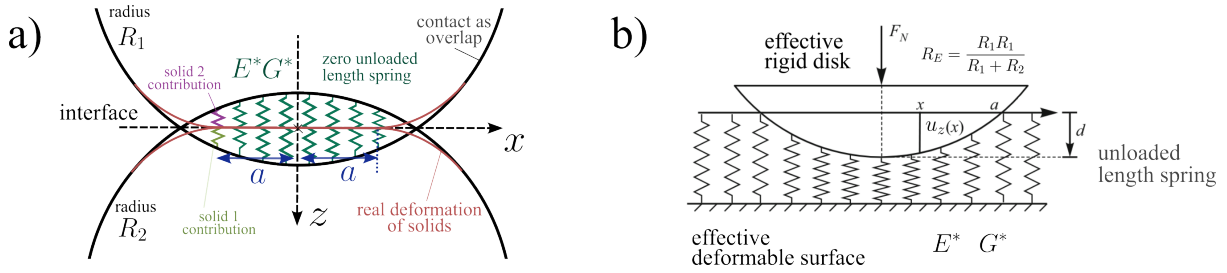


FIGURE C.1: **(a) Contact between two disks.** The red lines depict the deformation of the disks of radius R_1 and R_2 , while the black lines represent the undeformed state. The contact is modelled using parallel springs with zero unloaded length, each end of the spring connected to the respective disk profiles. Each spring can be divided into two springs in series, representing the contribution of each material, with the junction at the interface between the two disks. The contact size is denoted a . The springs' effective normal stiffness (E^*) and tangential stiffness (G^*) represent the combined material properties. **(b) Equivalent contact model.** The contact between the two disks described in (a) can be equivalently modelled as a contact between an undeformable disk with an effective or equivalent radius (R_e) and a deformable surface composed of springs with non-zero unloaded length. This equivalence is valid for small contact zones compared to the radius of the disks. The right-hand image provides a simpler visualisation of this concept and will be used for subsequent illustrations. To illustrate how equivalence may occur, we can draw an analogy with the two-body problem in physics. The solution typically involves decomposing the motion into two components: the movement of the system's centre of mass and the relative motion of the bodies with respect to this centre. Analogously, in contact mechanics, we focus on the relative motion between two body profiles in contact. The equivalence manifests also through the concept of reduced radius, which plays a role similar to that of reduced mass in the two-body problem. This approach simplifies the analysis by condensing the geometric properties of both bodies into a single parameter, much as the reduced mass encapsulates the inertial properties of two bodies into one effective mass. The schemes (a) and (b) are adapted from Popov and Heß (2015) and Wang and Zhu (2013b) respectively.

The stiffness of two springs in series is determined by the reciprocal sum of their reciprocals. Additionally, the stiffness of springs in parallel is the sum of their stiffnesses, which are the same here. Therefore, for a segment of springs with length Δx , the normal stiffness denoted Δk_z , and the tangential stiffness is given by¹:

$$\begin{aligned} \Delta k_z &= E^* \Delta x \text{ with } \frac{1}{E^*} = \frac{1 - \nu_1^2}{E_1} + \frac{1 - \nu_2^2}{E_2} \\ \Delta k_x &= G^* \Delta x \text{ with } \frac{1}{G^*} = \frac{2 - \nu_1}{4G_1} + \frac{2 - \nu_2}{4G_2} \end{aligned} \quad (\text{C.1})$$

Given these assumptions, each portion Δx of springs obeys the following Hooke's law:

$$\begin{aligned} \Delta F_N &= \Delta k_z u_z(x) \\ \Delta F_x &= \Delta k_x u_x(x) \end{aligned} \quad (\text{C.2})$$

where $u_z(x)$ denotes the spring elongation at position x . Furthermore, one can incorporate viscous

¹For the detailed relations between ν , E and G , refer to Young et al. (2002).

damping to model energy loss during impacts, which is particularly relevant for pedestrians. Indeed, when examining the relationship between strain and stress for pedestrians, as observed in Fig. 1.24, a hysteresis curve is present where the enclosed area is related to energy dissipation (the larger the area, the more energy is dissipated). Two primary models for viscoelastic behaviour are the Kelvin-Voigt model, which incorporates dashpots (with damping constant $\Delta\gamma$) in parallel with elastic springs as shown in Fig. C.2, and the Maxwell model, which places dashpots in series with elastic springs. More complex generalisations of these models have been proposed, as described by Popov and Heß (2015). During the Festival of Lights, the Kelvin-Voigt model would suggest that when pedestrians push against one another, they will not simply bounce apart like billiard balls. Instead, significant energy would be dissipated in the interaction.

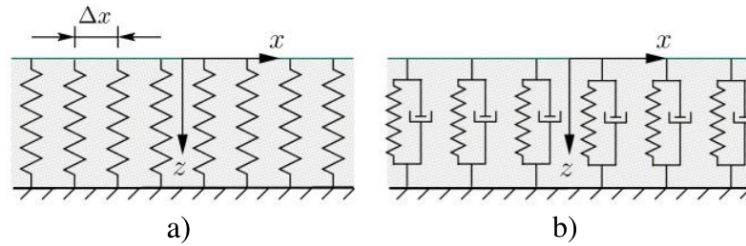


FIGURE C.2: One-dimensional model of different materials, adapted from Popov and Heß (2015): (a) elastic model, (b) viscoelastic model also known as Kelvin-Voigt model.

C.1.2.1 NORMAL FORCE

To derive the total normal force generated by a portion Δx of springs, let's consider the limiting case where the spring spacing becomes infinitesimally small, $\Delta x \rightarrow dx$. In this scenario, the sum over a 1D surface contact ranging from $-a$ to a turns into an integral:

$$F_N(a) = E^* \int_{-a}^a u_z(x) dx \quad (\text{C.3})$$

For analogous computations related to damping, refer to Popov and Heß (2015, Chap. 3). The displacement function, denoted $u_z(x)$, illustrated in Fig. C.1, is given by:

$$u_z(x) = \sqrt{R_e^2 - x^2} - \sqrt{R_e^2 - a^2} \quad (\text{C.4})$$

Here, $u_z(x)$ equals zero at the interface boundary and reaches its maximum at the mid-interface. Assuming $a \ll R_e$, we can use a Taylor expansion to approximate the integral, yielding:

$$F_N(a) \simeq \frac{E^*}{R_e} a^3 \quad (\text{C.5})$$

Given that the maximum indentation depth of the contact, denoted as h , equals $u_z(0)$, we can express a as a function of h :

$$a \simeq \sqrt{2R_e h} \quad (\text{C.6})$$

This leads to the following expression:

$$F_N \underset{h \geq 0}{\propto} E^* \sqrt{R_E} h^{\frac{3}{2}} \quad (\text{C.7})$$

However, Hertz approached the problem slightly differently (Popov et al., 2010). Indeed, he assumed a

semi-circular pressure distribution within the contact area as shown in orange colour in Fig. C.3. By integrating over the resulting circular contact surface between two spherical balls, we obtain:

$$F_N = 2\pi \int_0^a p_0 \sqrt{a^2 - r^2} r \, dr = p_0 \frac{2\pi}{3} a^3 \quad (\text{C.8})$$

leading to $F_N \propto h^{\frac{3}{2}}$, which is the same contact law as for the contact between two disks using a spring foundation as seen previously. Similarly, by integrating over the resulting rectangular contact surface between two cylinders with parallel axes, we derive:

$$F_N = L \int_{-a}^a p_0 \sqrt{a^2 - x^2} \, dx = p_0 \frac{\pi}{2} a^2 L \quad (\text{C.9})$$

leading to $F_N \propto h$. In this case, the normal force is directly proportional to the penetration depth. This approach to compute forces normal to surface contact simplifies the analysis of complex elastic systems. However, it may not fully capture all aspects of real thorax behaviour, especially in significant tangential interaction between thoraxes.

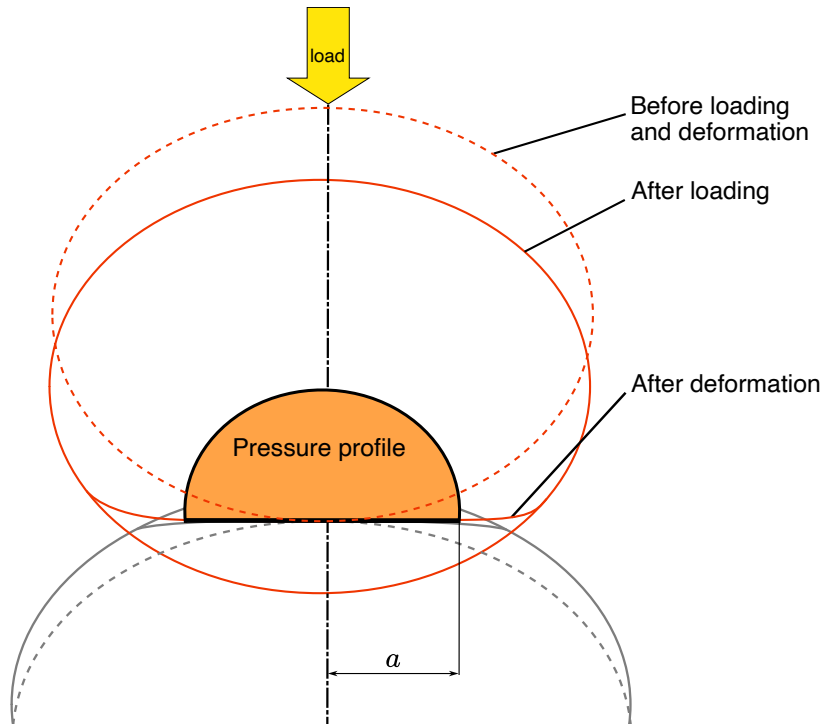


FIGURE C.3: Schematic representation of Hertzian contact between two elastic bodies under a normal load. The initial undeformed shapes are shown in dashed lines, while the deformed shapes are represented by solid curves. The contact size is denoted a . The half-circular pressure profile is depicted in orange. The figure is adapted from Wang and Zhu (2013a).

C.1.2.2 TANGENTIAL FORCE

Tangential contacts exhibit distinctive characteristics that set them apart from normal contacts. These contacts feature **localized slip** zones, where portions of the contact area experience relative movement. Additionally, tangential contacts demonstrate **memory effects**, with the tangential force retaining information about the contact's loading history. Unlike normal contacts, which can be described by a single parameter, such as indentation depth, tangential contacts require a comprehensive understanding

of the entire loading history. For simplicity, we will focus on contacts with a constant normal force F_N followed by an increasing moment that induces a tangential force F_x in the x-direction. Within this

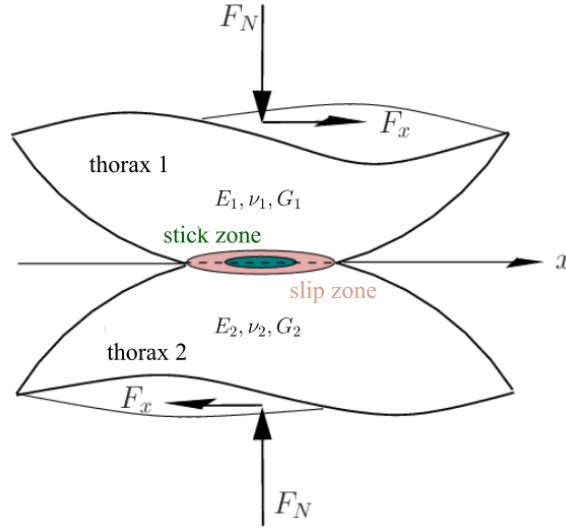


FIGURE C.4: Tangential contact between two spheres. The contact area consists of two regions: a central stick zone (shown in green), where there is no relative motion between the surfaces, and an outer slip zone (shown in pink), where the surfaces slide relative to each other. As the tangential force increases, the slip zone initially appears at the edge of the contact area. It grows inward, expanding the pink region. The stick zone (green) shrinks. Eventually, the entire contact area may enter the slip state if the tangential force is large enough. This same pattern of stick and slip zones would also occur for the tangential contact between two flat circular disks. The figure is adapted from [Popov et al. \(2019\)](#).

scenario, a slip zone extends from the contact boundary, spanning a length of $2a$. As this zone gradually expands inward, it simultaneously reduces the size of the inner stick zone, which is characterised by a length of $2c$. For visual clarity, Fig. C.4 illustrates this concept using the contact between two spheres, effectively demonstrating the interplay between the expanding slip zone and the contracting stick zone. Readers interested in delving deeper into complex loading histories will find valuable insights in the seminal work of [Mindlin and Deresiewicz \(1953\)](#). To analyse this scenario, we must first examine the relationship between tangential force t_x and normal stress n_x . In its simplest form, Coulomb's law of friction governs this relationship. Imagine two rough surfaces meeting. As you increase the pressure, pushing them together (the normal force) and sliding them against one another becomes progressively more challenging. Intuitively, the surfaces have microscopic bumps and irregularities. Pressing harder causes these bumps to interlock more tightly, increasing the number of contact points. Consequently, overcoming this interlocking to initiate sliding demands a proportionally larger force. This principle manifests in everyday experiences like opening a stubborn jar lid. By squeezing harder, you amplify the normal force, thus increasing friction and improving your grip for twisting. Mathematically, Coulomb's law takes the following form:

$$\begin{aligned} t_x(x) &< \mu n_x(x) \text{ for stick} \\ t_x(x) &= \mu n_x(x) \text{ for slip} \end{aligned} \tag{C.10}$$

where μ is the dynamic coefficient of friction. This law indicates that the surface remains stuck if the tangential stress is smaller than μ times the normal stress. Once slip initiates, the tangential stress remains constant, equals to $\mu n_x(x)$. Assuming for simplicity that all points within the stick domain undergo the same tangential displacement δ_x as illustrated in Fig. C.5, one can express the tangential

force per unit length as follows:

$$t_x(x) = \begin{cases} G^* \delta_x & \text{for } |x| \leq c \text{ (stick)} \\ \mu E^* u_z(x) & \text{for } c < |x| \leq a \text{ (slip)} \end{cases} \quad (\text{C.11})$$

This equation incorporates both the rigid-body translation of the stick area and the Coulomb friction

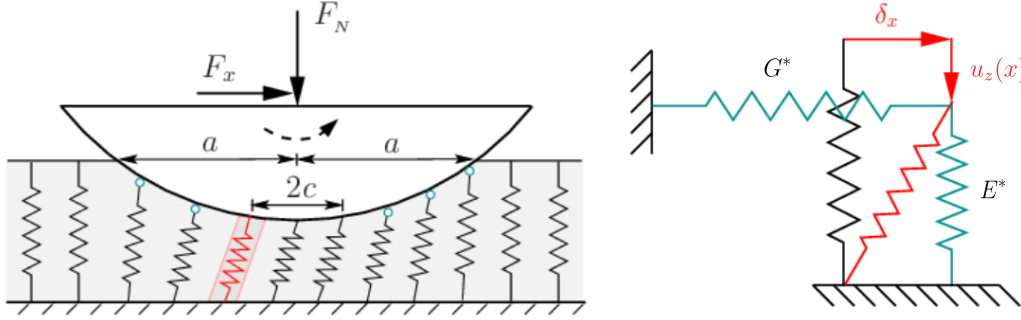


FIGURE C.5: Each spring in the model has independent normal and tangential stiffness. All springs experience the same elongation in the stick zone, denoted δ_x , while those in the slip zone - identifiable by their small green edge circles - demonstrate a variable elongation. This elongation is proportional to the applied normal force, allowing for dynamic adjustment based on the normal force's magnitude. The schemes are adapted from [Popov and Heiß \(2015\)](#).

in the sliding area. The stick length is determined by ensuring the continuity of the tangential line load at the transition between the stick and slip domains:

$$\lim_{x \rightarrow c^-} t_x(x) = \lim_{x \rightarrow c^+} t_x(x) = t_x(c) \implies \delta_x = \mu \frac{E^*}{G^*} u_z(c) \quad (\text{C.12})$$

Then, analogously to the normal contact problem, we can determine the tangential force by summing the tangential spring forces:

$$F_x(a) = \int_{-a}^a t_x(x) dx = \mu [F_N(a) - F_N(c)] \quad (\text{C.13})$$

Consequently, we can express the tangential force as:

$$F_x(a) \underset{a \rightarrow 0}{\simeq} \mu F_N(a) \left(1 - \frac{c^3}{a^3} \right) \quad (\text{C.14})$$

It is worth noting that c represents the sum of all relative displacements occurring during contact, which can be expressed as a function of the whole history of relative velocity:

$$c = \frac{1}{2} \int_0^{\text{contact duration}} \left| \mathbf{v}_{1,C}^{\parallel}(t) - \mathbf{v}_{2,C}^{\parallel}(t) \right| dt \quad (\text{C.15})$$

where C denotes the contact point, i.e., the point at the interface with abscissa $x = 0$ in Fig. C.1. The symbol \parallel denotes the tangential component. Note that the factor $1/2$ arises solely from the definition of c (see Fig. C.5).

C.1.3 MECHANICAL INTERACTIONS (BACK ON PAGES 75, 76)

Consider two pedestrians, i and j , made of disks $i1, i2, \dots$, and $j1, j2, \dots$. The centres of pedestrian i 's disks are denoted as s_{i1}, s_{i2}, \dots . The position of s_{i1} relative to the **Center of Mass (CoM)** is given by the vector $\Delta_{i \rightarrow i1}$, which points toward s_{i1} as illustrated in Fig. C.6.

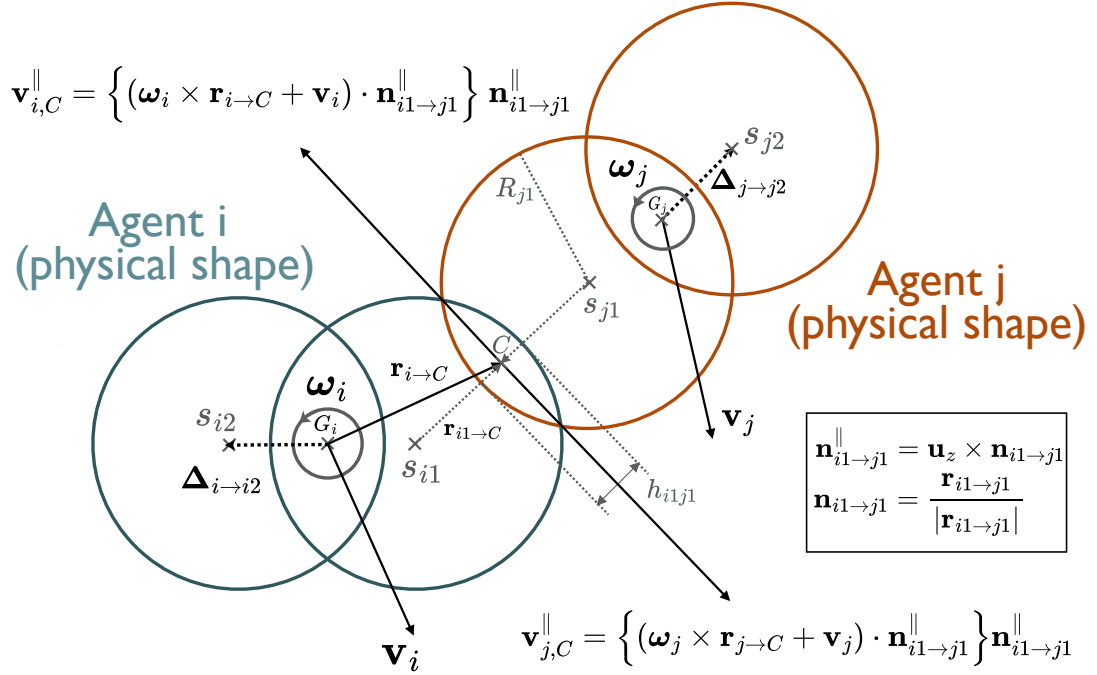


FIGURE C.6: Collision of two physical shapes, each composed of two disks.

Each pedestrian is also characterized by an orientation, defined by the direction normal to the line connecting the first and last disks. Specifically, for a pedestrian composed of n disks, the orientation is given by the vector $(\mathbf{r}_{in} - \mathbf{r}_{i1}) \times \mathbf{u}_z$ as illustrated in Fig. C.7. The CoM of pedestrian i moves with a velocity \mathbf{v}_i , and the pedestrian rotates with an angular velocity ω_i .

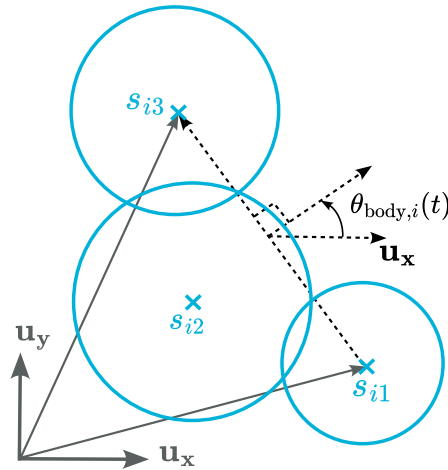


FIGURE C.7: Definition of a pedestrian's orientation

C.1.3.1 FORCES ACTING ON THE PEDESTRIAN CENTRE OF MASS

The motion of a pedestrian i can be broken down into two components: the motion of its **Center of Mass (CoM)** and rotational motion. The motion of the **CoM** is determined by applying the fundamental principle of dynamics at that point. Pedestrian i is subject to the following forces:

- ★ A self-propelling force that converts decisions into actions over a time period τ_{mech} , is given by $m_i \frac{\mathbf{v}_i^{\text{des}} - \mathbf{v}_i}{\tau_{\text{mech}}}$.

- ★ A force orthogonal to the contact surface and denoted as $\mathbf{F}_{\text{spring},j \rightarrow i}^{\perp \text{contact}}$, is proportional to the overlap between two disks. Additionally, there is a damping force that accounts for non-inelastic collisions, denoted as $\mathbf{F}_{\text{viscous},j \rightarrow i}^{\perp \text{contact}}$. When a contact occurs between the disks s_{i1} and s_{j1} , these two forces can be expressed as follows:

$$\begin{aligned} -\mathbf{F}_{\text{spring},j1 \rightarrow i1}^{\perp \text{contact}} &= \begin{cases} k_{\text{body}}^{\perp} h_{i1j1} \mathbf{n}_{i1j1}^{\perp} & \text{if } h_{i1j1} = R_{i1} + R_{j1} - |\mathbf{r}_{i1j1}| > 0 \text{ (i.e. an overlap occurs)} \\ \mathbf{0} & \text{otherwise} \end{cases} \\ -\mathbf{F}_{\text{viscous},j1 \rightarrow i1}^{\perp \text{contact}} &= \begin{cases} -\gamma_{\text{body}}^{\perp} \mathbf{v}_{ij}^{\perp} & \text{if } h_{i1j1} > 0 \text{ (i.e. an overlap occurs)} \\ \mathbf{0} & \text{otherwise} \end{cases} \end{aligned}$$

where $\mathbf{v}_{ij}^{\perp} = \mathbf{v}_{i,C}^{\perp} - \mathbf{v}_{j,C}^{\perp}$.

- ★ A force tangential to the contact surface, denoted as $\mathbf{F}_{j1 \rightarrow i1}^{\parallel \text{contact}}$, acts in the direction opposite to the slip. A straightforward way to model this force is through Coulomb interaction to describe the stick and slip mechanism, and a spring to more precisely describe the stick phase, as shown in Eq. (C.10). Since there is only one spring, the tangential contact law can be written more simply as follows:

$$\mathbf{F}_{\text{viscous},j1 \rightarrow i1}^{\parallel \text{contact}} = \begin{cases} \xi_{\text{body}}^{\text{static}} \delta s \frac{-\mathbf{v}_{ij}^{\parallel}}{|\mathbf{v}_{ij}^{\parallel}|} & \text{if } \xi_{\text{body}}^{\text{static}} \delta s < \mu_{\text{body}}^{\text{dyn}} |\mathbf{F}_{j1 \rightarrow i1}^{\perp \text{contact}}| \text{ (stick)} \\ \mu_{\text{body}}^{\text{dyn}} |\mathbf{F}_{j1 \rightarrow i1}^{\perp \text{contact}}| \frac{-\mathbf{v}_{ij}^{\parallel}}{|\mathbf{v}_{ij}^{\parallel}|} & \text{otherwise (slip)} \end{cases} \quad (\text{C.16})$$

which can be rewritten in a more condensed way as follows:

$$\mathbf{F}_{\text{spring},j1 \rightarrow i1}^{\parallel \text{contact}} = \min \left(\xi_{\text{body}}^{\text{static}} \delta s, \mu_{\text{body}}^{\text{dyn}} |\mathbf{F}_{j1 \rightarrow i1}^{\perp \text{contact}}| \right) \frac{-\mathbf{v}_{ij}^{\parallel}}{|\mathbf{v}_{ij}^{\parallel}|} \quad (\text{C.17})$$

A tangential damping force is then added to the tangential spring force:

$$\mathbf{F}_{\text{viscous},j1 \rightarrow i1}^{\parallel \text{contact}} = \begin{cases} -\gamma_{\text{body}}^{\parallel} \mathbf{v}_{ij}^{\parallel} & \text{if } h_{i1j1} > 0 \\ \mathbf{0} & \text{otherwise} \end{cases} \quad (\text{C.18})$$

C.1.3.2 TORQUE FOR ROTATION OF A PEDESTRIAN

The rotational motion of a pedestrian is obtained by applying the angular momentum theorem to the pedestrian's **Center of Mass (CoM)**. This is done in its principal inertia base, projected along the z-axis (the out-of-plane axis). The pedestrian experiences torque due to both the force normal and tangential to the contact surface:

$$\tau_{G_i,j1 \rightarrow i1} = \left\{ \mathbf{r}_{i \rightarrow C} \times \left(\mathbf{F}_{j1 \rightarrow i1}^{\parallel \text{contact}} + \mathbf{F}_{j1 \rightarrow i1}^{\perp \text{contact}} \right) \right\} \cdot \mathbf{u}_z \quad (\text{C.19})$$

The self-propelling force acts directly on the **CoM**, resulting in zero torque. To account for decision-making, a restoring force is applied to achieve the desired angular velocity ω_i^{des} within a τ_{mech} duration, expressed as: $I_i \frac{\omega_i^{\text{des}} - \omega_i}{\tau_{\text{mech}}}$.

C.1.4 MOMENT OF INERTIA CALCULATION (BACK ON PAGE 81)

Each pedestrian in our synthetic crowd is represented as a combination of five disks. While an analytical formula for the moment of inertia of such a configuration can be derived, it is quite cumbersome to implement. Instead, we approximate the pedestrian's boundary using an N -sided polygon, defined by the set of vertices:

$$\{(x_1, y_1), (x_2, y_2), \dots, (x_{N+1}, y_{N+1}) : (x_1, y_1) = (x_{N+1}, y_{N+1})\}, \quad (\text{C.20})$$

where $(x_1, y_1) = (x_{N+1}, y_{N+1})$ ensures the polygon is closed. Assuming that the mass m_i of pedestrian i is uniformly distributed within this polygon, the moment of inertia I_i for this polygon can then be computed using the following formula (Name, 1987):

$$I_i = \frac{m_i}{12} \sum_{j=1}^N (x_j y_{j+1} - x_{j+1} y_j) (x_j^2 + x_j x_{j+1} + x_{j+1}^2 + y_j^2 + y_j y_{j+1} + y_{j+1}^2), \quad (\text{C.21})$$

where j indexes the vertices of the polygon. One could raise several criticisms about calculating a pedestrian's moment of inertia using a two-dimensional shape. Indeed, this calculation does not account for variations in density within the pedestrian, nor does it consider the pedestrian deformable. Nevertheless, it introduces an inhomogeneity in the rotational equation, similar to the mass for Newton's equation.

C.1.5 MECHANICAL EQUATIONS SUMMARY (BACK ON PAGE 75)

Pedestrian CoM dynamics

$$\begin{aligned} \frac{d\mathbf{v}_i}{dt} = & \frac{\mathbf{v}_i^{\text{des}} - \mathbf{v}_i}{\tau_{\text{mech}}} + \frac{1}{m_i} \sum_{(j1, i1) \in \mathcal{C}_i^{\text{(ped)}}} \left(\mathbf{F}_{j1 \rightarrow i1}^{\parallel \text{contact}} + \mathbf{F}_{j1 \rightarrow i1}^{\perp \text{contact}} \right) \\ & + \frac{1}{m_i} \sum_{(w, i1) \in \mathcal{C}_i^{\text{(wall)}}} \left(\mathbf{F}_{w \rightarrow i1}^{\parallel \text{contact}} + \mathbf{F}_{w \rightarrow i1}^{\perp \text{contact}} \right) \end{aligned} \quad (\text{C.22})$$

Interaction forces with a pedestrian

$$\begin{aligned} \mathbf{F}_{j1 \rightarrow i1}^{\parallel \text{contact}} &= \mathbf{F}_{\text{spring}, j1 \rightarrow i1}^{\parallel \text{contact}} + \mathbf{F}_{\text{viscous}, j1 \rightarrow i1}^{\parallel \text{contact}} \\ \mathbf{F}_{\text{spring}, j1 \rightarrow i1}^{\parallel \text{contact}} &= \min \left(\xi_{\text{body}}^{\text{static}} \delta s, \mu_{\text{body}}^{\text{dyn}} \left| \mathbf{F}_{j1 \rightarrow i1}^{\perp \text{contact}} \right| \right) \frac{-\mathbf{v}_{ij}^{\parallel}}{\left| \mathbf{v}_{ij}^{\parallel} \right|} \\ \mathbf{F}_{\text{viscous}, j1 \rightarrow i1}^{\parallel \text{contact}} &= \begin{cases} -\gamma_{\text{body}}^{\parallel} \mathbf{v}_{ij}^{\parallel} & \text{if } h_{i1j1} > 0 \\ \mathbf{0} & \text{otherwise} \end{cases} \\ \mathbf{F}_{j1 \rightarrow i1}^{\perp \text{contact}} &= \mathbf{F}_{\text{spring}, j1 \rightarrow i1}^{\perp \text{contact}} + \mathbf{F}_{\text{viscous}, j1 \rightarrow i1}^{\perp \text{contact}} \\ \mathbf{F}_{\text{spring}, j1 \rightarrow i1}^{\perp \text{contact}} &= \begin{cases} k_{\text{body}}^{\perp} h_{i1j1} \mathbf{n}_{i1j1}^{\perp} & \text{if } h_{i1j1} > 0 \text{ (i.e. an overlap occurs)} \\ \mathbf{0} & \text{otherwise} \end{cases} \\ \mathbf{F}_{\text{viscous}, j1 \rightarrow i1}^{\perp \text{contact}} &= \begin{cases} -\gamma_{\text{body}}^{\perp} \mathbf{v}_{ij}^{\perp} & \text{if } h_{i1j1} > 0 \text{ (i.e. an overlap occurs)} \\ \mathbf{0} & \text{otherwise} \end{cases} \end{aligned} \quad (\text{C.23})$$

where

$$\begin{aligned} h_{i1j1} &= R_{i1} + R_{j1} - |\mathbf{r}_{i1 \rightarrow j1}| \\ \delta s &= \left| \int_0^{\text{contact duration}} \mathbf{v}_{ij}^{\parallel} dt \right| \end{aligned} \quad (\text{C.24})$$

Transport of forces to the pedestrian CoM

$$\begin{aligned} \mathbf{v}_{ij}^{\parallel} &= \left(\mathbf{v}_{ij} \cdot \mathbf{n}_{i1 \rightarrow j1}^{\parallel} \right) \mathbf{n}_{i1 \rightarrow j1}^{\parallel} \\ \mathbf{v}_{ij} &= \mathbf{v}_{i,C} - \mathbf{v}_{j,C} \\ \mathbf{v}_{i,C} &= \mathbf{v}_i + \boldsymbol{\omega}_i \times \mathbf{r}_{i \rightarrow C} \\ \mathbf{r}_{i \rightarrow C} &= \mathbf{r}_{i \rightarrow i1} + \mathbf{r}_{i1 \rightarrow C} \\ \mathbf{n}_{i1 \rightarrow j1}^{\parallel} &= \mathbf{u}_z \times \mathbf{n}_{i1 \rightarrow j1} \\ \mathbf{n}_{i1 \rightarrow j1} &= \frac{\mathbf{r}_{i1 \rightarrow j1}}{|\mathbf{r}_{i1 \rightarrow j1}|} \\ \mathbf{r}_{i1 \rightarrow j1} &= \mathbf{r}_j + \boldsymbol{\Delta}_{j \rightarrow j1} - (\mathbf{r}_i + \boldsymbol{\Delta}_{i \rightarrow i1}) \\ \mathbf{r}_{i1 \rightarrow C} &= \left(R_{i1} - \frac{h_{i1j1}}{2} \right) \mathbf{n}_{i1 \rightarrow j1} \\ \mathbf{v}_{ij}^{\perp} &= (\mathbf{v}_{ij} \cdot \mathbf{n}_{i1 \rightarrow j1}) \mathbf{n}_{i1 \rightarrow j1} \end{aligned} \quad (\text{C.25})$$

Interaction forces with wall

$$\begin{aligned} \mathbf{F}_{\text{spring}, w \rightarrow i1}^{\parallel \text{contact}} &= \min \left(c_{\text{wall}}^{\text{static}} \delta s_w, \mu_{\text{wall}}^{\text{dyn}} \left| \mathbf{F}_{w \rightarrow i1}^{\perp \text{contact}} \right| \right) \frac{-\mathbf{v}_{iw}^{\parallel}}{\left| \mathbf{v}_{iw}^{\parallel} \right|} \\ \mathbf{F}_{\text{viscous}, w \rightarrow i1}^{\parallel \text{contact}} &= \begin{cases} -\gamma_{\text{wall}}^{\parallel} \mathbf{v}_{i1w}^{\parallel} & \text{if } h_{i1w} > 0 \\ \mathbf{0} & \text{otherwise} \end{cases} \\ \mathbf{F}_{w \rightarrow i1}^{\perp \text{contact}} &= \mathbf{F}_{\text{spring}, w \rightarrow i1}^{\perp \text{contact}} + \mathbf{F}_{\text{viscous}, w \rightarrow i1}^{\perp \text{contact}} \\ \mathbf{F}_{\text{spring}, w \rightarrow i1}^{\perp \text{contact}} &= \begin{cases} k_{\text{wall}}^{\perp} h_{i1w} \mathbf{n}_{i1w}^{\perp} & \text{if } h_{i1w} > 0 \text{ (i.e. an overlap occurs)} \\ \mathbf{0} & \text{otherwise} \end{cases} \\ \mathbf{F}_{\text{viscous}, w \rightarrow i1}^{\perp \text{contact}} &= \begin{cases} -\gamma_{\text{wall}}^{\perp} \mathbf{v}_{iw}^{\perp} & \text{if } h_{i1w} > 0 \text{ (i.e. an overlap occurs)} \\ \mathbf{0} & \text{otherwise} \end{cases} \end{aligned} \quad (\text{C.26})$$

where

$$\begin{aligned} h_{i1w} &= R_{i1} - |\mathbf{r}_{i1 \rightarrow w}| \\ \delta s_w &= \left| \int_0^{\text{contact duration}} \mathbf{v}_{iw}^{\parallel} dt \right| \end{aligned} \quad (\text{C.27})$$

Transport of forces to the pedestrian CoM

$$\begin{aligned} \mathbf{v}_{iw}^{\parallel} &= \left(\mathbf{v}_{iw} \cdot \mathbf{n}_{i1 \rightarrow w}^{\parallel} \right) \mathbf{n}_{i1 \rightarrow w}^{\parallel} \\ \mathbf{v}_{iw} &= \mathbf{v}_{i,C} \\ \mathbf{n}_{i1 \rightarrow w}^{\parallel} &= \mathbf{u}_z \times \mathbf{n}_{i1 \rightarrow w} \\ \mathbf{n}_{i1 \rightarrow w} &= \frac{\mathbf{r}_{i1 \rightarrow w}}{|\mathbf{r}_{i1 \rightarrow w}|} \\ \mathbf{v}_{iw}^{\perp} &= (\mathbf{v}_{iw} \cdot \mathbf{n}_{i1 \rightarrow w}) \mathbf{n}_{i1 \rightarrow w} \end{aligned} \quad (\text{C.28})$$

Rotational Dynamics

$$\frac{d\omega_i}{dt} = \frac{\omega_i^{\text{des}} - \omega_i}{\tau_{\text{mech}}} + \frac{1}{I_i} \sum_{(j1, i1) \in \mathcal{C}_i^{\text{(ped)}}} \tau_{G_i, j1 \rightarrow i1} + \frac{1}{I_i} \sum_{(j1, i1) \in \mathcal{C}_i^{\text{(wall)}}} \tau_{G_i, w \rightarrow i1} \quad (\text{C.29})$$

Torques

$$\begin{aligned}\tau_{G_i, j1 \rightarrow i1} &= \left\{ \mathbf{r}_{i \rightarrow C} \times \left(\mathbf{F}_{j1 \rightarrow i1}^{\parallel \text{contact}} + \mathbf{F}_{j1 \rightarrow i1}^{\perp \text{contact}} \right) \right\} \cdot \mathbf{u}_z \\ \tau_{G_i, w \rightarrow i1} &= \left\{ \mathbf{r}_{i \rightarrow C} \times \left(\mathbf{F}_{w \rightarrow i1}^{\parallel \text{contact}} + \mathbf{F}_{w \rightarrow i1}^{\perp \text{contact}} \right) \right\} \cdot \mathbf{u}_z\end{aligned}\quad (\text{C.30})$$

Dynamic equations without interactions

$$\begin{aligned}\frac{d\mathbf{v}_i}{dt} &= \frac{\mathbf{v}_i^{\text{des}} - \mathbf{v}_i}{\tau_{\text{mech}}} \\ \frac{d\omega_i}{dt} &= \frac{\omega_i^{\text{des}} - \omega_i}{\tau_{\text{mech}}}\end{aligned}\quad (\text{C.31})$$

where $\mathbf{v}_i^{\text{des}}$ and ω_i^{des} are constant within $[t, t + \delta t)$ and δt denotes the duration between each taken decision. Therefore $\forall \Delta t \in [0, \delta t)$,

$$\begin{aligned}\mathbf{v}_i(t + \Delta t) &= \mathbf{v}_i(t) e^{-\frac{\Delta t}{\tau_{\text{mech}}}} + \mathbf{v}_i^{\text{des}}(t) \left(1 - e^{-\frac{\Delta t}{\tau_{\text{mech}}}} \right) \\ \omega_i(t + \Delta t) &= \omega_i(t) e^{-\frac{\Delta t}{\tau_{\text{mech}}}} + \omega_i^{\text{des}}(t) \left(1 - e^{-\frac{\Delta t}{\tau_{\text{mech}}}} \right)\end{aligned}\quad (\text{C.32})$$

Summary of notations and definitions The Tab. C.1 provides a comprehensive overview of all the definitions and notations used throughout Chap. 3.

Symbol	Definition
s_{i1}	Centre of disk 1 of pedestrian i
$\Delta_{i \rightarrow i1}$	Position of the disk centre s_{i1} relative to the centre of mass of pedestrian i
G_i	Centre of mass of pedestrian i
C	Contact centre
R_{i1}	Radius of disk 1 from pedestrian i
$\mathbf{r}_{i1 \rightarrow C}$	Position of the contact centre relative to the disk centre s_{i1}
\mathbf{u}_z	Out-of-plane z-axis
h_{i1j1}	Overlap distance between disk centres s_{i1} and s_{j1}
\perp	Orthogonal to the surface contact
\parallel	Tangential to the surface contact
$\mathbf{v}_{ij}^{\parallel}$	Tangential component of the velocity of pedestrians i relative to j at the contact centre
δs	Magnitude of slip during contact

TABLE C.1: Definitions of the symbols that describe the geometrical aspects of the dynamics.

C.1.6 ALGORITHM STRUCTURE (BACK ON PAGE 76)

To simulate crowd dynamics in the various scenarios studied, we used an algorithm outlined in the flowchart shown in Fig. C.8. Specifically, to solve Newton's equations of motion governing the position and orientation of pedestrians, we employed a slightly modified Velocity Verlet algorithm introduced by Vyas et al. (2024). This adaptation allows us to handle equations involving forces that depend on velocity in a nonlinear manner. The method can be broken down into five distinct steps:

1. Compute forces at time t

The total force per unit mass, $\mathbf{f}_i(t)$, can be decomposed into three components: a constant and position-dependent term, a term linearly dependent on velocity, and a term non-linearly dependent on velocity, as follows

$$\mathbf{f}_i(t) = \mathbf{f}_{i,r}(t) + \mathbf{f}_{i,vl}(t) + \mathbf{f}_{i,vnl}(t) \quad (\text{C.33})$$

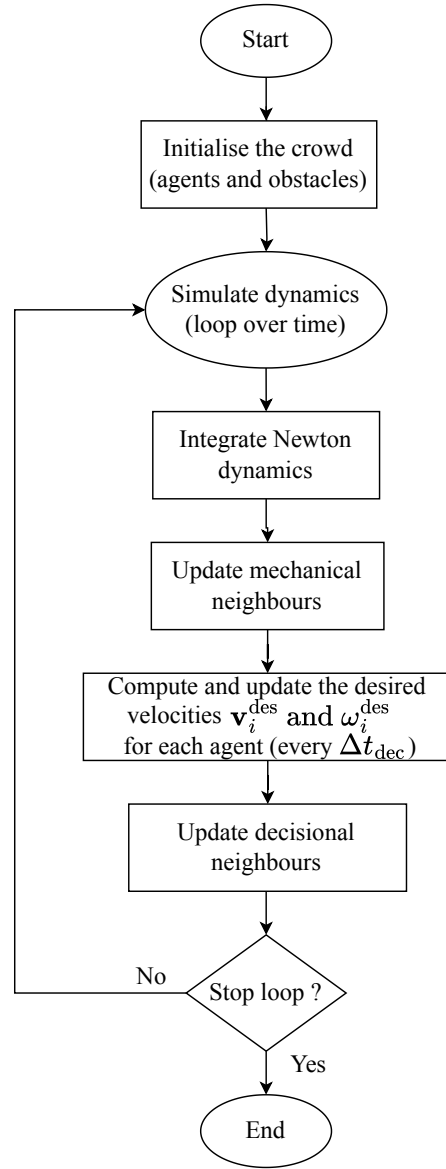


FIGURE C.8: Flowchart of the discrete element simulation algorithm used to simulate crowd dynamics.

where

$$\begin{aligned}
 \mathbf{f}_{i,r}(t) &= \frac{\mathbf{v}_i^{\text{des}}}{\tau_{\text{mech}}} + \frac{1}{m_i} \sum_{(j1,i1) \in \mathcal{C}_i^{(\text{ped})} \cup \mathcal{C}_i^{(\text{wall})}} \mathbf{F}_{j1 \rightarrow i1}^{\perp \text{contact}}(t) \\
 \mathbf{f}_{i,vl}(t) &= -\frac{\mathbf{v}_i(t)}{\tau_{\text{mech}}} \\
 \mathbf{f}_{i,vnl}(t) &= \frac{1}{m_i} \sum_{(j1,i1) \in \mathcal{C}_i^{(\text{ped})} \cup \mathcal{C}_i^{(\text{wall})}} \mathbf{F}_{j1 \rightarrow i1}^{\parallel \text{contact}}(t)
 \end{aligned} \tag{C.34}$$

One can also define the total torque per unit of moment of inertia $\tau_i(t)$.

2. Update position and orientation at time $t + \Delta t$

The new position $\mathbf{r}_i(t + \Delta t)$ is updated using

$$\mathbf{r}_i(t + \Delta t) = \mathbf{r}_i(t) + \Delta t \zeta_{2,m} \mathbf{v}_i(t) + \frac{(\Delta t)^2}{2} [\mathbf{f}_{i,r}(t) + \mathbf{f}_{i,vnl}(t)], \tag{C.35}$$

where $\zeta_{2,m} = 1 - \frac{\Delta t}{2\tau_{\text{mech}}}$. The orientation angle $\theta_i(t + \Delta t)$ is updated as

$$\theta_i(t + \Delta t) = \theta_i(t) + \Delta t \omega_i(t) + \frac{(\Delta t)^2}{2} \tau_i(t) \quad (\text{C.36})$$

3. Trial velocity calculation

To calculate velocities at $t + \Delta t$, we first compute trial velocities i.e. velocities at time $t + \frac{\Delta t}{2}$

- Trial translational velocity

$$\mathbf{v}_i^{\text{try}} = \zeta_{2,m} \mathbf{v}_i(t) + \frac{\Delta t}{2} [\mathbf{f}_{i,r}(t) + \mathbf{f}_{i,vnl}(t)] \quad (\text{C.37})$$

where $\zeta_{2,m} = 1 - \frac{\Delta t}{2\tau_{\text{mech}}}$

- Trial angular velocity

$$\omega_i^{\text{try}} = \omega_i(t) + \frac{\Delta t}{2} \tau_i(t) \quad (\text{C.38})$$

4. Recompute forces with trial velocities

Using the trial velocities $\mathbf{v}_i^{\text{try}}$ and ω_i^{try} , instead of $\mathbf{v}_i(t)$ and $\omega_i(t)$ compute the trial force and torque denoted as $\mathbf{f}_{i,vnl}|_{\mathbf{v}_i^{\text{try}}, \omega_i^{\text{try}}}(t)$ and $\tau_i|_{\omega_i^{\text{try}}, \mathbf{v}_i^{\text{try}}}(t)$.

5. Update final velocities

Finally, update the velocities using the recomputed forces

- Final translational velocity

$$\mathbf{v}_i(t + \Delta t) = \frac{1}{\zeta_{2,p}} \left[\zeta_{2,m} \mathbf{v}_i(t) + \frac{\Delta t}{2} [\mathbf{f}_{i,r}(t) + \mathbf{f}_{i,vnl}(t) + \mathbf{f}_{i,r}(t + \Delta t) + \mathbf{f}_{i,vnl}|_{\mathbf{v}_i^{\text{try}}, \omega_i^{\text{try}}}(t)] \right] \quad (\text{C.39})$$

where we recall that $\zeta_{2,m} = 1 - \frac{\Delta t}{2\tau_{\text{mech}}}$ and $\zeta_{2,p} = 1 + \frac{\Delta t}{2\tau_{\text{mech}}}$

- Final angular velocity

$$\omega_i(t + \Delta t) = \omega_i(t) + \frac{\Delta t}{2} [\tau_i(t) + \tau_i|_{\omega_i^{\text{try}}, \mathbf{v}_i^{\text{try}}}(t)] \quad (\text{C.40})$$

This completes one iteration of the modified Velocity Verlet algorithm for both position and orientation updates.

C.2 DECISION-MAKING COST

C.2.1 STATIC FLOOR FIELD TERM (BACK ON PAGE 42)

The **Static Floor Field (SFF)** term, denoted as \mathcal{E}^{SFF} , evaluates the attractiveness of a candidate position that would result from choosing a candidate velocity \mathbf{u} . This term is dependent on the shortest-path distance $\mathcal{D}(\mathbf{r}(t))$ to the pedestrian's target defined by the Eikonal equation $\|\nabla_{\mathbf{r}} \mathcal{D}\| = n(\mathbf{r})$ where $n(\mathbf{r})$ denotes the *refractive index* which measures the discomfort the pedestrian may feel about its surrounding environment at position \mathbf{r} as illustrated in Fig. C.9. In free space, this index is $n = 1$, but

proximity to a wall increases discomfort, which is penalised by:

$$n(\mathbf{r}(t)) = \frac{1}{\tanh\left(\frac{d_w(\mathbf{r}(t))}{d_c}\right)} \quad (\text{C.41})$$

where $d_w(\mathbf{r}(t))$ denotes the euclidean distance to the closest wall, and d_c is a model parameter.

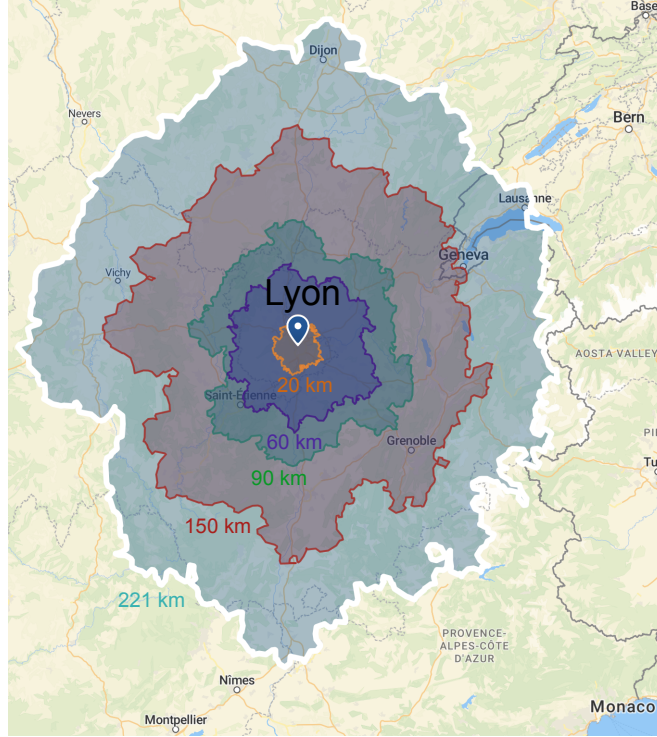


FIGURE C.9: This map illustrates some iso-distance travel lines to reach the city of Lyon. Interestingly, these lines are not perfect circles centred on Lyon as one should expect in an Euclidean space, indicating that some routes are shorter than others. By considering the map as a continuous space, we can define a function that modifies the Euclidean distance to reflect these variations in travel distances. This function, known as a refraction index, is connected to the distance metric through the Eikonal equation. From a broader perspective, this concept enables the transformation of a network map into a continuous map. It allows furthermore for converting a 3D terrain with valleys into a 2D representation, or in our case, the mapping of a comfort representation into a 2D format, thereby providing a more nuanced depiction of spatial dynamics. The map was created using the software [Smappen](#).

Therefore, one can define the static floor field cost as follows:

$$\mathcal{E}^{\text{SFF}}(\mathbf{u}) \propto \frac{\mathcal{D}(\mathbf{r}(t) + \delta t \mathbf{u}) - \mathcal{D}(\mathbf{r}(t))}{n(\mathbf{r}(t))} \quad (\text{C.42})$$

This equation can be interpreted as a cost associated with changes in distance to the target, incorporating an element of anticipation. If the chosen velocity results in moving further away from the target, the cost increases, indicating decreased satisfaction with the position. One can notice that $\mathcal{D}(\mathbf{r}(t))$ is independent of the candidate velocity. It can, therefore, be omitted from the equation. Overall, the static floor field term reads:

$$\mathcal{E}^{\text{SFF}}(\mathbf{u}) = \frac{K_{\text{SFF}}}{n(\mathbf{r}(t))} \mathcal{D}(\mathbf{r}(t) + \delta t \mathbf{u}) \quad (\text{C.43})$$

where K_{SFF} is a parameter that indicates the relative importance of this term compared to others in the cost function.

C.2.2 BIO-MECHANICAL TERM (BACK ON PAGE 42)

C.2.2.1 BIO-MECHANICAL COST ASSOCIATED WITH WALKING SPEED

The literature in physiology relates the energy expenditure of walking to the rate of oxygen consumption V_{O_2} , which has a ‘rest’ component and a speed-dependent component:

$$V_{O_2} = V_{O_2}^{(\text{rest})} + V_{O_2}^{(\text{walking})} \quad (\text{C.44})$$

We are interested in the second contribution, which, in the experimental work of [Ludlow and Weyand \(2016\)](#), is reasonably well fitted by an equation of the form:

$$\mathcal{E}^{\text{speed}}(u) = K_{s1} + K_{s2} u^2, \text{ for } u \geq u_c \quad (\text{C.45})$$

where u represents the magnitude of the candidate velocity \mathbf{u} , and u_c , K_{s1} , K_{s2} are coefficients to be determined. This quadratic relationship aligns with other empirical studies examining human energy expenditure during walking motion ([Cotes and Meade, 1960](#)). Finally, we choose to smoothly connect the above $\mathcal{E}^{\text{speed}}$ expression to 0 so as to avoid discontinuities with a second-order polynomial:

$$\mathcal{E}^{\text{speed}}(u) = K_{s3} u + K_{s4} u^2, \text{ for } u < u_c \quad (\text{C.46})$$

with coefficients such that they match at $u = u_c$, for single-point value and derivative. Therefore

$$\mathcal{E}^{\text{speed}}(u) = \delta t \begin{cases} K_{s3} u + K_{s4} u^2, & u < u_c \\ K_{s1} + K_{s2} u^2, & u \geq u_c \end{cases} \quad (\text{C.47})$$

with

$$K_{s1} = 0.4 \text{ J s}^{-1}, K_{s2} = 0.6 \text{ kg s}^{-1}, K_{s3} = 7.6 \text{ N}, K_{s4} = -35.4 \text{ kg s}^{-1}, u_c = 0.1 \text{ m s}^{-1} \quad (\text{C.48})$$

This functional form fits experimental data ([Ludlow and Weyand, 2016](#)) well, as shown in Fig. C.10.

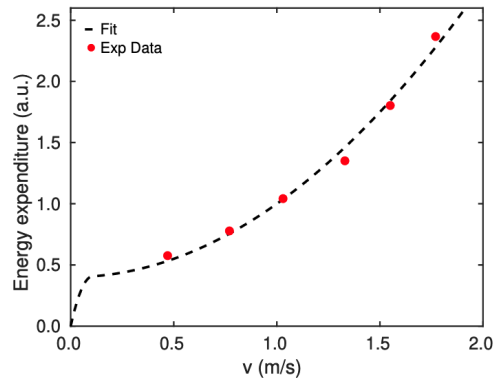


FIGURE C.10: Bio-mechanical cost $\mathcal{E}^{\text{speed}}$ associated with the walking speed v , described by Eq. (C.47). This cost is compared to the aggregated data from [Ludlow and Weyand \(2016\)](#) for the adult group, from which the base energy consumption (i.e., at rest) has been subtracted. The diagram is taken from [Echeverría-Huarte and Nicolas \(2023\)](#).

C.2.2.2 BIO-MECHANICAL COST ASSOCIATED WITH INERTIA

Abrupt changes in velocity should also be barred because they are uncomfortable and bio-mechanically costly, which suggests an ‘inertial’ contribution:

$$\mathcal{E}^{\text{inertia}}(\mathbf{u}) = \delta t K_I \|\mathbf{u} - \mathbf{v}(t)\|^2 \quad (\text{C.49})$$

where $\mathbf{v}(t)$ is the actual velocity at time t , \mathbf{u} is the candidate velocity, $K_I > 0$ and δt the anticipation time (put for harmony in notations).

C.2.2.3 BIO-MECHANICAL COST ASSOCIATED WITH THE DESIRED DIRECTION - BODY MISALIGNMENT

Currently, the model may permit a pedestrian to move backwards. It is therefore essential to understand how the desired velocity should align with the rest of the body. At first sight, we can assume that a pedestrian’s head points toward its desired direction of motion, as turning the head relative to the body incurs a structural cost. However, in some cases, like walking sideways on a familiar path, pedestrians may move without looking ahead, thus avoiding head rotation. This level of detail is not considered. We therefore must assess the cost of rotating the head or neck relative to other body parts. This aspect has been explored in studies such as Liu et al. (2024), which examines the mechanical response of the neck during passive motions. In these tests, participants’ heads are rotated by a mechanical apparatus while a load cell measures the torque required for this rotation (see Fig. A.3). As a first approximation, the torsional $\mathcal{E}^{\text{torsion}}(\omega)$ for a test angular velocity ω is well approximated by a parabolic function:

$$\mathcal{E}^{\text{torsion}}(\omega) = K_{\text{Tor}} [\theta_{\text{des}}(t) - (\theta_{\text{body}}(t) + \delta t \omega)]^2 \quad (\text{C.50})$$

where $K_{\text{Tor}} > 0$, $\mathbf{v}^{\text{des}}(t)$ is the desired velocity of the pedestrian at time t , $\theta_{\text{des}}(t)$ is given by the direction of $\mathbf{v}^{\text{des}}(t)$.

C.2.3 DECISION-MAKING EQUATIONS SUMMARY (BACK ON PAGE 42)

$$\begin{aligned} (\mathbf{v}^{\text{des}}, \omega^{\text{des}}) &= \arg \min_{(\mathbf{u}, \omega) \in \mathbb{R}^2 \times \mathbb{R}} \mathcal{E}(\mathbf{u}, \omega) \\ \mathcal{E}(\mathbf{u}, \omega) &= \mathcal{E}^{\text{speed}}(\|\mathbf{u}\|) + \mathcal{E}^{\text{inertia}}(\mathbf{u}) + \mathcal{E}^{\text{SFF}}(\mathbf{u}) + \mathcal{E}^{\text{torsion}}(\omega) \\ &\quad + \mathcal{E}^{\text{TTC}}(\mathbf{u}, \omega) + \mathcal{E}^{\text{privacy}}(\mathbf{u}, \omega) \\ \mathcal{E}^{\text{speed}}(\|\mathbf{u}\|) &= \delta t \begin{cases} K_{s3} u + K_{s4} u^2, & u < u_c \\ K_{s1} + K_{s2} u^2, & u \geq u_c \end{cases} \end{aligned} \quad (\text{C.51})$$

$$K_{s1} = 0.4 \text{ J s}^{-1}, K_{s2} = 0.6 \text{ kg s}^{-1}, K_{s3} = 7.6 \text{ N}, K_{s4} = -35.4 \text{ kg s}^{-1}, u_c = 0.1 \text{ m s}^{-1}$$

$$\mathcal{E}^{\text{inertia}}(\mathbf{u}) = \delta t K_I \|\mathbf{u} - \mathbf{v}(t)\|^2$$

$$\mathcal{E}^{\text{SFF}}(\mathbf{u}) = \frac{K_{\text{SFF}}}{n(\mathbf{r}(t))} \mathcal{D}(\mathbf{r}(t) + \delta t \mathbf{u})$$

$$\mathcal{E}^{\text{torsion}}(\omega) = K_{\text{Tor}} [\theta_{\text{des}}(t) - (\theta_{\text{body}}(t) + \delta t \omega)]^2$$

C.2.4 DERIVATION OF THE FREE WALKING SPEED (BACK ON PAGE 81)

To express the free-walking speed of pedestrians as a function of the model parameters, let us consider isolated pedestrians. By definition, they have no interactions with other pedestrians or the built

environment; thus, the perceived cost for motion at time t is given by:

$$\mathcal{E}(\mathbf{u}, \omega) = \mathcal{E}^{\text{speed}}(\|\mathbf{u}\|) + \mathcal{E}^{\text{inertia}}(\mathbf{u}) + \mathcal{E}^{\text{SFF}}(\mathbf{u}) + \mathcal{E}^{\text{torsion}}(\omega) \quad (\text{C.52})$$

Interestingly, this function (with its explicit dependencies given by Eqs. (C.43), (C.47), (C.49) and (C.50)) exhibits the same qualitative dependence on the (longitudinal) speed $\|\mathbf{u}\|$ as the potential empirically estimated by Corbetta et al. (2017) from their tracking of dilute (i.e., non-interacting) pedestrians walking on a staircase landing (see Fig. 5 in their study), with a local minimum at $\|\mathbf{u}\| = 0$ and a global minimum at the free walking speed $\|\mathbf{u}^\infty\| \approx 1$ m/s. It is important to note that, unlike Corbetta et al. (2017), no exogenous noise is introduced into our decisional layer. Therefore, in the stationary state, the actual walking speed of a given pedestrian does not fluctuate; instead, it matches the desired speed u^∞ , which is determined by extremizing $\mathcal{E}(\mathbf{u}, \omega)$, as follows:

$$\begin{aligned} 0 &= \left. \frac{1}{\delta t} \nabla_{\mathbf{u}} \mathcal{E} \right|_{\mathbf{u}=\mathbf{u}^\infty} \\ &= 2K_I(\mathbf{u}^\infty - \mathbf{v}(t)) + \frac{\partial \mathcal{E}^{\text{speed}}}{\partial \|\mathbf{u}\|} \frac{\mathbf{u}^\infty}{\|\mathbf{u}^\infty\|} + K_{\text{SFF}} \frac{\nabla_{\mathbf{r}} \mathcal{D}_{\text{SFF}}}{n(\mathbf{r}(t))} \\ &= 2K_I(\mathbf{u}^\infty - \mathbf{v}(t)) + 2K_{s2} \mathbf{u}^\infty - K_{\text{SFF}} \mathbf{t} \end{aligned} \quad (\text{C.53})$$

where we have used the expression of $\mathcal{E}^{\text{speed}}$ for $u \geq u_c$ from Eq. (C.47) and defined the unit vector $\mathbf{t} = -\nabla_{\mathbf{r}} \mathcal{D}_{\text{SFF}}/n(\mathbf{r}(t))$ which, by definition in section C.2.1, points towards the target. An isolated pedestrian quickly reaches its desired velocity \mathbf{u}^∞ , causing the first term to vanish in the steady state. Consequently, we find:

$$\mathbf{u}^\infty = \frac{K_{\text{SFF}}}{2K_{s2}} \mathbf{t} \quad (\text{C.54})$$

This expression can be used to determine the coefficient K_{SFF} based on the free-walking speed $\|\mathbf{u}^\infty\|$, which in a free-flow scenario is typically 1.4 m/s (see Fig. 1.12). A similar reasoning leads to $\omega^\infty = 0$.

C.2.5 DISCOMFORT CONTOUR LEVELS (BACK ON PAGE 78)

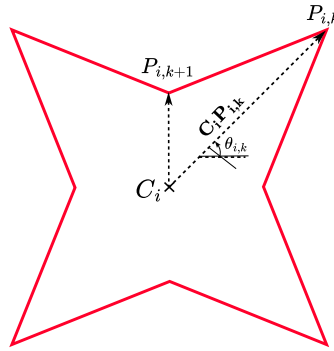


FIGURE C.11: An example of a pedestrian i 's discomfort contour level represented by a star-shaped polygon. The vertices labelled $P_{i,k}$ are indexed counter-clockwise. Each vertex is defined in polar coordinates, characterised by its distance from the polygon centroid C_i and its orientation in the plane, denoted as $\theta_{i,k}$.

C.2.6 COMPUTATION OF THE MINIMAL SWELLING COEFFICIENT SUCH THAT THE TWO DISCOMFORT FIELDS OVERLAP (BACK ON PAGE 79)

Determining the minimal swelling rate, denoted as η^* , at which two private spaces start to overlap, is a complex task without a straightforward formula for general shapes. However, a simple procedure can

be employed using a simple formula for star polygons.

Consider two discomfort contours, i and j , at a given swelling η , of pedestrian i and pedestrian j , respectively. An illustration is provided in Fig. C.12 for η equals η^* which we are seeking. Interestingly, two closed polygons are in contact if at least one vertex of one belongs to an edge or overlaps with a vertex of the other polygon. Therefore, the problem is reduced to determining the contact of one vertex with an edge, providing that we iterate over all vertex edges possible.

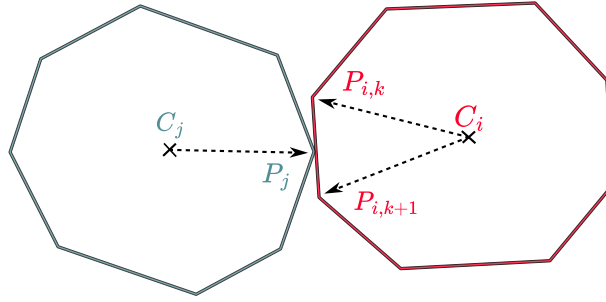


FIGURE C.12: Two discomfort contours at η^* —the minimum swelling at which the contours overlap—are illustrated.

You can proceed as follows. For each vertex-edge pair, compute the swelling $\hat{\eta}$ such that P_j^s lies on the line formed by the vertices $P_{i,k}^s$ and $P_{i,k+1}^s$. This swelling always exists (except in very specific situations when the two polygons have the same centroid and are perfectly aligned, for instance, for which the swelling is set to infinity). Additionally, if $\hat{\eta} < 0$, we set it to infinity as it is associated with a non-physical physical situation. Next, verify whether the vertex P_j^s , which lies on the line (generated by $P_{i,k}^s$ $P_{i,k+1}^s$), actually belongs to the edge itself by checking if:

- $\left| \mathbf{P}_{i,k}^s \mathbf{P}_j^s \right| < \left| \mathbf{P}_{i,k}^s \mathbf{P}_{i,k+1}^s \right|$
- The orientation of $\mathbf{P}_{i,k}^s \mathbf{P}_j^s$ has the same orientation as $\mathbf{P}_{i,k}^s \mathbf{P}_{i,k+1}^s$.

If these conditions are met, record the computed swelling value. This process should be repeated for all possible vertex-edge pairs². The minimal swelling rate η^* is then determined as the smallest value among all computed swellings.

To specify the computation of swelling, we state that P_j^s belongs to the line generated by the two vertices $P_{i,k}^s$ and $P_{i,k+1}^s$ if:

$$\left(\mathbf{P}_{i,k}^s \mathbf{P}_j^s \times \mathbf{P}_{i,k}^s \mathbf{P}_{i,k+1}^s \right) \cdot \mathbf{u}_z = 0 \quad (\text{C.55})$$

where $\mathbf{P}_{i,k}^s \mathbf{P}_j^s$ can be readily expressed in terms of the quantities at the initial swollen state:

$$\begin{aligned} \mathbf{P}_{i,k}^s \mathbf{P}_j^s &= -\hat{\eta} \mathbf{C}_i \mathbf{P}_{i,k} + \mathbf{C}_i \mathbf{C}_j + \hat{\eta} \mathbf{C}_j \mathbf{P}_j \\ \mathbf{P}_{i,k}^s \mathbf{P}_{i,k+1}^s &= \hat{\eta} (\mathbf{C}_i \mathbf{P}_{i,k+1} - \mathbf{C}_i \mathbf{P}_{i,k}) \end{aligned} \quad (\text{C.56})$$

Isolating $\hat{\eta}$ leads to:

$$\hat{\eta} = \frac{(\mathbf{C}_i \mathbf{P}_{i,k} \times \mathbf{C}_i \mathbf{C}_j) \cdot \mathbf{u}_z + (\mathbf{C}_i \mathbf{C}_j \times \mathbf{C}_i \mathbf{P}_{i,k+1}) \cdot \mathbf{u}_z}{(\mathbf{C}_j \mathbf{P}_j \times \mathbf{C}_i \mathbf{P}_{i,k}) \cdot \mathbf{u}_z + (\mathbf{C}_i \mathbf{P}_{i,k} \times \mathbf{C}_i \mathbf{P}_{i,k+1}) \cdot \mathbf{u}_z + (\mathbf{C}_i \mathbf{P}_{i,k+1} \times \mathbf{C}_j \mathbf{P}_j) \cdot \mathbf{u}_z} \quad (\text{C.57})$$

where the triple products can be computed very efficiently by utilising the property of invariance

²You will need two nested loops: the first iterates over the vertices of polygon i and the edges of polygon j , and the second reverses this order by looping over the vertices of polygon j and the edges of polygon i . The computation time is $\mathcal{O}(N^2)$, where N is the number of vertices. Although this may seem inefficient, it is still much simpler and faster than using ellipses, which first require solving a quartic nonlinear equation to determine if two ellipses intersect (Richter-Gebert, 2011, Chap. 11.3) and then finding the right swelling rate iteratively.

under circular permutation of the operands:

$$(\mathbf{C}_i \mathbf{P}_{i,k} \times \mathbf{C}_i \mathbf{C}_j) \cdot \mathbf{u}_z = (\mathbf{u}_z \times \mathbf{C}_i \mathbf{P}_{i,k}) \cdot \mathbf{C}_i \mathbf{C}_j \quad (\text{C.58})$$

The triple product is, therefore, just a dot product between a rotated vector by an angle of $\pi/2$ and the other vector.

In the event of contact between P_j from a pedestrian contour and a wall (for which the discomfort contours are set equals to the physical shape and does not swell), a similar line of reasoning results in:

$$\hat{\eta} = \frac{(\mathbf{C}_i \mathbf{C}_j \times \mathbf{C}_i \mathbf{P}_{i,k+1}) \cdot \mathbf{u}_z - (\mathbf{C}_i \mathbf{C}_j \times \mathbf{C}_i \mathbf{P}_{i,k}) \cdot \mathbf{u}_z - (\mathbf{C}_i \mathbf{P}_{i,k} \times \mathbf{C}_i \mathbf{P}_{i,k+1}) \cdot \mathbf{u}_z}{(\mathbf{C}_i \mathbf{P}_j \times \mathbf{C}_i \mathbf{P}_{i,k+1}) \cdot \mathbf{u}_z - (\mathbf{C}_j \mathbf{P}_j \times \mathbf{C}_i \mathbf{P}_{i,k}) \cdot \mathbf{u}_z} \quad (\text{C.59})$$

In case of contact between P_j from a wall and a pedestrian, one finds:

$$\hat{\eta} = \frac{1}{(\mathbf{C}_i \mathbf{P}_{i,k} \times \mathbf{C}_i \mathbf{P}_{i,k+1}) \cdot \mathbf{u}_z} \left[\begin{aligned} & (\mathbf{C}_i \mathbf{C}_j \times \mathbf{C}_i \mathbf{P}_{i,k+1}) \cdot \mathbf{u}_z - (\mathbf{C}_i \mathbf{C}_j \times \mathbf{C}_i \mathbf{P}_{i,k}) \cdot \mathbf{u}_z \\ & + (\mathbf{C}_j \mathbf{P}_j \times \mathbf{C}_i \mathbf{P}_{i,k+1}) \cdot \mathbf{u}_z - (\mathbf{C}_j \mathbf{P}_j \times \mathbf{C}_i \mathbf{P}_{i,k}) \cdot \mathbf{u}_z \end{aligned} \right] \quad (\text{C.60})$$

C.2.7 NUMERICAL CALCULATION OF THE INTEGRAL FOR THE TIME TO COLLISION COST (BACK ON PAGE 80)

Consider a subdivision of size $N + 1$ for the interval $[\eta_{\min}, \eta_{\max}]$ (equivalently $[\Delta t_{\text{TTC}}, \tau_{\text{TTC}}]$). Outside this interval, we set the kernel K to zero. Using the Riemann sum, the integral can be approximated as:

$$\mathcal{E}^{\text{TTC}}|_{ij}(\mathbf{u}, \omega) \approx \sum_{k=1}^{N+1} K(\eta_k) V_{ij}^{\text{TTC}}[\tau_{\eta_k}(\mathbf{u}, \omega)] |\eta_k - \eta_{k-1}| \quad (\text{C.61})$$

APPENDIX D

RECOVERING STOP-AND-GO DYNAMICS IN TRAFFIC FLOW WITH NOISE-INDUCED KAPITZA PENDULUM INSTABILITY

D.1 SIMULATION SETUP (BACK ON PAGE 94)

In this study, we simulate $N = 22$ vehicles on a single-lane roundabout with a length of $L = 231$ meters (refer to Fig. D.1) to replicate the experimental conditions of Sugiyama et al. (2008); Tadaki et al. (2013). We represent the positions and speeds of the vehicles at time $t \geq 0$ as $(x_n(t))_{n=1}^N$ and $(v_n(t))_{n=1}^N$, respectively, where $v_n(t) = \dot{x}_n(t)$ for each vehicle $n \in 1, \dots, N$.

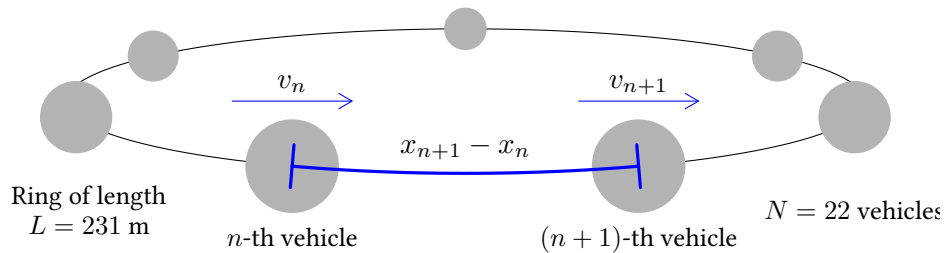


FIGURE D.1: Scheme of the simulation setting for the experiment conducted by Sugiyama et al. (2008).

We suppose that the vehicles are initially ordered by their indices, i.e.,

$$0 \leq x_1(0) \leq x_2(0) \leq \dots \leq x_N(0) \leq L \quad (\text{D.1})$$

We assume that the $(n+1)$ -th vehicle is the predecessor of the n -th vehicle at any time $t \geq 0$. Because of the periodic boundaries, the first vehicle is the predecessor of the N -th vehicle. The distance gap

between vehicles, $g_n(t)$, and the speed difference, $\Delta v_n(t)$, are defined as follows:

$$\begin{cases} g_n(t) = x_{n+1}(t) - x_n(t) - \ell, & n \in \{1, \dots, N-1\}, \\ g_N(t) = L + x_1(t) - x_N(t) - \ell, \end{cases} \quad (\text{D.2})$$

where $\ell = 5$ m is the vehicle length, and

$$\begin{cases} \Delta v_n(t) = v_{n+1}(t) - v_n(t), & n \in \{1, \dots, N-1\}, \\ \Delta v_N(t) = v_1(t) - v_N(t), \end{cases} \quad (\text{D.3})$$

respectively.

Stochastic Optimal Velocity (SOV) model A general class of optimal velocity and full velocity difference linear or near-linear stochastic car-following models is given by (Wagner, 2011; Treiber and Helbing, 2009; Wang et al., 2020; Friesen et al., 2021):

$$dv_n(t) = \left(\frac{V(g_n(t)) - v_n(t)}{T_1} + \frac{\Delta v_n(t)}{T_2} \right) dt + \sigma dW_n(t), \quad (\text{D.4})$$

where $T_1 = 2.5$ s, $T_2 = 2$ s are two relaxation times, $\sigma \in \mathbb{R}$ is the noise volatility and $V : \mathbb{R} \mapsto \mathbb{R}_+$ is the **Optimal-Velocity (OV)** function usually given by the sigmoid:

$$V(s) = v_0 \frac{\tanh(s/\ell_0 - \kappa) + \tanh(\kappa)}{1 + \tanh(\kappa)}, \quad (\text{D.5})$$

where $\kappa = 0.5$ and $\ell_0 = 20$ m are the shape and scale parameters respectively, and $v_0 = 20$ m s⁻¹ is the desired speed (Bando et al., 1995; Jiang et al., 2001; Treiber and Helbing, 2009).

Stochastic Inertial Car-Following (SICF) model from Tomer et al. (2000) reads:

$$\begin{aligned} dv_n(t) = & K \cdot \left(1 - \frac{2v_n(t)T + \ell}{g_n(t) + \ell} \right) dt + \frac{Z^2(-\Delta v_n(t))}{2g_n(t)} dt \\ & - 2Z(v_n(t) - v_0) dt + \sigma dW_n(t), \end{aligned} \quad (\text{D.6})$$

where $Z(x) = (x + |x|)/2$ denotes the positive part of x , $\ell = 5$ m is the length of the vehicles, $K = 5$ m/s² is a sensitivity parameter, $T = 1$ s is the desired time gap and $\sigma \in \mathbb{R}$ is the noise volatility.

Stochastic Intelligent Driver (SID) model from Treiber and Kesting (2017) is given by:

$$\begin{aligned} dv_n(t) = & a \left(1 - \left(\frac{f(v_n(t), \Delta v_n(t))}{g_n(t)} \right)^2 - \left(\frac{v_n(t)}{v_0} \right)^4 \right) dt + \sigma dW_n(t) \\ \text{with } f(v, \Delta v) = & s_0 + Tv - v \frac{\Delta v}{2\sqrt{ab}}, \end{aligned} \quad (\text{D.7})$$

where $a = b = 2$ m/s² are the desired acceleration and maximal deceleration parameter, $s_0 = 2$ m is a minimal gap, $T = 1$ s is the desired time gap, $v_0 = 20$ m s⁻¹ is the desired speed and $\sigma \in \mathbb{R}$ is the noise volatility.

Stochastic Adaptive Time Gap (SATG) model The **Adaptive Time Gap (ATG)** car-following model from Tordeux et al. (2010) is obtained by relaxing the time gap $T_n(t) = g_n/v_n$ as $\dot{T}_n(t) = \lambda(T - T_n(t))$ where λ is a sensitivity parameter and T is the desired time gap. Using speed and gap variables, the

model reads $\dot{v}_n(t) = [\lambda (g_n(t) - T v_n(t)) + \Delta v_n(t)] / T_n(t)$ while the **SATG** model is given by:

$$dv_n(t) = F(g_n(t), v_n(t), v_{n+1}(t)) dt + \sigma dW_n(t), \quad (\text{D.8})$$

where F denotes the acceleration function and reads:

$$F(g_n(t), v_n(t), v_{n+1}(t)) = \frac{\lambda (g_n(t) - T v_n(t)) + \Delta v_n(t)}{T_{T_{\min}, T_{\max}}^\varepsilon(g_n(t), v_n(t))}. \quad (\text{D.9})$$

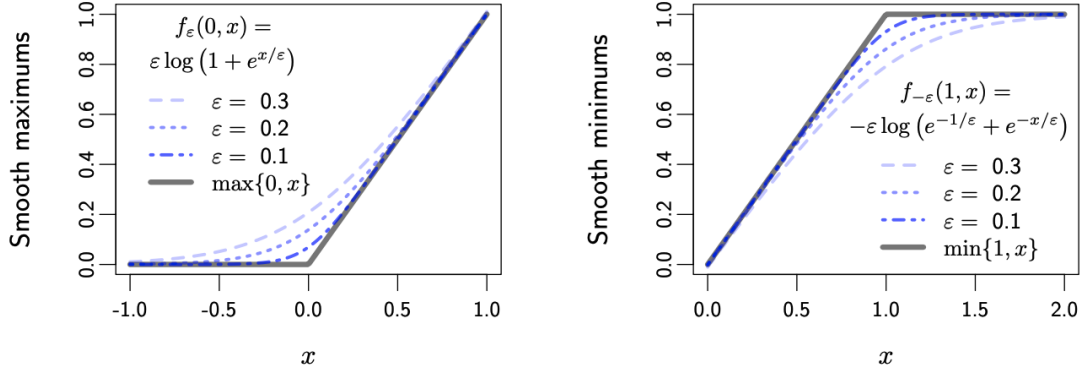


FIGURE D.2: Examples of *LogSumExp* functions.

Here, the time gap is approximated using the mollifier bounded between T_{\min} and T_{\max} :

$$T_{T_{\min}, T_{\max}}^\varepsilon(g_n, v_n) = f_\varepsilon\left(T_{\min}, f_{-\varepsilon}\left(T_{\max}, \frac{g_n}{f_\varepsilon(0, v_n)}\right)\right), \quad (\text{D.10})$$

where f_ε is the *LogSumExp* function

$$f_\varepsilon(a, b) = \varepsilon \log(\exp(a/\varepsilon) + \exp(b/\varepsilon)). \quad (\text{D.11})$$

The function $f_\varepsilon(a, b)$ converges to the maximum of a and b as $\varepsilon \rightarrow 0^+$ and the minimum as $\varepsilon \rightarrow 0^-$ as illustrated in Fig. D.2. This smoothing technique helps prevent singularities that may occur when vehicles collide due to noise or when their speed reaches zero.

Numerical simulation (back on page 95) We used an implicit/explicit Euler–Maruyama numerical solver (Kloeden and Platen, 1992) for the simulation with a time step $\delta t = 0.001$ s. The solver reads for the n -th agent, $n \in \{1, \dots, N\}$,

$$\begin{cases} x_n(t + \delta t) = x_n(t) + \delta t v_n(t + \delta t) \\ v_n(t + \delta t) = v_n(t) + \delta t A(g_n(t), v_n(t), v_{n+1}(t)) + \sqrt{\delta t} g(v_n(t)) \xi_n(t), \end{cases} \quad (\text{D.12})$$

where $(\xi_n(t), n = 1, \dots, N; t \in \delta t \mathbb{N})$ are independent normal random variables and

$$g(v) = \frac{\sigma}{1 + \exp(-\alpha(v - v_\sigma))}, \quad \sigma \geq 0, \alpha = 10^3 \quad (\text{D.13})$$

is the noise volatility, which is constructed to be close to zero as v becomes less than $v_\sigma = 0.1 \text{ m s}^{-1}$ to limit the collisions, and equal to the volatility constant parameter σ as $v \gg v_\sigma$. The parameter values for the simulation are $\lambda = 0.2 \text{ s}^{-1}$, $T_{\min} = 0.1 \text{ s}$, and $T_{\max} = 4 \text{ s}$, while the desired time gap is $T = 1 \text{ s}$ and $\varepsilon = 0.01$.

Online simulation platform (back on page 96) An online simulation platform for the solver described in Eq. (D.12) is available for the experimental setup from Sugiyama et al. (2008) and the stochastic car-following models outlined in Equations Eq. (D.4) to Eq. (D.8). You can access this platform at the following URL: [Simulation Platform](#).

Example of $\phi(t)$ (back on page 95)

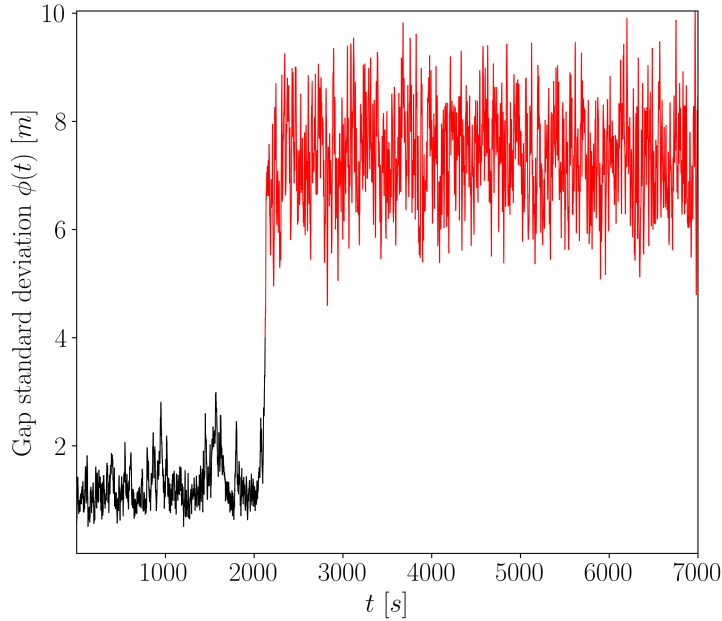


FIGURE D.3: The simulation of the **Stochastic Adaptive Time Gap (SATG)** was performed for $\sigma = 0.55 \text{ ms}^{-3/2}$. The stop-and-go wave state is shown in red, while the homogeneous state is depicted in black.

Details on Fig. 4.7 (back on page 96) In Fig. 4.7, we conduct simulations for 5000 seconds (which is reasonable to consider the system stationary). Following this, we average the gap standard deviation over the next 2000 seconds, as defined in Eq. (4.6). This process is repeated for 100 independent Monte Carlo simulations for each noise volatility level, which ranges from 0 to 1 in increments of 0.02. We apply this to each of the four stochastic car-following models described by Eq. (D.4)–Eq. (D.8). In the figure, the curves represent the mean values from these Monte Carlo simulations, while the coloured areas indicate the range of variation between the minimum and maximum values.

Details on Fig. 4.8 (back on page 97) In Fig. 4.8, we conducted simulations for 5000 seconds, a sufficient duration to consider the system stationary. Subsequently, we calculated the distribution of φ , as defined in Eq. (4.6), over the following 2000 seconds. This procedure was repeated for 1000 independent Monte Carlo simulations.

Details on Fig. 4.9 (back on pages 97, 98)

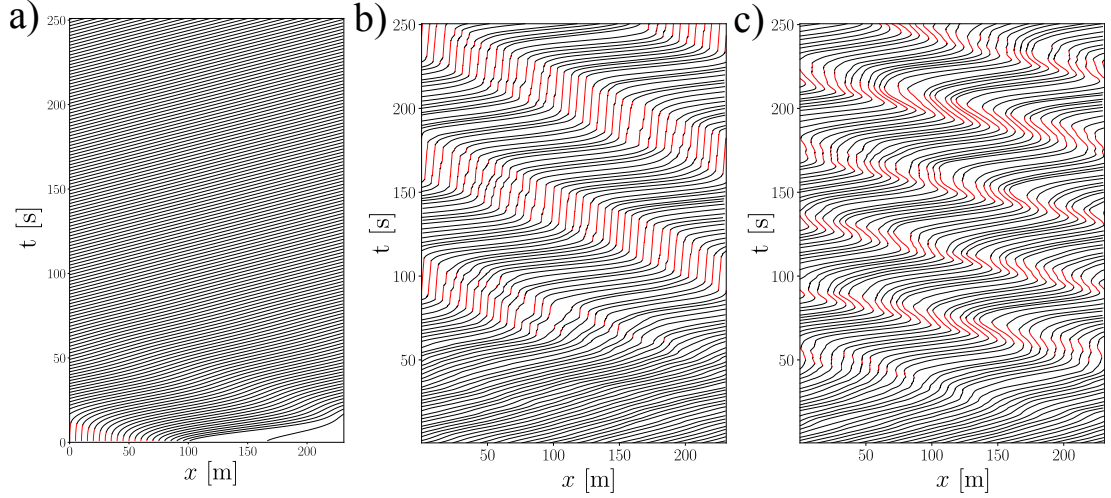


FIGURE D.4: The simulations of the **Stochastic Adaptive Time Gap (SATG)** were performed under three different conditions: with zero noise volatility (σ) and no amplitude (A) for the oscillatory driving **(a)**, with $\sigma = 0.8 \text{ ms}^{-3/2}$ and $A = 1 \text{ ms}^{-3/2}$ **(b)**, with $\sigma = 0.8 \text{ ms}^{-3/2}$ and $A = 9000 \text{ ms}^{-3/2}$ **(c)**. Each scenario involved 22 cars on a road of length 232 m. **a)** Without noise volatility, the system initially displays a stop-and-go wave pattern but eventually stabilises into a homogeneous state. **b)** In this setup, stop-and-go waves are observed, where cars periodically come to a complete stop, as indicated by the red lines. **c)** Here, stop-and-go waves occur, but cars do not remain stopped for long. Instead, they quickly reverse direction, ultimately maintaining a net positive flow. For clarity, the mollifier is present only in front of the white noise and not in front of the oscillating excitation.

D.2 EQUILIBRIUM SOLUTIONS AND LINEAR STABILITY ANALYSIS (BACK ON PAGE 95)

The deterministic biased adaptive time gap car-following model is given for the vehicle $n \in \{1, \dots, N\}$ by

$$\dot{v}_n(t) = F(g_n(t), v_n(t), \Delta v_n(t)) + b_n \quad (\text{D.14})$$

with

$$F(g, v, \Delta v) = \lambda v \left(1 - \frac{Tv}{g} \right) + \frac{v\Delta v}{g}, \quad \lambda, T > 0. \quad (\text{D.15})$$

where $v_n(t)$ is the speed, $g_n(t)$ is the gap, $\Delta v_n(t)$ the speed difference to the predecessor of n -th vehicle at time t as defined previously, λ is the sensitivity parameter, T is the desired time gap parameter, and b_n is the (constant and vehicle specific) bias in the acceleration.

Equilibrium solution We consider $N \geq 2$ vehicles of length $\ell \geq 0$ on a ring of length $L > N\ell$. The gap in a homogeneous configuration is given by

$$\boxed{g_e = L/N - \ell.} \quad (\text{D.16})$$

As a consequence of the bias, the equilibrium solution for which $\dot{v}_n = 0$ for all $n \in \{1, \dots, N\}$ is not a uniform distribution in space. These are the $(v_e, (g_n^e)_{n=1}^N)$ configurations satisfying

$$\begin{cases} \sum_{n=1}^N g_n^e = Ng_e \\ F(g_n^e, v_e, 0) + b_n = 0, \quad \forall n \in \{1, \dots, N\} \end{cases} \quad (\text{D.17})$$

We can deduce from the second part that

$$g_n^e = \frac{\lambda T v_e^2}{b_n + \lambda v_e}, \quad \forall n \in \{1, \dots, N\}, \quad (\text{D.18})$$

while, using the conservation of spacing $\sum_n g_n^e = N g_e$, the equilibrium speed becomes the solution of

$$\sum_{n=1}^N \frac{\lambda T v_e^2}{b_n + \lambda v_e} = N g_e. \quad (\text{D.19})$$

Remark 1. *The equilibrium gaps (D.18) are positive for each vehicle if*

$$v_e > -\frac{1}{\lambda} \min_n b_n. \quad (\text{D.20})$$

Remark 2. *We recover the equilibrium solution of the homogeneous ATG model*

$$\boxed{v_e = \frac{g_e}{T} \quad \text{and} \quad g_n^e = g_e \text{ for all } n \in \{1, \dots, N\},} \quad (\text{D.21})$$

if the biases are zero, i.e., $b_n = 0$ for all $n \in \{1, \dots, N\}$.

Remark 3. *In the case where the bias $b_n = b$ is identical for all vehicles $n \in \{1, \dots, N\}$, we have directly*

$$\frac{\lambda T v_e^2}{b + \lambda v_e} = g_e \quad (\text{D.22})$$

Assuming $b > -\lambda v_e$ (see (D.20)), we obtain

$$\lambda T v_e^2 - (b + \lambda v_e) g_e = 0, \quad (\text{D.23})$$

and we can deduce that

$$\boxed{v_e = \frac{g_e \lambda + \sqrt{(g_e \lambda)^2 + 4 \lambda T b g_e}}{2 \lambda T} = \frac{g_e}{2T} \left(1 + \sqrt{1 + \frac{4Tb}{\lambda g_e}} \right)} \quad (\text{D.24})$$

The equilibrium speed exists if $1 + \frac{4Tb}{\lambda g_e} \geq 0$ and we obtain the condition

$$b \geq -\frac{\lambda g_e}{4T}. \quad (\text{D.25})$$

Note that (D.25) implies the preliminary condition $b > -\lambda v_e$.

Linearisation of the system The partial derivatives of the model (D.15) at equilibrium are given by

$$\begin{aligned} f_n^g &= \frac{\partial F}{\partial g}(g_n^e, v_e, 0) = \frac{\lambda T v_e^2}{(g_n^e)^2}, & f_n^v &= \frac{\partial F}{\partial v}(g_n^e, v_e, 0) = \lambda \left(1 - \frac{2T v_e}{g_n^e}\right), \\ \text{and } f_n^{\Delta v} &= \frac{\partial F}{\partial \Delta v}(g_n^e, v_e, 0) = \frac{v_e}{g_n^e} \end{aligned} \quad (\text{D.26})$$

The characteristic equation of the resulting linear ODE system reads

$$\prod_{n=1}^N [z^2 - z(f_n^v - f_n^{\Delta v}) + f_n^g] - e^{-i\theta N} \prod_{n=1}^N [z f_n^{\Delta v} + f_n^g] = 0, \quad z \in \mathbb{C}, \theta \in [0, 2\pi]. \quad (\text{D.27})$$

A sufficient general linear stability condition for which all eigenvalues z have non-positive real parts, except one equal to zero (due to the periodic boundaries), is given by Ngoduy (2015, Eq. (5))

$$\sum_{n=1}^N \left[\frac{1}{2} \left(\frac{f_n^v}{f_n^g} \right)^2 - \frac{f_n^v f_n^{\Delta v}}{f_n^g f_n^g} - \frac{1}{f_n^g} \right] \geq 0. \quad (\text{D.28})$$

We have

$$\frac{f_n^v}{f_n^g} = \frac{\lambda \left(1 - \frac{2T v_e}{g_n^e}\right)}{\frac{\lambda T v_e^2}{(g_n^e)^2}} = \frac{g_n^e (g_n^e - 2T v_e)}{T v_e^2}, \quad (\text{D.29})$$

while

$$\frac{f_n^v f_n^{\Delta v}}{f_n^g f_n^g} = \frac{\lambda \left(1 - \frac{2T v_e}{g_n^e}\right) \frac{v_e}{g_n^e}}{\frac{\lambda^2 T^2 v_e^4}{(g_n^e)^4}} = \frac{(g_n^e)^2 (g_n^e - 2T v_e)}{\lambda T^2 v_e^3}. \quad (\text{D.30})$$

The sufficient linear stability condition (D.28) is then given by

$$\sum_{n=1}^N \left[\frac{1}{2} \left(\frac{g_n^e (g_n^e - 2T v_e)}{T v_e^2} \right)^2 - \frac{(g_n^e)^2 (g_n^e - 2T v_e)}{\lambda T^2 v_e^3} - \frac{(g_n^e)^2}{\lambda T v_e^2} \right] \geq 0, \quad (\text{D.31})$$

or again

$$\begin{aligned} \sum_{n=1}^N (g_n^e)^2 \left[\frac{\lambda (g_n^e - 2T v_e)^2}{2T v_e^2} - \frac{g_n^e - 2T v_e}{T v_e} - 1 \right] \\ = \sum_{n=1}^N (g_n^e)^2 \left[\frac{\lambda (g_n^e - 2T v_e)^2}{2T v_e^2} - \frac{g_n^e - T v_e}{T v_e} \right] \geq 0. \end{aligned} \quad (\text{D.32})$$

Then, using $g_n^e = \frac{\lambda T v_e^2}{b_n + \lambda v_e}$ and remarking that $g_n^e - 2T v_e = -T v_e \frac{2b_n + \lambda v_e}{b_n + \lambda v_e}$ while $g_n^e - T v_e = -T v_e \frac{b_n}{b_n + \lambda v_e}$, we obtain

$$\sum_{n=1}^N \left(\frac{\lambda T v_e^2}{b_n + \lambda v_e} \right)^2 \left[\frac{\left(T v_e \frac{2b_n + \lambda v_e}{b_n + \lambda v_e} \right)^2}{2T v_e^2} + \frac{T v_e \frac{b_n}{b_n + \lambda v_e}}{T v_e} \right] \geq 0. \quad (\text{D.33})$$

After simplifications (we have $\lambda, T, v_e > 0$), it follows

$$\sum_{n=1}^N \frac{1}{(b_n + \lambda v_e)^2} \left[\frac{\lambda T}{2} \left(\frac{2b_n + \lambda v_e}{b_n + \lambda v_e} \right)^2 + \frac{b_n}{b_n + \lambda v_e} \right] \geq 0, \quad (\text{D.34})$$

or again

$$\sum_{n=1}^N \frac{1}{(b_n + \lambda v_e)^4} \left[\frac{\lambda T}{2} (2b_n + \lambda v_e)^2 + b_n(b_n + \lambda v_e) \right] \geq 0. \quad (\text{D.35})$$

We have

$$\begin{aligned} \frac{\lambda T}{2} (2b_n + \lambda v_e)^2 + b_n(b_n + \lambda v_e) &= 2\lambda T b_n^2 + \frac{1}{2} \lambda^3 T v_e^2 + 2\lambda^2 T b_n v_e + b_n^2 + b_n \lambda v_e \\ &= b_n^2 (2\lambda T + 1) + b_n (2\lambda T + 1) \lambda v_e + \frac{1}{2} \lambda^3 T v_e^2 \\ &= b_n (2\lambda T + 1) (b_n + \lambda v_e) + \frac{1}{2} \lambda^3 T v_e^2, \end{aligned} \quad (\text{D.36})$$

and the linear stability condition can be written

$$\boxed{\sum_{n=1}^N \frac{b_n (2\lambda T + 1)}{(b_n + \lambda v_e)^3} + \frac{\lambda^3 T v_e^2}{2(b_n + \lambda v_e)^4} \geq 0.} \quad (\text{D.37})$$

Remark 4. Since $\lambda, T > 0$, the model is unconditionally linearly stable if $b_n = 0$ for all $b_n \in \{1, \dots, N\}$. Indeed the homogeneous ATG model is unconditionally linearly stable [Khound et al. \(2023\)](#).

Remark 5. When all the biases are identical, i.e., $b_n = b > -\lambda g_e / (4T)$ for all $b_n \in \{1, \dots, N\}$, dividing by $\lambda T v_e^2$ the last line of (D.36) and using (D.22), we obtain the linear stability condition of the ATG model

$$\frac{b(2\lambda T + 1)}{g_e} + \frac{\lambda^2}{2} \geq 0. \quad (\text{D.38})$$

This is

$$\boxed{b \geq \frac{-\lambda^2 g_e}{4T\lambda + 2}.} \quad (\text{D.39})$$

The bias has to be negative and sufficiently low, especially for high λ or low T , to destabilise the system.

D.3 EXTENDED STABILITY ANALYSIS OF THE PERIODICALLY DRIVEN SYSTEM (BACK ON PAGE 98)

This Section details the extended stability analysis of the car-following system in which the noise term is substituted by an externally applied deterministic cyclic driving, with vanishing residual noise:

$$\dot{v}_n(t) = F(\Delta x_n(t), v_n(t), v_{n+1}(t)) + C \cos(\omega t + \varphi_n). \quad (\text{D.40})$$

We assume that the driving frequency is low enough so that a pseudo-stationary approximation can be performed, i.e., at each time t the system follows the biased deterministic equation of Eq. (D.14) with $b_n = \cos(\omega t + \varphi_n)$. Perturbations around the thus grow at rates ν given by the real parts of the eigenvalues z given by Eq. (D.27). Unfortunately, finding the roots z of this equation is far from straightforward analytically. The equation is thus solved numerically, first by deducing the equilibrium speed from Eq. (D.19) and the associated gaps, and then finding the nontrivial complex roots $z \neq 0$ (the eigenvalue 0 is not relevant physically) of Eq. (D.27) using a Newton-Raphson method with multiple starting points located on a regular lattice in complex space; we check that no eigenvalue has been missed by quadrupling the number of starting points. Numerically, identifying that z is a root of Eq. (D.27) can be challenging for small λ or large T because a quasi-continuum of z values yield a vanishingly small, but nonzero products. Accordingly, the validity of candidate roots is checked by

calculating the ratio of the two products. We denote by $\nu(\{b_n\}) = \max \Re(z)$ the largest growth rate over all roots z .

If the eigenmode associated with this growth rate is roughly the same throughout the cycle (which is reasonable, because it tends to be the mode with the largest possible wavelength in the system), then the fastest growing perturbation (under our pseudo-stationary assumption) will unfurl as

$$\exp\left(\int_0^{2\pi} \frac{dx}{\omega} \nu(\{C \cos(x + \varphi_n)\})\right) \quad (\text{D.41})$$

over a period, hence an effective growth rate

$$\nu_{\text{eff}}(C) = \langle \nu(\{C \cos(x_n)\}) \rangle_x, \quad (\text{D.42})$$

where x_n is used as a shorthand for $x + \varphi_n$ and the angular brackets denote an average over $x \in [0, 2\pi[$. We surmise that averaging $\nu_{\text{eff}}(C)$ over random, uniformly distributed phases φ_n is tantamount to averaging it over uniformly distributed x_n in $\mathbb{R}/2\pi\mathbb{Z}$. Numerical simulations confirm that this is a decent approximation.

BIBLIOGRAPHY

- Augustus Ababio-Donkor, Wafaa Saleh, and Achille Fonzone. Understanding transport mode choice for commuting: the role of affect. *Transportation planning and technology*, 43(4):385–403, 2020. URL <https://doi.org/10.1080/03081060.2020.1747203>. (Cited on page 7.)
- M. Ahmed and A. Farag. Nonmetric calibration of camera lens distortion: Differential methods and robust estimation. *IEEE Transactions on Image Processing*, 14(8):1215–1230, August 2005. ISSN 1941-0042. URL <https://doi.org/10.1109/TIP.2005.846025>. (Cited on page 117.)
- Javad Amirian, Bingqing Zhang, Francisco Valente Castro, Juan Jose Baldelomar, Jean-Bernard Hayet, and Julien Pettré. Opentraj: Assessing prediction complexity in human trajectories datasets. In *Proceedings of the asian conference on computer vision*, 2020. URL https://doi.org/10.1007/978-3-030-69544-6_34. (Cited on page 45.)
- Archives Municipales de Lyon. Hôtel de ville, 2024. URL https://www.archives-lyon.fr/pages/hotel_ville. Accessed: 2024-08-18. (Cited on page 49.)
- Nicolas Bain and Denis Bartolo. Dynamic response and hydrodynamics of polarized crowds. *Science*, 363(6422): 46–49, January 2019. doi: 10.1126/science.aat9891. URL <https://doi.org/10.1126/science.aat9891>. (Cited on page 17.)
- Michele Ballerini, Nicola Cabibbo, Raphael Candelier, Andrea Cavagna, Evaristo Cisbani, Irene Giardina, Vivien Lecomte, Alberto Orlandi, Giorgio Parisi, Andrea Procaccini, et al. Interaction ruling animal collective behavior depends on topological rather than metric distance: Evidence from a field study. *Proceedings of the national academy of sciences*, 105(4):1232–1237, 2008. URL <https://doi.org/10.1073/pnas.0711437105>. (Cited on page 19.)
- M. Bando, K. Hasebe, A. Nakayama, A. Shibata, and Y. Sugiyama. Dynamical model of traffic congestion and numerical simulation. *Physical Review E*, 51(2):1035–1042, 1995. URL <https://doi.org/10.1103/PhysRevE.51.1035>. (Cited on pages 91, 94, and 142.)
- Masako Bando, Katsuya Hasebe, Ken Nakanishi, and Akihiro Nakayama. Analysis of optimal velocity model with explicit delay. *Physical Review E*, 58(5):5429, 1998. URL <https://doi.org/10.1103/PhysRevE.58.5429>. (Cited on page 91.)
- R. Barlovic, L. Santen, A. Schadschneider, and M. Schreckenberg. Metastable states in cellular automata for traffic flow. *The European Physical Journal B*, 5:793–800, 1998. URL <https://doi.org/10.1007/s100510050504>. (Cited on page 94.)
- Roy F. Baumeister and Brad J. Bushman. *Social Psychology and Human Nature*. Wadsworth Publishing, 1st edition, 2007. URL <https://www.buchah.ch/detail/ISBN-9780357946305/Baumeister-Roy-F./Social-Psychology-and-Human-Nature>. (Cited on page 7.)
- Gordon M Becker, Morris H DeGroot, and Jacob Marschak. Stochastic models of choice behavior. *Behavioral science*, 8(1):41–55, 1963. URL <https://doi.org/10.1002/bs.3830080106>. (Cited on page 14.)
- Nicola Bellomo and Christian Dogbe. On the modelling crowd dynamics from scaling to hyperbolic macroscopic models. *Mathematical Models and Methods in Applied Sciences*, 18(supp01):1317–1345, 2008. URL <https://doi.org/10.1142/S0218202508003054>. (Cited on page 16.)
- Ioana Bena, Chaouqi Misbah, and Alexandre Valance. Nonlinear evolution of a terrace edge during step-flow growth. *Physical Review B*, 47(12):7408–7419, March 1993. doi: 10.1103/PhysRevB.47.7408. URL <https://doi.org/10.1103/PhysRevB.47.7408>. (Cited on page 21.)
- P Bergé. Aspects expérimentaux de l’instabilité thermique de rayleigh-benard. *Le Journal de Physique Colloques*, 37 (C1):C1–23, 1976. URL <https://dx.doi.org/10.1051/jphyscol:1976105>. (Cited on page 93.)
- Joseph Berkson. Application of the logistic function to bio-assay. *Journal of the American statistical association*, 39 (227):357–365, 1944. URL <https://www.tandfonline.com/doi/pdf/10.1080/01621459.1944.10500699>. (Cited on page 14.)
- Andrew Best, Sahil Narang, Sean Curtis, and Dinesh Manocha. Densesense: Interactive crowd simulation using density-dependent filters. In *Symposium on Computer Animation*, pages 97–102, 2014. URL <https://doi.org/10.2312/sca.20141127>. (Cited on page 45.)

- Andrew Best, Sahil Narang, and Dinesh Manocha. Real-time reciprocal collision avoidance with elliptical agents. In *2016 IEEE International Conference on Robotics and Automation (ICRA)*, pages 298–305. IEEE, 2016. URL <https://doi.org/10.1109/ICRA.2016.7487148>. (Cited on pages 29 and 30.)
- Maik Boltes and Armin Seyfried. Collecting pedestrian trajectories. *Neurocomputing*, 100(0):127–133, 2013a. ISSN 0925-2312. URL <https://doi.org/10.1016/j.neucom.2012.01.036>. (Cited on page 48.)
- Maik Boltes and Armin Seyfried. Collecting pedestrian trajectories. *Neurocomputing*, 100:127–133, 2013b. URL <https://doi.org/10.1016/j.neucom.2012.01.036>. (Cited on page 48.)
- Jean-Yves Bouguet. Pyramidal implementation of the lucas kanade feature tracker: Description of the algorithm. Technical report, Intel Corporation Microprocessor Research Labs, 2004. URL http://robots.stanford.edu/cs223b04/algo_tracking.pdf. (Cited on page 49.)
- Piet H Bovy and Eliahu Stern. *Route choice: Wayfinding in transport networks: Wayfinding in transport networks*, volume 9. Springer Science & Business Media, 2012. URL <https://doi.org/10.1007/978-94-009-0633-4>. (Cited on pages 13 and 14.)
- Marcus Brazil, Ronald L Graham, Doreen A Thomas, and Martin Zachariassen. On the history of the euclidean steiner tree problem. *Archive for history of exact sciences*, 68:327–354, 2014. URL <https://doi.org/10.1007/s00407-013-0127-z>. (Cited on page 9.)
- Luca Bruno, Andrea Tosin, Paolo Triccerri, and Fiammetta Venuti. Non-local first-order modelling of crowd dynamics: A multidimensional framework with applications. *Applied Mathematical Modelling*, 35(1):426–445, 2011. URL <https://doi.org/10.1016/j.apm.2010.07.007>. (Cited on pages 16 and 17.)
- Marin Bukov. Reinforcement learning for autonomous preparation of floquet-engineered states: Inverting the quantum kapitza oscillator. *Physical Review B*, 98(22):224305, 2018. URL <https://doi-org.docelec.uni-v-lyon1.fr/10.1103/PhysRevB.98.224305>. (Cited on page 93.)
- C Burstedde, K Klauack, A Schadschneider, and J Zittartz. Simulation of pedestrian dynamics using a two-dimensional cellular automaton. *Physica A: Statistical Mechanics and its Applications*, 295(3):507–525, June 2001. ISSN 0378-4371. doi: 10.1016/S0378-4371(01)00141-8. URL [https://doi.org/10.1016/S0378-4371\(01\)00141-8](https://doi.org/10.1016/S0378-4371(01)00141-8). (Cited on page 15.)
- Eugene I. Butikov. Kapitza pendulum : A physically transparent simple explanation. , 2017. URL <https://api.semanticscholar.org/CorpusID:42824256>. (Cited on pages 90 and 93.)
- Scott Camazine, Jean-Louis Deneubourg, Nigel R Franks, James Sneyd, Guy Theraula, and Eric Bonabeau. Self-organization in biological systems. In *Self-Organization in Biological Systems*. Princeton university press, 2020. URL <https://www.degruyter.com/document/doi/10.1515/9780691212920/html>. (Cited on page 106.)
- Liyu Cao and Joachim Gross. Cultural differences in perceiving sounds generated by others: Self matters. *Frontiers in psychology*, 6:1865, 2015. URL <https://doi.org/10.3389/fpsyg.2015.01865>. (Cited on page 38.)
- Shuchao Cao, Armin Seyfried, Jun Zhang, Stefan Holl, and Weiguo Song. Fundamental diagrams for multidirectional pedestrian flows. *Journal of Statistical Mechanics: Theory and Experiment*, 2017(3):033404, 2017. URL <https://doi.org/10.1088/1742-5468/aa620d>. (Cited on page 44.)
- Fryar Cd, Gu Q, and Ogden Cl. Anthropometric reference data for children and adults: United States, 2007-2010. *Vital and health statistics. Series 11, Data from the National Health Survey*, October 2012. ISSN 0083-1980. URL https://www.cdc.gov/nchs/data/series/sr_03/sr03_039.pdf. (Cited on page 72.)
- David Chandler. Introduction to modern statistical. *Mechanics. Oxford University Press, Oxford, UK*, 5(449):11, 1987. URL https://pcossgroup.xmu.edu.cn/old/users/xlu/group/courses/apc/ims_m_chandler.pdf. (Cited on page 40.)
- Robert E Chandler, Robert Herman, and Elliott W Montroll. Traffic dynamics: studies in car following. *Operations Research*, 6(2):165–184, 1958. URL <https://doi.org/10.1287/opre.6.2.165>. (Cited on page 91.)
- Satish Chandra and Anish Kumar Bharti. Speed distribution curves for pedestrians during walking and crossing. *Procedia-Social and Behavioral Sciences*, 104:660–667, 2013. URL <https://doi.org/10.1016/j.sbspro.2013.11.160>. (Cited on page 81.)
- Jun Chen, Xinran Lehto, Mark Lehto, and Jonathon Day. Can colored sidewalk nudge city tourists to walk? an experimental study of the effect of nudges. *Tourism Management*, 95:104683, 2023. URL <https://doi.org/10.1016/j.tourman.2022.104683>. (Cited on pages 11 and 12.)
- Xu Chen, Martin Treiber, Venkatesan Kanagaraj, and Haiying Li. Social force models for pedestrian traffic–state of the art. *Transport reviews*, 38(5):625–653, 2018. URL <https://doi.org/10.1080/01441647.2017.1396265>. (Cited on pages 1, 17, 28, 106, and 107.)
- Mohcine Chraïbi, Armin Seyfried, and Andreas Schadschneider. Generalized centrifugal force model for pedestrian dynamics. *Physical Review E*, 82:046111, 2010. URL <https://doi.org/10.1103/PhysRevE.82.046111>. (Cited on page 32.)
- Gabriele Bleser Christiano Gava. 3d computer vision lecture 4, 2011. URL https://web.archive.org/web/20171226115739/https://ags.cs.uni-kl.de/fileadmin/inf_ags/3dcv-ws11-12/3DCV_WS11-12_lec04.pdf. (Cited on page 113.)
- Communication Theory Collective. Proxemics and its types – explained with examples, 2022. URL <https://www.communicationtheory.org/proxemics-and-its-types-explained-with-examples/>. (Cited on page 38.)
- Alessandro Corbetta, Chung-min Lee, Roberto Benzi, Adrian Muntean, and Federico Toschi. Fluctuations around mean walking behaviors in diluted pedestrian flows. *Physical Review E*, 95(3):032316, March 2017. doi: 10.1103/PhysRevE.95.032316. URL <https://doi.org/10.1103/PhysRevE.95.032316>. (Cited on page 137.)

BIBLIOGRAPHY

- Jakob Cordes, Andreas Schadschneider, and Alexandre Nicolas. Dimensionless numbers reveal distinct regimes in the structure and dynamics of pedestrian crowds. *PNAS nexus*, 3(4):pgae120, 2024. URL <https://doi.org/10.1093/pnasnexus/pgae120>. (Cited on page 45.)
- Vincenzo Coscia and Cinzia Canavesio. First-order macroscopic modelling of human crowd dynamics. *Mathematical Models and Methods in Applied Sciences*, 18(supp01):1217–1247, 2008. URL <https://doi.org/10.1142/S0218202508003017>. (Cited on pages 15 and 16.)
- JE Cotes and F Meade. The energy expenditure and mechanical energy demand in walking. *Ergonomics*, 3(2): 97–119, 1960. URL <https://doi.org/10.1080/00140136008930473>. (Cited on pages 36 and 135.)
- Felipe Cucker and Steve Smale. Emergent behavior in flocks. *IEEE Transactions on automatic control*, 52(5):852–862, 2007. URL <https://doi.org/10.1109/TAC.2007.895842>. (Cited on page 19.)
- Joe Cusdin. Iventis an event mapping software for collaborative geospatial planning, 2015. URL <https://www.iventis.com>. (Cited on page 7.)
- András Czirók and Tamás Vicsek. Collective behavior of interacting self-propelled particles. *Physica A: Statistical Mechanics and its Applications*, 281(1-4):17–29, 2000. URL [https://doi.org/10.1016/S0378-4371\(00\)00013-3](https://doi.org/10.1016/S0378-4371(00)00013-3). (Cited on page 2.)
- Gregory C Dachner, Trenton D Wirth, Emily Richmond, and William H Warren. The visual coupling between neighbours explains local interactions underlying human ‘flocking’. *Proceedings of the Royal Society B*, 289 (1970):20212089, 2022. URL <https://doi.org/10.1098/rspb.2021.2089>. (Cited on page 19.)
- M Danny Raj and Arvind Nayak. Collective traffic of agents that remember. In *International Conference on Traffic and Granular Flow*, pages 3–10. Springer, 2022. URL https://doi.org/10.1007/978-981-99-7976-9_1. (Cited on page 26.)
- Daria and Roberto. Castel del monte. *ImaginApulia*, 2024. URL <https://imaginapulia.com/points-of-interest/castel-del-monte/>. (Cited on page 78.)
- Supravat Dey, Dibyendu Das, and R Rajesh. Spatial structures and giant number fluctuations in models of active matter. *Physical review letters*, 108(23):238001, 2012. URL <https://doi.org/10.1103/PhysRevLett.108.238001>. (Cited on page 64.)
- Edsger W Dijkstra. A note on two problems in connexion with graphs. In *Edsger Wybe Dijkstra: His Life, Work, and Legacy*, pages 287–290. Springer, 2022. doi: 10.1007/BF01386390. URL <https://doi.org/10.1145/3544585.3544600>. (Cited on page 10.)
- Leo Dorst and Karen Trovato. Optimal path planning by cost wave propagation in metric configuration space. In *Mobile Robots III*, volume 1007, pages 186–197. SPIE, 1989. URL <https://doi.org/10.1117/12.949097>. (Cited on page 11.)
- Oscar Dufour, Huu-Tu Dang, Jakob Cordes, Raphael Korbmacher, Gaudou Benoit, Mohcine Chraïbi, Alexandre Nicolas, and Antoine Tordeux. Dense Crowd Dynamics and Pedestrian Trajectories: A Multiscale Field Study at the Fête des Lumières in Lyon, 2024a. URL <https://doi.org/10.5281/zenodo.13830435>. (Cited on page 43.)
- Oscar Dufour, Huu-Tu Dang, Jakob Cordes, Raphael Korbmacher, Gaudou Benoit, Mohcine Chraïbi, Alexandre Nicolas, and Antoine Tordeux. Dense Crowd Dynamics and Pedestrian Trajectories: A Multiscale Field Study at the Fête des Lumières in Lyon » GPS traces and physical contacts , 2024b. URL <https://doi.org/10.5281/zenodo.13830435>. (Cited on page 43.)
- Oscar Dufour, Huu-Tu Dang, Jakob Cordes, Raphael Korbmacher, Gaudou Benoit, Mohcine Chraïbi, Alexandre Nicolas, and Antoine Tordeux. Dense Crowd Dynamics and Pedestrian Trajectories: A Multiscale Field Study at the Fête des Lumières in Lyon » Geometry.csv, 2024c. URL <https://doi.org/10.5281/zenodo.13830435>. (Cited on page 43.)
- Oscar Dufour, Huu-Tu Dang, Jakob Cordes, Raphael Korbmacher, Gaudou Benoit, Mohcine Chraïbi, Alexandre Nicolas, and Antoine Tordeux. Dense Crowd Dynamics and Pedestrian Trajectories: A Multiscale Field Study at the Fête des Lumières in Lyon » TopView trajectories, 2024d. URL <https://doi.org/10.5281/zenodo.13830435>. (Cited on page 43.)
- Oscar Dufour, Huu-Tu Dang, Jakob Cordes, Raphael Korbmacher, Gaudou Benoit, Mohcine Chraïbi, Alexandre Nicolas, and Antoine Tordeux. Dense Crowd Dynamics and Pedestrian Trajectories: A Multiscale Field Study at the Fête des Lumières in Lyon » Surveys , 2024e. URL <https://doi.org/10.5281/zenodo.13830435>. (Cited on page 44.)
- Oscar Dufour, Huu-Tu Dang, Jakob Cordes, Raphael Korbmacher, Gaudou Benoit, Mohcine Chraïbi, Alexandre Nicolas, and Antoine Tordeux. Dense Crowd Dynamics and Pedestrian Trajectories: A Multiscale Field Study at the Fête des Lumières in Lyon. working paper or preprint, September 2024f. URL <https://hal.science/hal-04714451>. (Cited on page 43.)
- Oscar Dufour, Alexandre Nicolas, David Rodney, Antoine Tordeux, Jakob Cordes, and Andreas Schadschneider. Recovering stop-and-go dynamics in traffic flow with noise-induced kapitza’s pendulum instability. *Physical Review Letters*, December 2024g. (Cited on page 90.)
- Oscar Daniel Dufour. *Decoding model for decision task under risk*. PhD thesis, Politecnico di Torino, 2021. URL <https://webthesis.biblio.polito.it/19296/>. (Cited on page 35.)
- A. Dziugys and B. Peters. *Numerical Simulation of the Motion of Granular Material*. Forschungszentrum Karlsruhe, 1998. URL <https://www.sciencedirect.com/science/article/abs/pii/S0045782501003644>. (Cited on pages 32, 74, and 75.)

-
- Ottavia D'Agostino, Serena Castellotti, and Maria Michela Del Viva. Time estimation during motor activity. *Frontiers in human neuroscience*, 17:1134027, 2023. URL <https://doi.org/10.3389/fnhum.2023.1134027>. (Cited on page 13.)
- I. Echeverría-Huarte, I. Zuriguel, and R. C. Hidalgo. Pedestrian evacuation simulation in the presence of an obstacle using self-propelled spherocylinders. *Physical Review E*, 102(1):012907, July 2020. doi: 10.1103/PhysRevE.102.012907. URL <https://doi.org/10.1103/PhysRevE.102.012907>. (Cited on pages 32 and 33.)
- Iñaki Echeverría-Huarte and Alexandre Nicolas. Body and mind: Decoding the dynamics of pedestrians and the effect of smartphone distraction by coupling mechanical and decisional processes. *Transportation research part C: emerging technologies*, 157:104365, 2023. URL <https://doi.org/10.1016/j.trc.2023.104365>. (Cited on pages 28, 42, 63, 70, 71, 82, 83, and 135.)
- Iñaki Echeverría-Huarte, Alexandre Nicolas, Raúl Cruz Hidalgo, Angel Garcimartín, and Iker Zuriguel. Spontaneous emergence of counterclockwise vortex motion in assemblies of pedestrians roaming within an enclosure. *Scientific reports*, 12(1):2647, 2022. URL <https://doi.org/10.1038/s41598-022-06493-0>. (Cited on page 102.)
- Matthias Ehrhardt and Antoine Tordeux. Stability of heterogeneous linear and nonlinear car-following models. *Franklin Open*, 9:100181, 2024. URL <https://doi.org/10.1016/j.fraope.2024.100181>. (Cited on page 90.)
- Cara L Evans, Emily RR Burdett, Keelin Murray, and Malinda Carpenter. When does it pay to follow the crowd? children optimize imitation of causally irrelevant actions performed by a majority. *Journal of Experimental Child Psychology*, 212:105229, 2021. URL <https://doi.org/10.1016/j.jecp.2021.105229>. (Cited on page 34.)
- Salman Faraji, Amy R Wu, and Auke J Ijspeert. A simple model of mechanical effects to estimate metabolic cost of human walking. *Scientific reports*, 8(1):10998, 2018. URL <https://doi.org/10.1038/s41598-018-29429-z>. (Cited on pages 36 and 104.)
- Jérôme Fehrenbach, Jacek Narski, Jiale Hua, Samuel Lemercier, Asja Jelic, Cécile Appert-Rolland, Stéphane Donikian, Julien Pettré, and Pierre Degond. Time-delayed Follow-the-Leader model for pedestrians walking in line. *Networks & Heterogeneous Media*, 10(3):579–608, 2015. ISSN 1556-181X. doi: 10.3934/nhm.2015.10.579. URL <https://doi.org/10.3934/nhm.2015.10.579>. (Cited on pages 14 and 18.)
- Sina Feldmann and Juliane Adrian. Forward propagation of a push through a row of people. *Safety Science*, 164:106173, August 2023. ISSN 0925-7535. doi: 10.1016/j.ssci.2023.106173. URL <https://doi.org/10.1016/j.ssci.2023.106173>. (Cited on pages 83 and 84.)
- C. Feliciani. *Measurement and numerical modeling of pedestrian flows*. PhD thesis, University of Tokyo, 2017. URL <https://repository.dl.itc.u-tokyo.ac.jp/record/52504/files/A34319.pdf>. (Cited on pages 8, 58, and 119.)
- Claudio Feliciani, Alessandro Corbetta, Milad Haghani, and Katsuhiko Nishinari. Trends in crowd accidents based on an analysis of press reports. *Safety science*, 164:106174, 2023. URL <https://doi.org/10.1016/j.ssci.2023.106174>. (Cited on page 44.)
- Adriano Festa, Andrea Tosin, and Marie-Therese Wolfram. Kinetic description of collision avoidance in pedestrian crowds by sidestepping. *Kinetic & Related Models*, 11(3):491–520, 2018. ISSN 1937-5077. doi: 10.3934/krm.2018022. URL <https://doi.org/10.48550/arXiv.1610.05056>. (Cited on pages 14, 15, and 40.)
- DJ Finney. The estimation from individual records of the relationship between dose and quantal response. *Biometrika*, 34(3/4):320–334, 1947. URL <https://doi.org/10.2307/2332443>. (Cited on page 14.)
- Peter C Fishburn, Peter C Fishburn, et al. *Utility theory for decision making*. Krieger NY, 1979. URL <https://apps.dtic.mil/sti/citations/AD0708563>. (Cited on page 33.)
- Kimberly Fisher and John Robinson. Daily routines in 22 countries: Diary evidence of average daily time spent in thirty activities. *FISHER, Kimberly; ROBINSON, John. Technical Paper. Oxford: Centre of Time Use Research*, 2010. URL https://www.timeuse.org/sites/default/files/public/ctur_technical_paper/869/CTUR_Technical_Paper_2010-01.pdf. (Cited on page 7.)
- Forschungszentrum Jülich. Pedestrian dynamics data archive, 2020. URL <https://ped.fz-juelich.de/dataarchive/doku.php>. (Cited on pages 44 and 119.)
- Martin Friesen, Hanno Gottschalk, Barbara Rüdiger, and Antoine Tordeux. Spontaneous wave formation in stochastic self-driven particle systems. *SIAM Journal on Applied Mathematics*, 81(3):853–870, 2021. URL <https://doi.org/10.1137/20M1315567>. (Cited on pages 94 and 142.)
- Michel Fruchart, Ryo Hanai, Peter B Littlewood, and Vincenzo Vitelli. Non-reciprocal phase transitions. *Nature*, 592(7854):363–369, 2021. URL <https://doi.org/10.1038/s41586-021-03375-9>. (Cited on page 99.)
- John Joseph Fruin. *Designing for pedestrians a level of service concept*. Polytechnic University, 1970. URL <https://www.proquest.com/openview/3c12613f79ad5037d1379872a5851932/1?pq-origsite=gscholar&cbl=18750&diss=y>. (Cited on pages 44 and 45.)
- Alessandro Gabbana, Federico Toschi, Philip Ross, Antal Haans, and Alessandro Corbetta. Fluctuations in pedestrian dynamics routing choices. *PNAS nexus*, 1(4):pgac169, 2022. URL <https://doi.org/10.1093/pnasnexus/pgac169>. (Cited on page 12.)
- Jason AC Gallas and Stefan Sokolowski. Grain non-sphericity effects on the angle of repose of granular material. *International Journal of Modern Physics B*, 7(09n10):2037–2046, 1993. URL <https://doi.org/10.1142/S0217979293002754>. (Cited on page 32.)

- Deep Ganguli and Eero P Simoncelli. Efficient sensory encoding and bayesian inference with heterogeneous neural populations. *Neural computation*, 26(10):2103–2134, 2014. URL https://doi.org/10.1162/NECO_a_00638. (Cited on page 34.)
- Angel Garcimartín, Daniel R Parisi, Jose M Pastor, César Martín-Gómez, and Iker Zuriguel. Flow of pedestrians through narrow doors with different competitiveness. *Journal of Statistical Mechanics: Theory and Experiment*, 2016(4):043402, 2016. URL <https://doi.org/10.1088/1742-5468/2016/04/043402>. (Cited on page 33.)
- A. Garcimartín, J.M. Pastor, C. Martín-Gómez, D. Parisi, and I. Zuriguel. Evacuation narrow door dataset, 2013. URL <http://ped.fz-juelich.de/extda/garcimartin2013>. Data collected during evacuation drills at the University of Navarra, Pamplona, Spain on October 26th, 2013. (Cited on pages 70, 84, and 86.)
- Crispin Gardiner. *Elements of Stochastic Methods*. AIP Publishing LLC, 2021. ISBN 978-0-7354-2368-8. doi: 10.1063/9780735423718. URL <https://doi.org/10.1063/9780735423718>. (Cited on pages 90 and 97.)
- Gereshes. Kapitza’s pendulum, February 2019. URL <https://gereshes.com/2019/02/25/kapitzas-pendulum/>. (Cited on page 93.)
- Martin Gérin-Lajoie, Carol L Richards, Joyce Fung, and Bradford J McFadyen. Characteristics of personal space during obstacle circumvention in physical and virtual environments. *Gait & posture*, 27(2):239–247, 2008. URL <https://doi.org/10.1016/j.gaitpost.2007.03.015>. (Cited on page 39.)
- James J Gibson. *The perception of the visual world*. Houghton Mifflin, 1950. URL <https://psycnet.apa.org/record/1951-04286-000>. (Cited on page 16.)
- Robert L Goldstone and Michael E Roberts. Self-organized trail systems in groups of humans. *Complexity*, 11(6): 43–50, 2006. URL <https://doi.org/10.1002/cplx.20135>. (Cited on page 9.)
- PA Golovinski and VA Dubinkin. Quantum states of the kapitza pendulum. *Russian Physics Journal*, 65(1):21–32, 2022. URL <https://doi.org/10.1007/s11182-022-02603-7>. (Cited on page 93.)
- Luis Gómez-Nava, Richard Bon, and Fernando Peruani. Intermittent collective motion in sheep results from alternating the role of leader and follower. *Nature Physics*, 18(12):1494–1501, 2022. URL <https://doi.org/10.1038/s41567-022-01769-8>. (Cited on page 34.)
- Claire C. Gordon, Cynthia L. Blackwell, Bruce Bradtmiller, Joseph L. Parham, Patricia Barrientos, Stephen P. Paquette, Brian D. Corner, Jeremy M. Carson, Joseph C. Venezia, Belva M. Rockwell, Michael Mucher, and Shirley Kristensen. 2012 anthropometric survey of u.s. army personnel: Methods and summary statistics. Technical report, Defense Technical Information Center, 2012a. URL <https://apps.dtic.mil/sti/citations/ADA611869>. Database available at <https://ph.health.mil/topics/workplacehealth/ergo/Pages/Aanthropometric-Database.aspx>. (Cited on pages 69, 72, and 73.)
- Claire C. Gordon, Cynthia L. Blackwell, Bruce Bradtmiller, Joseph L. Parham, Patricia Barrientos, Stephen P. Paquette, Brian D. Corner, Jeremy M. Carson, Joseph C. Venezia, Belva M. Rockwell, Michael Mucher, and Shirley Kristensen. 2012 anthropometric survey of u.s. army personnel: Methods and summary statistics. Technical Report NATICK/TR-15/007, U.S. Army Natick Soldier Research, Development and Engineering Center, Natick, Massachusetts 01760-2642, December 2012b. URL <http://tools.openlab.psu.edu/publicData/ANSURII-TR15-007.pdf>. Approved for public release; distribution is unlimited. (Cited on page 71.)
- Simone Göttlich, Sebastian Kühn, Jan Peter Ohst, Stefan Ruzika, and Markus Thiemann. Evacuation dynamics influenced by spreading hazardous material. *Networks and heterogeneous media*, 6(3):443–464, 2011. URL <https://doi.org/10.3934/nhm.2011.6.443>. (Cited on pages 14 and 15.)
- George Gunter, Derek Gloudemans, Raphael E Stern, Sean McQuade, Rahul Bhadani, Matt Bunting, Maria Laura Delle Monache, Roman Lysecky, Benjamin Seibold, Jonathan Sprinkle, et al. Are commercially implemented adaptive cruise control systems string stable? *IEEE Transactions on Intelligent Transportation Systems*, 22(11): 6992–7003, 2020. URL <https://doi.org/10.1109/TITS.2020.3000682>. (Cited on page 91.)
- Stephen J Guy and Ioannis Karamouzas. Guide to anticipatory collision avoidance. In *Game AI Pro 360: Guide to Movement and Pathfinding*, pages 159–172. CRC Press, 2019. URL https://www.gameai.pro.com/GameAIPro2/GameAIPro2_Chapter19_Guide_to_Anticipatory_Collision_Avoidance.pdf. (Cited on page 27.)
- Peter K. Haff and Robert S. Anderson. Grain scale simulations of loose sedimentary beds: The example of grain-bed impacts in aeolian saltation. *Sedimentology*, 40(2):175–198, 1993. URL <https://onlinelibrary.wiley.com/doi/abs/10.1111/j.1365-3091.1993.tb01760.x>. (Cited on page 32.)
- Milad Haghani. Empirical methods in pedestrian, crowd and evacuation dynamics: Part ii. field methods and controversial topics. *Safety science*, 129:104760, 2020. URL <https://doi.org/10.1016/j.ssci.2020.104760>. (Cited on page 45.)
- Milad Haghani, Majid Sarvi, and Zahra Shahhoseini. Evacuation behaviour of crowds under high and low levels of urgency: Experiments of reaction time, exit choice and exit-choice adaptation. *Safety science*, 126:104679, 2020. URL <https://doi.org/10.1016/j.ssci.2020.104679>. (Cited on page 45.)
- Edmund T Hall and Edward T Hall. *The hidden dimension*, volume 609. Anchor, 1966. URL https://books.google.fr/books/about/The_Hidden_Dimension.html?id=wZSfCu44DyMC&redir_esc=y. (Cited on pages 37, 38, and 39.)
- Leslie A Hayduk. The shape of personal space: An experimental investigation. *Canadian Journal of Behavioural Science/Revue canadienne des sciences du comportement*, 13(1):87, 1981. URL <https://psycnet.apa.org/doi/10.1037/h0081114>. (Cited on page 39.)
- Heiko Hecht, Robin Welsch, Jana Viehoff, and Matthew R Longo. The shape of personal space. *Acta psychologica*, 193:113–122, 2019. URL <https://doi.org/10.1016/j.actpsy.2018.12.009>. (Cited on page 39.)

- Janne Heikkilä and Olli Silvén. A four-step camera calibration procedure with implicit image correction. In *Proceedings of IEEE computer society conference on computer vision and pattern recognition*, pages 1106–1112. IEEE, 1997. URL <https://doi.org/10.1109/CVPR.1997.609468>. (Cited on pages 109 and 113.)
- Dirk Helbing and Peter Molnar. Social force model for pedestrian dynamics. *Physical review E*, 51(5):4282, 1995. URL <https://doi.org/10.1103/PhysRevE.51.4282>. (Cited on pages 1, 15, 24, 26, and 39.)
- Dirk Helbing, Joachim Keltsch, and Peter Molnar. Modelling the evolution of human trail systems. *Nature*, 388(6637):47–50, 1997. URL <https://doi.org/10.1038/40353>. (Cited on pages 8, 9, and 63.)
- Dirk Helbing, Illés Farkas, and Tamás Vicsek. Simulating dynamical features of escape panic. *Nature*, 407(6803):487–490, September 2000a. ISSN 1476-4687. doi: 10.1038/35035023. URL <https://doi.org/10.1038/35035023>. (Cited on page 26.)
- Dirk Helbing, Illés J Farkas, and Tamás Vicsek. Freezing by heating in a driven mesoscopic system. *Physical review letters*, 84(6):1240, 2000b. URL <https://doi.org/10.1103/PhysRevLett.84.1240>. (Cited on page 99.)
- Dirk Helbing, Anders Johansson, and Habib Zein Al-Abideen. Dynamics of crowd disasters: An empirical study. *Physical Review E—Statistical, Nonlinear, and Soft Matter Physics*, 75(4):046109, 2007. URL <https://doi.org/10.1103/PhysRevE.75.046109>. (Cited on pages 15, 30, 44, and 70.)
- Robert Herman, Elliott W. Montroll, Renfrey B. Potts, and Richard W. Rothery. Traffic dynamics: Analysis of stability in car following. *Operations Research*, 7(1):86–106, 1959. ISSN 0030-364X. URL <https://doi.org/10.1287/opre.7.1.86>. (Cited on page 91.)
- Heinrich Hertz. Über die berührung fester elastischer körper. *Journal für die reine und angewandte Mathematik*, 92: 156–171, 1882. URL <http://eudml.org/doc/148490>. (Cited on page 74.)
- R. C. Hidalgo, D. R. Parisi, and I. Zuriguel. Simulating competitive egress of noncircular pedestrians. *Physical Review E*, 95(4):042319, April 2017. doi: 10.1103/PhysRevE.95.042319. URL <https://doi.org/10.1103/PhysRevE.95.042319>. (Cited on page 33.)
- Andrew P Hills, Najat Mokhtar, and Nuala M Byrne. Assessment of physical activity and energy expenditure: an overview of objective measures. *Frontiers in nutrition*, 1:5, 2014. URL <https://doi.org/10.3389/fnut.2014.00005>. (Cited on page 36.)
- Mario Höcker, Volker Berkhahn, Angelika Kneidl, André Borrmann, and Wolfram Klein. Graph-based approaches for simulating pedestrian dynamics in building models. In *Proc. of the 8th European Conference on Product and Process Modeling (ECPM)*, 2010. URL <https://mediatum.ub.tum.de/doc/1160270/document.pdf>. (Cited on pages 11 and 12.)
- Caroline Hogue and David Newland. Efficient computer simulation of moving granular particles. *Powder Technology*, 78(1):51–66, 1994. URL [https://doi.org/10.1016/0032-5910\(93\)02748-Y](https://doi.org/10.1016/0032-5910(93)02748-Y). (Cited on pages 32, 74, and 75.)
- Audrey Hood. Geometric transformations overview, 2015. URL <https://slideplayer.com/slide/5947730/>. (Cited on page 114.)
- S. P. Hoogendoorn and P. H. L. Bovy. Pedestrian route-choice and activity scheduling theory and models. *Transportation Research Part B: Methodological*, 38(2):169–190, February 2004. ISSN 0191-2615. doi: 10.1016/S0191-2615(03)00007-9. URL [https://doi.org/10.1016/S0191-2615\(03\)00007-9](https://doi.org/10.1016/S0191-2615(03)00007-9). (Cited on pages 5 and 14.)
- Serge Hoogendoorn and Piet H.L. Bovy. Simulation of pedestrian flows by optimal control and differential games. *Optimal Control Applications and Methods*, 24(3):153–172, 2003. ISSN 1099-1514. doi: 10.1002/oca.727. URL <https://doi.org/10.1002/oca.727>. (Cited on page 2.)
- Serge P Hoogendoorn and Winnie Daamen. Pedestrian behavior at bottlenecks. *Transportation science*, 39(2): 147–159, 2005. URL <https://doi.org/10.1287/trsc.1040.0102>. (Cited on page 26.)
- Mark A. Hopkins. Numerical simulation of systems of multitudinous polygonal blocks. Report, Cold Regions Research and Engineering Laboratory (U.S.), December 1992. URL <https://apps.dtic.mil/sti/citations/ADA262556>. (Cited on page 32.)
- Xiangmin Hu, Tao Chen, and Yushan Song. Anticipation dynamics of pedestrians based on the elliptical social force model. *Chaos: An Interdisciplinary Journal of Nonlinear Science*, 33(7), 2023. URL <https://doi.org/10.1063/5.0149995>. (Cited on page 27.)
- Yong-Xian Huang, Ning Guo, Rui Jiang, and Mao-Bin Hu. Instability in car-following behavior: new nagel-schreckenberg type cellular automata model. *Journal of Statistical Mechanics: Theory and Experiment*, 2018(8): 083401, 2018. URL <https://doi.org/10.1088/1742-5468/aad3f9>. (Cited on page 94.)
- Ciaran Hughes, Martin Glavin, Edward Jones, and Patrick Denny. Review of geometric distortion compensation in fish-eye cameras. *IET Irish Signals and Systems Conference*, 2008. URL <https://doi.org/10.1049/cp:20080656>. (Cited on page 117.)
- Véronique Izard and Stanislas Dehaene. Calibrating the mental number line. *Cognition*, 106(3):1221–1247, 2008. URL <https://doi.org/10.1016/j.cognition.2007.06.004>. (Cited on page 13.)
- Rui Jiang, Qingsong Wu, and Zuojin Zhu. Full velocity difference model for a car-following theory. *Physical Review E*, 64:017101, 2001. URL <https://doi.org/10.1103/PhysRevE.64.017101>. (Cited on pages 91, 94, and 142.)
- Rui Jiang, Mao-Bin Hu, HM Zhang, Zi-You Gao, Bin Jia, Qing-Song Wu, Bing Wang, and Ming Yang. Traffic experiment reveals the nature of car-following. *PLoS one*, 9(4):e94351, 2014. URL <https://doi.org/10.1371/journal.pone.0094351>. (Cited on page 55.)

- Rui Jiang, Cheng-Jie Jin, H. M. Zhang, Yong-Xian Huang, Jun-Fang Tian, Wei Wang, Mao-Bin Hu, Hao Wang, and Bin Jia. Experimental and Empirical Investigations of Traffic Flow Instability. *Transportation Research Procedia*, 23:157–173, January 2017a. ISSN 2352-1465. doi: 10.1016/j.trpro.2017.05.010. URL <https://doi.org/10.1016/j.trpro.2017.05.010>. (Cited on page 92.)
- Rui Jiang, Cheng-Jie Jin, HM Zhang, Yong-Xian Huang, Jun-Fang Tian, Wei Wang, Mao-Bin Hu, Hao Wang, and Bin Jia. Experimental and empirical investigations of traffic flow instability. *Transportation research part C: emerging technologies*, 94:83–98, 2018. URL <https://doi.org/10.1016/j.trpro.2017.05.010>. (Cited on pages 91 and 92.)
- Yan-Qun Jiang, Bo-Kui Chen, Bing-Hong Wang, Weng-Fai Wong, and Bing-Yang Cao. Extended social force model with a dynamic navigation field for bidirectional pedestrian flow. *Frontiers of Physics*, 12:1–9, 2017b. URL <https://doi.org/10.1007/s11467-017-0689-3>. (Cited on page 27.)
- Anders Johansson, Dirk Helbing, and Pradyumn K Shukla. Specification of the social force pedestrian model by evolutionary adjustment to video tracking data. *Advances in complex systems*, 10(supp02):271–288, 2007. URL <https://doi.org/10.1142/S0219525907001355>. (Cited on pages 2 and 25.)
- Anders Johansson, Dirk Helbing, Habib Z Al-Abideen, and Salim Al-Bosta. From crowd dynamics to crowd safety: a video-based analysis. *Advances in Complex Systems*, 11(04):497–527, 2008. URL <https://doi.org/10.1142/S0219525908001854>. (Cited on page 50.)
- Dominic Jost and Kai Nagel. *Probabilistic traffic flow breakdown in stochastic car following models*. Springer, 2005. URL https://doi.org/10.1007/3-540-28091-X_9. (Cited on pages 93, 99, and 100.)
- Sidney M Jourard. An exploratory study of body-accessibility 1. *British Journal of Social and Clinical Psychology*, 5(3):221–231, 1966. URL <https://doi.org/10.1111/j.2044-8260.1966.tb00978.x>. (Cited on page 38.)
- Daniel Kahneman and Amos Tversky. Prospect theory: An analysis of decision under risk. *Econometrica*, 47(2):363–391, 1979. URL https://doi.org/10.1142/9789814417358_0006. (Cited on page 13.)
- Ioannis Karamouzas, Peter Heil, Pascal Van Beek, and Mark H Overmars. A predictive collision avoidance model for pedestrian simulation. In *Motion in Games: Second International Workshop, MIG 2009, Zeist, The Netherlands, November 21-24, 2009. Proceedings 2*, pages 41–52. Springer, 2009. URL https://doi.org/10.1007/978-3-642-10347-6_4. (Cited on pages 26 and 27.)
- Ioannis Karamouzas, Brian Skinner, and Stephen J. Guy. Universal Power Law Governing Pedestrian Interactions. *Physical Review Letters*, 113(23):238701, 2014. doi: 10.1103/PhysRevLett.113.238701. URL <https://doi.org/10.1103/PhysRevLett.113.238701>. (Cited on pages 1, 40, 41, 79, and 81.)
- Ioannis Karamouzas, Nick Sohre, Rahul Narain, and Stephen J. Guy. Implicit crowds: Optimization integrator for robust crowd simulation. *ACM Transactions on Graphics*, 36(4):136:1–136:13, July 2017. ISSN 0730-0301. doi: 10.1145/3072959.3073705. URL <https://doi.org/10.1145/3072959.3073705>. (Cited on pages 37, 41, and 54.)
- J Kaupužs, R Mahnke, and RJ Harris. Zero-range model of traffic flow. *Physical Review E*, 72(5):056125, 2005. URL <https://doi.org/10.1103/PhysRevE.72.056125>. (Cited on page 94.)
- Li Ke-Ping and Gao Zi-You. Noise-induced phase transition in traffic flow. *Communications in Theoretical Physics*, 42(3):369, sep 2004. doi: 10.1088/0253-6102/42/3/369. URL <https://dx.doi.org/10.1088/0253-6102/42/3/369>. (Cited on page 94.)
- Parthib Khound, Peter Will, Antoine Tordeux, and Frank Gronwald. Extending the adaptive time gap car-following model to enhance local and string stability for adaptive cruise control systems. *Journal of Intelligent Transportation Systems*, 27(1):36–56, 2023. URL <https://doi.org/10.1080/15472450.2021.1983810>. (Cited on page 148.)
- Benio Kibushi, Shota Hagio, Toshio Moritani, and Motoki Kouzaki. Speed-dependent modulation of muscle activity based on muscle synergies during treadmill walking. *Frontiers in human neuroscience*, 12:4, 2018. URL <https://doi.org/10.3389/fnhum.2018.00004>. (Cited on page 35.)
- Tohru Kidokoro, Ryohei Arai, and Masato Saeki. Investigation of dynamics simulation of granular particles using spherocylinder model. *Granular Matter*, 17(6):743–751, December 2015. ISSN 1434-7636. doi: 10.1007/s10035-015-0595-8. URL <https://doi.org/10.1007/s10035-015-0595-8>. (Cited on page 32.)
- Benedikt Kleinmeier, Benedikt Zönnchen, Marion Gödel, and Gerta Köster. Vadere: An open-source simulation framework to promote interdisciplinary understanding. *Collective Dynamics*, 4, 2019. URL <https://doi.org/10.48550/arXiv.1907.09520>. (Cited on page 7.)
- Peter E. Kloeden and Eckhard Platen. *Numerical Solution of Stochastic Differential Equations*. Stochastic Modelling and Applied Probability. Springer-Verlag Berlin Heidelberg, Berlin, Heidelberg, 1992. ISBN 978-3-540-54062-5. doi: 10.1007/978-3-662-12616-5. URL <https://doi.org/10.1007/978-3-662-12616-5>. (Cited on page 143.)
- Teruhisa S Komatsu and Shin-ichi Sasa. Kink soliton characterizing traffic congestion. *Physical Review E*, 52(5):5574, 1995. URL <https://doi.org/10.1103/PhysRevE.52.5574>. (Cited on pages 17, 21, 22, and 91.)
- EIJI Kometani and TSUNA Sasaki. On the stability of traffic flow (report-i). *Journal of the Operations Research Society of Japan*, 2(1):11–26, 1958. URL https://orsj.org/wp-content/or-archives50/pdf/e_mag/Vol.02_01_011.pdf. (Cited on page 91.)
- Raphael Korbacher and Antoine Tordeux. Review of pedestrian trajectory prediction methods: Comparing deep learning and knowledge-based approaches. *IEEE Transactions on Intelligent Transportation Systems*, 23(12):24126–24144, 2022. URL <https://doi.org/10.1109/TITS.2022.3205676>. (Cited on page 45.)

- Raphael Korbmacher, Alexandre Nicolas, Antoine Tordeux, and Claudia Totzeck. Time-continuous microscopic pedestrian models: an overview. *Crowd Dynamics, Volume 4: Analytics and Human Factors in Crowd Modeling*, pages 55–80, 2023. URL https://doi.org/10.1007/978-3-031-46359-4_3. (Cited on page 31.)
- Stephen Michael Kosslyn. Measuring the visual angle of the mind’s eye. *Cognitive psychology*, 10(3):356–389, 1978. URL [https://doi.org/10.1016/0010-0285\(78\)90004-X](https://doi.org/10.1016/0010-0285(78)90004-X). (Cited on page 16.)
- Gerta Köster, Franz Tremel, and Marion Gödel. Avoiding numerical pitfalls in social force models. *Physical Review E—Statistical, Nonlinear, and Soft Matter Physics*, 87(6):063305, 2013. URL <https://doi.org/10.1103/PhysRevE.87.063305>. (Cited on page 7.)
- Stefan Krauß, Peter Wagner, and Christian Gawron. Continuous limit of the nagel-schreckenberg model. *Physical Review E*, 54(4):3707, 1996. URL <https://doi.org/10.1103/PhysRevE.54.3707>. (Cited on pages 93 and 100.)
- Melissa Kremer, Brandon Haworth, Mubbasir Kapadia, and Petros Faloutsos. Modelling distracted agents in crowd simulations. *The Visual Computer*, 37(1):107–118, 2021. URL <https://doi.org/10.1007/s00371-020-01969-4>. (Cited on page 27.)
- Tobias Kretz. On oscillations in the social force model. *Physica A: Statistical Mechanics and its Applications*, 438:272–285, 2015. URL <https://arxiv.org/pdf/1507.02566>. (Cited on page 26.)
- Charles K Kroell, Dennis C Schneider, and Alan M Nahum. Impact tolerance and response of the human thorax ii. *SAE Transactions*, pages 3724–3762, 1974. URL <https://www.jstor.org/stable/44723986>. (Cited on pages 30 and 31.)
- H. W. Kuhn and A. W. Tucker. Nonlinear programming. In *Proceedings of the Second Berkeley Symposium on Mathematical Statistics and Probability*, pages 481–492. University of California Press, Berkeley, Calif., 1951. URL <https://projecteuclid.org/ebooks/berkeley-symposium-on-mathematical-statistics-and-probability/Proceedings-of-the-Second-Berkeley-Symposium-on-Mathematical-Statistics-and-probability/Chapter/Nonlinear-Programming/bsmsp/1200500249>. (Cited on page 29.)
- Arthur D Kuo. The six determinants of gait and the inverted pendulum analogy: A dynamic walking perspective. *Human movement science*, 26(4):617–656, 2007. URL <https://doi.org/10.1016/j.humov.2007.04.003>. (Cited on page 36.)
- Charlotte Lang, Axel Schleichardt, Frank Warschun, Nico Walter, Daniel Fleckenstein, Fides Berkel, and Olaf Ueberschär. Relationship between longitudinal upper body rotation and energy cost of running in junior elite long-distance runners. *Sports*, 11(10):204, 2023. URL <https://doi.org/10.3390/sports11100204>. (Cited on page 36.)
- Jean-Claude Latombe. *Robot motion planning*, volume 124. Springer Science & Business Media, 1991. URL <https://doi.org/10.1007/978-1-4615-4022-9>. (Cited on page 10.)
- Steven Michael Lavalley. *A Game-Theoretic Framework for Robot Motion Planning*. PhD thesis, University of Illinois at Urbana-Champaign, USA, September 1996. URL <https://citeseerx.ist.psu.edu/document?repid=rep1&type=pdf&doi=7b8f29fbde3f522f7cf7e08ae7f059bb195d920d>. (Cited on page 35.)
- Le Progrès. Fête des lumières 2022 : plus de 2 millions de visiteurs cette année. *Le Progrès*, 12 Dec. 2022. URL <https://www.leprogres.fr/culture-loisirs/2022/12/12/plus-de-2-millions-de-visiteurs-a-la-fete-des-lumieres-la-mairie-affiche-de-bons-chiffres-de-frequentation>. (Cited on page 46.)
- HK Lee, H-W Lee, and D Kim. Macroscopic traffic models from microscopic car-following models. *Physical Review E*, 64(5):056126, 2001. URL <https://doi.org/10.1103/PhysRevE.64.056126>. (Cited on page 20.)
- Alon Lerner, Yiorgos Chrysanthou, and Dani Lischinski. Crowds by example. In *Computer graphics forum*, volume 26, pages 655–664. Wiley Online Library, 2007. URL <https://doi.org/10.1111/j.1467-8659.2007.01089.x>. (Cited on page 46.)
- Michael James Lighthill and Gerald Beresford Whitham. On kinematic waves ii. a theory of traffic flow on long crowded roads. *Proceedings of the royal society of london. series a. mathematical and physical sciences*, 229(1178):317–345, 1955. URL <https://doi.org/10.1098/rspa.1955.0089>. (Cited on pages 17 and 18.)
- Jing Lin, Runhe Zhu, Nan Li, and Burcin Becerik-Gerber. Do people follow the crowd in building emergency evacuation? a cross-cultural immersive virtual reality-based study. *Advanced Engineering Informatics*, 43:101040, 2020. URL <https://doi.org/10.1016/j.aei.2020.101040>. (Cited on pages 34 and 45.)
- Xiaoshan Lin and T-T Ng. A three-dimensional discrete element model using arrays of ellipsoids. *Geotechnique*, 47(2):319–329, 1997. URL <https://www.icvirtuallibrary.com/doi/abs/10.1680/geot.1997.47.2.319>. (Cited on page 32.)
- Carolyn Liss. Maritime piracy in southeast asia. In Daljit Singh and Chin Kin Wah, editors, *Southeast Asian Affairs 2003*, pages 52–70. ISEAS Publishing, Singapore, 2003. ISBN 981-230-216-6. URL <https://www.degruyter.com/document/doi/10.1355/9789812306937-006/pdf?licenseType=restricted>. (Cited on page 71.)
- Mingyue Liu, Ryan D Quarrington, Baptiste Sandoz, William SP Robertson, and Claire F Jones. Neck stiffness and range of motion for young males and females. *Journal of Biomechanics*, 168:112090, 2024. URL <https://doi.org/10.1016/j.jbiomech.2024.112090>. (Cited on pages 37, 105, and 136.)
- TE Lobdell, CK Kroell, DC Schneider, WE Hering, and AM Nahum. Impact response of the human thorax. *Human impact response: Measurement and simulation*, pages 201–245, 1973. URL https://doi.org/10.1007/978-1-4757-1502-6_11. (Cited on page 30.)
- Graham Loomes and Robert Sugden. Incorporating a stochastic element into decision theories. *European Economic Review*, 39(3-4):641–648, 1995. URL [https://doi.org/10.1016/0014-2921\(94\)00071-7](https://doi.org/10.1016/0014-2921(94)00071-7). (Cited on page 14.)

BIBLIOGRAPHY

- Ugo Lopez, Jacques Gautrais, Iain D Couzin, and Guy Theraulaz. From behavioural analyses to models of collective motion in fish schools. *Interface focus*, 2(6):693–707, 2012. URL <https://doi.org/10.1098/rsfs.2012.0033>. (Cited on page 2.)
- Boris D Lubachevsky, Vladimir Privman, and Subhas C Roy. Casting pearls ballistically: Efficient massively parallel simulation of particle deposition. *Journal of Computational Physics*, 126(1):152–164, 1996. URL <https://www.sciencedirect.com/science/article/pii/S0021999196901278>. (Cited on page 32.)
- Lindsay W Ludlow and Peter G Weyand. Energy expenditure during level human walking: seeking a simple and accurate predictive solution. *Journal of Applied Physiology*, 120(5):481–494, 2016. URL <https://doi.org/10.1152/japplphysiol.00864.2015>. (Cited on page 135.)
- R Mahnke and N Pieret. Stochastic master-equation approach to aggregation in freeway traffic. *Physical Review E*, 56(3):2666, 1997. URL <https://doi.org/10.1103/PhysRevE.56.2666>. (Cited on pages 14 and 15.)
- Barbara Majecka. Statistical models of pedestrian behaviour in the forum. Master’s thesis, School of Informatics, University of Edinburgh, 2009. URL https://homepages.inf.ed.ac.uk/rbf/DISSERTATIONS/msc_20090787.pdf. (Cited on page 46.)
- Michail Makridis, Konstantinos Mattas, Aikaterini Anesiadou, and Biagio Ciuffo. OpenACC. an open database of car-following experiments to study the properties of commercial ACC systems. *Transportation Research Part C: Emerging Technologies*, 125:103047, 2021. URL <https://doi.org/10.1016/j.trc.2021.103047>. (Cited on page 91.)
- M Lisa Manning. Essay: Collections of deformable particles present exciting challenges for soft matter and biological physics. *Physical Review Letters*, 130(13):130002, 2023. URL <https://doi.org/10.1103/PhysRevLett.130.130002>. (Cited on page 64.)
- Bertrand Maury and Juliette Venel. A discrete contact model for crowd motion. *ESAIM: Mathematical Modelling and Numerical Analysis*, 45(1):145–168, January 2011. ISSN 0764-583X, 1290-3841. URL <https://doi.org/10.1051/m2an/2010035>. (Cited on pages 28, 29, and 30.)
- MechanicalTurk. Amazon mechanical turk. <https://www.mturk.com/>, 2005. (Cited on page 12.)
- Laurentius Antonius Meerhoff, Julien Bruneau, Alexandre Vu, A-H Olivier, and Julien Pettré. Guided by gaze: Prioritization strategy when navigating through a virtual crowd can be assessed through gaze activity. *Acta psychologica*, 190:248–257, 2018. URL <https://doi.org/10.1016/j.actpsy.2018.07.009>. (Cited on page 19.)
- George A. Miller. The magical number seven, plus or minus two: Some limits on our capacity for processing information. *Psychological Review*, 63(2):81–97, 1956. ISSN 1939-1471. doi: 10.1037/h0043158. URL <https://psycnet.apa.org/record/1957-02914-001>. (Cited on page 20.)
- Raymond D Mindlin and HERBERT Deresiewicz. Elastic spheres in contact under varying oblique forces. *Journal of Applied Mechanics*, 1953. URL <https://doi.org/10.1115/1.4010702>. (Cited on page 125.)
- Raymond David Mindlin. Compliance of elastic bodies in contact. *J. Appl. Mech.*, 1949. URL <https://doi.org/10.1115/1.4009973>. (Cited on page 74.)
- Chraïbi Mohcine and Oscar Dufour. madras-data-app, feb 2024. URL <https://madras-data-app.streamlit.app/>. (Cited on page 59.)
- Masamitsu Mōri and Hiroshi Tsukaguchi. A new method for evaluation of level of service in pedestrian facilities. *Transportation Research Part A: General*, 21(3):223–234, 1987. URL [https://doi.org/10.1016/0191-2607\(87\)90016-1](https://doi.org/10.1016/0191-2607(87)90016-1). (Cited on pages 15 and 83.)
- Alexander N Morozov and Wim van Saarloos. An introductory essay on subcritical instabilities and the transition to turbulence in visco-elastic parallel shear flows. *Physics Reports*, 447(3-6):112–143, 2007. URL <https://doi.org/10.1016/j.physrep.2007.03.004>. (Cited on page 97.)
- Jürgen Moser. Is the solar system stable? *The Mathematical Intelligencer*, 1:65–71, 1978. URL https://people.math.harvard.edu/~knill/teaching/mathe320_2014/blog/MoserSolar.pdf. (Cited on page 90.)
- Mehdi Moussaïd, Niriaska Perozo, Simon Garnier, Dirk Helbing, and Guy Theraulaz. The walking behaviour of pedestrian social groups and its impact on crowd dynamics. *PloS one*, 5(4):e10047, 2010. URL <https://doi.org/10.1371/journal.pone.0010047>. (Cited on page 27.)
- Hisashi Murakami, Claudio Feliciani, Yuta Nishiyama, and Katsuhiro Nishinari. Mutual anticipation can contribute to self-organization in human crowds. *Science Advances*, 7(12):eabe7758, 2021. URL <https://doi.org/10.1126/sciadv.abe7758>. (Cited on page 45.)
- RR Mussabayev, MN Kalimoldayev, Ye N Amirgaliyev, AT Tairova, and TR Mussabayev. Calculation of 3d coordinates of a point on the basis of a stereoscopic system. *Open Engineering*, 8(1):109–117, 2018. URL <https://doi.org/10.1515/eng-2018-0016>. (Cited on page 49.)
- Takashi Nagatani. Modified kdv equation for jamming transition in the continuum models of traffic. *Physica A: Statistical Mechanics and Its Applications*, 261(3-4):599–607, 1998a. URL [https://doi.org/10.1016/S0378-4371\(98\)00347-1](https://doi.org/10.1016/S0378-4371(98)00347-1). (Cited on page 17.)
- Takashi Nagatani. Thermodynamic theory for the jamming transition in traffic flow. *Physical Review E*, 58(4):4271, 1998b. URL <https://doi.org/10.1103/PhysRevE.58.4271>. (Cited on page 99.)
- Takashi Nagatani. Density waves in traffic flow. *Physical Review E*, 61(4):3564, 2000. URL <https://doi.org/10.1103/PhysRevE.61.3564>. (Cited on page 21.)
- Takashi Nagatani. The physics of traffic jams. *Reports on progress in physics*, 65(9):1331, 2002. URL <https://doi.org/10.1088/0034-4885/65/9/203>. (Cited on page 99.)

-
- Takashi Nagatani and Ken Nakanishi. Delay effect on phase transitions in traffic dynamics. *Physical Review E*, 57(6):6415, 1998. URL <https://doi.org/10.1103/PhysRevE.57.6415>. (Cited on pages 91 and 100.)
- Akihiro Nakayama, Minoru Fukui, Macoto Kikuchi, Katsuya Hasebe, Katsuhiko Nishinari, Yuki Sugiyama, Shin-ichi Tadaki, and Satoshi Yukawa. Metastability in the formation of an experimental traffic jam. *New Journal of Physics*, 11(8):083025, 2009. URL <https://doi.org/10.1088/1367-2630/11/8/083025>. (Cited on pages 91 and 96.)
- Author's Name. Analysis of polygonal shapes. Technical Report ADA183444, Defense Technical Information Center, 1987. URL <https://apps.dtic.mil/sti/citations/ADA183444>. (Cited on page 129.)
- Sahil Narang, Andrew Best, and Dinesh Manocha. Interactive simulation of local interactions in dense crowds using elliptical agents. *Journal of Statistical Mechanics: Theory and Experiment*, 2017(3):033403, 2017. URL <https://doi.org/10.1088/1742-5468/aa58ab>. (Cited on page 29.)
- Margot M. E. Neggers, Raymond H. Cuijpers, Peter A. M. Ruijten, and Wijnand A. IJsselsteijn. Determining Shape and Size of Personal Space of a Human when Passed by a Robot. *International Journal of Social Robotics*, 14(2):561–572, March 2022. ISSN 1875-4805. doi: 10.1007/s12369-021-00805-6. URL <https://doi.org/10.1007/s12369-021-00805-6>. (Cited on pages 39 and 78.)
- Erik Neumann. myphysicslab: Physics simulations, 2001. URL <https://www.mypysicslab.com/>. (Cited on page 93.)
- Gordon Frank Newell. Nonlinear effects in the dynamics of car following. *Operations research*, 9(2):209–229, 1961. URL <https://pubsonline.informs.org/doi/abs/10.1287/opre.9.2.209>. (Cited on page 18.)
- Robert C Newman and Donald Pollack. Proxemics in deviant adolescents. *Journal of Consulting and Clinical Psychology*, 40(1):6, 1973. URL <https://psycnet.apa.org/doi/10.1037/h0033961>. (Cited on page 39.)
- D. Ngoduy. Noise-induced instability of a class of stochastic higher order continuum traffic models. *Transportation Research Part B: Methodological*, 150:260, 2021. URL <https://doi.org/10.1016/j.trb.2021.06.013>. (Cited on pages 92 and 97.)
- Dong Ngoduy. Effect of the car-following combinations on the instability of heterogeneous traffic flow. *Transportmetrica B: Transport Dynamics*, 3(1):44–58, 2015. URL <https://doi.org/10.1080/21680566.2014.960503>. (Cited on page 147.)
- Alexandre Nicolas and Fadratul Hafinaz Hassan. Social groups in pedestrian crowds: review of their influence on the dynamics and their modelling. *Transportmetrica A: transport science*, 19(1):1970651, 2023. URL <https://doi.org/10.1080/23249935.2021.1970651>. (Cited on page 59.)
- Alexandre Nicolas, Marcelo Kuperman, Santiago Ibañez, Sebastián Bouzat, and Cécile Appert-Rolland. Mechanical response of dense pedestrian crowds to the crossing of intruders. *Scientific reports*, 9(1):105, 2019. URL <https://doi.org/10.1038/s41598-018-36711-7>. (Cited on pages 45, 64, and 70.)
- S.J. Older. *Movement of Pedestrians on Footways in Shopping Streets*. Traffic engineering & control, 1968. URL <https://books.google.fr/books?id=mOdYcgAACAAJ>. (Cited on pages 15 and 83.)
- Anne-Hélène Olivier. *Analyse dans le plan courbure-vitesse d'un changement de direction lors de la marche*. Theses, Université Rennes 2 ; Université Rennes 1, December 2008. URL <https://theses.hal.science/tel-00370546>. (Cited on page 79.)
- Anne-Hélène Olivier, Julien Bruneau, Gabriel Cirio, and Julien Pettré. A virtual reality platform to study crowd behaviours. *Transportation Research Procedia*, 2:114–122, 2014. URL <https://doi.org/10.1016/j.trpro.2014.09.015>. (Cited on page 45.)
- Donald M Olsson and Lloyd S Nelson. The nelder-mead simplex procedure for function minimization. *Technometrics*, 17(1):45–51, 1975. URL <https://doi.org/10.1080/00401706.1975.10489269>. (Cited on page 77.)
- Gábor Orosz, R.E. Wilson, and Bernd Krauskopf. Global bifurcation investigation of an optimal velocity traffic model with driver reaction time. *Physical Review E*, 70(2):026207, 2004. URL <https://doi.org/10.1103/PhysRevE.70.026207>. (Cited on pages 91, 95, and 96.)
- Gábor Orosz, Bernd Krauskopf, and R.E. Wilson. Bifurcations and multiple traffic jams in a car-following model with reaction-time delay. *Physica D: Nonlinear Phenomena*, 211(3):277–293, 2005. ISSN 0167-2789. doi: 10.1016/j.physd.2005.09.004. (Cited on page 97.)
- Gábor Orosz, R.E. Wilson, and Gábor Stépán. Traffic jams: dynamics and control, 2010. URL <https://doi.org/10.1098/rsta.2010.0205>. (Cited on page 91.)
- Carolyn O'Fallon and Charles Sullivan. Understanding and managing weekend traffic congestion. In *at 26th ATRF Conference*, 2003. URL https://australasiantransportresearchforum.org.au/wp-content/uploads/2022/03/2003_OFallon_Sullivan_c.pdf. (Cited on page 6.)
- Daniel R Parisi, Raúl Cruz Hidalgo, and Iker Zuriguel. Active particles with desired orientation flowing through a bottleneck. *Scientific Reports*, 8(1):9133, 2018. URL <https://doi.org/10.1038/s41598-018-27478-y>. (Cited on page 41.)
- José M Pastor, Angel Garcimartín, Paula A Gago, Juan P Peralta, César Martín-Gómez, Luis M Ferrer, Diego Maza, Daniel R Parisi, Luis A Pugnali, and Iker Zuriguel. Experimental proof of faster-is-slower in systems of frictional particles flowing through constrictions. *Physical Review E*, 92(6):062817, 2015. URL <https://doi.org/10.1103/PhysRevE.92.062817>. (Cited on pages 45 and 70.)
- Aftab E Patla. Understanding the roles of vision in the control of human locomotion. *Gait & posture*, 5(1):54–69, 1997. URL [https://doi.org/10.1016/S0966-6362\(96\)01109-5](https://doi.org/10.1016/S0966-6362(96)01109-5). (Cited on page 16.)

- Pakpoom Patompak, Sungmoon Jeong, Itthisek Nilkhamhang, and Nak Young Chong. Learning proxemics for personalized human–robot social interaction. *International Journal of Social Robotics*, 12:267–280, 2020. URL <https://doi.org/10.1007/s12369-019-00560-9>. (Cited on pages 38, 39, and 42.)
- Stefano Pellegrini, Andreas Ess, Konrad Schindler, and Luc Van Gool. You’ll never walk alone: Modeling social behavior for multi-target tracking. In *2009 IEEE 12th international conference on computer vision*, pages 261–268. IEEE, 2009. URL <https://doi.org/10.1109/ICCV.2009.5459260>. (Cited on page 46.)
- Julien Pettre. Chaos: Crowd animation open software, 2024. URL <https://project.inria.fr/crowdscience/project/ocsr/chaos/>. Inria Research Project. (Cited on page 15.)
- Frederike H Petzschner, Stefan Glasauer, and Klaas E Stephan. A bayesian perspective on magnitude estimation. *Trends in cognitive sciences*, 19(5):285–293, 2015. URL https://www.researchgate.net/profile/Frederike-Petzschner/publication/274406769_A_Bayesian_perspective_on_magnitude_estimation/links/5b9235bf92851c78c4f3f134/A-Bayesian-perspective-on-magnitude-estimation.pdf. (Cited on pages 13 and 35.)
- Benedetto Piccoli and Andrea Tosin. Pedestrian flows in bounded domains with obstacles. *Continuum Mechanics and Thermodynamics*, 21:85–107, 2009. URL <https://doi.org/10.1007/s00161-009-0100-x>. (Cited on page 16.)
- Louis A. Pipes. An operational analysis of traffic dynamics. *Journal of Applied Physics*, 24(3):274–281, 1953. URL <https://doi.org/10.1063/1.1721265>. (Cited on page 91.)
- Valentin L Popov and Markus Heß. *Method of dimensionality reduction in contact mechanics and friction*. Springer, 2015. URL https://www.researchgate.net/profile/Valentin-Popov-2/publication/326902750_Method_of_Dimensionality_Reduction_in_Contact_Mechanics_User’s_Manual/links/5b73d2bda6fdcc87df7dc572/Method-of-Dimensionality-Reduction-in-Contact-Mechanics-Users-Manual.pdf. (Cited on pages 74, 122, 123, and 126.)
- Valentin L Popov, Markus Heß, and Emanuel Willert. *Handbook of contact mechanics: exact solutions of axisymmetric contact problems*. Springer Nature, 2019. URL <https://library.oapen.org/bitstream/handle/20.500.12657/23291/1006864.pdf?sequence>. (Cited on page 125.)
- Valentin L Popov et al. *Contact mechanics and friction*. Springer, 2010. URL <https://doi.org/10.1007/978-3-662-53081-8>. (Cited on page 123.)
- Micha Popper. Why do people follow? In Laurent M. Lapiere and Melissa K. Carsten, editors, *Followership: What is it and Why do People Follow?*, pages 109–120. Emerald, 2014. URL <https://www.emeraldgroupublishing.com/archived/products/books/notable/page.htm%3Fid%3D9781783505159>. (Cited on page 34.)
- Thorsten Pöschel and Volkhard Buchholtz. Complex flow of granular material in a rotating cylinder. *Chaos, Solitons & Fractals*, 5(10):1901–1912, 1995. URL [https://doi.org/10.1016/0960-0779\(94\)00193-T](https://doi.org/10.1016/0960-0779(94)00193-T). (Cited on page 32.)
- Emmanuel Ravalet. Modes de vie et modes de ville, activités et déplacements quotidiens à montréal et lyon. *Environnement urbain/Urban Environment*, Volume 1, 2007. URL <https://journals.openedition.org/eue/1054>. (Cited on page 7.)
- Jürgen Richter-Gebert. *Perspectives on projective geometry: a guided tour through real and complex geometry*. Springer, 2011. URL <https://doi.org/10.1007/978-3-642-17286-1>. (Cited on page 138.)
- Alexandre Robicquet, Amir Sadeghian, Alexandre Alahi, and Silvio Savarese. Stanford drone dataset, 2016. URL https://cvgl.stanford.edu/projects/uav_data/. (Cited on page 46.)
- Gabriel Robins and Alexander Zelikovsky. Minimum steiner tree construction. In *Handbook of algorithms for physical design automation*, pages 487–508. Auerbach Publications, 2008. URL https://www.cs.virginia.edu/~robins/papers/Steiner_chapter.pdf. (Cited on page 10.)
- José I Ronda and Antonio Valdés. Geometrical analysis of polynomial lens distortion models. *Journal of Mathematical Imaging and Vision*, 61:252–268, 2019. URL <https://doi.org/10.1007/s10851-018-0833-x>. (Cited on page 117.)
- Leo Rothenburg and Richard J Bathurst. Numerical simulation of idealized granular assemblies with plane elliptical particles. *Computers and geotechnics*, 11(4):315–329, 1991. URL [https://doi.org/10.1016/0266-352X\(91\)90015-8](https://doi.org/10.1016/0266-352X(91)90015-8). (Cited on page 32.)
- A. Schadschneider, D. Chowdhury, and K. Nishinari. *Stochastic Transport in Complex Systems: From Molecules to Vehicles*. Elsevier Science, 2010. ISBN 9780080560526. URL <https://books.google.fr/books?id=dRcxsa4sobQC>. (Cited on pages 15, 92, 94, and 96.)
- Andreas Schadschneider. Cellular automaton approach to pedestrian dynamics-theory. *arXiv preprint cond-mat/0112117*, 2001. URL <https://doi.org/10.48550/arXiv.cond-mat/0112117>. (Cited on page 14.)
- Schrödter, Tobias and The PedPy Development Team. Pedestriandynamics/pedpy: v1.0.2, oct 2023. URL <https://doi.org/10.5281/zenodo.10016938>. (Cited on page 59.)
- Claudio Sedazzari. Image quality basics, 2015. URL <https://www.opto-e.com/en/basics/image-quality>. (Cited on page 117.)
- Michael J Seitz and Gerta Köster. Natural discretization of pedestrian movement in continuous space. *Physical Review E—Statistical, Nonlinear, and Soft Matter Physics*, 86(4):046108, 2012. URL <https://doi.org/10.1103/PhysRevE.86.046108>. (Cited on page 7.)
- Michael J Seitz, Nikolai WF Bode, and Gerta Köster. How cognitive heuristics can explain social interactions in spatial movement. *Journal of the Royal Society Interface*, 13(121):20160439, 2016. URL <https://doi.org/10.1098/rsif.2016.0439>. (Cited on page 34.)

- Prianka N Seneviratne and John F Morrall. Analysis of factors affecting the choice of route of pedestrians. *Transportation Planning and Technology*, 10(2):147–159, 1985. URL <https://doi.org/10.1080/03081068508717309>. (Cited on pages 7 and 10.)
- Avinash Sharma, Brian McCloskey, David S. Hui, Aayushi Rambia, Adam Zumla, Tieble Traore, Shuja Shafi, Sherif A. El-Kafrawy, Esam I. Azhar, Alimuddin Zumla, and Alfonso J. Rodriguez-Morales. Global mass gathering events and deaths due to crowd surge, stampedes, crush and physical injuries – lessons from the seoul halloween and other disasters. *Travel Medicine and Infectious Disease*, 52:102524, 2023a. ISSN 1477-8939. URL <https://doi.org/10.1016/j.tmaid.2022.102524>. (Cited on page 44.)
- Avinash Sharma, Brian McCloskey, David S Hui, Aayushi Rambia, Adam Zumla, Tieble Traore, Shuja Shafi, Sherif A El-Kafrawy, Esam I Azhar, Alimuddin Zumla, et al. Global mass gathering events and deaths due to crowd surge, stampedes, crush and physical injuries-lessons from the seoul halloween and other disasters. *Travel medicine and infectious disease*, 52, 2023b. URL <https://doi.org/10.1016/j.tmaid.2022.102524>. (Cited on page 44.)
- Alastair Shipman, Arnab Majumdar, Zhenan Feng, and Ruggiero Lovreglio. A quantitative comparison of virtual and physical experimental paradigms for the investigation of pedestrian responses in hostile emergencies. *Scientific reports*, 14(1):6892, 2024. URL <https://doi.org/10.1038/s41598-024-55253-9>. (Cited on page 45.)
- Anna Sieben and Armin Seyfried. Inside a life-threatening crowd: Analysis of the love parade disaster from the perspective of eyewitnesses. *Safety science*, 166:106229, 2023. URL <https://doi.org/10.1016/j.ssci.2023.106229>. (Cited on pages 44 and 46.)
- RA Smith and LB Lim. Experiments to investigate the level of ‘comfortable’ loads for people against crush barriers. *Safety science*, 18(4):329–335, 1995. URL [https://doi.org/10.1016/0925-7535\(94\)00052-5](https://doi.org/10.1016/0925-7535(94)00052-5). (Cited on page 30.)
- Michaël Soullignac and Patrick Taillibert. Fast trajectory planning for multiple site surveillance through moving obstacles and wind. In *Proceedings of the Workshop of the UK Planning and Scheduling Special Interest Group*, pages 25–33, 2006. URL https://www.cs.nott.ac.uk/~pszrq/PlanSIG/soullignac_taillibert.pdf. (Cited on pages 10 and 11.)
- Martijn Sparnaaij, Yufei Yuan, Winnie Daamen, and Dorine C Duives. A novel activity choice and scheduling model to model activity schedules of customers and staff in dutch restaurants. *arXiv preprint arXiv:2204.06775*, 2022. URL <https://doi.org/10.48550/arXiv.2204.06775>. (Cited on page 7.)
- Raphael E. Stern, Shumo Cui, Maria Laura Delle Monache, Rahul Bhadani, Matt Bunting, Miles Churchill, Nathaniel Hamilton, R’mani Haulcy, Hannah Pohlmann, Fangyu Wu, Benedetto Piccoli, Benjamin Seibold, Jonathan Sprinkle, and Daniel B. Work. Dissipation of stop-and-go waves via control of autonomous vehicles: Field experiments. *Transportation Research Part C: Emerging Technologies*, 89:205–221, 2018. ISSN 0968-090X. URL <https://doi.org/10.1016/j.trc.2018.02.005>. (Cited on page 91.)
- Yuki Sugiyama, Minoru Fukui, Macoto Kikuchi, Katsuya Hasebe, Akihiro Nakayama, Katsuhiko Nishinari, Shin-ichi Tadaki, and Satoshi Yukawa. Traffic jams without bottlenecks—experimental evidence for the physical mechanism of the formation of a jam. *New journal of physics*, 10(3):033001, 2008. URL <https://doi.org/10.1088/1367-2630/10/3/033001>. (Cited on pages 17, 18, 90, 91, 94, 95, 96, 141, and 144.)
- T. Editors of Encyclopaedia Britannica. Erector spinae. <https://www.britannica.com/science/erector-spinae>, August 2023. (Cited on page 103.)
- Shin-ichi Tadaki, Macoto Kikuchi, Minoru Fukui, Akihiro Nakayama, Katsuhiko Nishinari, Akihiro Shibata, Yuki Sugiyama, Taturu Yosida, and Satoshi Yukawa. Phase transition in traffic jam experiment on a circuit. *New Journal of Physics*, 15(10):103034, 2013. URL <https://dx.doi.org/10.1088/1367-2630/15/10/103034>. (Cited on pages 91, 94, 96, 100, and 141.)
- Junfang Tian, Rui Jiang, Bin Jia, Ziyou Gao, and Shoufeng Ma. Empirical analysis and simulation of the concave growth pattern of traffic oscillations. *Transportation Research Part B: Methodological*, 93:338–354, 2016. URL <https://doi.org/10.1016/j.trb.2016.08.001>. (Cited on page 91.)
- Junfang Tian, HM Zhang, Martin Treiber, Rui Jiang, Zi-You Gao, and Bin Jia. On the role of speed adaptation and spacing indifference in traffic instability: Evidence from car-following experiments and its stochastic model. *Transportation research part B: methodological*, 129:334–350, 2019. URL <https://doi.org/10.1016/j.trb.2019.09.014>. (Cited on pages 91 and 92.)
- Peter M Todd and Gerd Gigerenzer. Précis of simple heuristics that make us smart. *Behavioral and brain sciences*, 23(5):727–741, 2000. URL <https://doi.org/10.1017/S0140525X00003447>. (Cited on page 34.)
- Elad Tomer, Leonid Safonov, and Shlomo Havlin. Presence of many stable nonhomogeneous states in an inertial car-following model. *Physical Review Letters*, 84(2):382, 2000. URL <https://doi.org/10.1103/PhysRevLett.84.382>. (Cited on pages 91, 94, and 142.)
- Antoine Tordeux, Sylvain Lassarre, and Michel Roussignol. An adaptive time gap car-following model. *Transportation Research Part B: Methodological*, 44(8-9):1115–1131, 2010. URL <https://doi.org/10.1016/j.trb.2009.12.018>. (Cited on pages 91 and 142.)
- Antoine Tordeux, Michel Roussignol, and Sylvain Lassarre. Linear stability analysis of first-order delayed car-following models on a ring. *Physical Review E*, 86(3):036207, 2012. ISSN 1539-3755, 1550-2376. URL <https://doi.org/10.1103/PhysRevE.86.036207>. (Cited on page 91.)
- Antoine Tordeux, Guillaume Costeseque, Michael Herty, and Armin Seyfried. From Traffic and Pedestrian Follow-the-Leader Models with Reaction Time to First Order Convection-Diffusion Flow Models. *SIAM Journal on Applied Mathematics*, 78(1):63–79, January 2018. ISSN 0036-1399. doi: 10.1137/16M110695X. URL <https://doi.org/10.1137/16M110695X>. (Cited on pages 15, 23, and 91.)

- Anna Torén. Muscle activity and range of motion during active trunk rotation in a sitting posture. *Applied Ergonomics*, 32(6):583–591, 2001. URL [https://doi.org/10.1016/S0003-6870\(01\)00040-0](https://doi.org/10.1016/S0003-6870(01)00040-0). (Cited on page 37.)
- M Treiber and Dirk Helbing. Hamilton-like statistics in onedimensional driven dissipative many-particle systems. *The European Physical Journal B*, 68:607–618, 2009. URL <https://doi.org/10.1140/epjb/e2009-00121-8>. (Cited on pages 94 and 142.)
- Martin Treiber and Arne Kesting. The intelligent driver model with stochasticity-new insights into traffic flow oscillations. *Transportation research procedia*, 23:174–187, 2017. URL <https://doi.org/10.1016/j.trpro.2017.05.011>. (Cited on pages 92, 94, 95, 97, and 142.)
- Martin Treiber, Ansgar Hennecke, and Dirk Helbing. Congested traffic states in empirical observations and microscopic simulations. *Physical Review E*, 62(2):1805–1824, August 2000. URL <https://doi.org/10.1103/PhysRevE.62.1805>. (Cited on page 91.)
- U.S. National Library of Medicine. Visible human project, 1994, 1995. URL https://datadiscovery.nlm.nih.gov/Images/Visible-Human-Project/ux2j-9i9a/about_data. (Cited on pages 72 and 73.)
- Jur Van Den Berg, Stephen J Guy, Ming Lin, and Dinesh Manocha. Reciprocal n-body collision avoidance. In *Robotics Research: The 14th International Symposium ISRR*, pages 3–19. Springer, 2011. URL https://doi.org/10.1007/978-3-642-19457-3_1. (Cited on page 54.)
- Wouter van Toll, Fabien Grzeskowiak, Axel López Gandía, Javad Amirian, Florian Berton, Julien Bruneau, Beatriz Cabrero Daniel, Alberto Jovane, and Julien Pettré. Generalized microscopic crowd simulation using costs in velocity space. In *Symposium on Interactive 3D Graphics and Games*, pages 1–9, 2020. URL <https://doi.org/10.1145/3384382.3384532>. (Cited on page 1.)
- Lakshmi Devi Vanumu, K Ramachandra Rao, and Geetam Tiwari. Fundamental diagrams of pedestrian flow characteristics: A review. *European transport research review*, 9:1–13, 2017. URL <https://doi.org/10.1007/s12544-017-0264-6>. (Cited on page 54.)
- Cédric Villani. La meilleure et la pire des erreurs de poincaré. In *Conférence donnée à l'Université de Lille1*, 2012. URL https://www.apmep.fr/IMG/pdf/503_Villani-Metz.pdf. (Cited on page 90.)
- John Von Neumann and Oskar Morgenstern. *Theory of games and economic behavior, 2nd rev.* Princeton university press, 1947. URL <https://psycnet.apa.org/record/1947-03159-000>. (Cited on page 13.)
- Dhairya R Vyas, Julio M Ottino, Richard M Lueptow, and Paul B Umbanhowar. Improved velocity-verlet algorithm for the discrete element method. *arXiv preprint arXiv:2410.14798*, 2024. URL <https://doi.org/10.48550/arXiv.2410.14798>. (Cited on page 131.)
- Peter Wagner. A time-discrete harmonic oscillator model of human car-following. *The European Physical Journal B*, 84:713–718, 2011. URL <https://doi.org/10.1140/epjb/e2011-20722-8>. (Cited on pages 94 and 142.)
- Jiajia Wang, Zhihui Qian, Lei Ren, and Luquan Ren. A dynamic finite element model of human cervical spine with in vivo kinematic validation. *Chinese science bulletin*, 59:4578–4588, 2014. URL <https://doi.org/10.1007/s11434-014-0452-x>. (Cited on page 105.)
- Jinghui Wang, Wei Lv, Huihua Jiang, Zhiming Fang, and Jian Ma. Exploring crowd persistent dynamism from pedestrian crossing perspective: An empirical study. *Transportation research part C: emerging technologies*, 157:104400, 2023. URL <https://doi.org/10.1016/j.trc.2023.104400>. (Cited on pages 62 and 64.)
- Q. Jane Wang and Dong Zhu. Hertz theory: Contact of ellipsoidal surfaces. In *Encyclopedia of Tribology*, pages 1647–1654. Springer US, Boston, MA, 2013a. ISBN 978-0-387-92897-5. URL https://doi.org/10.1007/978-0-387-92897-5_493. (Cited on page 124.)
- Q.J. Wang and D. Zhu. Hertz theory: Contact of spherical surfaces. In Q.J. Wang and Y.W. Chung, editors, *Encyclopedia of Tribology*, pages 1876–1882. Springer, Boston, MA, 2013b. ISBN 978-0-387-92896-8. doi: 10.1007/978-0-387-92897-5_492. URL https://link.springer.com/referenceworkentry/10.1007/978-0-387-92897-5_492. (Cited on page 122.)
- Yu Wang, Xiaopeng Li, Junfang Tian, and Rui Jiang. Stability analysis of stochastic linear car-following models. *Transportation Science*, 54(1):274–297, 2020. URL <https://doi.org/10.1287/trsc.2019.0932>. (Cited on pages 94 and 142.)
- Ulrich Weidmann. Transporttechnik der fußgänger: transporttechnische eigenschaften des fußgängerverkehrs, literaturauswertung. *IVT Schriftenreihe*, 90, 1993. URL <https://doi.org/10.3929/ethz-a-000687810>. (Cited on pages 15 and 83.)
- Kurt Wiesenfeld. Noisy precursors of nonlinear instabilities. *Journal of Statistical Physics*, 38:1071–1097, 1985. URL <https://doi.org/10.1007/BF01010430>. (Cited on page 92.)
- John R Williams and Alex P Pentland. Superquadrics and modal dynamics for discrete elements in interactive design. *Engineering Computations*, 9(2):115–127, 1992. URL <https://www.emerald.com/insight/content/doi/10.1108/eb023852/full/pdf>. (Cited on page 32.)
- R Eddie Wilson. Mechanisms for spatio-temporal pattern formation in highway traffic models. *Philosophical Transactions of the Royal Society A: Mathematical, Physical and Engineering Sciences*, 366(1872):2017–2032, 2008. URL <https://doi.org/10.1098/rsta.2008.0018>. (Cited on page 92.)
- R.E. Wilson and J.A. Ward. Car-following models: Fifty years of linear stability analysis – a mathematical perspective. *Transportation Planning and Technology*, 34(1):3–18, 2011. ISSN 0308-1060. URL <https://doi.org/10.1080/03081060.2011.530826>. (Cited on page 91.)

-
- Trenton D Wirth, Gregory C Dachner, Kevin W Rio, and William H Warren. Is the neighborhood of interaction in human crowds metric, topological, or visual? *PNAS nexus*, 2(5):pgad118, 2023. URL <https://doi.org/10.1093/pnasnexus/pgad118>. (Cited on pages 19 and 20.)
- Martin Wirz, Tobias Franke, Daniel Roggen, Eve Mitleton-Kelly, Paul Lukowicz, and Gerhard Tröster. Probing crowd density through smartphones in city-scale mass gatherings. *EPJ Data Science*, 2:1–24, 2013. URL <https://doi.org/10.1140/epjds17>. (Cited on pages 45 and 54.)
- Hiroki Yamamoto, Daichi Yanagisawa, Claudio Feliciani, and Katsuhiko Nishinari. Body-rotation behavior of pedestrians for collision avoidance in passing and cross flow. *Transportation Research Part B: Methodological*, 122:486–510, April 2019. ISSN 0191-2615. doi: 10.1016/j.trb.2019.03.008. URL <https://doi.org/10.1016/j.trb.2019.03.008>. (Cited on page 87.)
- Tairan Yin, Ludovic Hoyet, Marc Christie, Marie-Paule Cani, and Julien Pettré. The one-man-crowd: Single user generation of crowd motions using virtual reality. *IEEE Transactions on Visualization and Computer Graphics*, 28(5):2245–2255, 2022. URL <https://doi.org/10.1109/TVCG.2022.3150507>. (Cited on page 45.)
- Warren Clarence Young, Richard Gordon Budynas, Ali M Sadegh, et al. *Roark's formulas for stress and strain*, volume 7. McGraw-hill New York, 2002. URL <https://jackson.engr.tamu.edu/wp-content/uploads/sites/229/2023/03/Roarks-formulas-for-stress-and-strain.pdf>. (Cited on page 122.)
- Alessandro Zanardi, Enrico Mion, Mattia Bruschetta, Saverio Bolognani, Andrea Censi, and Emilio Frazzoli. Urban driving games with lexicographic preferences and socially efficient nash equilibria. *IEEE Robotics and Automation Letters*, 6(3):4978–4985, 2021. URL <https://doi.org/10.3929/ethz-b-000476638>. (Cited on page 2.)
- Jun Zhang and Armin Seyfried. Comparison of intersecting pedestrian flows based on experiments. *Physica A: Statistical Mechanics and its Applications*, 405:316–325, 2014. URL <https://doi.org/10.1016/j.physa.2014.03.004>. (Cited on page 44.)
- Jun Zhang, Wolfram Klingsch, Andreas Schadschneider, and Armin Seyfried. Transitions in pedestrian fundamental diagrams of straight corridors and t-junctions. *Journal of Statistical Mechanics: Theory and Experiment*, 2011 (06):P06004, 2011. URL <https://doi.org/10.1088/1742-5468/2011/06/P06004>. (Cited on pages 15 and 83.)
- Yongxiang Zhao and HM Zhang. A unified follow-the-leader model for vehicle, bicycle and pedestrian traffic. *Transportation research part B: methodological*, 105:315–327, 2017. URL <https://doi.org/10.1016/j.trb.2017.09.004>. (Cited on page 34.)
- Bolei Zhou, Xiaogang Wang, and Xiaoou Tang. Grand central station dataset, 2012. URL <https://www.ee.cuhk.edu.hk/~xgwang/grandcentral.html>. (Cited on page 46.)
- Verena Ziemer, Armin Seyfried, and Andreas Schadschneider. Congestion dynamics in pedestrian single-file motion. In Victor L. Knoop and Winnie Daamen, editors, *Traffic and Granular Flow '15*, pages 89–96, Cham, 2016. Springer International Publishing. URL doi.org/10.1007/978-3-319-33482-0_12. (Cited on pages 17, 89, and 90.)
- Iker Zuriguel, Daniel Ricardo Parisi, Raúl Cruz Hidalgo, Celia Lozano, Alvaro Janda, Paula Alejandra Gago, Juan Pablo Peralta, Luis Miguel Ferrer, Luis Ariel Pugnaroni, Eric Clément, Diego Maza, Ignacio Pagonabarraga, and Angel Garcimartín. Clogging transition of many-particle systems flowing through bottlenecks. *Scientific Reports*, 4(1):7324, December 2014. ISSN 2045-2322. doi: 10.1038/srep07324. URL <https://doi.org/10.1038/srep07324>. (Cited on page 33.)
- Émilie Josse. Graphisme pour la science - des visuels efficaces, 2024. URL <https://graphismepourlascience.fr>. (Cited on page 77.)